

(12)

AD-A140 803

ARVIN/CALSPAN

ADVANCED TECHNOLOGY CENTER

STUDIES OF BOUNDARY LAYER TRANSITION AND
SURFACE ROUGHNESS EFFECTS IN HYPERSONIC FLOW

FINAL REPORT

Covering Period 1 November 1978 - 30 September 1982
Calspan Report No. 6430-A-5
October 1983

TECHNICAL REPORT

DTIC FILE COPY

DTIC
EL
S MAY 7 1984
A

PO BOX 400, BUFFALO, NEW YORK 14225

APPLIED TECHNOLOGY GROUP OF ARVIN INDUSTRIES INC

AG
ARVIN

84 04 24 008

Approved for public release
Distribution unlimited.

(12)

ARVIN/CALSPAN

STUDIES OF BOUNDARY LAYER TRANSITION AND SURFACE ROUGHNESS EFFECTS IN HYPERSONIC FLOW

FINAL REPORT

Covering Period 1 November 1978 - 30 September 1982
Calspan Report No. 6430-A-5
October 1983

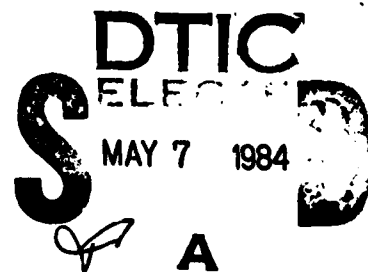
Contract No. F49620-79-C-0003

Prepared for:

AIR FORCE OFFICE OF SCIENTIFIC RESEARCH
BOLLING AIR FORCE BASE, D.C. 20332

Principal Investigator:

Michael S. Holden
Physical Sciences Department
Telephone No. (716) 631-6853



ADVANCED TECHNOLOGY CENTER P.O. BOX 400 BUFFALO, NEW YORK 14225

AIR FORCE OFFICE OF SCIENTIFIC RESEARCH (AFOSR)
NOTICE OF TECHNICAL INFORMATION
This technical report is available to the public in the
unclassified form in which it was submitted.
Distribution is unlimited.
MATTHEW J. H. [unclear]
Chief, Technical Information Division

UNCLASSIFIED

SECURITY CLASSIFICATION OF THIS PAGE (When Data Entered)

REPORT DOCUMENTATION PAGE		READ INSTRUCTIONS BEFORE COMPLETING FORM
1. REPORT NUMBER AFOSR-TR- 84-0251	2. GOVT ACCESSION NO. A140803K	3. RECIPIENT'S CATALOG NUMBER
4. TITLE (and Subtitle) STUDIES OF BOUNDARY LAYER TRANSITION AND SURFACE ROUGHNESS EFFECTS IN HYPERSONIC FLOW		5. TYPE OF REPORT & PERIOD COVERED Final Report 1 Nov 1978 - 30 Sept 1982
7. AUTHOR(s) Michael S. Holden		6. PERFORMING ORG. REPORT NUMBER 6430-A-5
9. PERFORMING ORGANIZATION NAME AND ADDRESS Calspan Advanced Technology Center P.O. Box 400, Buffalo, N.Y. 14225		8. CONTRACT OR GRANT NUMBER(s) F49620-79-C-0003
11. CONTROLLING OFFICE NAME AND ADDRESS Air Force Office of Scientific Research / NA Bolling Air Force Base, D.C. 20332		10. PROGRAM ELEMENT, PROJECT, TASK AREA & WORK UNIT NUMBERS 61102F 2307 / A1
14. MONITORING AGENCY NAME & ADDRESS (if different from Controlling Office)		12. REPORT DATE October 1983
		13. NUMBER OF PAGES 156
		15. SECURITY CLASS. (of this report) Unclassified
		15a. DECLASSIFICATION/DOWNGRADING SCHEDULE
16. DISTRIBUTION STATEMENT (of this Report) Approved for public release; distribution unlimited.		
17. DISTRIBUTION STATEMENT (of the abstract entered in Block 20, if different from Report)		
18. SUPPLEMENTARY NOTES		
19. KEY WORDS (Continue on reverse side if necessary and identify by block number)		
Hypersonic Flow	Stagnation-Region Heating	Maneuverable
Turbulent Boundary Layers	Heat Transfer	Re-entry
Surface Roughness	Skin Friction	Blunt-Body Flows
Boundary Layer Transition	Ballistic	Dust-Particle Effects
20. ABSTRACT (Continue on reverse side if necessary and identify by block number)		
<p>Four studies were conducted to investigate fundamental fluid-dynamics phenomena of importance to the aerothermal performance of hypersonic re-entry vehicles which have, in general, proved untractable to theoretical analysis.</p> <p>(continued)</p>		

UNCLASSIFIED

UNCLASSIFIED

SECURITY CLASSIFICATION OF THIS PAGE(When Data Entered)

20. ABSTRACT (continued)

A The first of the

The first study was a detailed experimental investigation of the effects of the shape and spacing of roughness elements on a maneuverable re-entry vehicle (MRV) configuration on the roughness-enhanced heating and skin friction. Measurements were made on slender cones and control flaps to define the relationships between roughness-element shape and spacing and the incremental heating and skin friction induced by the surface roughness. It was demonstrated that similar measurements in subsonic flows cannot be directly extrapolated to predict trends in high-speed compressible flows.

In the second study, the transition process in the stagnation region of a blunt body in hypersonic flow was examined in detail. The main focus was on determining what fluid-dynamic mechanics are responsible for enhanced heating in the stagnation region of high Reynolds number blunt-body flows. Investigated was whether upstream influence from transition, surface roughness in the stagnation region, minute dust particles in the freestream, or blowing in the stagnation region is the principal cause of stagnation-point heating enhancement.

The third study investigated the basic mechanics which occur when a number of minute dust particles interact with the shock layer ahead of a blunt body. The resulting considerable increases in stagnation heating were linked with the shear layers generated by particle-shock/bow-shock interactions and the tripping of the boundary layer in the stagnation region as each dust particle enters it.

In the fourth study, microsecond photographs and high-frequency thin-film measurements on slender cones were used to examine the breakdown of flow in and preceding the hypersonic boundary layer transition region. The results obtained provide insight into the mechanisms by which the laminar/turbulent boundary becomes unstable in high-speed boundary layers.



Accession For	
GRA&I	<input checked="checked" type="checkbox"/>
TAB	<input type="checkbox"/>
Unpublished	<input type="checkbox"/>
Classification	
Distribution/	
Availability Codes	
Dist	Avail and/or Special
A-1	

UNCLASSIFIED

SECURITY CLASSIFICATION OF THIS PAGE(When Data Entered)

CONTENTS

<u>Section</u>	<u>Title</u>	<u>Page</u>
1	SUMMARY	1
2	STUDIES OF EFFECTS OF SURFACE ROUGHNESS ON AEROTHERMAL PERFORMANCE OF SLENDER CONICAL VEHICLES WITH FLAP CONTROLS	3
2.1	INTRODUCTION AND SUMMARY	3
2.2	MODELS AND INSTRUMENTATION	7
2.2.1	The Models	7
2.2.2	Preparation of Model Sand-Grain and Patterned Rough Surfaces	10
2.2.3	Heat Transfer Instrumentation	15
2.2.4	Skin-Friction and Pressure Instrumentation	23
2.3	STUDIES OF SURFACE ROUGHNESS EFFECTS ON SLENDER CONES	23
2.3.1	Studies With Sand-Grain Roughness	23
2.3.2	Studies With Patterned Roughness	42
2.4	STUDIES OF SURFACE ROUGHNESS EFFECTS ON VISCOUS/INVISCID INTERACTION OVER FLAP CONTROLS	54
2.4.1	Studies With Sand-Grain Roughness	54
2.4.2	Studies With Patterned Roughness	67
3	STUDIES OF POTENTIAL FLUID-MECHANICAL MECHANISMS FOR ENHANCED STAGNATION-REGION HEATING	79
3.1	INTRODUCTION	79
3.2	MODELS AND INSTRUMENTATION	80
3.3	RESULTS AND DISCUSSION	86
4	STUDIES OF BASIC MECHANISMS OF ENHANCED HEATING IN HYPERSONIC DUSTY FLOWS OVER BLUNT BODIES	95
4.1	INTRODUCTION	95
4.2	MODEL AND INSTRUMENTATION	96
4.3	DISCUSSIONS OF BASIC MECHANISMS OF PARTICLE-ENHANCED HEATING	101
4.3.1	Minute-Particle/Boundary Layer Interaction	101
4.3.2	Toroidal-Vortex/Boundary Layer Interaction	102
4.3.3	Particle-Shock/Body-Shock Interaction	102
4.3.4	Effects of Separated Pulsating Flow	105
4.3.5	Multiple-Particle-Shock/Shock-Layer Interaction	115
4.3.6	Conclusions	125

CONTENTS (Cont.)

<u>Section</u>	<u>Title</u>	<u>Page</u>
5	EXPERIMENTAL STUDIES OF MECHANISMS OF BOUNDARY LAYER TRANSITION IN HYPERSONIC FLOW	127
5.1	INTRODUCTION	127
	5.1.1 Background	127
	5.1.2 Objectives of Experimental Program	129
5.2	MODEL AND INSTRUMENTATION	129
5.3	SIGNIFICANCE OF TEST FACILITY USED IN THESE STUDIES (TUNNEL NOISE VS. TRANSITION)	131
5.4	RESULTS OF PHOTOGRAPHIC AND HEAT TRANSFER OBSERVATIONS OF BOUNDARY LAYER TRANSITION IN HYPERSONIC FLOW	137
	5.4.1 Observations on General Characteristics of Transition Regions	137
	5.4.2 Wake-Like Instability Region	140
	5.4.3 Gross-Instability Region	140
	5.4.4 Gross-Mixing Region	140
	5.4.5 Conclusions	146
REFERENCES		147

ILLUSTRATIONS

<u>Figure</u>	<u>Title</u>	<u>Page</u>
1	Effect of Surface Roughness on Frustum Heating	4
2	Effect of Surface Roughness on Flap Forces, Heating and Pressure	5
3	Flow Over the Rough MRV Configuration With a 30° Flap Deflection	6
4	Conical MRV Configuration	8
5	Biconic MRV Configuration	9
6	Profilometer Traces of a 4-Mil Thick, Rough Surface. An Air-Drying Adhesive (Krylon) Was Used to Bond the Roughness to the Surface	11
7	Profilometer Traces of a 4-Mil Thick, Rough Surface. Pressure-Sensitive Tape Adhesive Was Used To Bond the Roughness to the Surface	12
8	Surface-Roughness Characterization	13
9	Typical Layouts of Roughness Patterns on Gages	14
10	Molds for Six Types of Surface Topography	16
11	Rough 6° Cone Model Mounted in 96" Shock Tunnel	17
12	Rough Heat Transfer Gages Used in the Current Studies	18
13	Sequence of Construction of New Rough Thin-Film "S" Gages	19
14	Sequence of Construction of the Rough Calorimeter Gages	20
15	Typical Calorimeter Elements	21
16	Calspan Calorimeter Gage	22
17	Temperature/Time Record Exhibiting Excellent Response and Linearity of Calorimeter Instrumentation	24
18	Comparison Between Heat Transfer Measurement Made with Smooth Thin-Film and Calorimeter Heat Transfer Gages	25
19	Drawing of Section Through Skin-Friction Transducer	26
20	Typical Calibration and Run Traces	27

ILLUSTRATIONS (Cont.)

<u>Figure</u>	<u>Title</u>	<u>Page</u>
21	Heat Transfer Measurements on the Rough and Smooth 6° Cone for $\alpha = 0$	28
22	Heat Transfer Measurements on the Rough and Smooth 6° Cone for $\alpha = 8^\circ$	29
23	Heat Transfer Measurements on the Rough and Smooth 6° Cone for $\alpha = 16^\circ$	30
24	Distribution of Skin Friction Along Sharp 6° Cone With Smooth and 10-Mil Sand-Grain Roughness at $\alpha = 0^\circ$	32
25	Distribution of Skin Friction Along Sharp 6° Cone With Smooth and 10-Mil Sand-Grain Roughness at $\alpha = 8^\circ$	33
26	Distribution of Skin Friction Along Sharp 6° Cone With Smooth and 10-Mil Sand-Grain Roughness at $\alpha = 16^\circ$	34
27	Heat Transfer Distributions Along 6° Cone With Smooth and 15-Mil Sand-Grain Roughness at $\alpha = 8^\circ$	35
28	Distribution of Skin Friction Along Sharp 6° Cone With Smooth and 15-Mil Sand-Grain Roughness at $\alpha = 8^\circ$	36
29	Roughness Augmentation Measurements in 6° Cone	37
30	Variation of Reynolds Analogy Factor With Roughness Parameter	38
31	Computed Heat Transfer Augmentation Versus Skin-Friction Augmentation	39
32	Streamwise Variation of Skin-Friction Enhancement Ratio Downstream of Discontinuity in Surface Roughness on Sharp 6° Cone	40
33	Streamwise Variation of Heating-Enhancement Ratio Downstream of Discontinuity in Surface Roughness on Sharp 6° Cone	41
34	Rough 6° Cone Model Mounted in 96" Shock Tunnel	43
35	Simpson's Correlation for the Effect of Roughness Density	44
36	Distribution of Heating Along Windward Ray of Sharp Cone for Various Roughness Patterns ($\alpha = 12^\circ$), $Re_\infty = 11 \times 10^6$, $M_\infty = 11.2$	45

ILLUSTRATIONS (Cont.)

<u>Figure</u>	<u>Title</u>	<u>Page</u>
37	Correlation of Patterned Roughness Heating on Sharp Cones in Terms of Roughness Spacing Parameter (D^*/k)	46
38	Correlation of Patterned Roughness Heating on Sharp Cones in Terms of Effective Windward Area (A_p/A_s)	48
39	Correlation of Patterned Roughness Heating on Sharp Cones in Terms of Dirling's Shape Parameter	49
40	Simplified Drag Model For Rough-Wall Skin Friction	51
41	Variation of Nondimensional Roughness Heating With Roughness Shape and Spacing Parameter (A_p/A_s)	52
42	Variation of Nondimensional Roughness Heating With Roughness Shape and Spacing Parameter ($D^*/k)(A_{ws}/A_p)^{4/3}$	53
43a	Correlation of Roughness-Augmented Heating on MRV and Biconic Configurations, and Comparison with PANT Correlation	55
43b	Correlation of Rough-Wall Augmentation Heating Factors From the Present and Previous Studies at Calspan	56
43c	Correlation of Roughness-Augmented Heating on MRV and Biconic Configurations, and Comparison with PANT Correlation	57
44	Correlation of Biconic Measurements in Terms of $K_S/^\circ$	58
45	Effect of Nosetip Bluntness on Flap Forces, Heating and Pressure	60
46	Flap Force Measurements With the Sharp 6° Cone MRV Configuration at $\alpha = 0^\circ$	62
47	Variation of Heat Transfer Distribution Along the Flap With Surface Roughness for Conical MRV Configuration	63
48	Variation of Heat Transfer Distribution Along the Flap With Surface Roughness for the Conical Configuration	64
49	Variation of Heat Transfer Distribution Along Flap With Surface Roughness for 6° Sharp Cone Forebody Configuration	65
50	Correlation of Flap Roughness-Augmented Heating Measurements Made Close to the Trailing Edge With the Local Roughness Reynolds Number	66
51	Variation of Rough Flap Heating Distribution With Flap Angle	68

ILLUSTRATIONS (Cont.)

<u>Figure</u>	<u>Title</u>	<u>Page</u>
52	Variation of Flap Heating With Roughness Shape and Spacing	69
53	Variation of Flap Heating With Roughness Shape for Three Different Flap Angles	70
54	Correlation of Patterned Flap Heating in Terms of Dirling's Shape Parameter	71
55	Correlation of Patterned Flap Heating With Effective Windward Area Parameter (A_p/A_s)	72
56	Correlation of Patterned Flap Heating in Terms of Dirling's Shape Parameter	73
57	Correlation of Patterned Flap Heating With Effective Windward Area Parameter (A_p/A_s)	74
58	Correlation of Effective Heating Parameter C_H/C_{HSG} on Flaps With Dirling's Shape Parameter	76
59	Correlation of Effective Heating Parameter C_H/C_{HSG} on Flaps With Dirling's Shape Parameter	77
60	Hemispherical Model for Blunt-Body Transition and Roughness Studies	81
61	Spherical Nosetip With 12.5-Mil Conical Rough Surface	82
62a	Detailed View of Model in Shock Tunnel	83
62b	SCANT Nostip Installed in Tunnel for Mass Flow Calibration	84
63	Stagnation-Region Heating Model Showing Position of Trip Ring	85
64	Distribution of Heating Over the Smooth Hemispherical Model With Trip at 7° Position	87
65	Rough-Wall Heating to Hemisphere ($M_\infty = 11$, $k = 12.5$ mils)	89
66	Comparison Between the Turbulent Theories of Lin and Crowell for Smooth-Wall and Rough-Wall Measurements of Holden on 12" Diameter Hemisphere ($M = 11.2$, $Re_D = 11 \times 10^6$, $K = 12.5$)	90
67	Comparison 11×10^6 , Between Predicting From Four of the Shape-Change Codes Currently in Use and Smooth Wall-Heat Transfer Measurements on Hemispherical Nostip	91

ILLUSTRATIONS (Cont.)

<u>Figure</u>	<u>Title</u>	<u>Page</u>
68	Heat Transfer Measurements on Scant and Smooth Hemispherical Nosetip Showing How Small Blowing Brings Down Heating Levels to Smooth-Wall Values	93
69	Heat Transfer Measurements Indicating that Small Blowing on Rough Nosetip Initially Acts to Bring Down Heating Levels to Smooth-Wall Values	94
70	Particle-Launch Model Equipped with Three Particle Launchers, 105 Heat Transfer Gages, 27 Pressure Gages, and 4 Skin-Friction Gages	97
71	Instrumented Segment of Particle-Launch Model	98
72	Impact Particle Launcher	99
73	Schematic of Instrumentation of Particle-Launch Model	100
74	Shock/Particle Interaction Over a Blunt Ellipsoid	103
75	Heating Augmentation Associated With Particle-Induced Ring Vortex Interaction	104
76	"Stable" Flow Resulting from Small Penetration	106
77a	Particle-Induced Large-Scale ("E") Oscillation (Mach 6.5)	107
77b	Particle-Induced Large-Scale ("E") Oscillation (Mach 6.5)	108
78a	Particle-Induced Large-Scale ("E") Oscillation of Flow Field (Mach 13)	109
78b	Particle-Induced Large-Scale ("E") Oscillation of Flow Field (Mach 13)	110
79	"E" Oscillation on AO Configuration at Zero Angle of Attack	112
80	Typical Heat Transfer Record from Thin-Film Gages	113
81	Heat Transfer Distribution to the Face of the Disc for a Fully Oscillating Flow Over the Model	114
82	Typical Pressure Oscillogram, Run 3	116
83a	Photographic Sequence From Single Particle Launch	117
83b	Photographic Sequence From Single Particle Launch	118

ILLUSTRATIONS (Cont.)

<u>Figure</u>	<u>Title</u>	<u>Page</u>
84a	Multiple Particle Interactions Over the Blunt Nose Tip	119
84b	Multiple Particle Interactions Over the Blunt Nose Tip	120
85	Heating Rates Resulting from Multiple Particle Interactions	121
86	Dust Interactions in the Shock Layer	122
87	Sequential Laser Photographs of Debris from Water-Drop Impact (AEDC Ballistic Range)	123
88	Heat Transfer Augmentation in a Dust Environment	124
89	Cordin Model 375 High-Speed Camera Used in Calspan Transition Studies	130
90	Correlation of Transition Showing Effects of Tunnel Size	132
91	Correlation of Flat-Plate Transition Data in Terms of Parameters Suggested by Pate and Schueler	133
92	Correlation of Transition Measurements in Calspan Shock Tunnels With Ballistic and Downrange Measurements	135
93	Transition Reynolds Number vs. Unit Reynolds Numbers; Present Data vs. Potter and Scheetz	136
94	Distribution of Heat Transfer Through a Transition Region on Surface of a 6° Cone in Hypersonic Flow	138
95	Schlieren Photograph Showing Development of Transition of a Conical Boundary Layer in Hypersonic Flow	139
96	Photographs of "Wave-Like" Instabilities	141
97	Photographs of Gross-Instability Region	143
98	Photographs of Gross-Mixing Region	145

Section 1

SUMMARY

In this report, we summarize the results of four studies to investigate fundamental fluid-dynamic phenomena of importance to the aerothermal performance of hypersonic re-entry vehicles. These phenomena: (1) the effects of surface roughness on the aerothermal characteristics of slender maneuverable re-entry vehicles, (2) boundary layer transition and surface roughness effects on blunt bodies, (3) the interaction between dust particles and the shock layer over blunt bodies, and (4) boundary layer transition on slender bodies, have in general proved untractable to theoretical analysis.

The first study (Section 2) was a detailed experimental investigation of the effects of the shape and spacing of roughness elements on the roughness-enhanced heating and skin friction on a maneuverable re-entry vehicle (MRV) configuration. In this work, measurements were made on slender cones and control flaps to define the relationships between roughness-element shape and spacing and the incremental heating and skin friction induced by the surface roughness. This study demonstrated that similar measurements in subsonic flows cannot be directly extrapolated to predict trends in high-speed compressible flows.

In the second study (Section 3), we examined in detail the transition process in the stagnation region of a blunt body in hypersonic flow. Here, the main focus was on determining what fluid-dynamic mechanics are responsible for enhanced heating in the stagnation region of high Reynolds number blunt-body flows. In the course of this work, we investigated whether upstream influence from transition, surface roughness in the stagnation region, minute dust particles in the freestream, or blowing in the stagnation region is the principal cause of stagnation-point heating enhancement.

The third study (Section 4) investigated the basic mechanics which occur when a number of minute dust particles interact with the shock layer ahead of a blunt body. In this effort, we linked the considerable increases in stagnation heating with the shear layers generated by particle-shock/bow-shock interactions and the tripping of the boundary layer in the stagnation region as each dust particle enters it.

Finally, we present (in Section 5) results of a study of hypersonic boundary layer transition in which we obtained microsecond photographs and high-frequency thin-film measurements on slender cones of the breakdown of flow in and preceding the transition region. The results obtained provide insight into the mechanisms by which the laminar/turbulent boundary becomes unstable in high-speed boundary layers.

Section 2

STUDIES OF EFFECTS OF SURFACE ROUGHNESS ON
AEROTHERMAL PERFORMANCE OF SLENDER CONICAL
VEHICLES WITH FLAP CONTROLS

2.1 INTRODUCTION AND SUMMARY OF EARLIER RESULTS

The studies which were conducted earlier¹ to examine the effects of "sand-grain" surface roughness on the heat transfer to and skin friction of slender conical vehicles with flap controls in high Mach number flows have demonstrated (as illustrated in Figures 1 and 2) that the heating rates of the heatshield just downstream of the nosetip, and on the flap close to the trailing edge, can be typically two to three times the heating rates of the smooth configuration. In addition, the increased momentum thickness induced by surface roughness can reduce the control forces by factors of up to 2. From the more fundamental viewpoint, we have observed compressibility and turbulent relaxation effects in our studies at high Mach numbers which are not described in existing theoretical analyses. We have also found that there is a significant variation of heat transfer with the shape and spacing of the roughness elements, and, for typical carbon/phenolic heatshields—where the ablated roughness is well-spaced $2 < D/K < 5$, the heating levels can be 50% lower than the values calculated for sand-grain rough surfaces. Our studies suggest that the basic mechanisms of heat and mass transfer in high Mach number flows over highly cooled walls may differ significantly from those in subsonic, or low Mach number, flows. The studies of the effects of surface roughness on the flow characteristics and the distribution of heating in regions of shock-wave/boundary layer interaction have demonstrated that both the incipient separation and the structure of these regions are strongly influenced by surface roughness. Because the mechanism of turbulent boundary layer separation is so strongly influenced by the structure of the boundary layer at its base, and it is in this region that surface roughness has the largest influence on the structure and momentum defect, it is not difficult to understand the first-order effects that roughness has on boundary layer separation. A graphic illustration of the effect of surface roughness on the structure on an interaction region is shown in Figure 3. Here, it can be seen that the flow over the smooth compression surface remains attached; while flow separation, indicated by the presence of separation and reattachment shocks, is clearly observed over the rough compression surface. Separation has extended approximately two boundary layer thicknesses ahead of the



SMOOTH



ROUGH

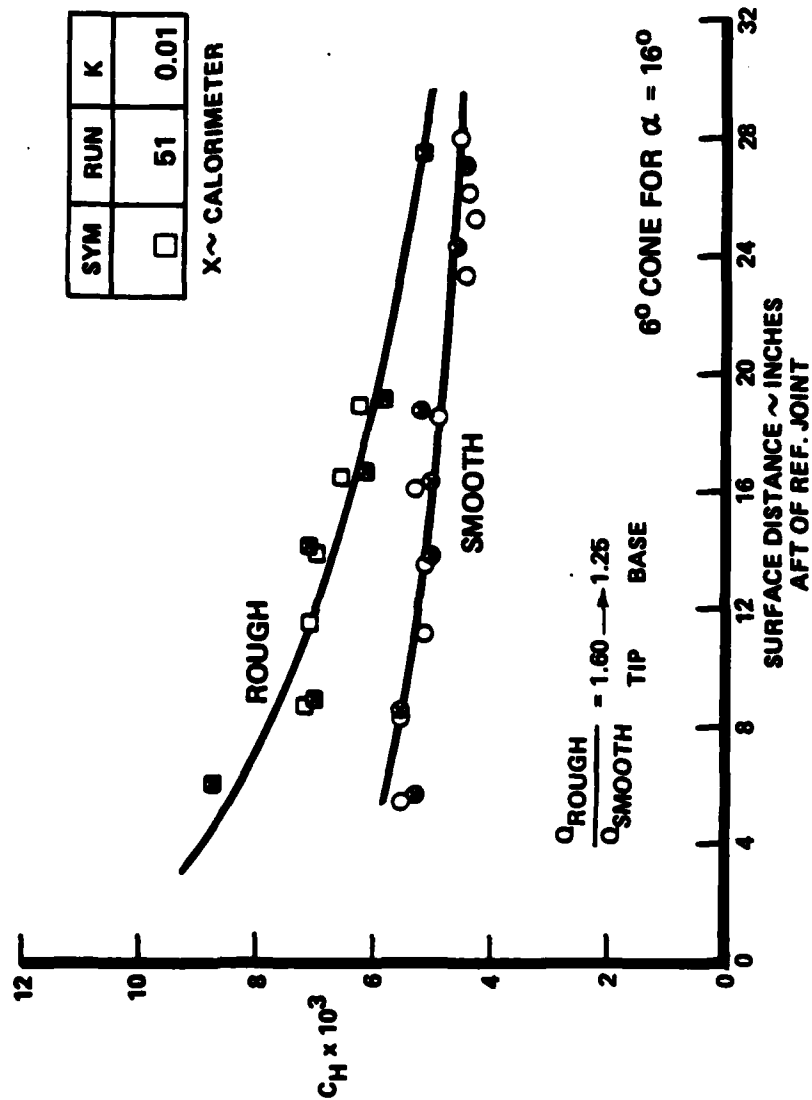
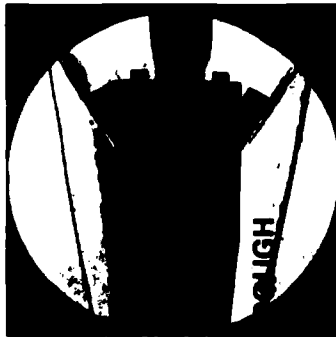


Figure 1 EFFECT OF SURFACE ROUGHNESS ON FRUSTUM HEATING



FLAP FORCE

$$\frac{C_{N\text{ROUGH}}}{C_{N\text{SMOOTH}}} = \frac{0.175}{0.530} = 0.33$$

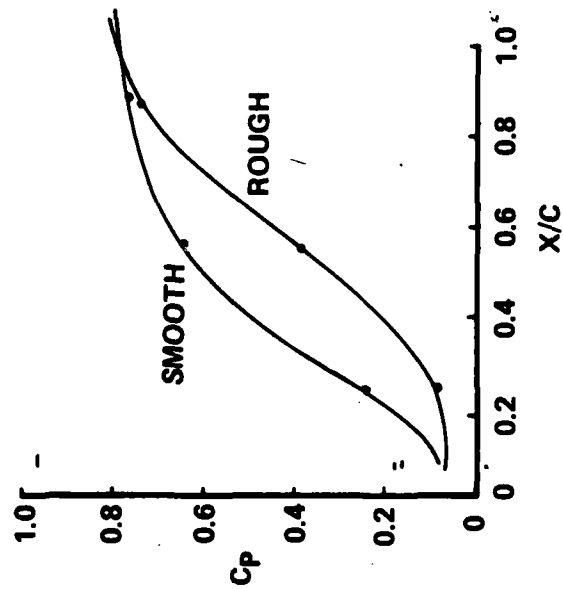
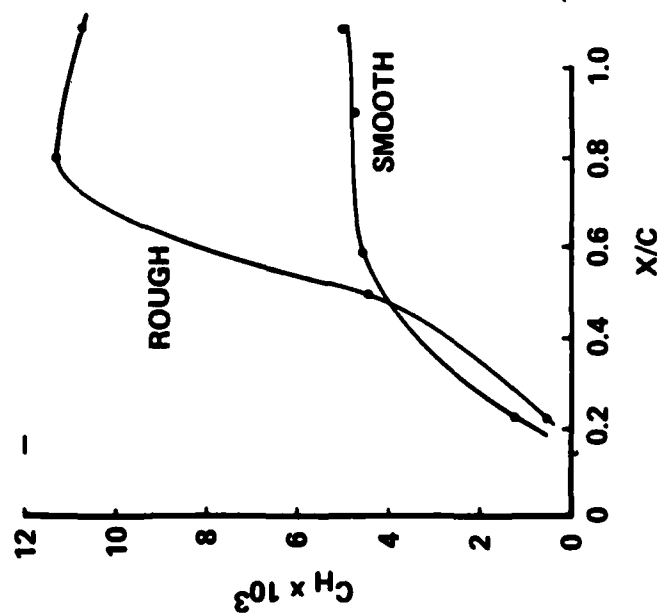


Figure 2 EFFECT OF SURFACE ROUGHNESS ON FLAP FORCES, HEATING AND PRESSURE



(a) UNSEPARATED



(b) SEPARATED

Figure 3 FLOW OVER THE ROUGH MRV CONFIGURATION WITH A 30° FLAP DEFLECTION

flap on the rough configuration, and the compression shocks have been moved well downstream on the flap. The change in the shock structure over the flap resulting from surface roughness is a clear indication that the pressures at the base of the flap, and the forces generated by the flap, are both reduced. Just as in the flows over indented noseshapes, the most significant effects of surface roughness occur in the reattachment compression region, where the thinning of the boundary layer and the increase in the local static pressure, together, cause peak values in K/θ and local density which result in roughness-augmented heating factors of 3, in a region which already is subjected to peak heating on the smooth configuration.

This section contains the results from the experimental studies we have conducted to examine surface roughness effects on slender conical frusta and flap control systems at local Mach numbers of up to 11. First, we describe the models and instrumentation used in these studies. Then, we describe the studies conducted with models coated with sand-grain rough surfaces. Next, we describe our extensive series of studies, conducted with surfaces of well-defined roughness characteristics (hemispherical and conical roughness elements). Here, the major emphasis was placed on examining the effects of roughness shape and spacing on the heat transfer to, and skin friction of, rough surfaces. The models and instrumentation used in this study have been described earlier in this section. We first review the measurements made on rough and smooth, slender cones at various angles of attack and then discuss the results from the study of the effects of roughness on the aerothermal characteristics of flap control surfaces.

2.2 MODELS AND INSTRUMENTATION

2.2.1 The Models

The measurements of roughness effects on the aerothermal characteristics of slender conical frusta and control surfaces were conducted with the conical and biconic frusta models shown in Figures 4 and 5, each of which formed an integral part of an MRV configuration. The studies were conducted for various bluntness ratios and with roughness heights of 10, 12.5, and 15 mils for sand-grain and patterned rough surfaces. Studies were also made to examine the effects of discontinuous changes in surface roughness on the downstream distribution, heat transfer, and skin friction. Measurements of skin friction, heat transfer and pressure were made on both the

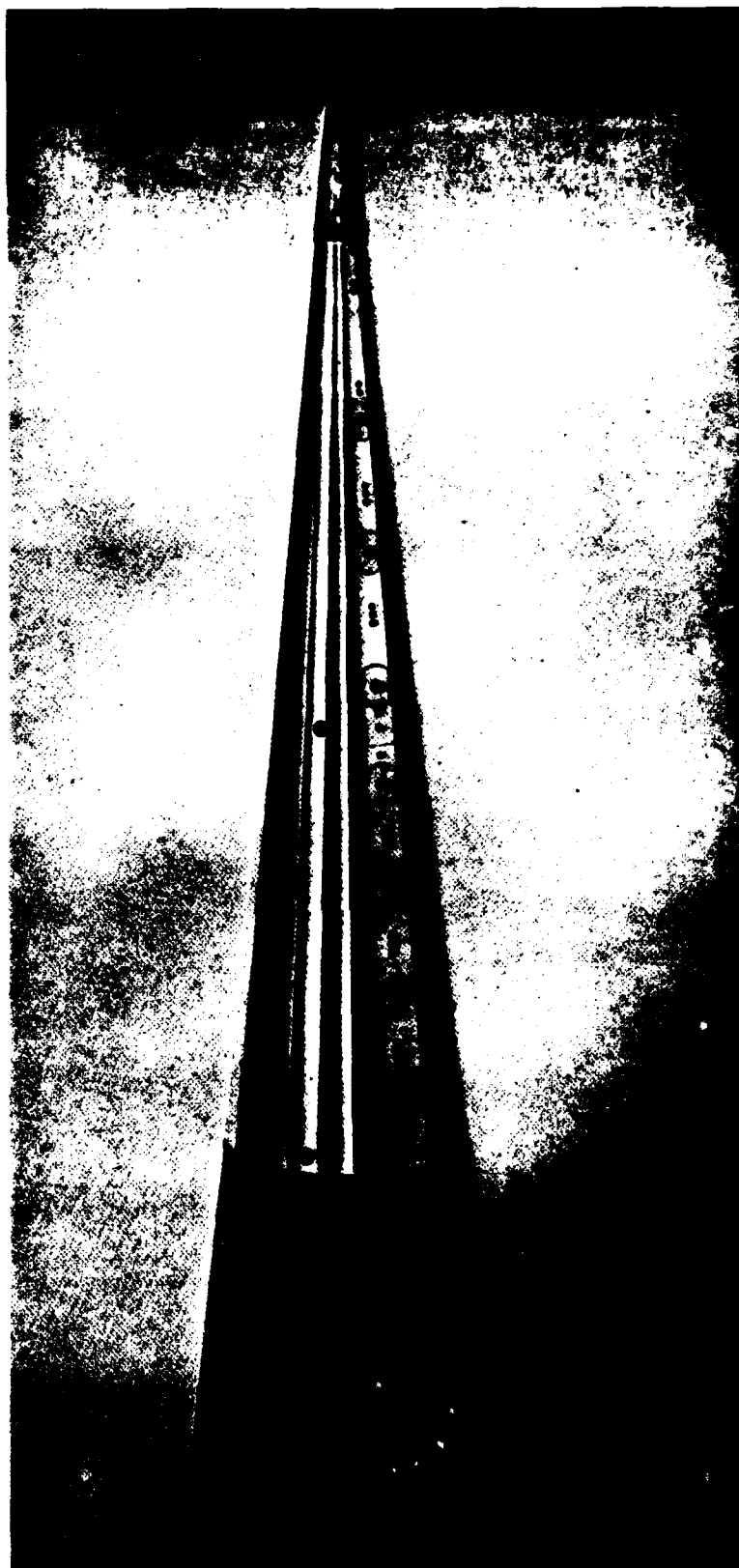


Figure 4 CONICAL MRV CONFIGURATION

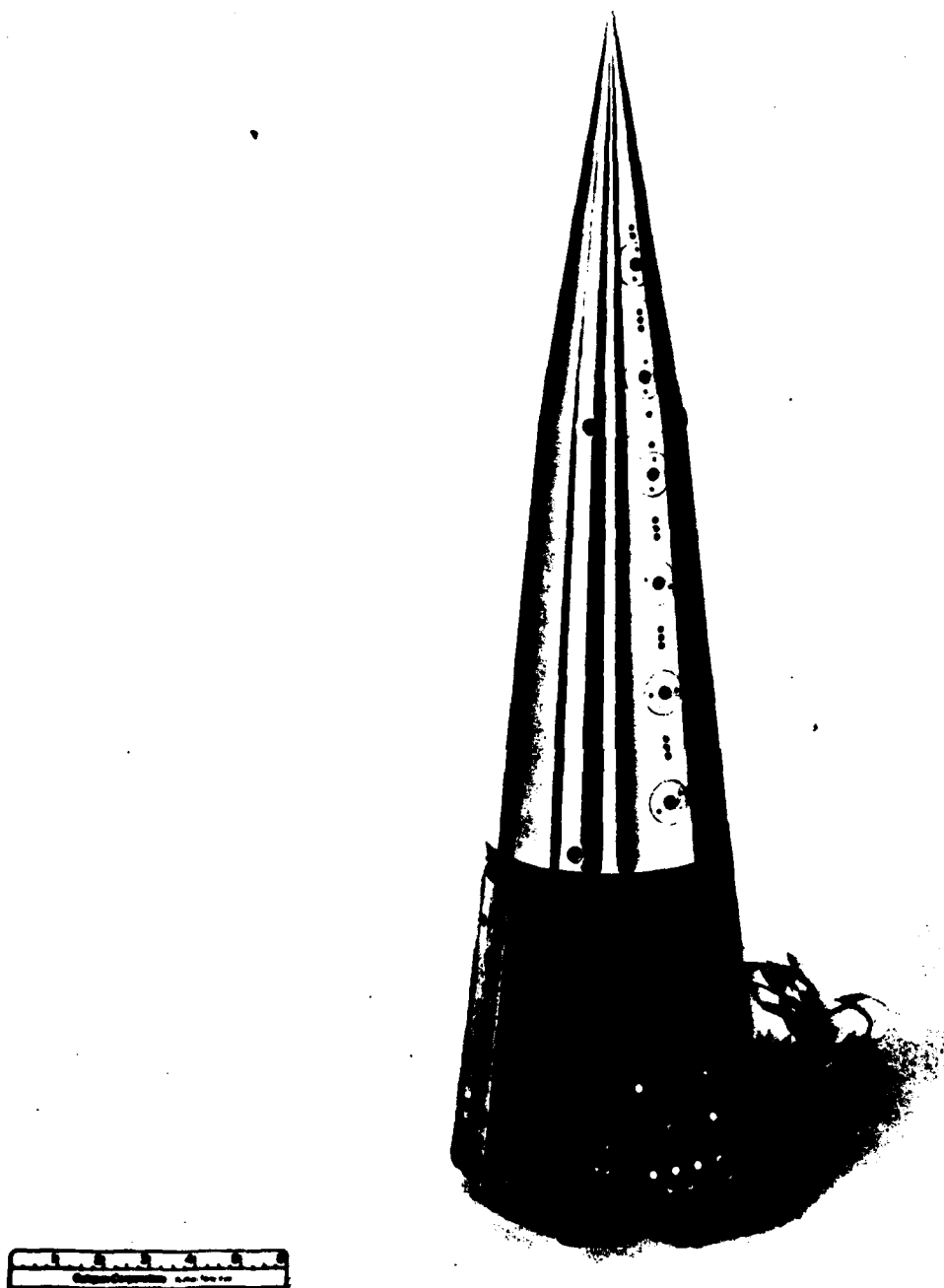


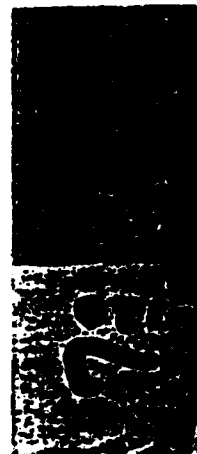
Figure 5 BICONIC MRV CONFIGURATION

windward and leeward sides of the model to examine compressibility and turbulent non-equilibrium effects in high Mach number, high Reynolds number flows.

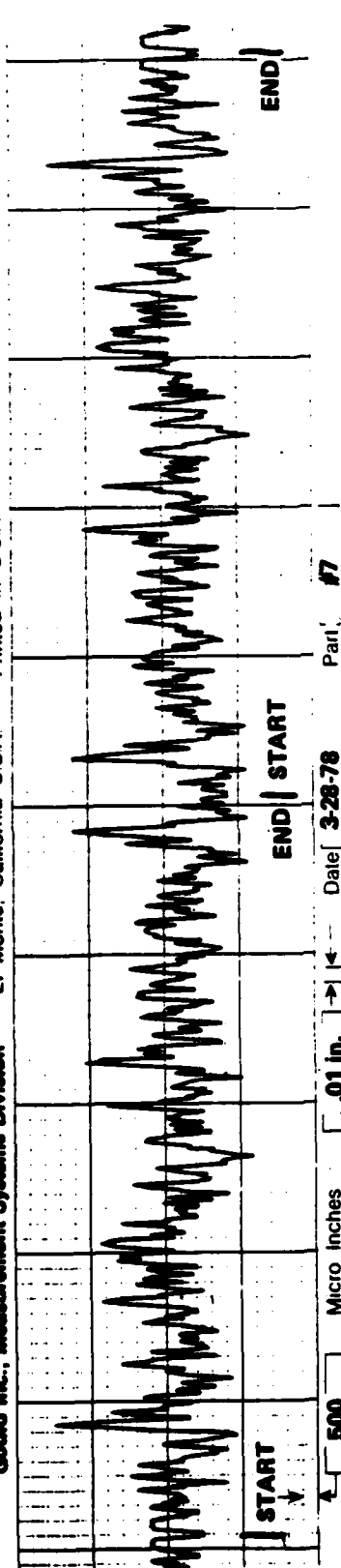
2.2.2 Preparation of Model Sand-Grain and Patterned Rough Surfaces

We used models coated with sand-grain roughness as well geometrically well-defined (patterned) roughness in these studies. In the work with sand-grain rough surfaces, we used two different techniques to bond the sand (carbide grit) to the model surface. Our major object was to determine, for a common grain-size roughness, how the effects of different roughness spacings and orientations resulting from two different bonding techniques influenced roughness-induced augmentation in skin friction and heat transfer. In the first set of studies, we bonded the carbide grit to the surface with an air-drying plastic-film adhesive. Using this technique, considerable care and time was expended in preparing a tight matrix and avoiding particle agglomeration. In the second set of studies, we used a pressure-sensitive adhesive; with this technique, we were able to apply and reapply the grit without agglomeration occurring until an extremely high-density packing was obtained. The pressure-sensitive adhesive also has the property that, when activated (by removing its backing), it generates a strong electrostatic charge which exerts a powerful attractive force on the grit particles, causing them to align themselves with their principal axis perpendicular to the surface. A surface produced in this way has an intrinsically greater roughness height than one constructed using the same size grit and an air-drying adhesive, as can be seen by comparing the profilometer traces shown in Figures 6 and 7. While both surfaces have a maximum peak-to-valley roughness of approximately 4 mils, the sand-grain surface constructed on pressure-sensitive adhesive clearly has the greater percentage of large roughness particles, as can be seen from the k_{30} values shown in Figure 8. We selected the 30th-percentile height (k_{30})—the height at which 70% of the surface lies beneath that elevation—as a representative dimension for characterizing sand-grain surfaces, because it embodies information on both roughness height and roughness spacing within a single dimension.

In our patterned-roughness studies, we employed rough surfaces constructed from hemispherical and conical roughness elements, set in a hexagonal matrix for three different spacing ratios. The hemispherical and conical roughness elements, which had a common height of 12.5 mils and equal base areas, were placed in the hexagonal pattern so that they covered either 12%, 34%, or 64% of the total surface area (Figure



Gould Inc., Measurement Systems Division El Monte, California USA Printed in U.S.A.



Gould Inc., Measurement Systems Division El Monte, California USA Printed in U.S.A.

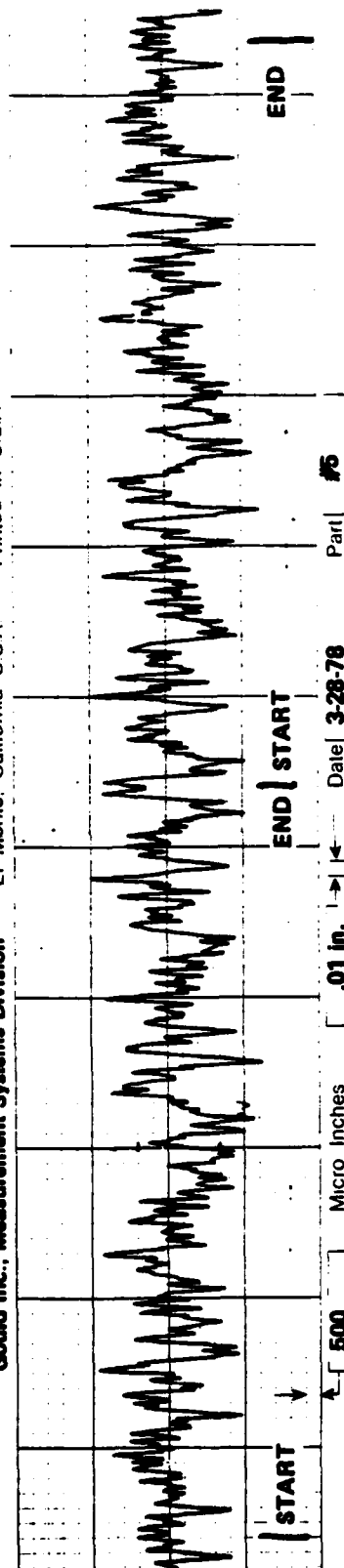


Figure 6 PROFILEMETER TRACES OF A 4-MIL THICK, ROUGH SURFACE. AN AIR-DRYING ADHESIVE (KRYLON) WAS USED TO BOND THE ROUGHNESS TO THE SURFACE

I 20
II 21

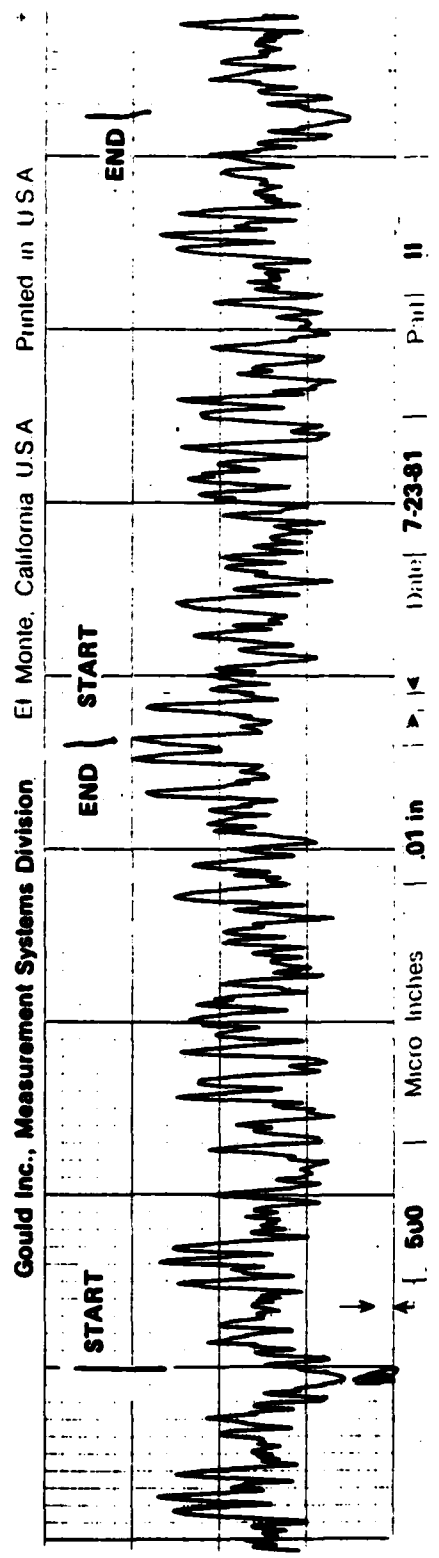
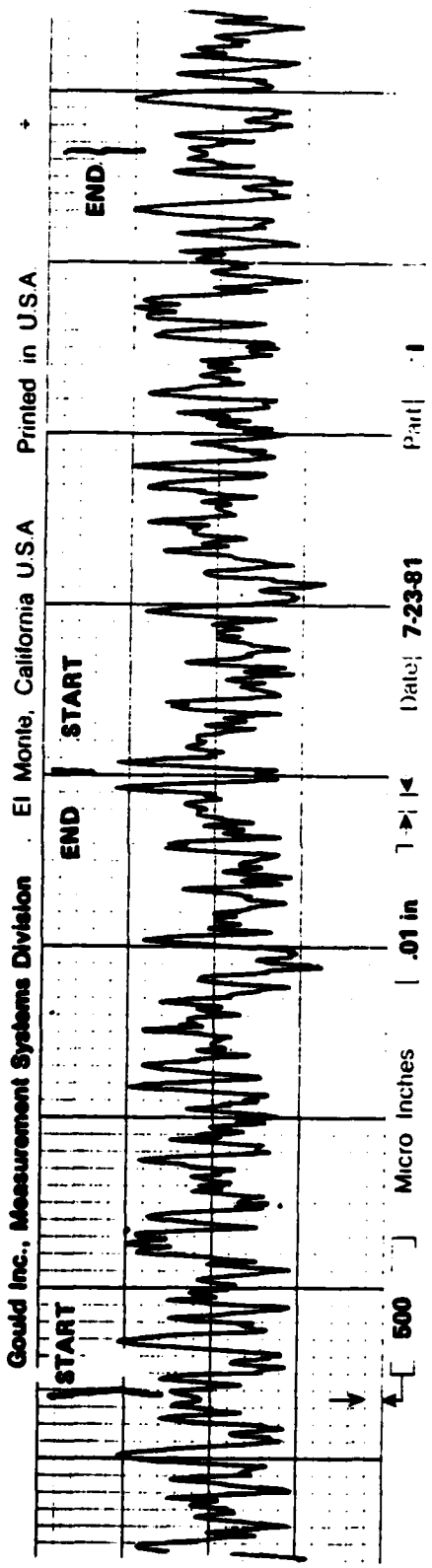


Figure 7 PROFILEMETER TRACES OF A 4-MIL THICK, ROUGH SURFACE. PRESSURE - SENSITIVE TAPE ADHESIVE WAS USED TO BOND THE ROUGHNESS TO THE SURFACE

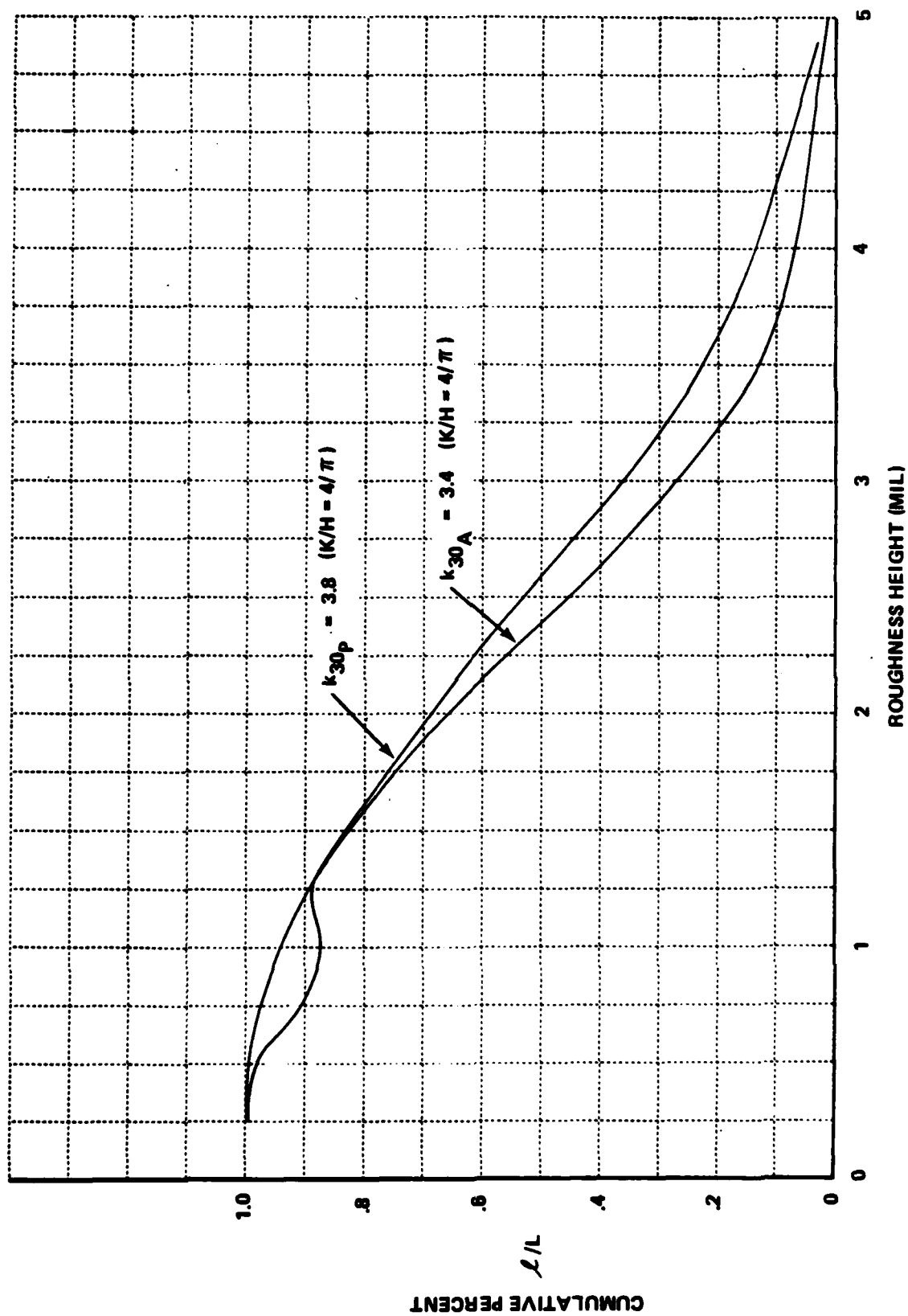
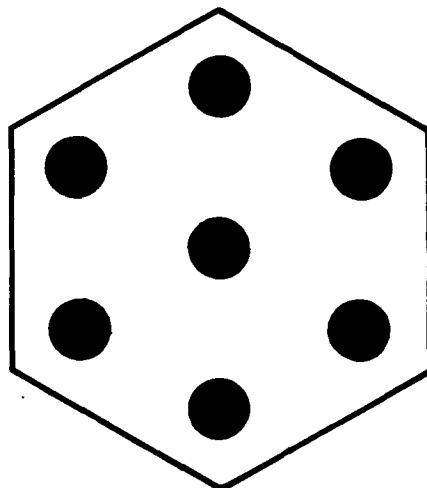
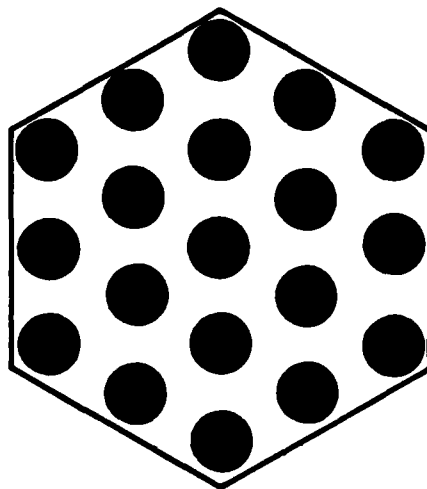


Figure 8 SURFACE ROUGHNESS CHARACTERIZATION

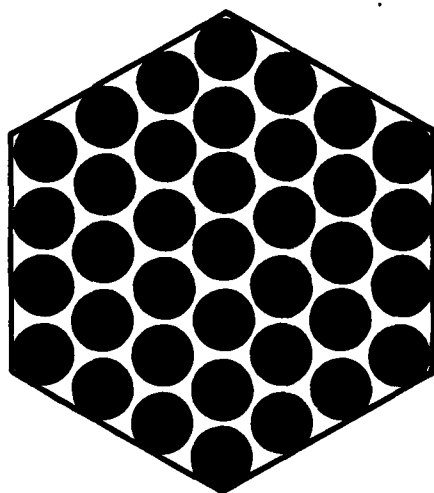
AIRFLOW



7 CONES OR HEMISPHERES



19 CONES OR HEMISPHERES



37 CONES OR HEMISPHERES

Figure 9 TYPICAL LAYOUTS OF ROUGHNESS PATTERNS ON GAGES

9). The six different patterns of surface roughness were fabricated in silicone rubber "skins," which were then bonded to the surface with a specially prepared and applied silicone adhesive. Selection and correct application of an adhesive which would retain the skin when subjected to the large shear and heating levels developed in the shock tunnel, and yet would allow relatively simple removal when a change in surface roughness was required, represented a significant effort. The six computer-milled molds, and an example of one of the silicone skins molded in them, are shown in Figure 10. Each skin, which had the 12.5-mil roughness elements molded on a 3-mil-thick base, had to be vacuum molded to accurately preserve the detailed roughness shapes. An example of the application of the skins to the model, a painstaking process, is shown in Figure 11.

2.2.3 Heat Transfer Instrumentation

We employed both thin-film ("S") and silver-calorimeter heat transfer gages to measure rough-wall and smooth-wall heating rates in our studies. Photographs of these two types of gages are shown in Figure 12 for a sand-grain surface. For sand-grain surfaces, both types of gages were constructed by first copying the required surface in a ceramic mold and then forming the glass substrate for the thin-film or silver-calorimeter gage element in the mold, as shown in Figures 13 and 14, respectively. As earlier noted, studies with patterned roughness employed silver-calorimeter elements constructed with hemispherical and conical roughness elements, set in a hexagonal matrix. The silver-calorimeter elements for the patterned surfaces were "minted" in the hexagonal dies shown in Figure 15. This figure also shows the six surface geometries used on the calorimeter elements. After each calorimeter element was minted, its front and side faces were cleaned and the back face highly polished before a thin, electrically insulating but thermally conducting, film was vacuum-deposited on the back of the calorimeter element. A nickel resistance thermometer was then deposited and bonded to the insulating layer to measure the temperature of the calorimeter element. A sectional diagram of the gage is shown in Figure 16. The silver-calorimeter element was bonded to a ceramic holder using an extremely low-conductivity polyurethane resin. By employing an isolated calorimeter element whose thermal properties and mass can be accurately specified, together with a temperature-sensing element that is accurately calibrated, substrate heating can be determined directly from the gage output. This removes the inaccuracies associated with calibration using a radiant source, a method which must be used to calibrate the rough thin-film gages. The silver-calorimeter gage has a response time of less than 800 microseconds and has been used to resolve heating

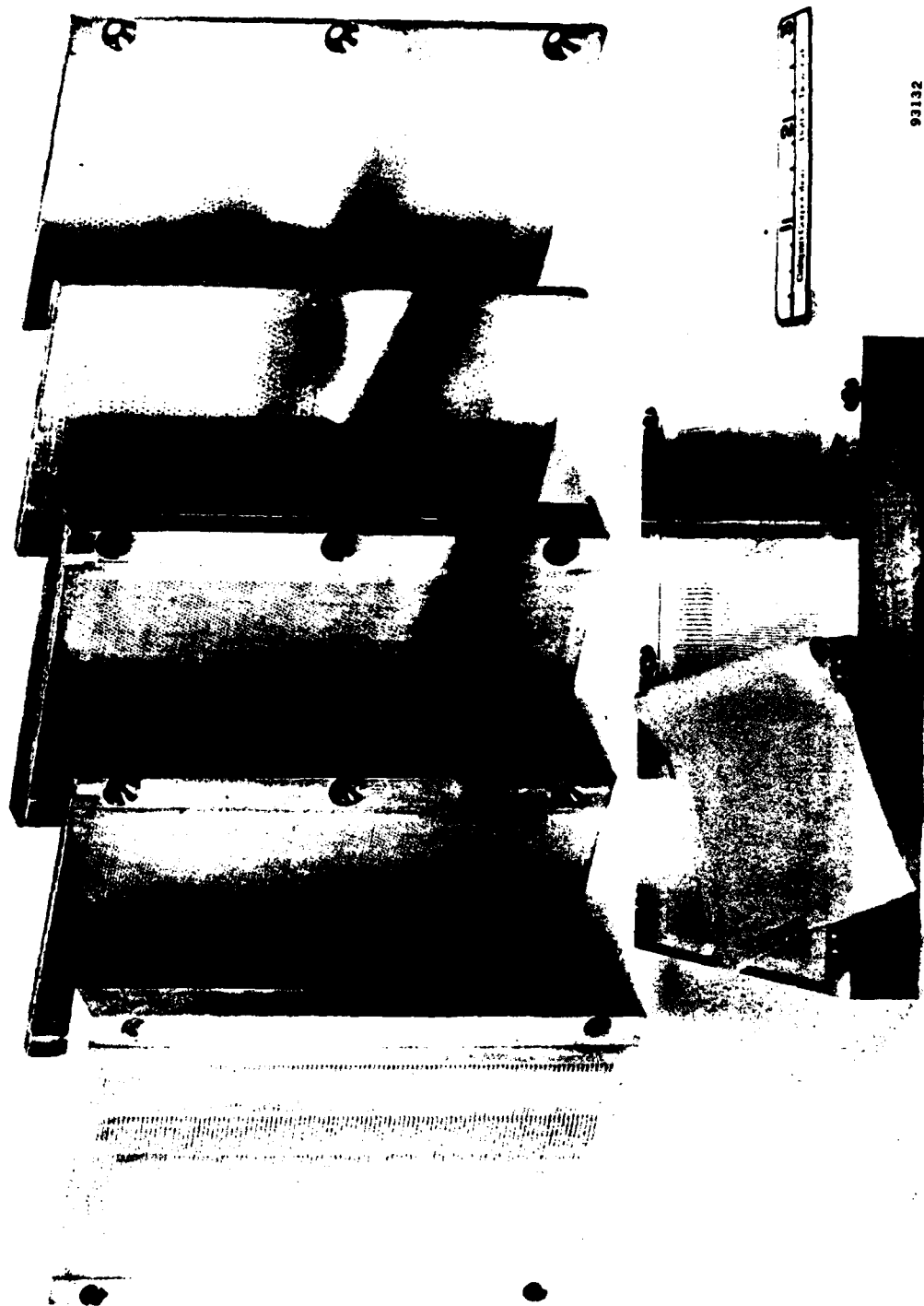


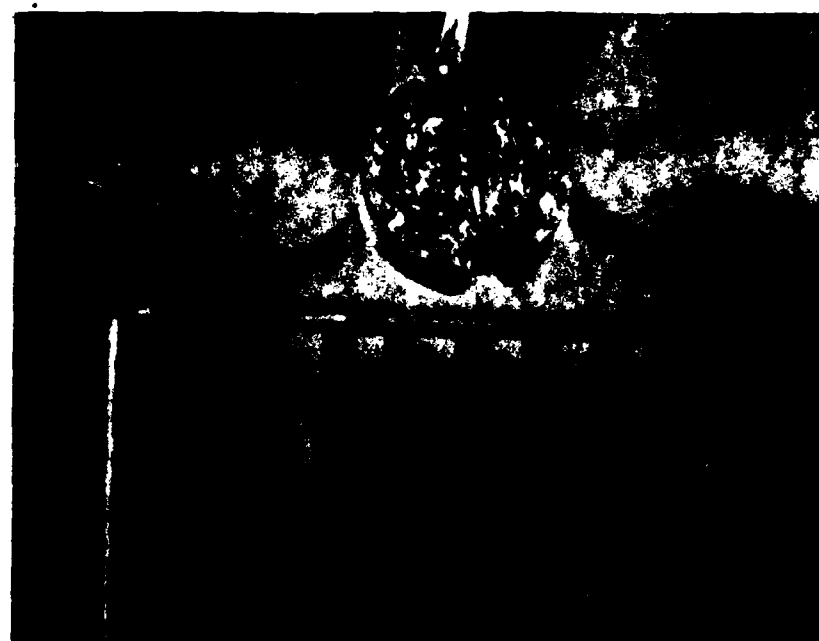
Figure 10 MOLDS FOR SIX TYPES OF SURFACE TOPOGRAPHY



Figure 11 ROUGH 6° CONE MODEL MOUNTED IN 96" SHOCK TUBE



(a) SILVER-CALORIMETER GAGE



(b) THIN-FILM "S" GAGE

Figure 12 ROUGH HEAT TRANSFER GAGES USED IN THE CURRENT STUDIES

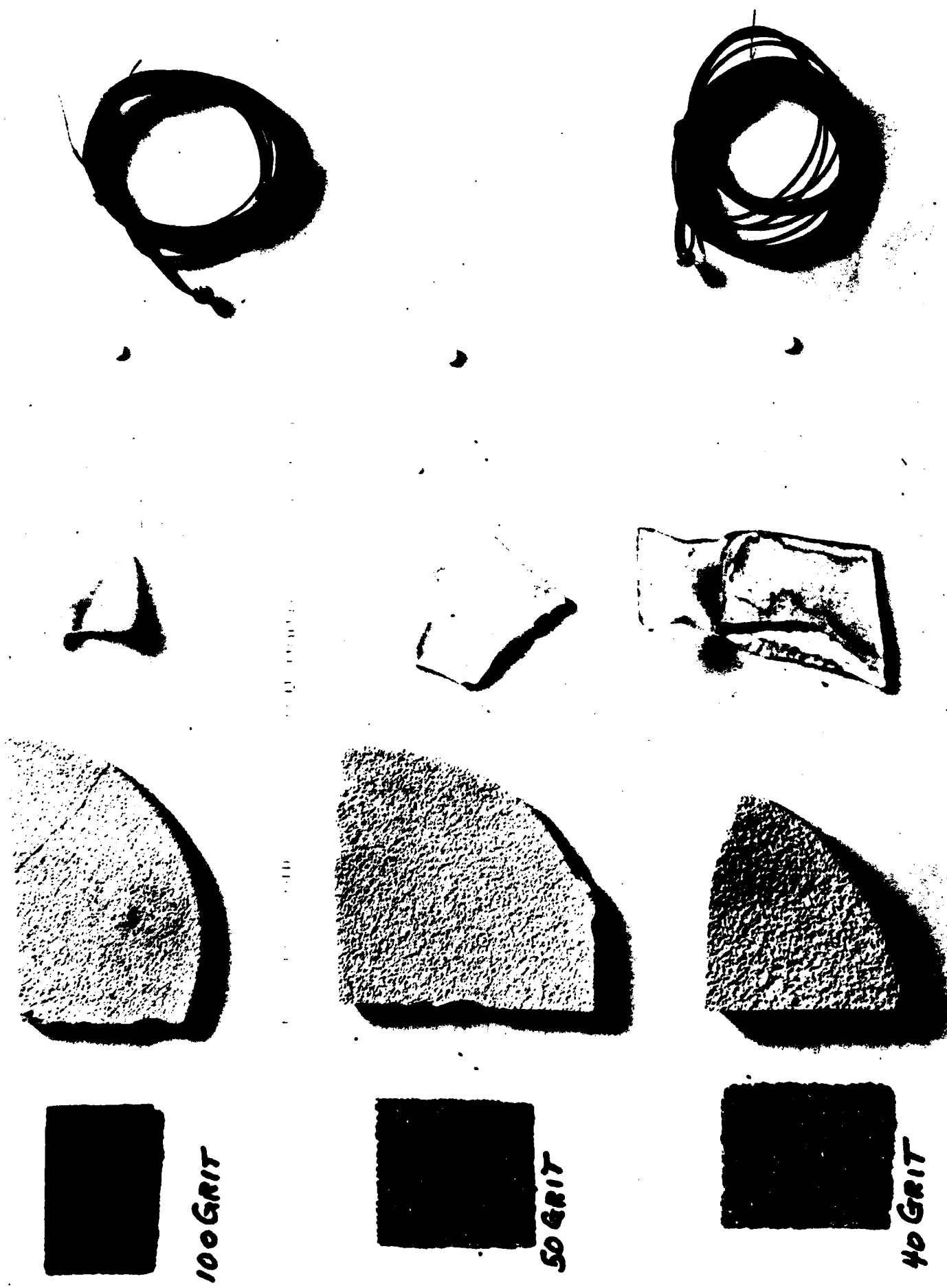


Figure 13 SEQUENCE OF CONSTRUCTION OF NEW ROUGH THIN-FILM "S" GAGES

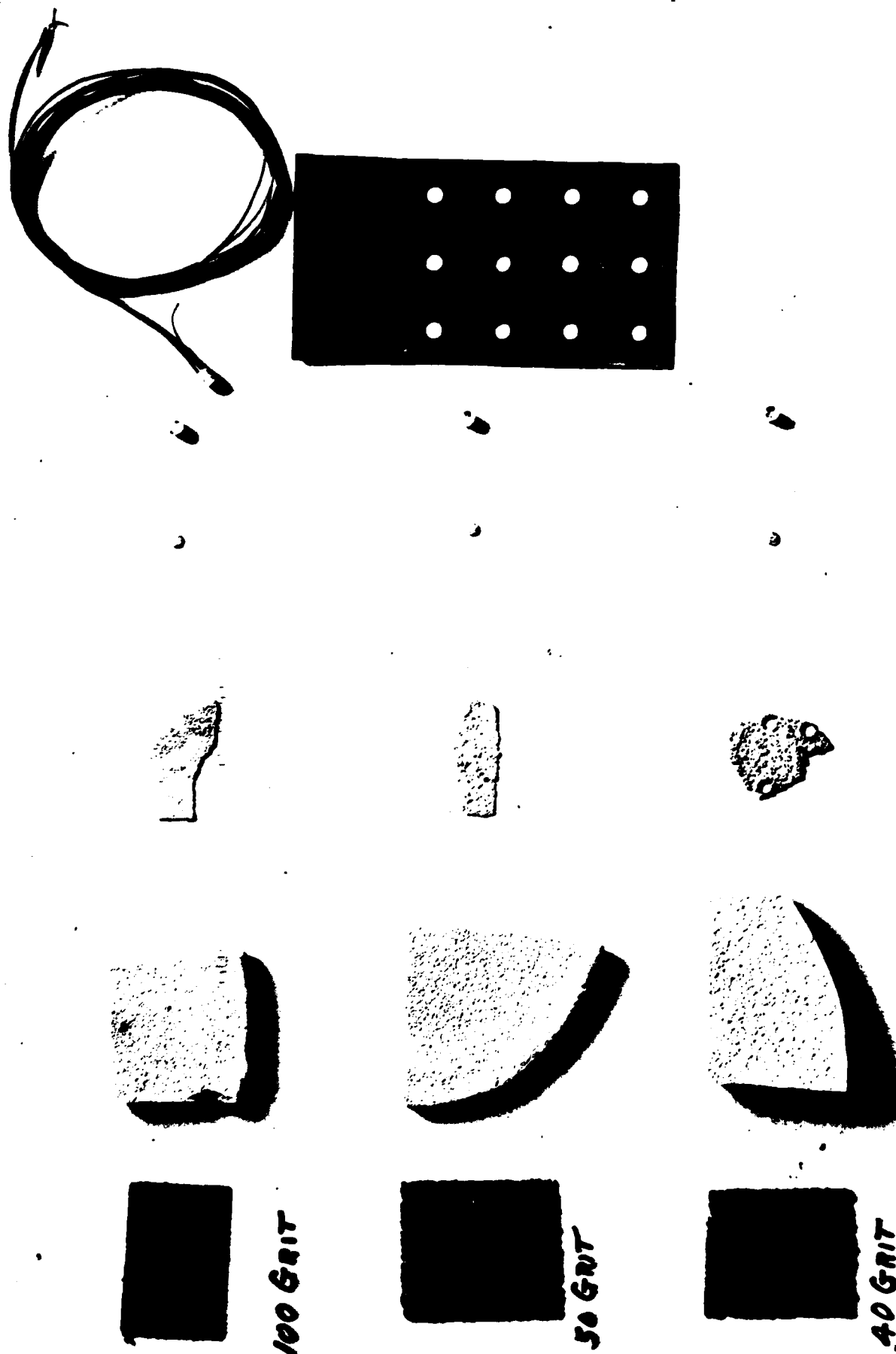
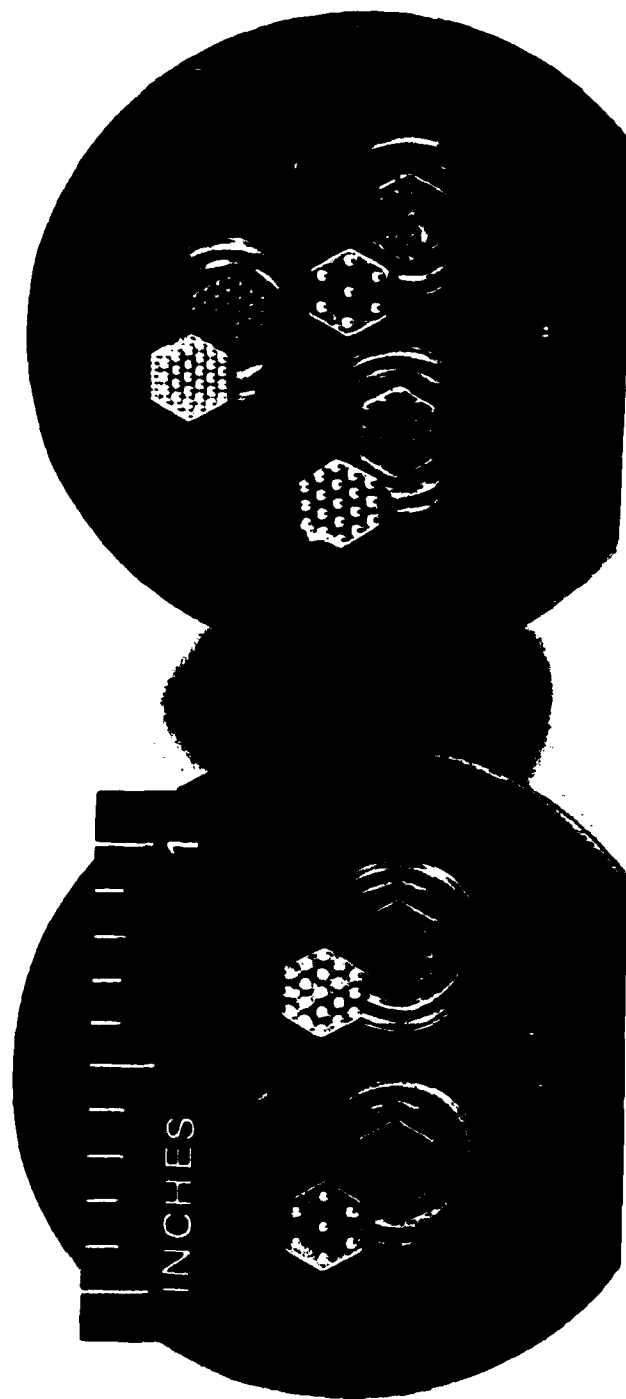


Figure 14 SEQUENCE OF CONSTRUCTION OF THE ROUGH CALORIMETER GAGES



93133

Figure 15 TYPICAL CALORIMETER ELEMENTS

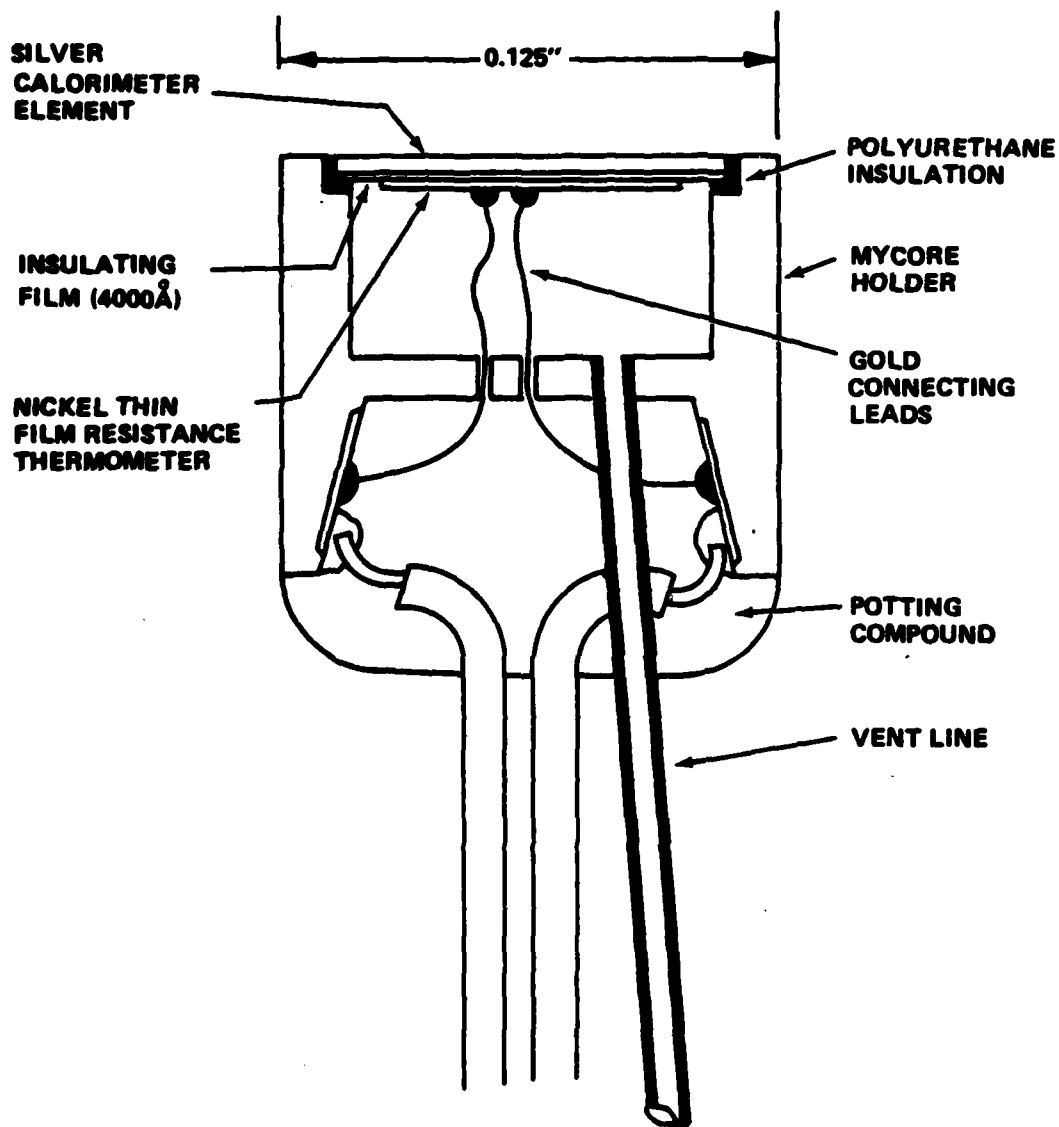


Figure 16 CALSPAN CALORIMETER GAGE

rates down to 5 Btu/ft²/sec with an accuracy of close to 5%. The output/time trace of Figure 17 shows the excellent response and linearity of this gage. The heat transfer measurements made with both the thin-film and the calorimeter instrumentation were found to be in excellent agreement for both smooth and rough configurations, as shown in Figure 18.

2.2.4 Skin-Friction and Pressure Instrumentation

In the studies with both sand-grain and patterned roughness, we employed skin-friction gages of the type shown in Figure 19. This gage is a single-component strain-gage force balance, which is compensated for acceleration and normal pressure, and has a diaphragm which is contoured to the local surface in which the gage is installed. The diaphragm is mounted flush with the metallic surface and the surface coating applied to the top of the diaphragm in a manner similar to that described for the preparation of rough surfaces. Typical calibration and run traces from the skin-friction gages are given in Figure 20.

Pressure distributions were obtained over the rough models with both ported and flush-mounted pressure instrumentation. For the roughness scales at which the studies were conducted, we found no differences between the measurements on rough and smooth surfaces with either type of gage.

2.3 STUDIES OF SURFACE ROUGHNESS EFFECTS ON SLENDER CONES

2.3.1 Studies With Sand-Grain Roughness

In these studies,¹ measurements were made of heat transfer, skin friction, and pressure distribution to the windward and leeward rays of the 6° conical and the 10.4° biconic configurations for a range of angles of attack between 0 and 16°. The measurements with the models coated with sand-grain roughness were made for roughness heights of 4, 10, and 15 mils. Typical examples of heat transfer and skin-friction measurements on smooth and sand-grain rough sharp 6° cones for model incidences of 8° and 16° are shown in Figures 21 through 23. While we observe little or no roughness-induced heating enhancement on the cone surface close to the base for $\alpha = 0^\circ$, the heating rates just downstream of the nosetip are close to twice the smooth-wall values. The heat transfer distributions along the rough cone at low angles of attack (high local

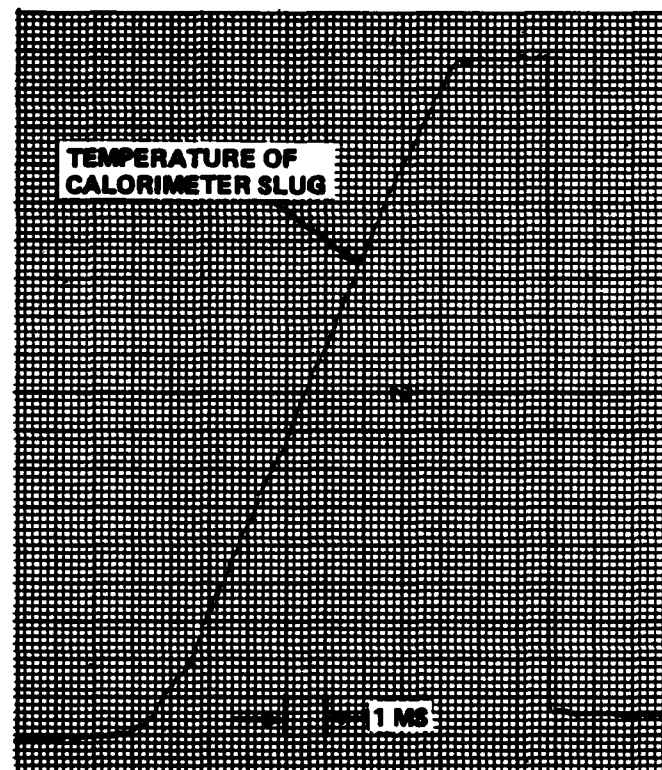


Figure 17 TEMPERATURE/TIME RECORD EXHIBITING EXCELLENT RESPONSE AND LINEARITY OF CALORIMETER INSTRUMENTATION

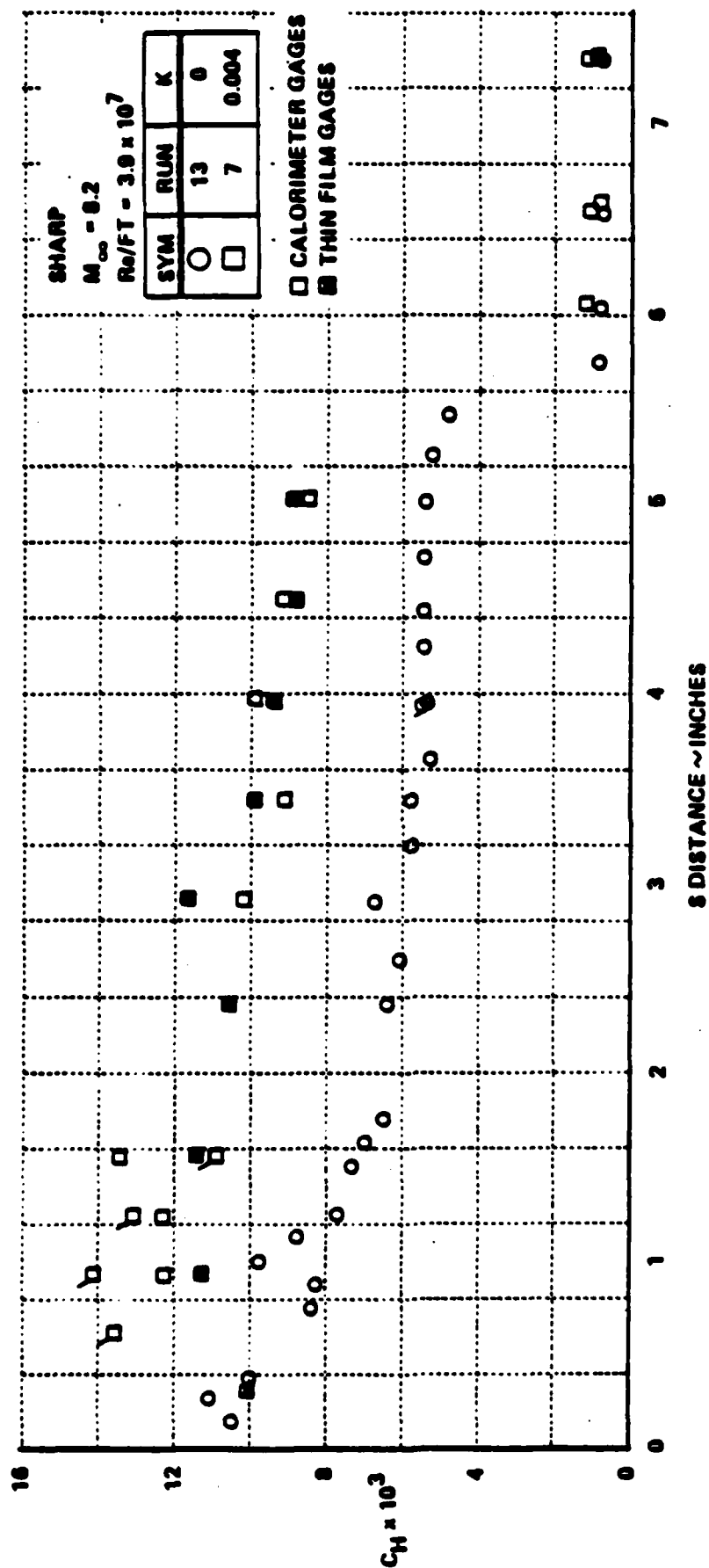


Figure 18 HEAT TRANSFER MEASUREMENTS ON ROUGH AND SMOOTH SHARP BICONIC CONFIGURATION

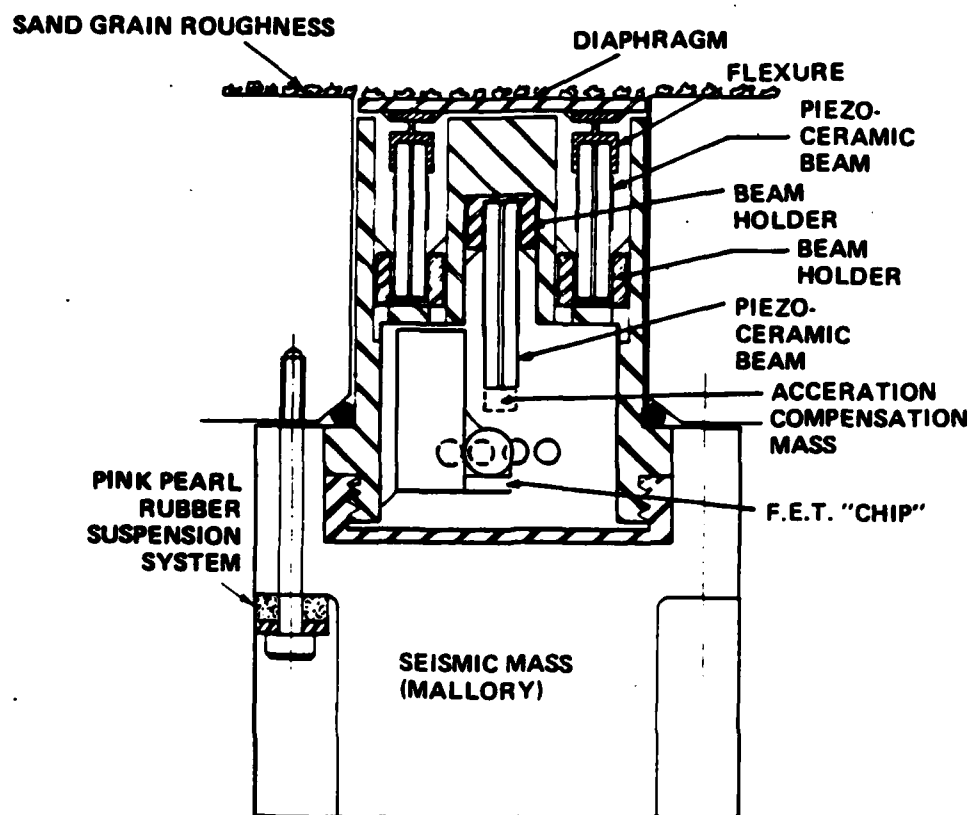
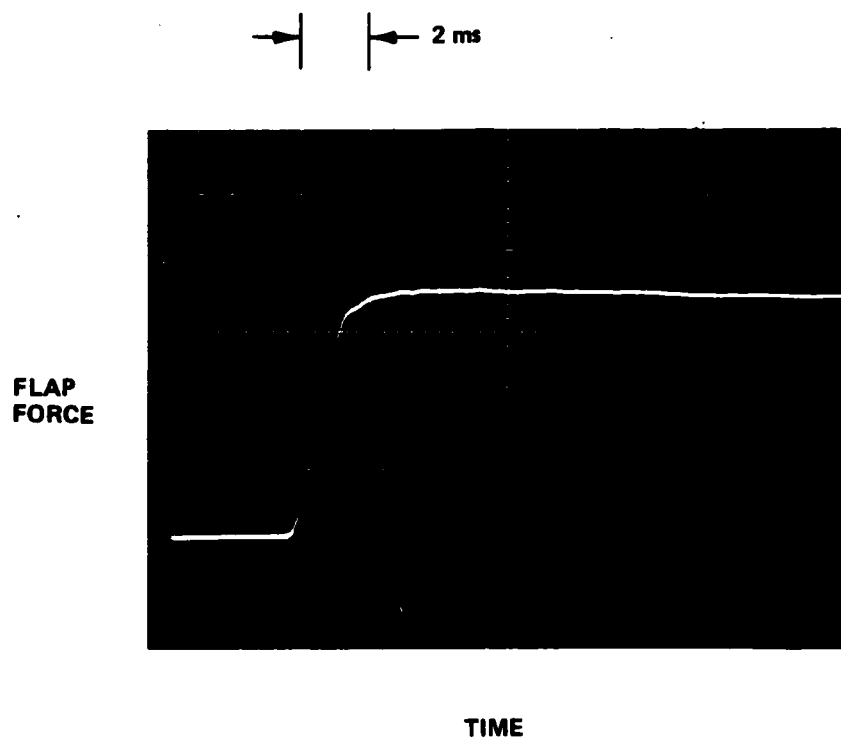
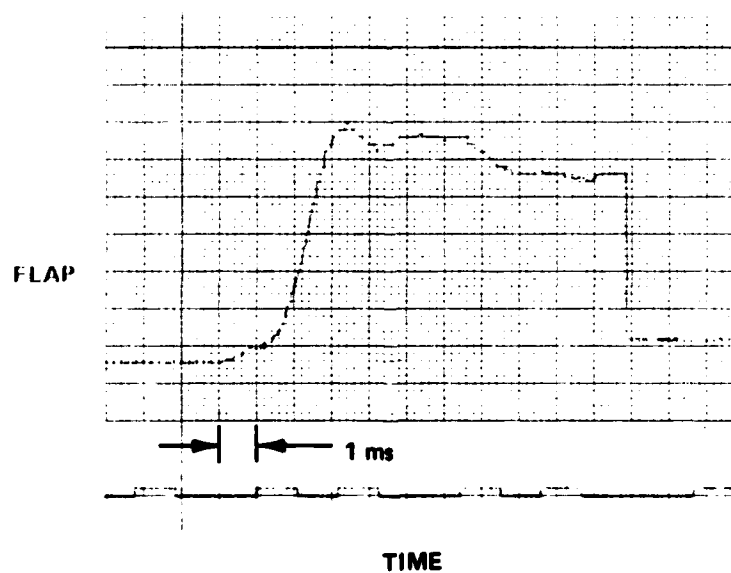


Figure 19 DRAWING OF SECTION THROUGH SKIN FRICTION TRANSDUCER



(a) "IN TUNNEL" CALIBRATION TRACES FROM SKIN-FRICTION GAGE



(b) TUNNEL RUN SKIN-FRICTION GAGE TRACES

Figure 20 TYPICAL CALIBRATION AND RUN TRACES

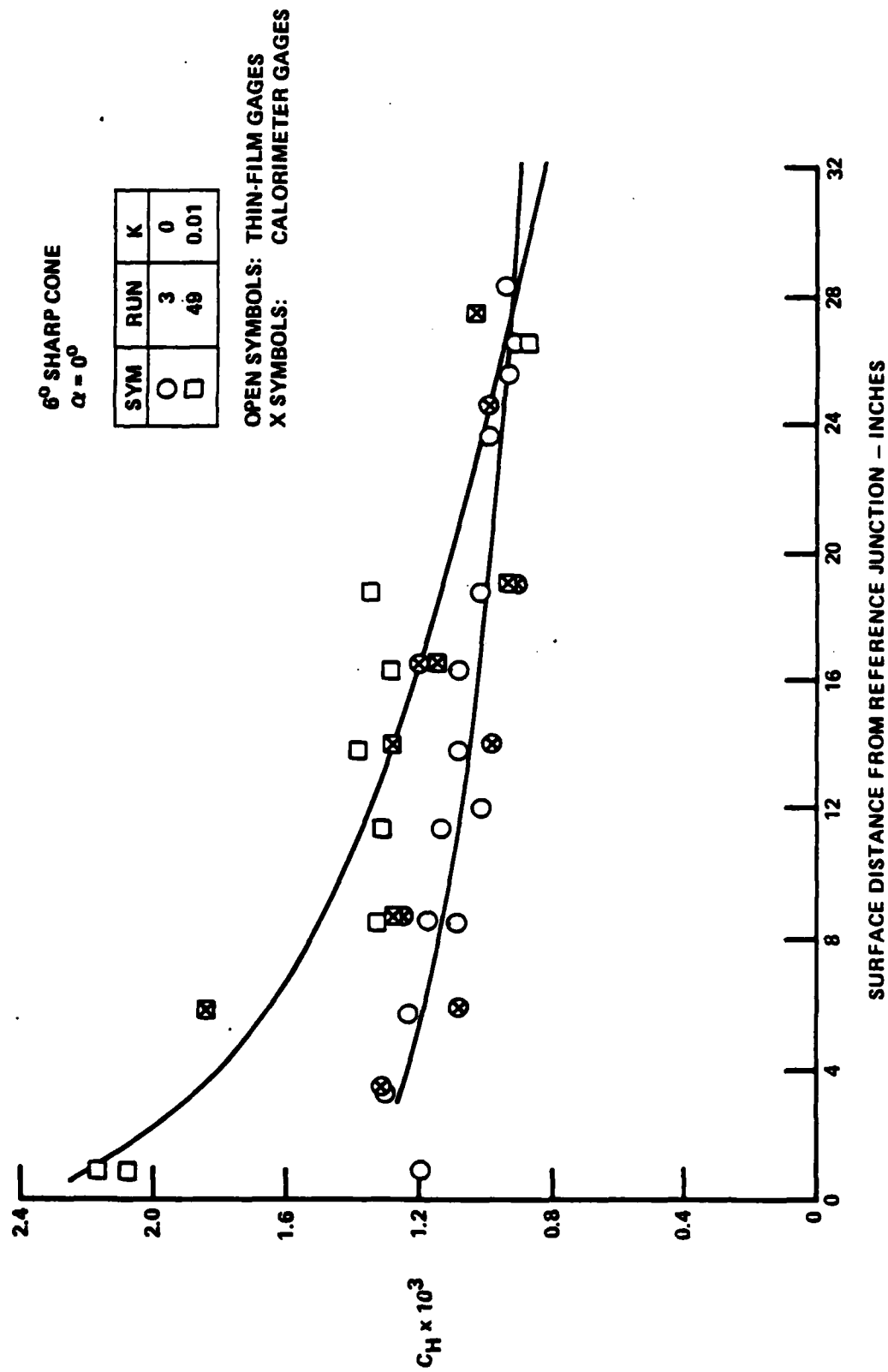


Figure 21 HEAT TRANSFER MEASUREMENTS ON THE ROUGH AND SMOOTH 6° CONE FOR $\alpha = 0$

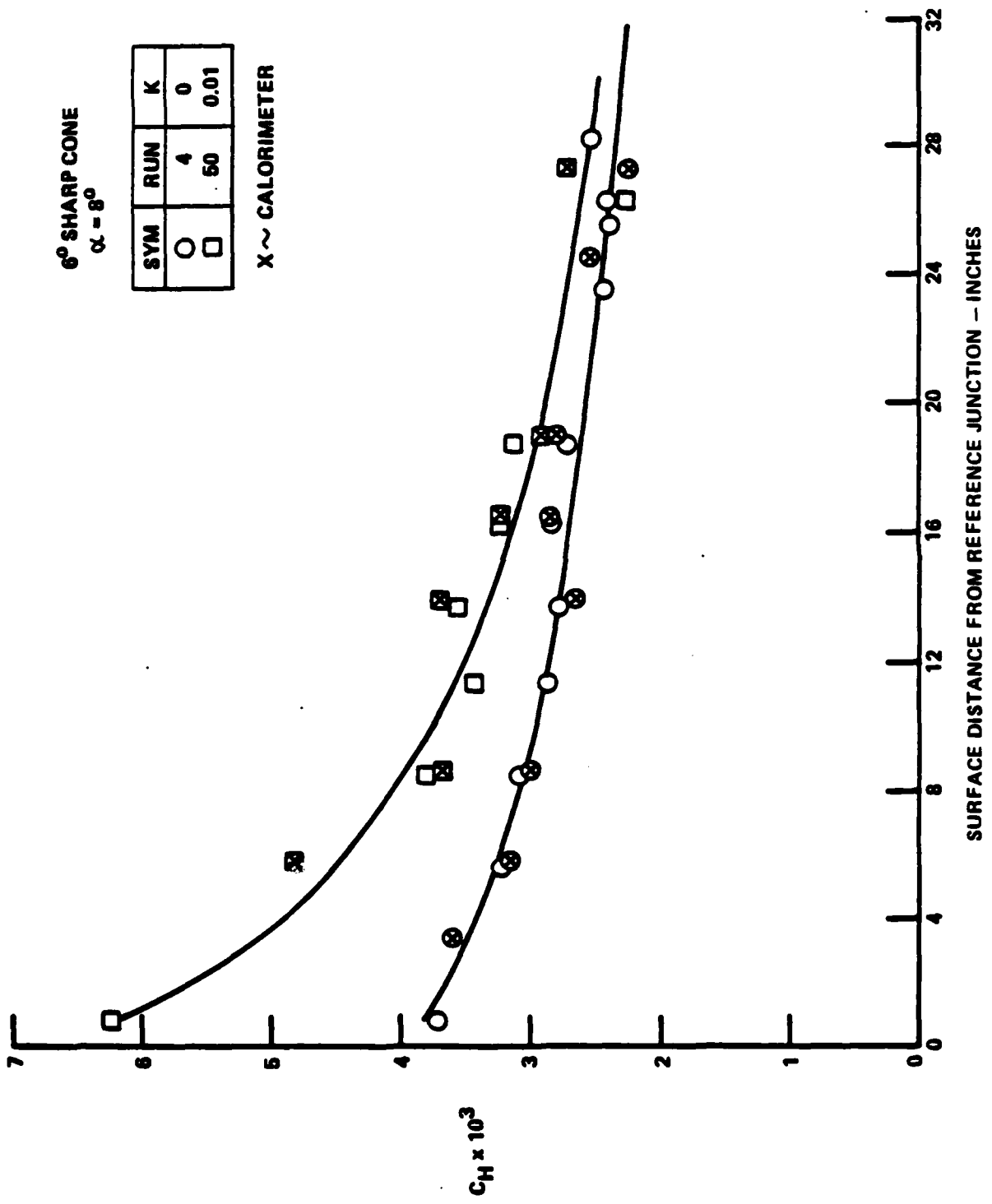


Figure 22 HEAT TRANSFER MEASUREMENTS ON THE ROUGH AND SMOOTH 6° CONE FOR $\alpha = 8^\circ$

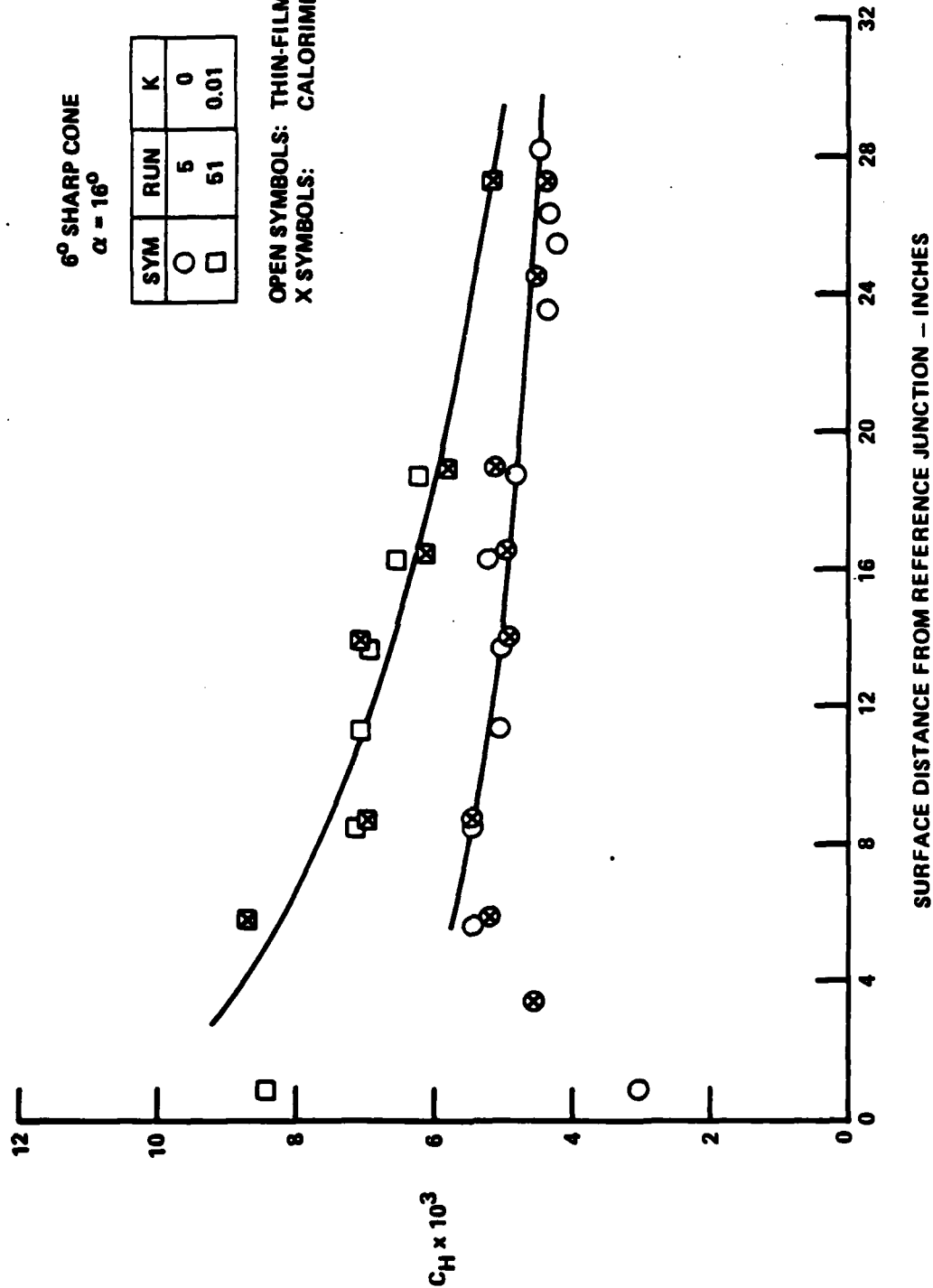


Figure 23 HEAT TRANSFER MEASUREMENTS ON THE ROUGH AND SMOOTH 6° CONE FOR $\alpha = 16^\circ$

Mach numbers) exhibit much larger streamwise gradients than the turbulent smooth-wall values or those predicted by the most recent analyses of Finson². At angles of attack of more than 8° , where the local windward-plane Mach numbers drop to less than 4, the distributions of heat transfer to the rough models do not exhibit the large streamwise gradients found at the smaller angle of attack. The corresponding set of skin-friction measurements made on the rough and smooth models, shown in Figures 24 through 26, exhibits the same trends as heating data; however, the roughness-induced skin-friction augmentation factors are significantly larger than the corresponding heating ratios. Here, roughness-induced skin-friction augmentation factors of up to 1.7 are observed on the windward ray close to the base of the cone. A similar set of heat transfer and skin-friction measurements on the cone coated with 15-mil sand-grain roughness are shown in Figures 27 and 28 for $\alpha = 8^\circ$. The absolute values of the heating ratios are larger on the 15-mil rough configuration, and the streamwise distributions of heat transfer and skin friction exhibit less streamwise gradients.

The measurements of heating and skin-friction augmentation factors, the Reynolds analogy factors, and the incremented heat transfer and skin-friction factors made in these studies with sand-grain surfaces are shown in Figures 29 through 31.

The large streamwise variations in augmentation heating factor, measured along the slender cones makes \tilde{R}_{eK} a poor correlating parameter, as shown in Figure 29. However, the roughness-augmentation factors close to the base of the cone are in relatively good agreement with those made on the biconic nosetips. The measurements of incremental heat transfer and skin friction plotted in Figure 31 are in relatively good agreement with Finson's² and Dahm's³ correlations for measurements made close to the base of the cone; however, the incremental heating just behind the nosetip is well above the predictions. These results suggest that there are compressibility or turbulent relaxation effects in these flows which are not modeled correctly in the theories. Plotting Reynolds analogy factor in terms of K_s/δ^* for both the wide-angle and slender cone measurements as shown in Figure 30, we observe that both sets of measurements are in relatively good agreement.

To examine the importance of turbulent relaxation effects, we performed measurements with roughness removed from the first 9 inches along the surface of the sharp cone at zero angle of attack. The heat transfer and skin-friction measurements downstream of the beginning of the rough surface are shown in Figures 32 and 33.

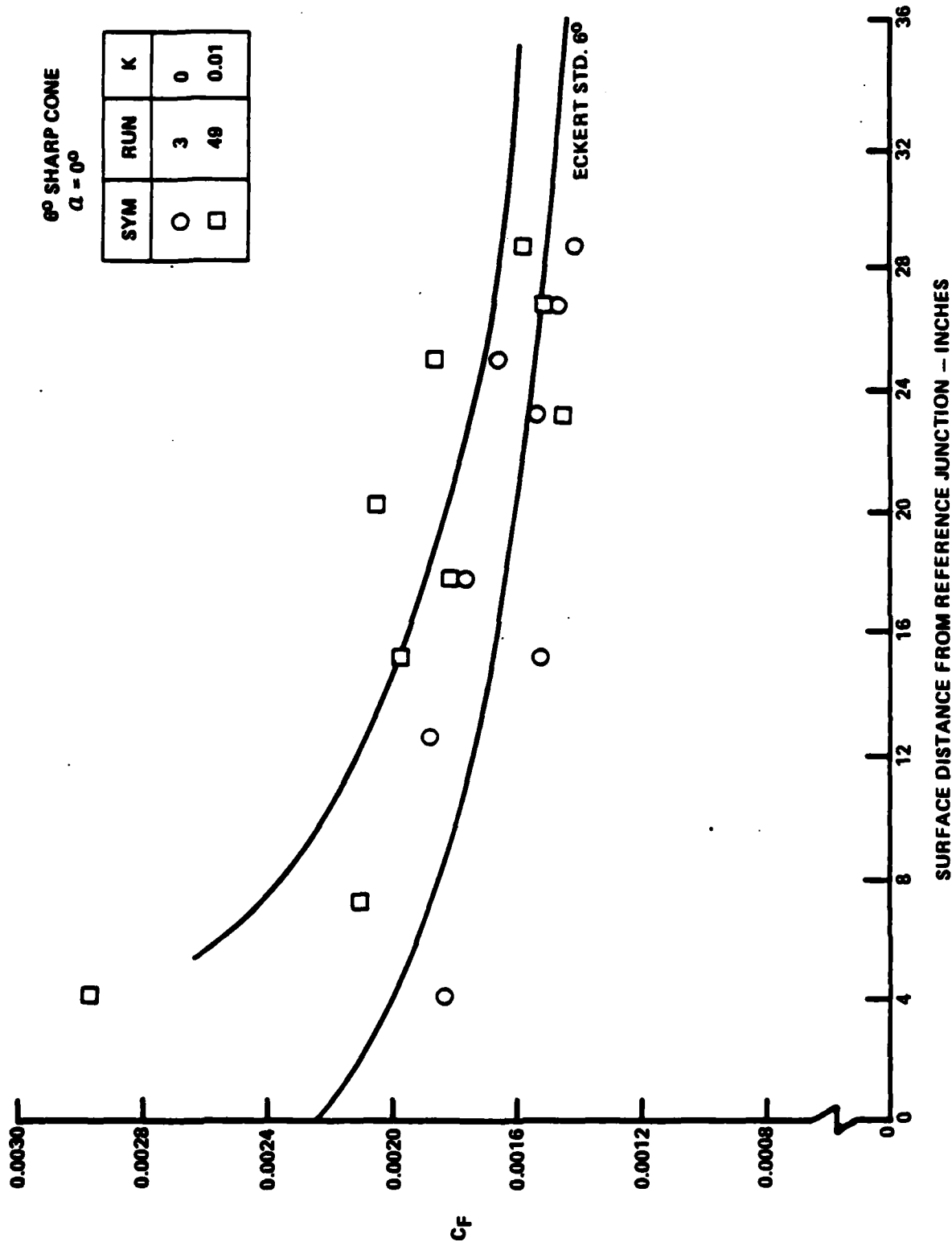


Figure 24 DISTRIBUTION OF SKIN FRICTION ALONG SHARP 6° CONE WITH SMOOTH AND 10-MIL SAND-GRAIN ROUGHNESS AT $\alpha = 0^\circ$

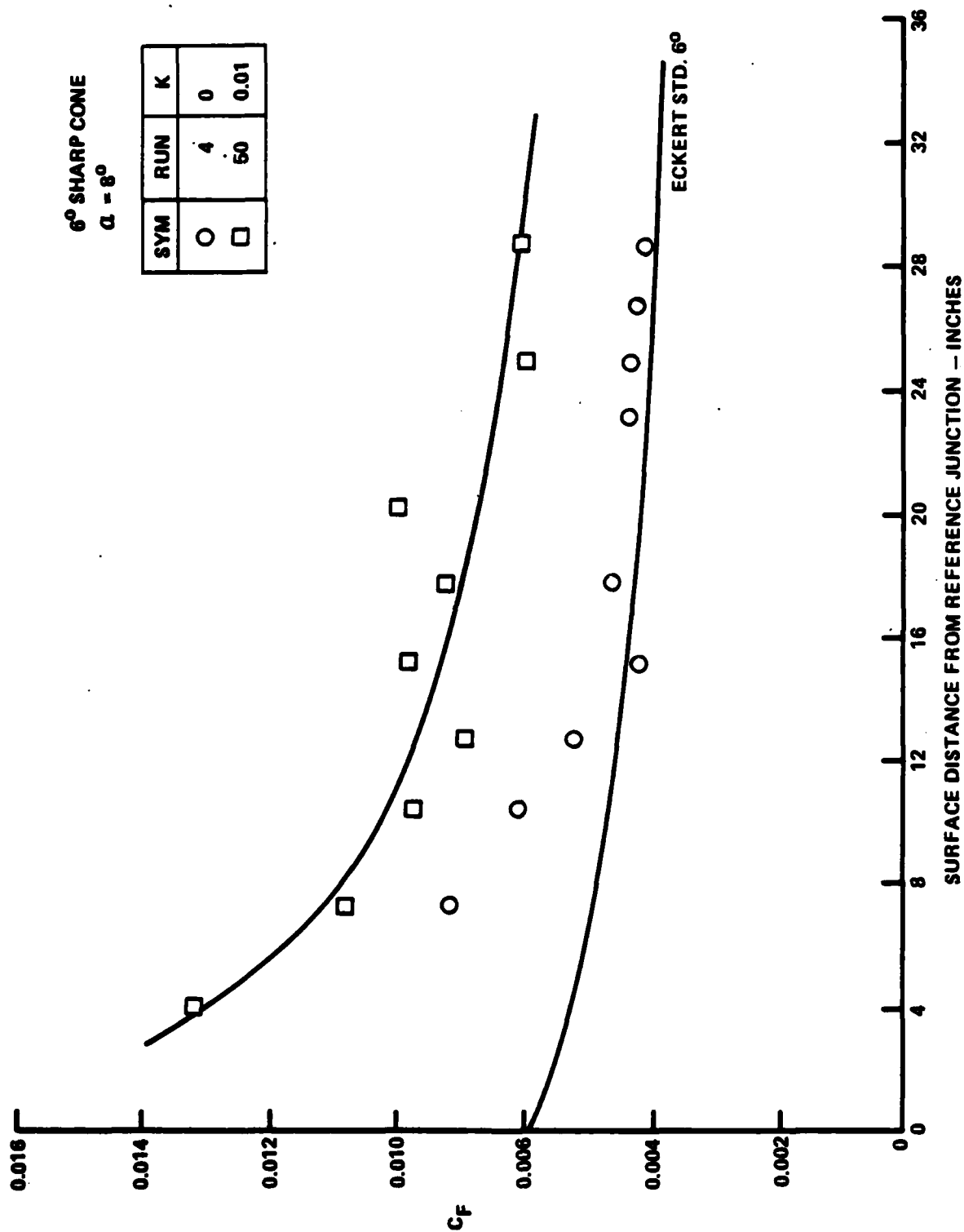


Figure 25 DISTRIBUTION OF SKIN FRICTION ALONG SHARP 6° CONE WITH SMOOTH AND 10-MIL SAND-GRAIN ROUGHNESS AT $\alpha = 8^\circ$

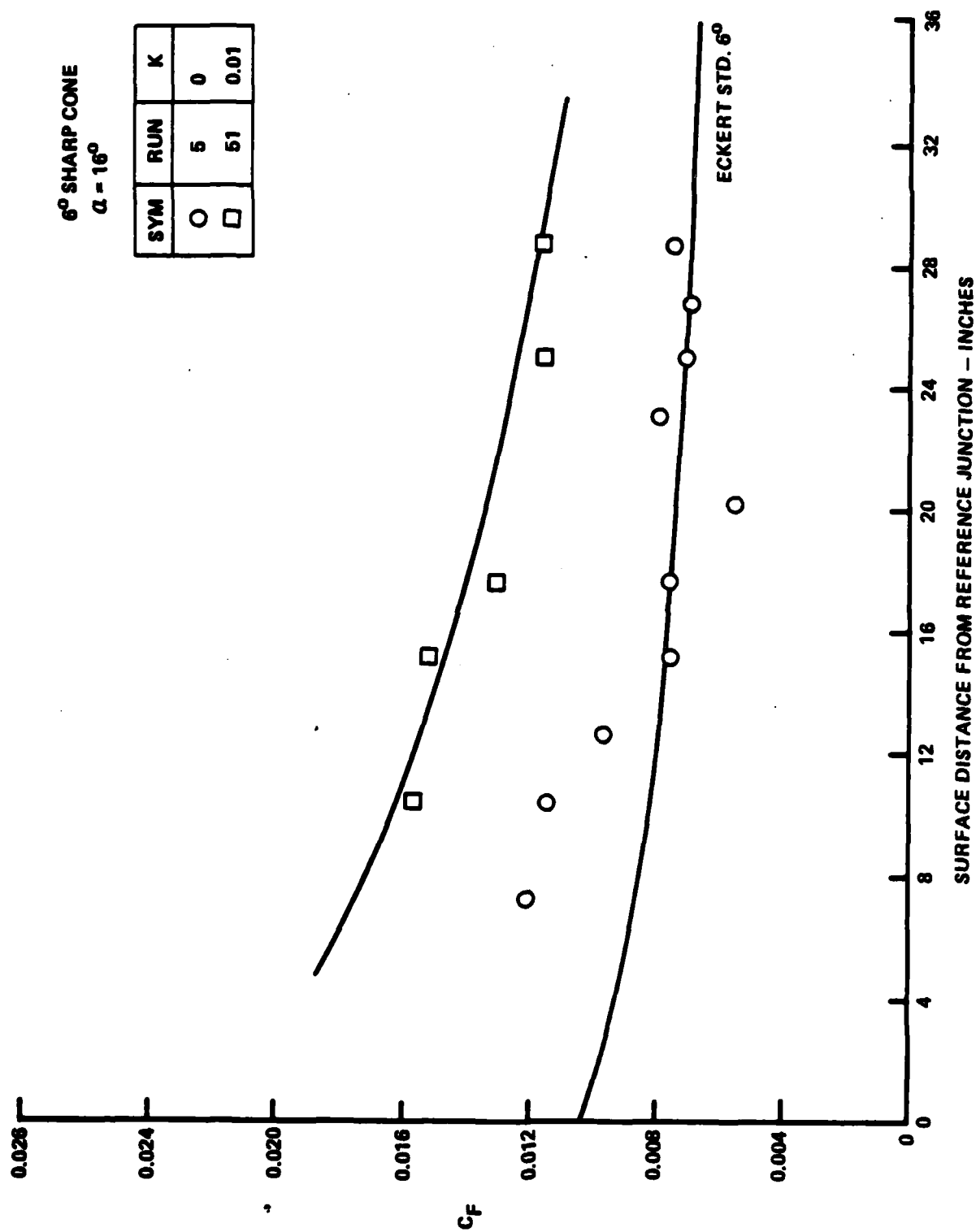


Figure 26 DISTRIBUTION OF SKIN FRICTION ALONG SHARP 6° CONE WITH SMOOTH AND 10-MIL SAND-GRAIN ROUGHNESS AT $\alpha = 16^\circ$

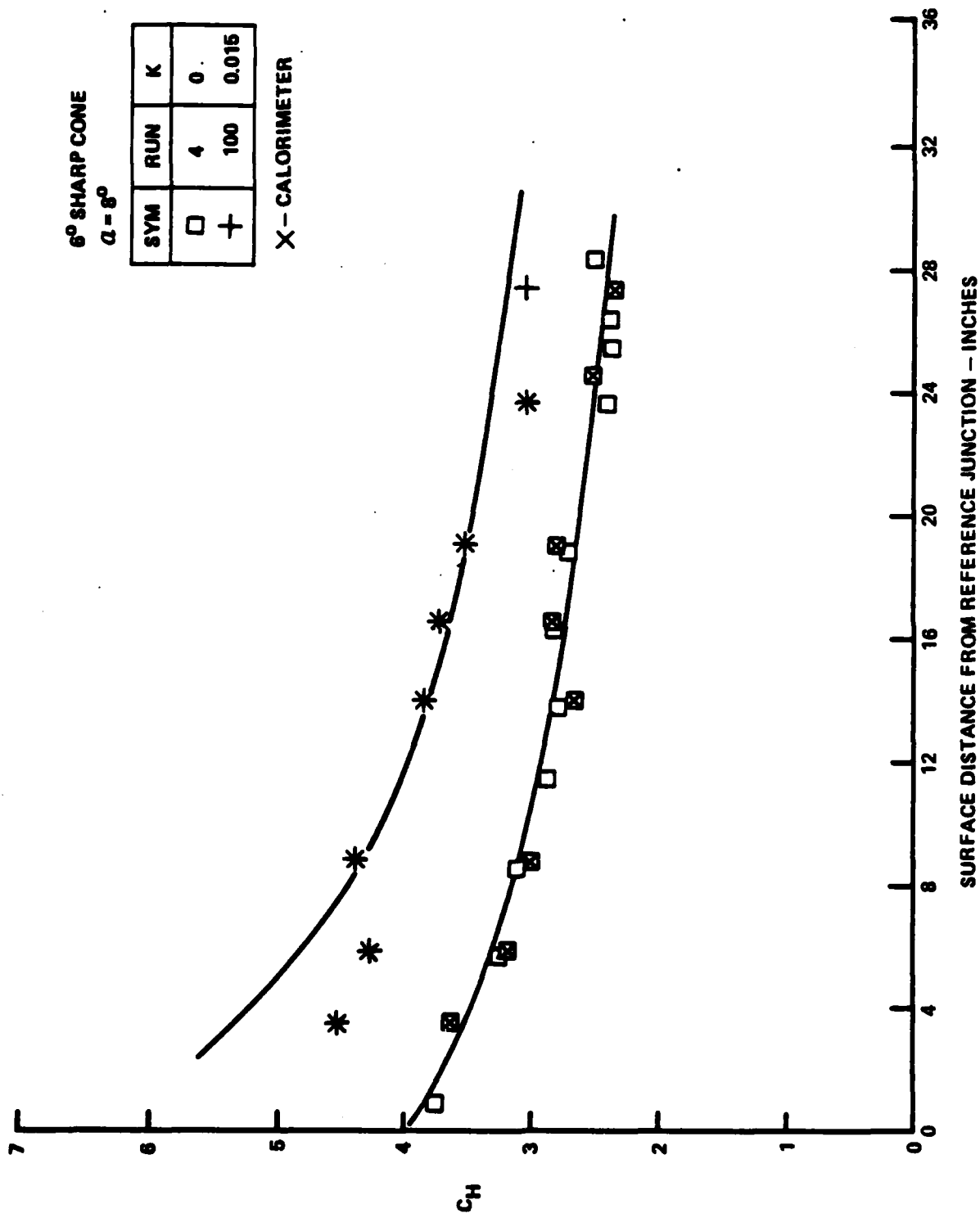


Figure 27 HEAT TRANSFER DISTRIBUTIONS ALONG 6° CONE WITH SMOOTH AND 15-MIL SAND-GRAIN ROUGHNESS AT $\alpha = 8^\circ$

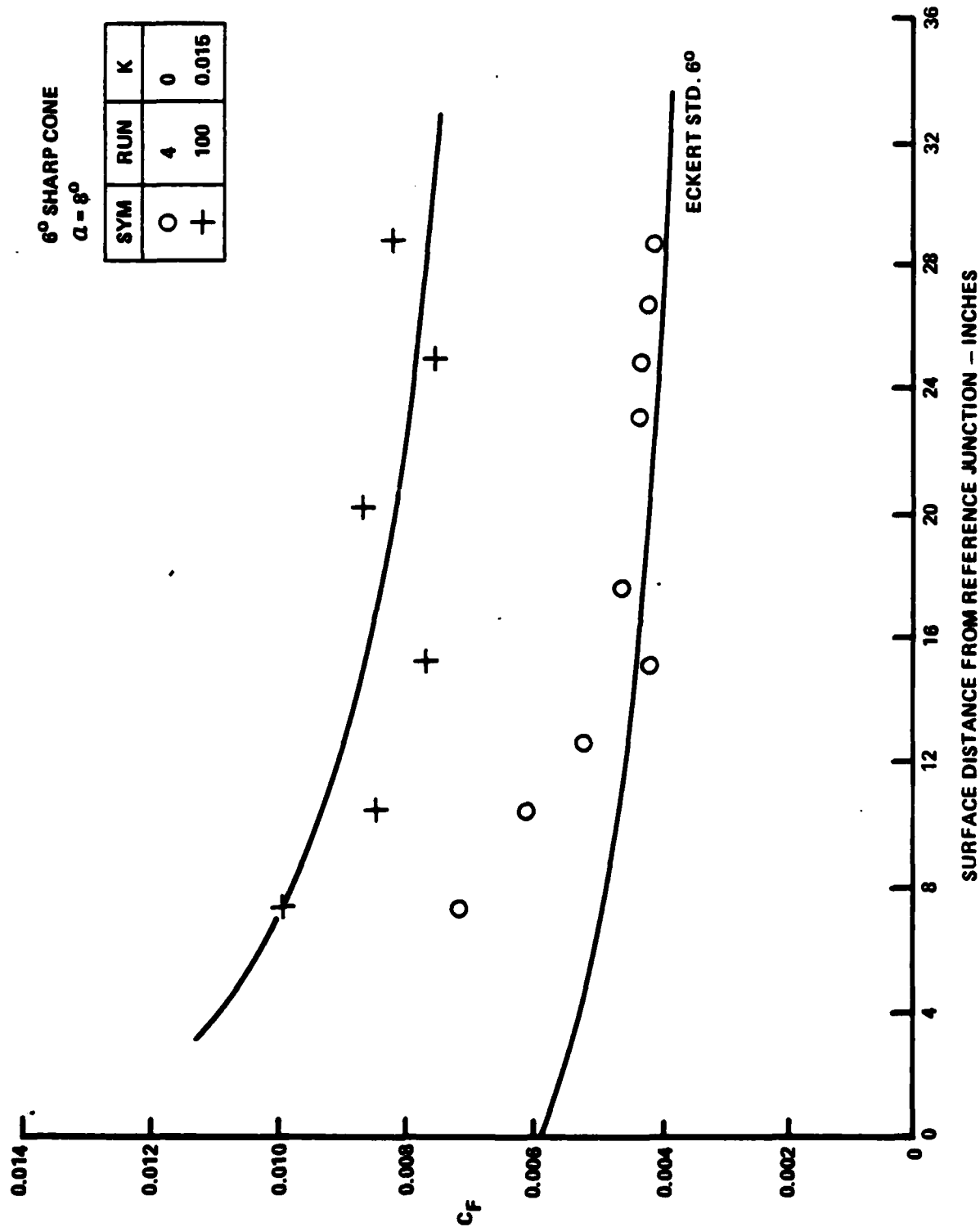


Figure 28 DISTRIBUTION OF SKIN FRICTION ALONG SHARP 6° CONE WITH SMOOTH AND 15-MIL SAND-GRAIN ROUGHNESS AT $\alpha = 8^\circ$

SYM	α	M_∞	R_∞	K
○	0	11.3	10×10^6	0.01
△	4	↓	↓	↓
□	8	↓	↓	↓
●	16	↓	↓	↓

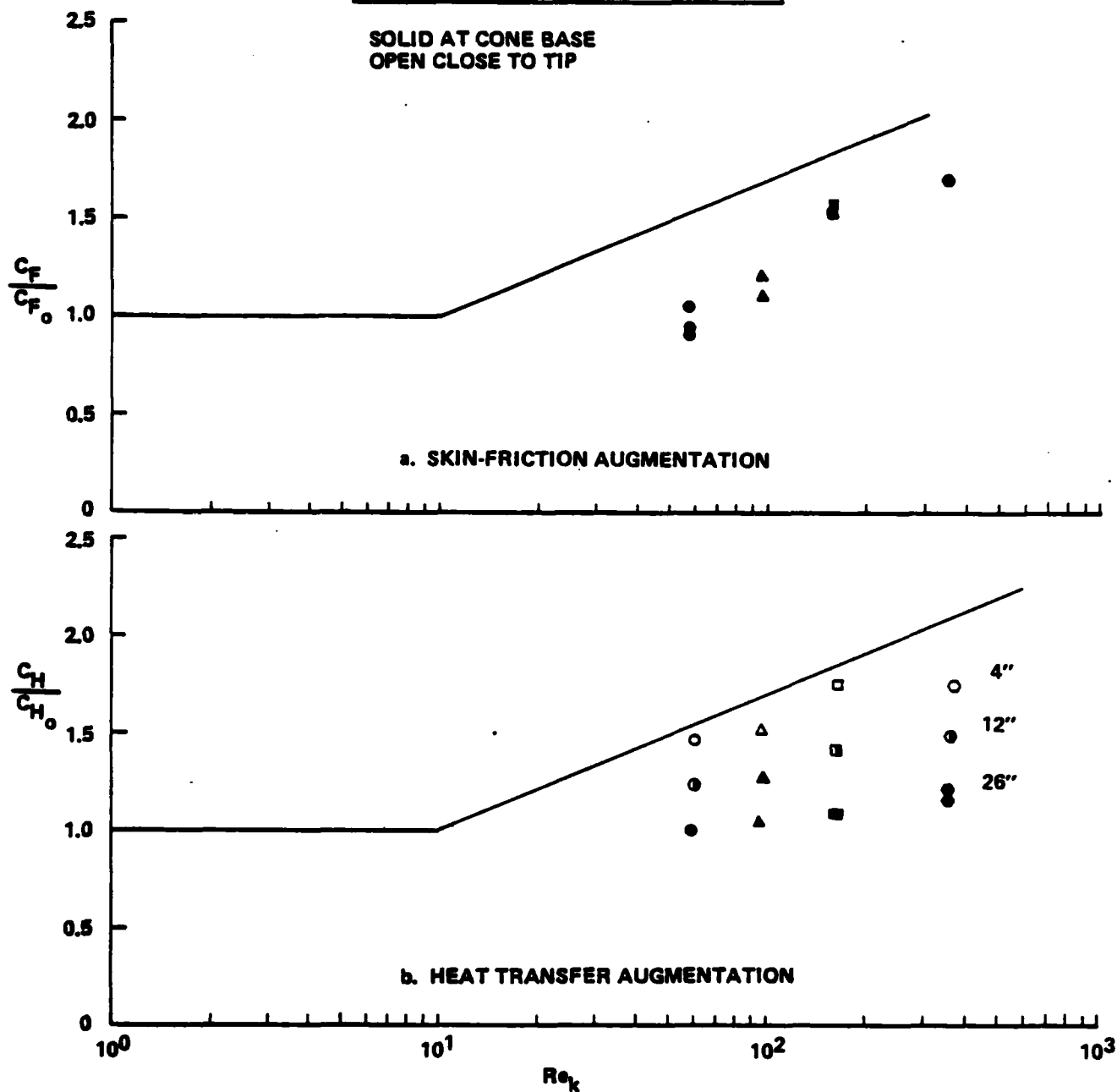


Figure 29 ROUGHNESS AUGMENTATION MEASUREMENTS IN 6° CONE

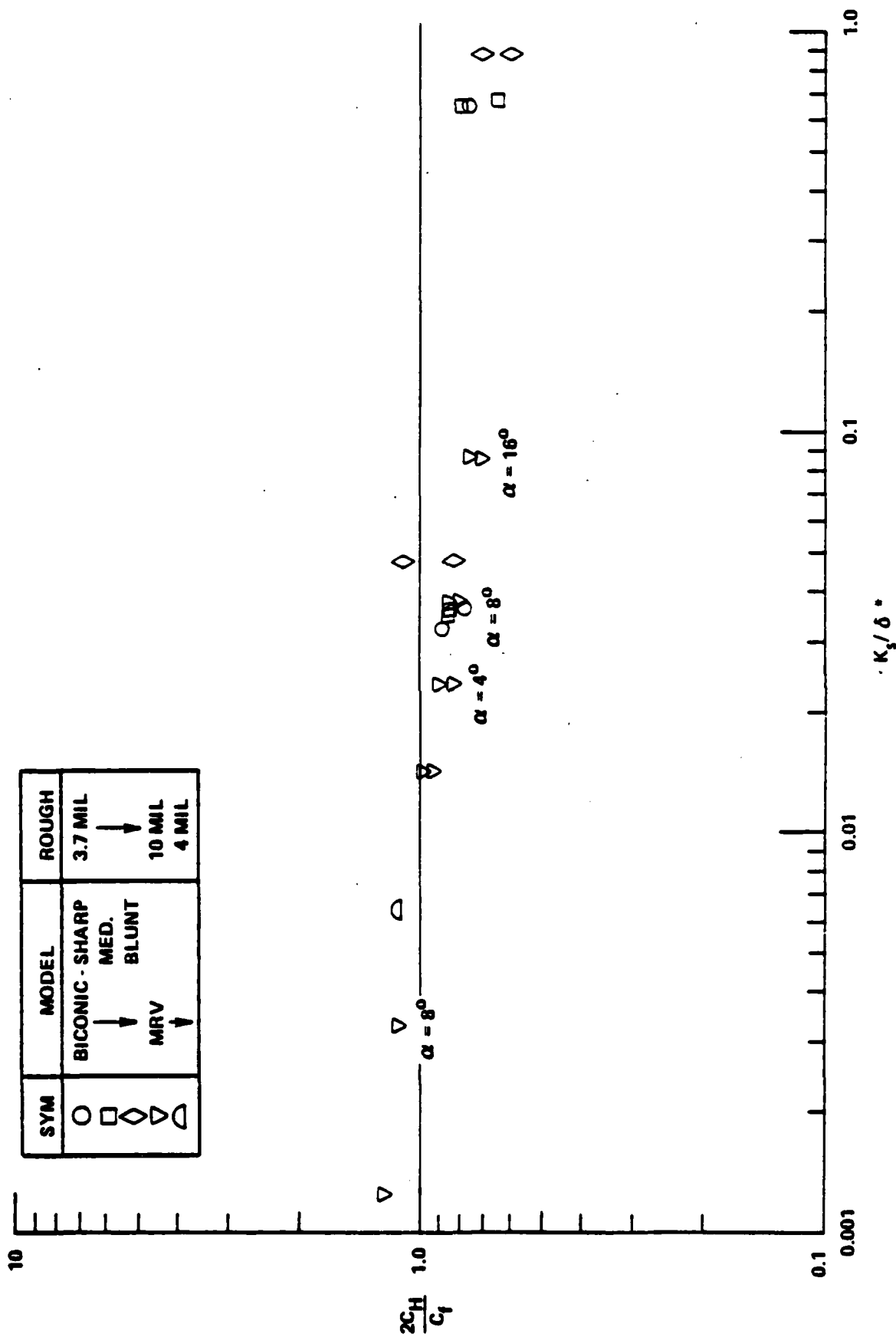


Figure 30 VARIATION OF REYNOLDS ANALOGY FACTOR WITH ROUGHNESS PARAMETER

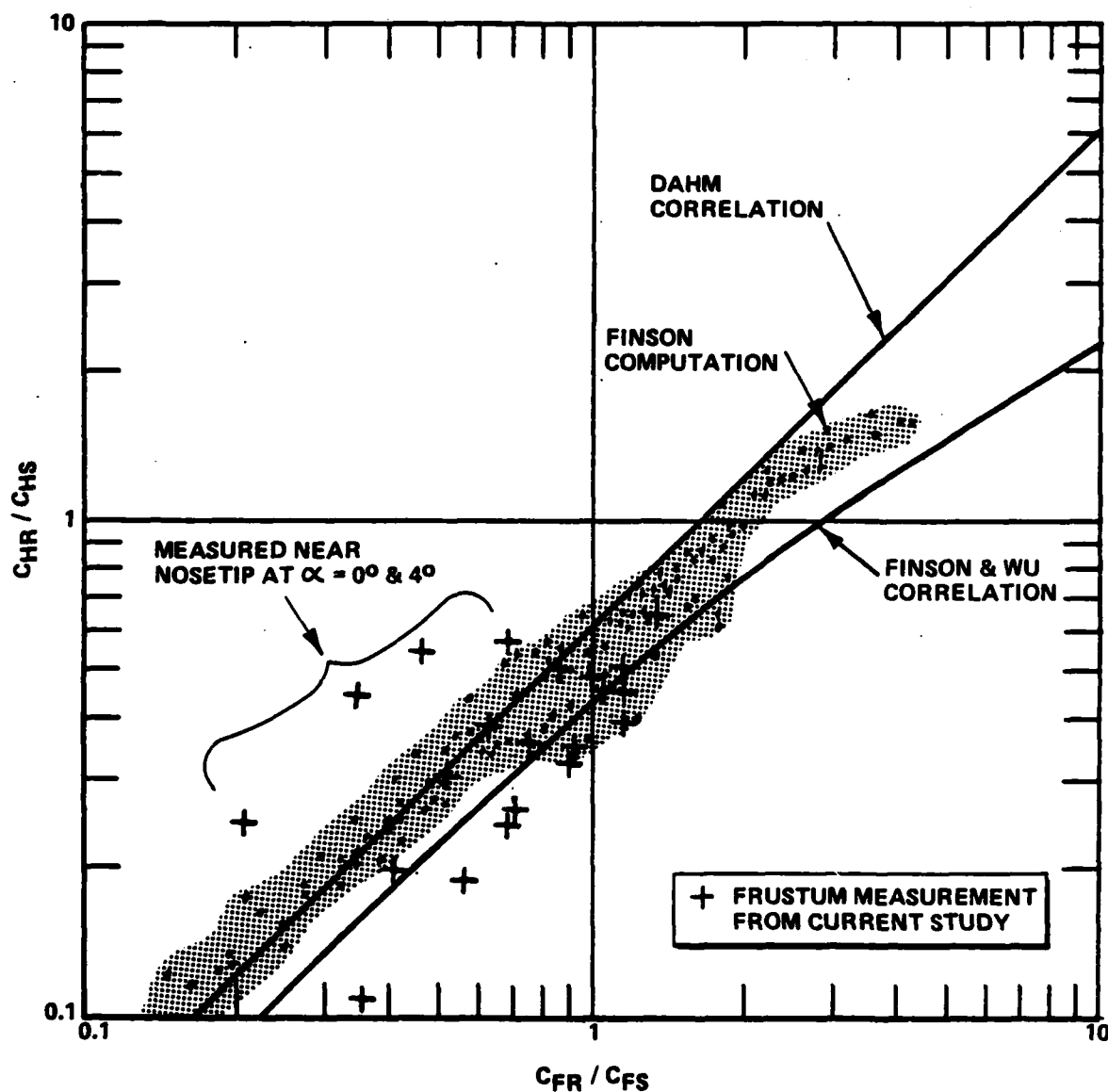


Figure 31 COMPUTED HEAT TRANSFER AUGMENTATION VERSUS SKIN-FRICTION AUGMENTATION

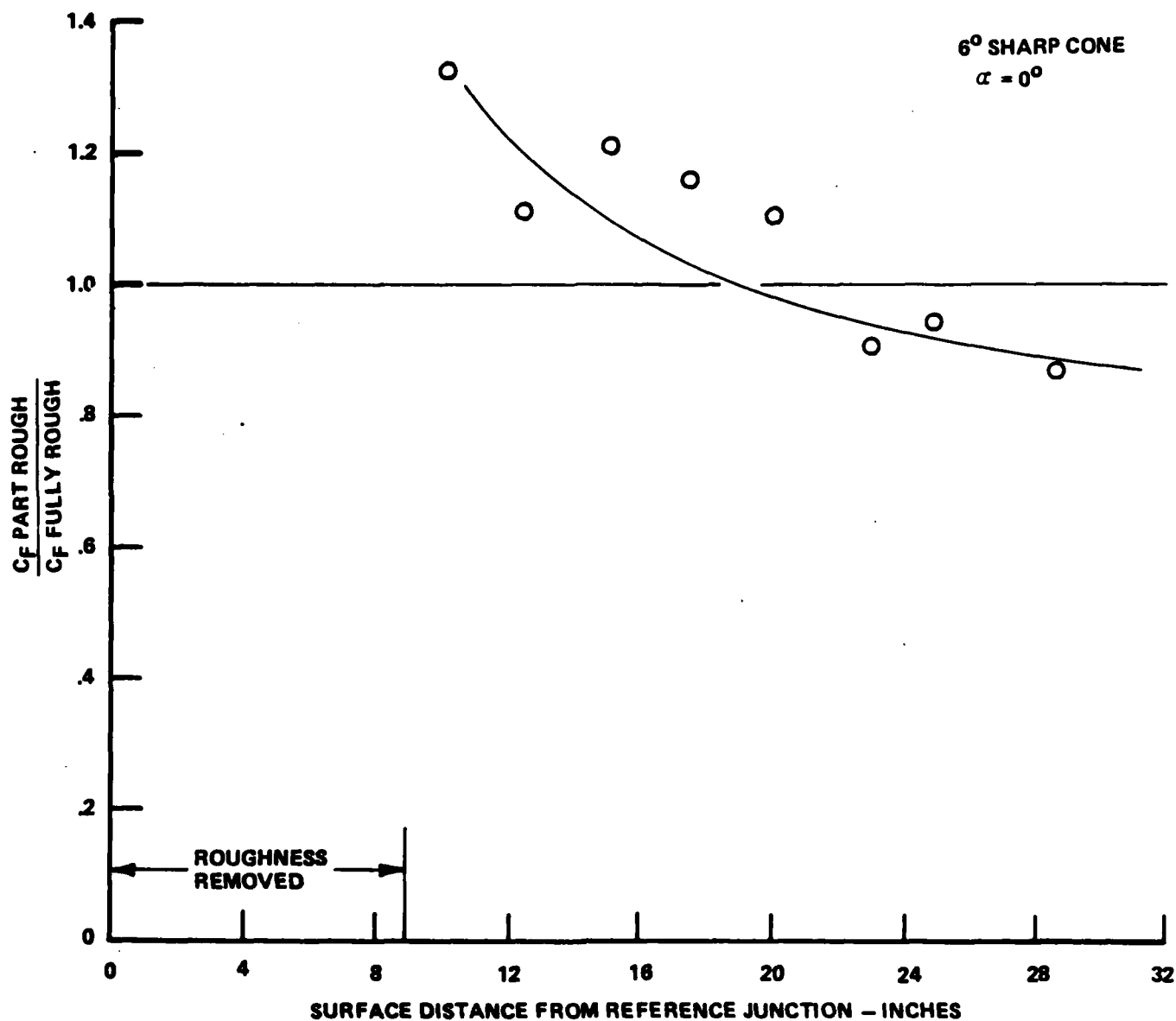


Figure 32 STREAMWISE VARIATION OF SKIN-FRICTION ENHANCEMENT RATIO DOWNSTREAM OF DISCONTINUITY IN SURFACE ROUGHNESS ON SHARP 6° CONE

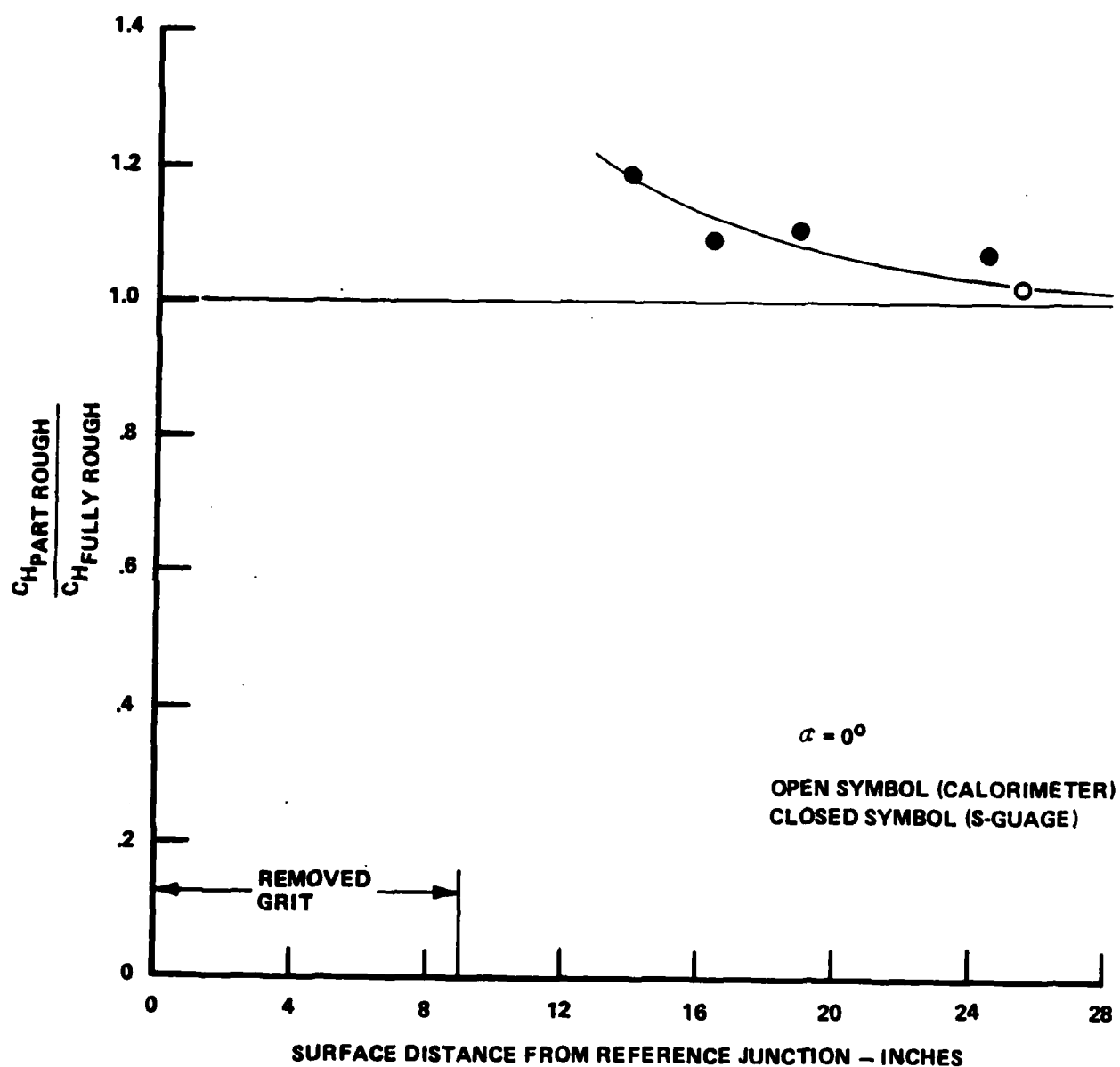


Figure 33 STREAMWISE VARIATION OF HEATING-ENHANCEMENT RATIO
 DOWNSTREAM OF DISCONTINUITY IN SURFACE ROUGHNESS
 ON SHARP 6° CONE

The heat transfer measurements exhibit a significant overshoot above the turbulent heating to a uniformly rough surface, while the comparable skin-friction measurements exhibit an overshoot/undershoot behavior. Clearly, turbulent non-equilibrium effects are important in hypersonic flows over a rough wall; further, more definitive flow-field measurements are required to define the key mechanisms of importance in these flows. The measurements made in these studies with sand-grain roughness using models prepared in different ways indicate that the shape, orientation, and spacing of the roughness elements can significantly influence roughness-enhanced heating. These observations were instrumental in the formulation of the studies with hemispherical and conical roughness elements described in the following subsection.

2.3.2 Studies With Patterned Roughness

The measurements to examine the effects of roughness shape and spacing on heat transfer to and skin friction of slender vehicles in hypersonic flow constitute the second part of a comprehensive series with surfaces of well-defined geometric characteristics. These studies were conducted in the 96-Inch Shock Tunnel with the basic 6° cone model used earlier in the sand-grain roughness studies. The model, which is shown mounted in the 96-Inch Shock Tunnel in Figure 34, was coated and instrumented successively with six different patterned surfaces and the corresponding heat transfer, skin-friction, and pressure instrumentation. The rough surface was designed so that measurements could be obtained from the closest to the most widely spaced roughness packing of practical interest ($2.5 < A_p/A_s^{-1} < 25$), spanning the "peak" in effective sand-grain roughness as depicted in the correlation shown in Figure 35. The roughness height, the position of the instrumentation, the angle of attack of the model, and the freestream conditions were selected so that the measurements covered the fully rough to the smooth regimes. Typical examples of the heat transfer distributions along the windward ray of the sharp cone for the different surface textures are shown in Figure 36. Here, the local Mach number is 4, and K/δ^* is large enough for the flow to be considered fully rough. A maximum heating-enhancement factor of 1.5 was recorded for the most closely packed conical roughness elements, with this factor decreasing with increased element frontal area per unit surface. Plotting these heat transfer measurements and those made for a range of angles of attack in terms of the non-dimensional spacing parameter D^*/K , as shown in Figure 37, results in a relatively poor correlation, reflecting the importance of roughness shape and spacing. As discussed earlier, we can introduce a correction for the shape of the roughness elements by



Figure 34 ROUGH 6° CONE MODEL MOUNTED IN 96" SHOCK TUNNEL

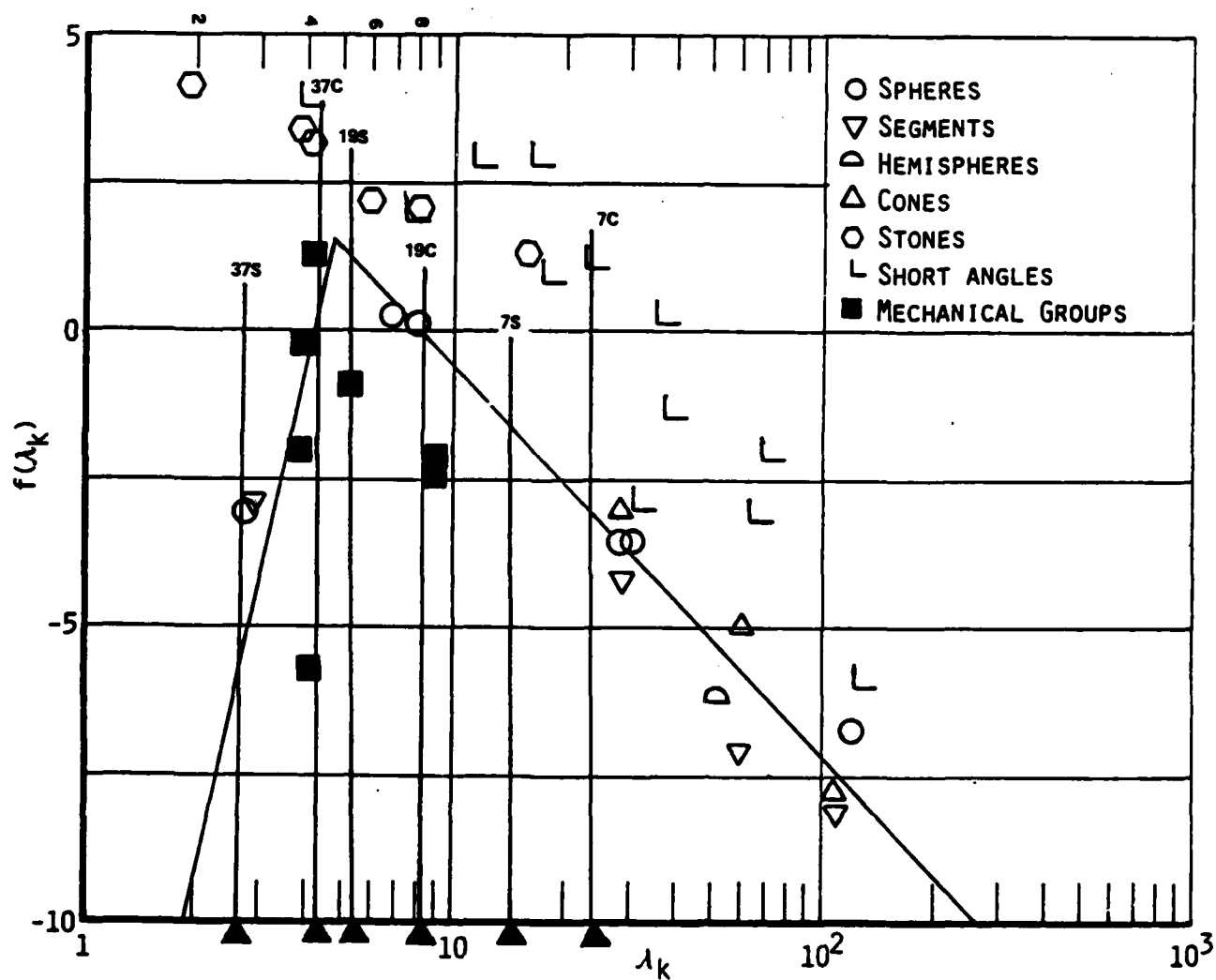


Figure 35 SIMPSON'S CORRELATION FOR THE EFFECT OF ROUGHNESS DENSITY

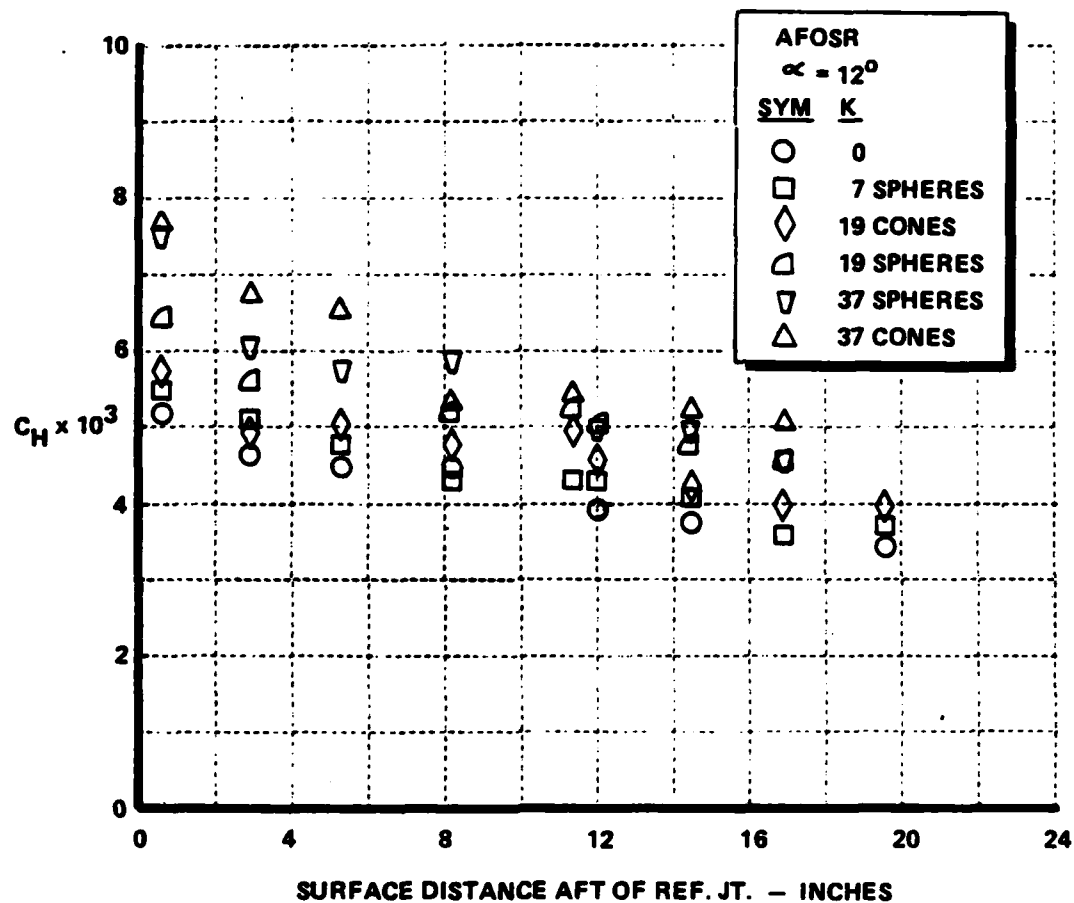


Figure 36 DISTRIBUTION OF HEATING ALONG WINDWARD RAY OF SHARP CONE FOR VARIOUS ROUGHNESS PATTERNS ($\alpha = 12^\circ$), $Re_\infty = 11 \times 10^6$, $M_\infty = 11.2$

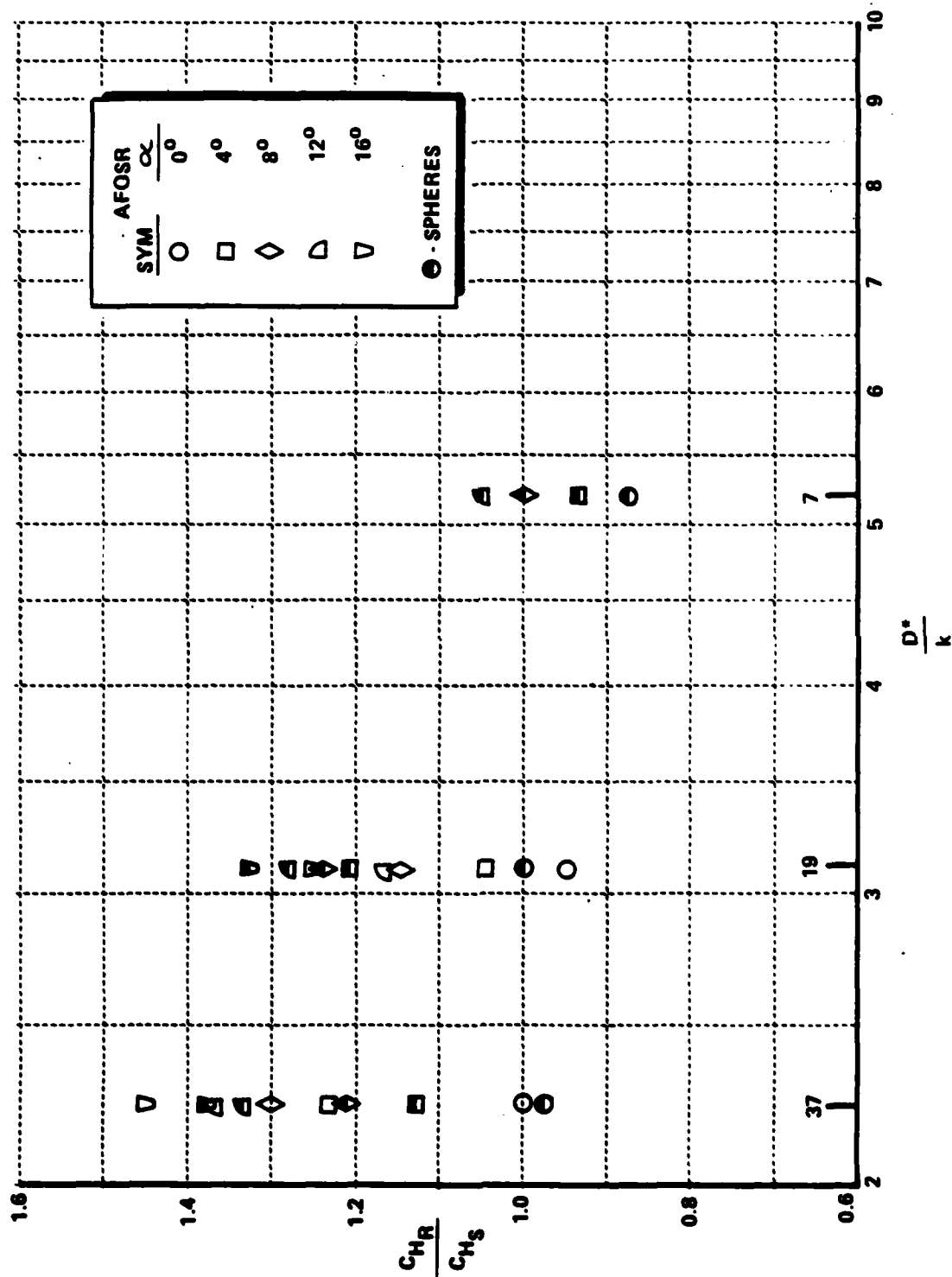


Figure 37 CORRELATION OF PATTERNED ROUGHNESS HEATING ON SHARP CONES
IN TERMS OF ROUGHNESS SPACING PARAMETER (D^*/k)

multiplying D^*/K by a factor proportional to the element drag coefficient, $C_D(C_D/C_{DREF})^{4/3}$ or, following Dirling⁴, an equivalent factor $(A_{ws}/A_p)^{4/3}$. Alternatively, following Simpson⁵, the heat transfer measurements can be correlated in terms of a single parameter A_p/A_s , the frontal area of the roughness per unit plan form surface area. Correlations of the heating-enhancement factors with the shape and spacing parameter $(A_p/A_s)^{-1}$ and $(D^*/K)(A_{ws}/A_p)^{4/3}$ are presented in Figures 38 and 39. The measurements at each angle of attack show a consistent trend, which, unlike the nosetip measurements—exhibits a local maximum for a certain combination of spacing and shape. It is interesting to note that, at high local Mach numbers, the measurements made on the less densely packed surface toward the base of the cone exhibited heating levels below those measured on smooth configurations. This confirms our earlier findings with the sand-grain rough model for small K/δ^* and large M_e . However, again it should be noted that, for these cases, large heating-enhancement factors were also recorded close to the tip of the cone. In general, the heat transfer measurements are equally well-correlated when plotted in terms of either (A_p/A_s) or $(D/K)(A_{ws}/A_p)^{4/3}$.

Finson's engineering model (based on concepts proposed by Lupmann and Goddard, together with his detailed numerical calculations), provides a good basis for interpreting the physical phenomena of key importance in rough wall heating, as well as a relatively simple prediction technique. The shear on a rough wall can be expressed as the sum of the viscous and form drag of the rough surface:

$$C_f = C_{f_{BASE}} + \int_B^T \frac{\rho u^2}{\rho_e u_e^2} C_D B(y) \cdot \frac{d^2(y)}{D^2} dy$$

where $B(y)$ is the blockage factor, and $d(y)$ and D are the diameter of the roughness element and the spacing between elements, respectively. From his detailed numerical solutions, Finson showed that ρ and u were relatively constant between the base and top of the roughness element at values ρ_R, u_R close to the top of the roughness. Equation (7) becomes

$$C_f = C_{f_B} + \frac{\rho_R u_R^2}{\rho_e u_e^2} C_D B\left(\frac{K}{2}\right) \frac{A_p}{A_s}$$

where A_p/A_s is the ratio of projected area of the roughness element in the direction of the flow to total area of the flow on which they stand, and $B(\frac{K}{2})$ is the average value of $B(y)$.

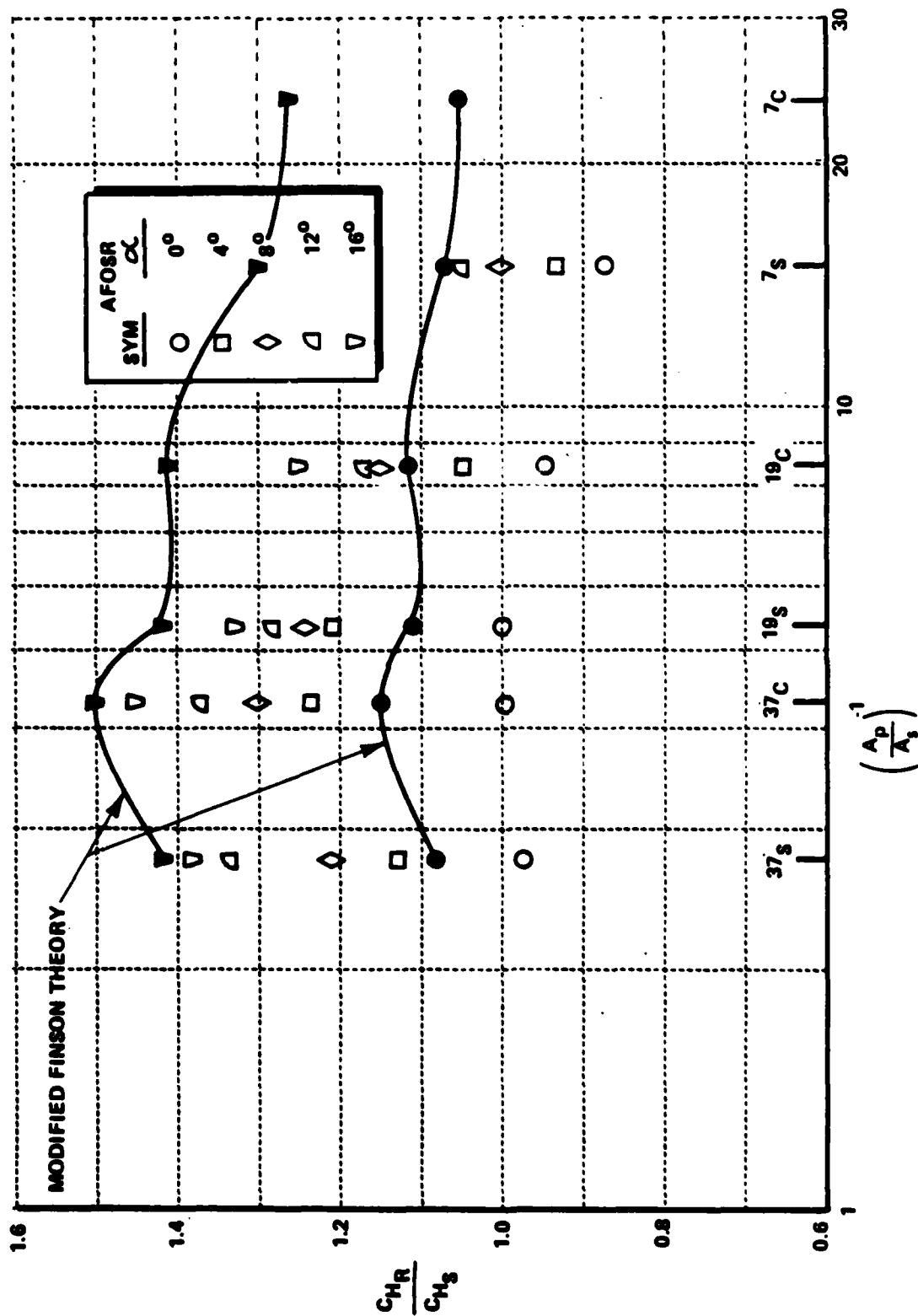


Figure 38 CORRELATION OF PATTERNED ROUGHNESS HEATING ON SHARP CONES
IN TERMS OF EFFECTIVE WINDWARD AREA (A_p/A_s)

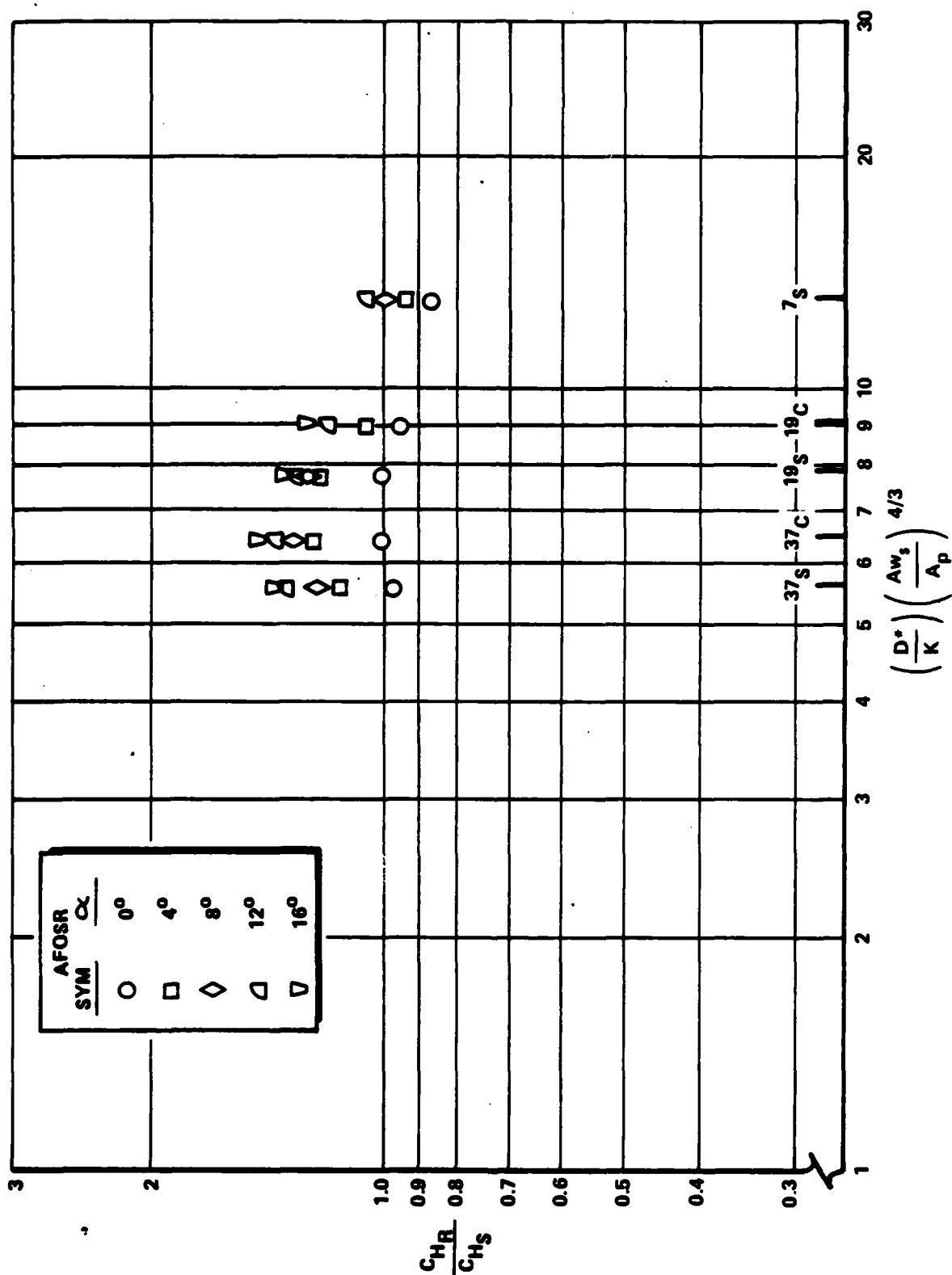


Figure 39 CORRELATION OF PATTERNED ROUGHNESS HEATING ON SHARP CONES
IN TERMS OF DIRLING'S SHAPE PARAMETER

For compressible flows Finson found that

$$U_R/U_e = 0.247 + .234 \log \left(\frac{P_R A_S}{P_e A_P} \right)$$

where

$$\frac{P_R}{P_e} = \left[\frac{T_w}{T_e} + \left(1 + \frac{\gamma-1}{2} M_e^2 - \frac{T_w}{T_e} \right) \left(\frac{U_R}{U_e} \right) - \frac{\gamma-1}{2} M_e^2 \frac{U_R^2}{U_e^2} \right]$$

Therefore, assuming C_{F_B} is the smooth wall heating level, it is possible to relate the rough wall skin friction to the smooth wall value in the generalized form

$$\frac{C_{H \text{ ROUGH}}}{C_{H \text{ SMOOTH}}} = f_1 \left(M_e, T_w, \frac{K}{\theta} \right) * f_2 \left(\lambda, B, \left(\frac{K}{D} \right), C_D \right)$$

The relationship for heat transfer is assumed of the same form

$$\frac{C_{H \text{ ROUGH}}}{C_{H \text{ SMOOTH}}} = f'_1 \left(M_e, \frac{T_w}{T_e}, \frac{K}{\theta} \right) * f'_2 \left(\lambda, B, \left(\frac{K}{D} \right), C_D \right)$$

If we assume that the product of the blockage factor and C_D are invariant with rough shape and space, then for constant local free stream condition, we get the Dvorak-Simpson Parameter:

$$\frac{C_{H \text{ ROUGH}}}{C_{H \text{ SMOOTH}}} = f \left(\frac{A_P}{A_S} \right)$$

A slightly different form can be obtained by the subsonic blunt body approximation

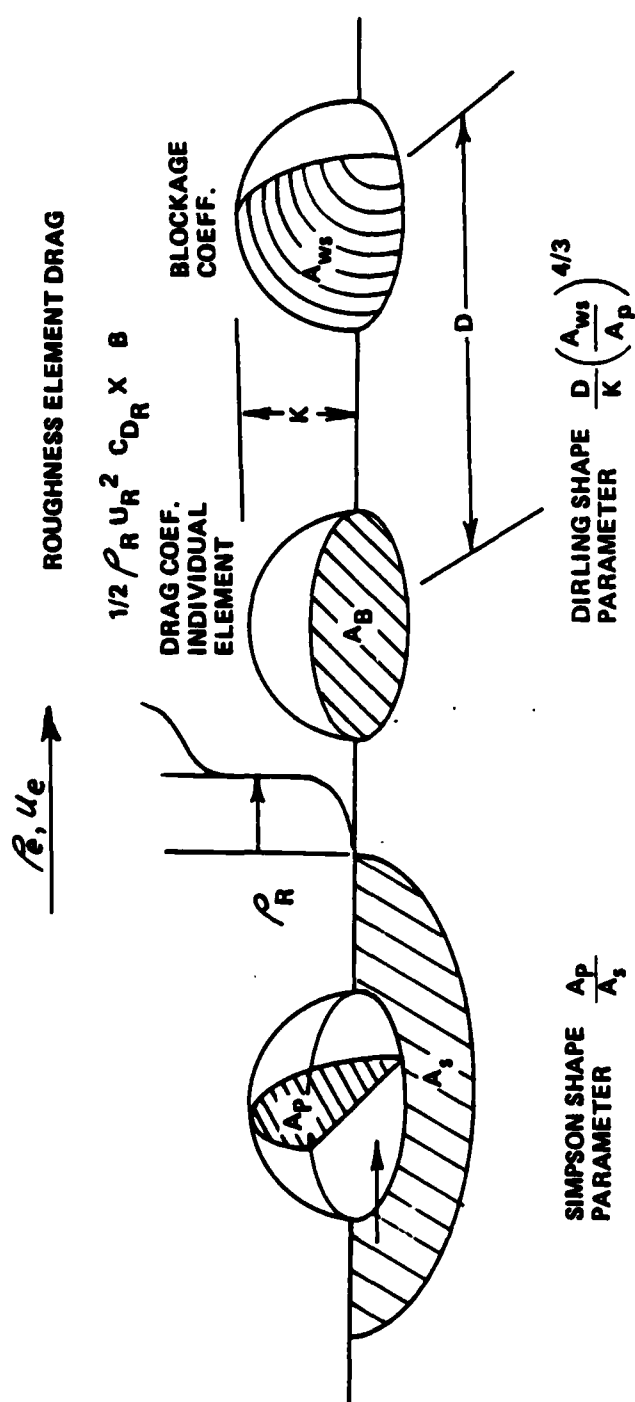
$$C_D = C_{D \text{ REF}} \left(A_P/A_{WS} \right)$$

and using D/K rather than A_S/A_P to obtain the correlation in terms of the Dirling parameter,

$$\frac{C_{H \text{ ROUGH}}}{C_{H \text{ SMOOTH}}} = f \left(\frac{D}{K} \cdot \left(\frac{A_{WS}}{A_P} \right)^{4/3} \right)$$

where Figure 40 defines the nomenclature used in this analysis.

A more universal format in which local freestream effects are removed to a first order, is a correlation in which heat transfer to the patterned surface is non-dimensionalized by transfer rate to a sand-grain surface with the same roughness height. Figures 41 and 42 show the measurements plotted in this format. The most important features demonstrated by these measurements and the earlier measurements on the biconic nosetips is that, in contrast to the results from the subsonic studies, the maximum heating levels on the patterned surface were no more than 10% larger than the sand-grain values. This figure is at least 50% lower than would be predicted from methods based on the subsonic measurements, where equivalent roughness heights of up



SMOOTH WALL DRAG $\Sigma \Delta D_S$

$$\Delta D_S = 1/2 \rho_e u_e^2 C_{FS} A_S$$

$$\Delta D_T = \Delta D_S + \Delta D_R$$

FORM DRAG OF ROUGHNESS ELEMENT ΔD_R

$$\Delta D_R = 1/2 \rho_R u_R^2 \cdot C_{DR} A_p \cdot B$$

$$\Sigma \Delta D_T = 1/2 \rho_e u_e^2 C_{FR} \Sigma A_S$$

$$\frac{C_{FR}}{C_{FS}} = 1 + \frac{1}{C_{FS}} \cdot \frac{\rho_R u_R^2}{\rho_e u_e^2} \cdot B \cdot C_{DR} \cdot \left(\frac{A_s}{A_p} \right)^{1/3}$$

Figure 40 SIMPLIFIED DRAG MODEL FOR ROUGH-WALL SKIN FRICTION

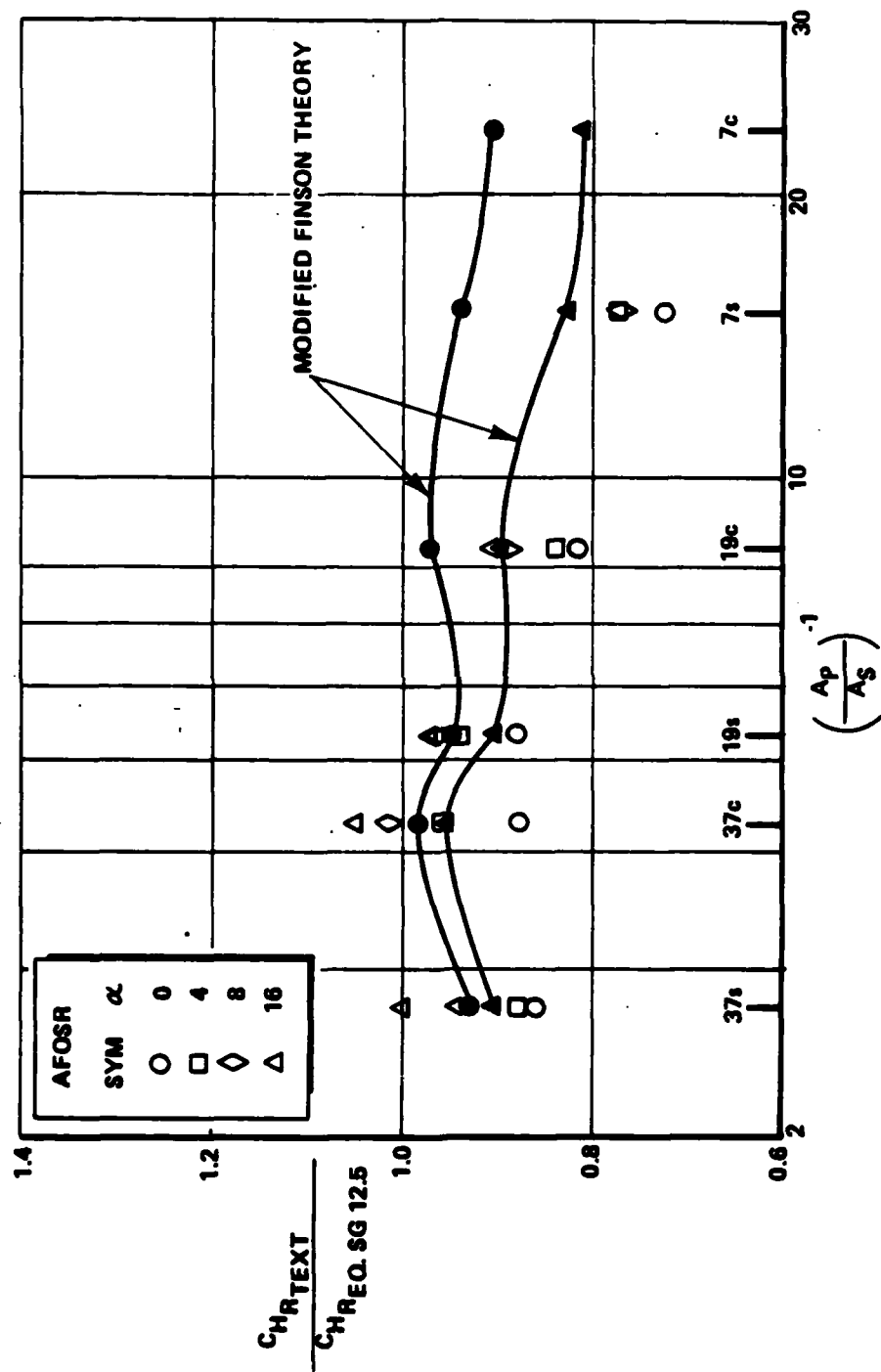


Figure 41 VARIATION OF NONDIMENSIONAL ROUGHNESS HEATING WITH ROUGHNESS SHAPE AND SPACING PARAMETER (A_p/A_s)

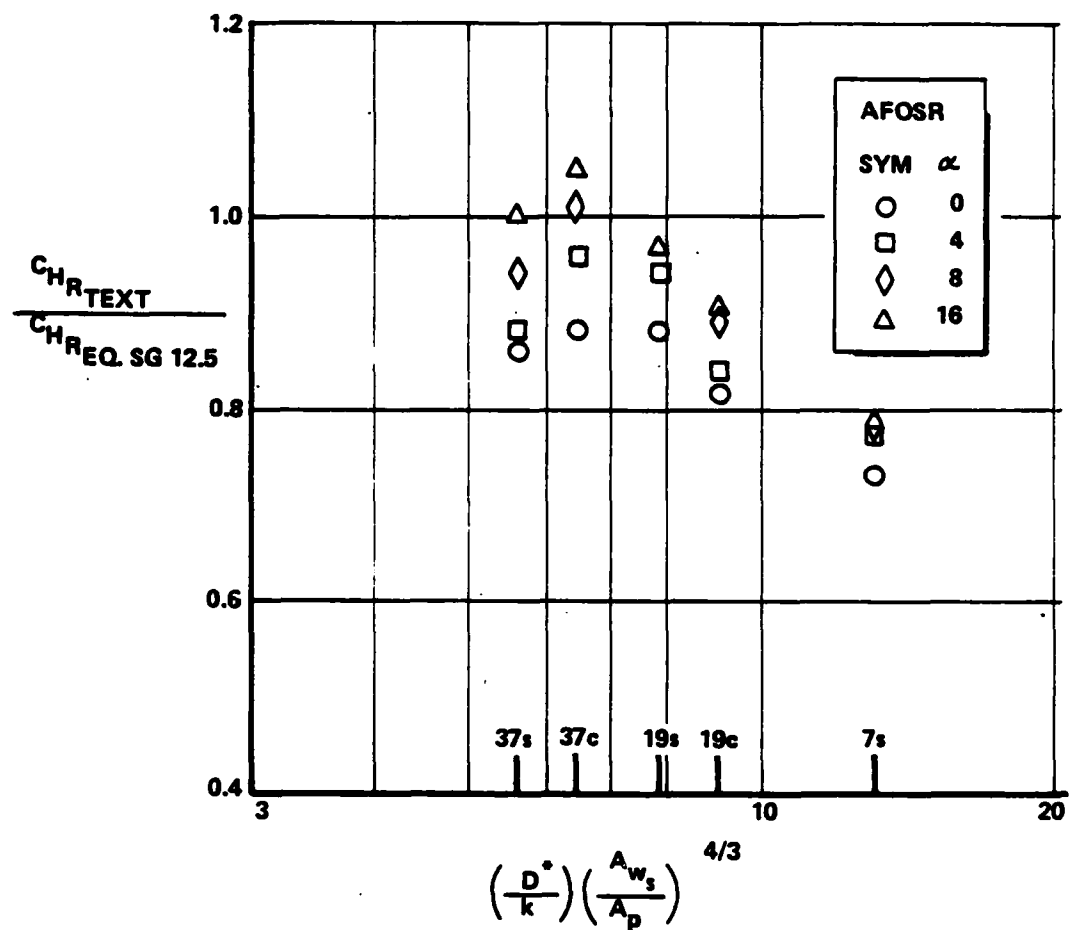


Figure 42 VARIATION OF NONDIMENSIONAL ROUGHNESS HEATING WITH ROUGHNESS SHAPE AND SPACING PARAMETER $(D^*/k) (A_{ws}/A_p)^{4/3}$

to six times the sand-grain height were recorded. We do, however, observe a similar rapid decrease in relative heating levels with increased roughness spacing and decreased drag coefficient, as found in the earlier studies in low-speed flows over adiabatic walls. Again, our measurements correlate equally well with either of the roughness density parameters. Using correlations such as those given in Figures 41 and 42, together with the correlations for the roughness-augmented heating to sand-grain rough surfaces, for example those presented in Figures 42 through 44, a rapid estimate of the heating to a non-ablating surface of arbitrary roughness can be made. In general, for high-speed flows, the heating rates computed by this technique will be significantly less than those computed on the basis of, for example, the PANT data base and the Dirling correlation⁴ of the low-speed measurements.

2.4 STUDIES OF SURFACE ROUGHNESS EFFECTS ON VISCOUS/INVISCID INTERACTION OVER FLAP CONTROLS

2.4.1 Studies With Sand-Grain Roughness

Surface roughness effects have their greatest impact on the aerothermal performance of high-speed vehicles with embedded regions of shock-wave/boundary layer interaction, with or without flow separation. Surface roughness thickens the boundary layer and decreases the momentum close to the wall, each of which serves to cause lengthening of the interaction region and make the boundary layer more susceptible to flow separation. However, of greater importance is the rapid thinning of the boundary layer which occurs in the recompression region of such interactions, causing a rapid local increase in K/θ (and, hence, the heating rate). Generally, for interacting flows over rough surfaces, it is not possible to use the current codes to calculate with accuracy either the scale of the interaction or the magnitude or position of peak heating.

As in the earlier studies with slender and wide-angle cones, the research to investigate the effects of surface roughness on the aerothermal performance of re-entry vehicle control systems was conducted in two phases. In the first phase, measurements were obtained on the flap control system on slender, sharp and blunted conical and biconic models, coated with sand-grain rough surfaces for ranges of roughness heights, local Mach numbers, and roughness Reynolds numbers. The second phase of

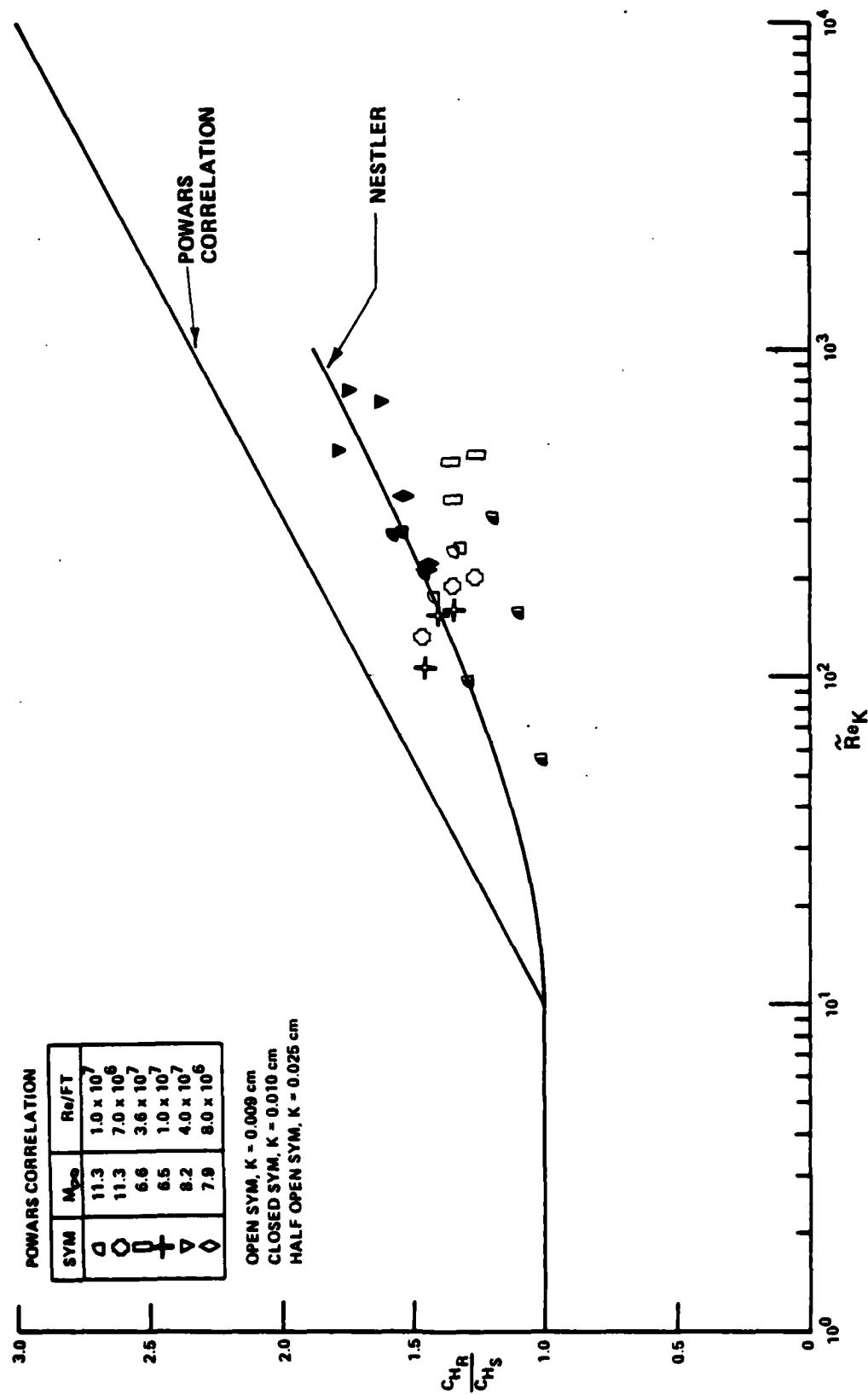


Figure 43a CORRELATION OF ROUGHNESS-AUGMENTED HEATING ON MRV AND BICONIC CONFIGURATIONS, AND COMPARISON WITH PANT CORRELATION

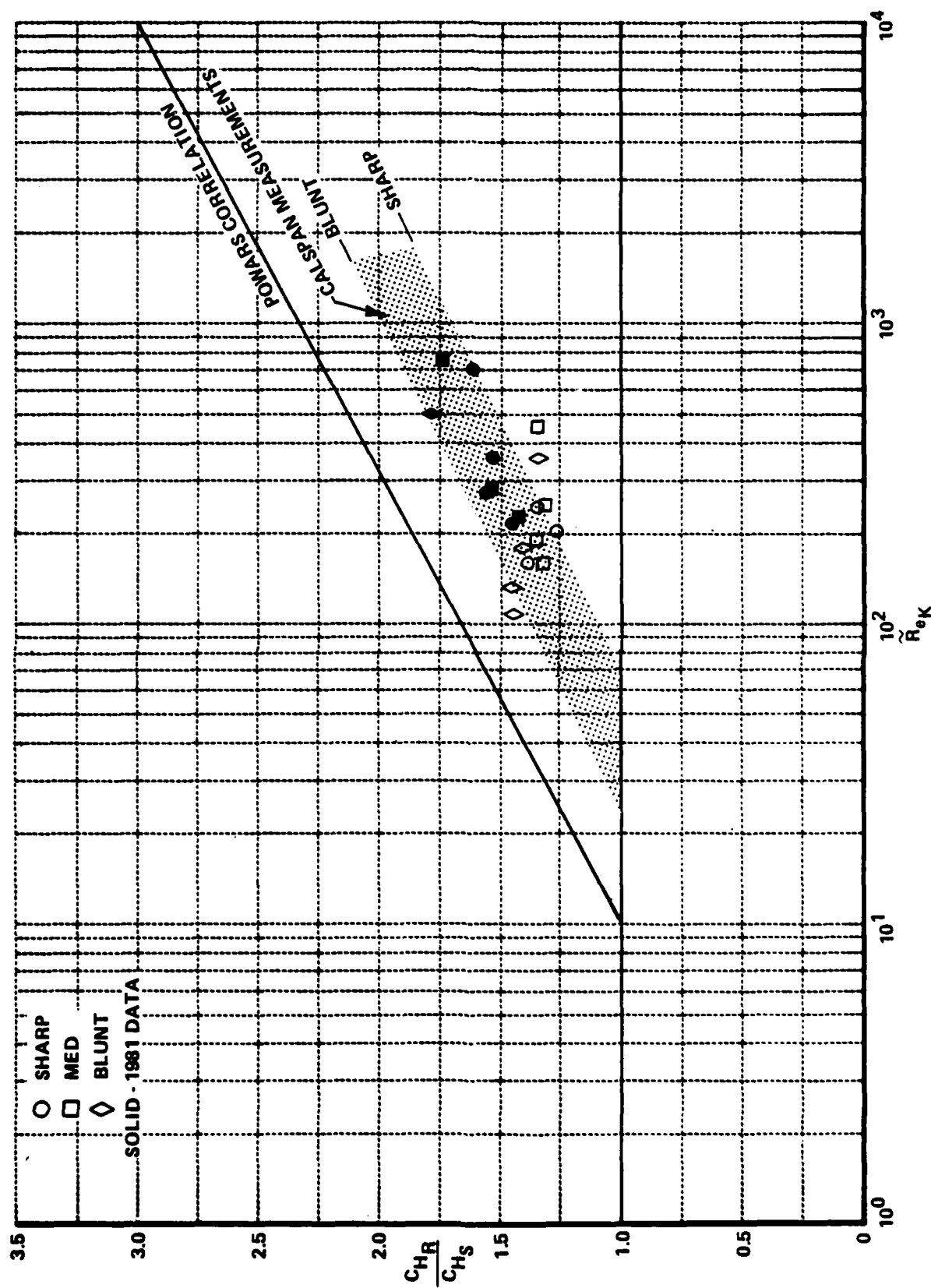


Figure 43b CORRELATION OF ROUGH-WALL AUGMENTATION HEATING FACTORS
FROM THE PRESENT AND PREVIOUS STUDIES AT CALSPAN

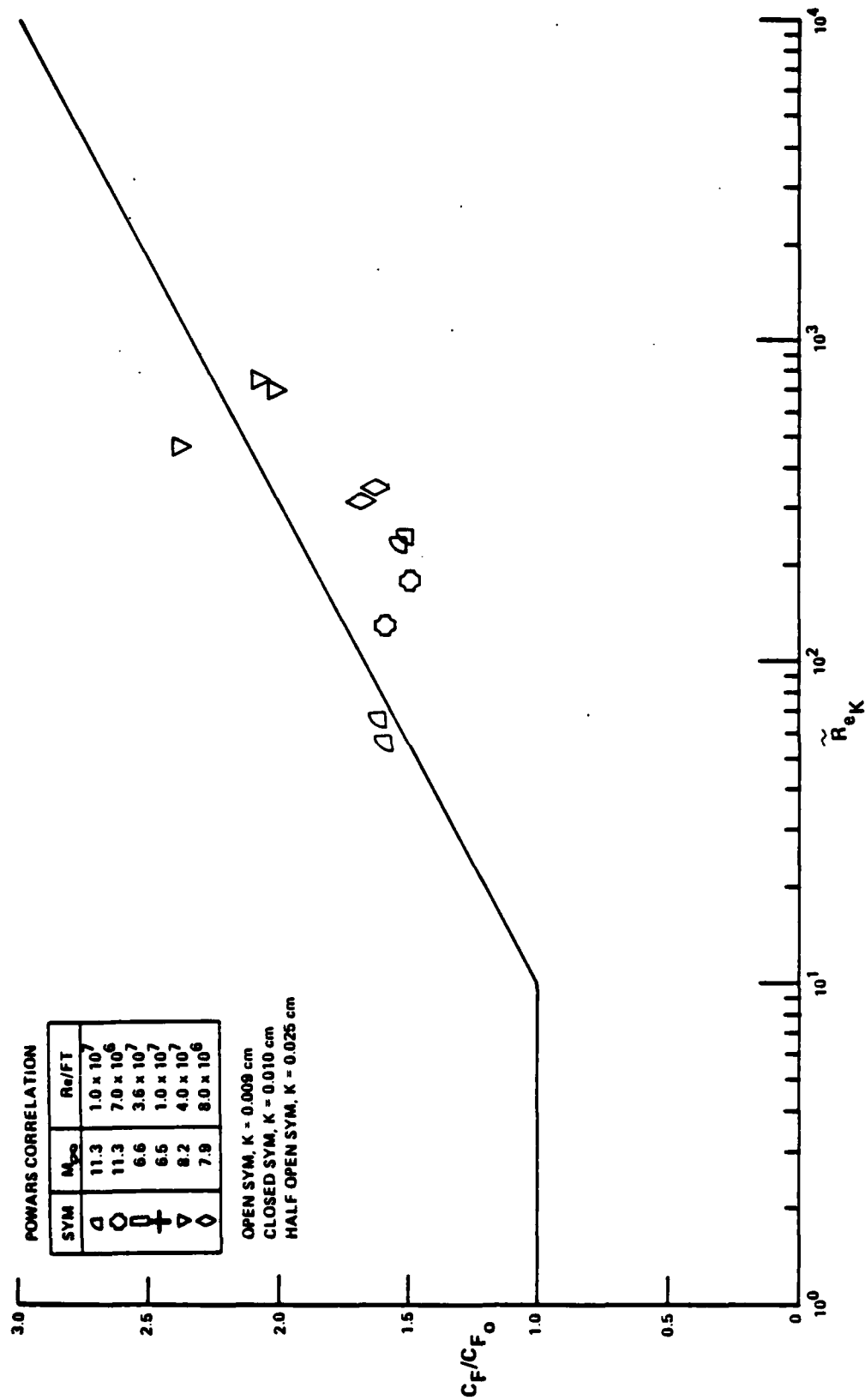


Figure 43c CORRELATION OF ROUGHNESS-AUGMENTED HEATING ON MRV AND BICONIC CONFIGURATIONS, AND COMPARISON WITH PANT CORRELATION

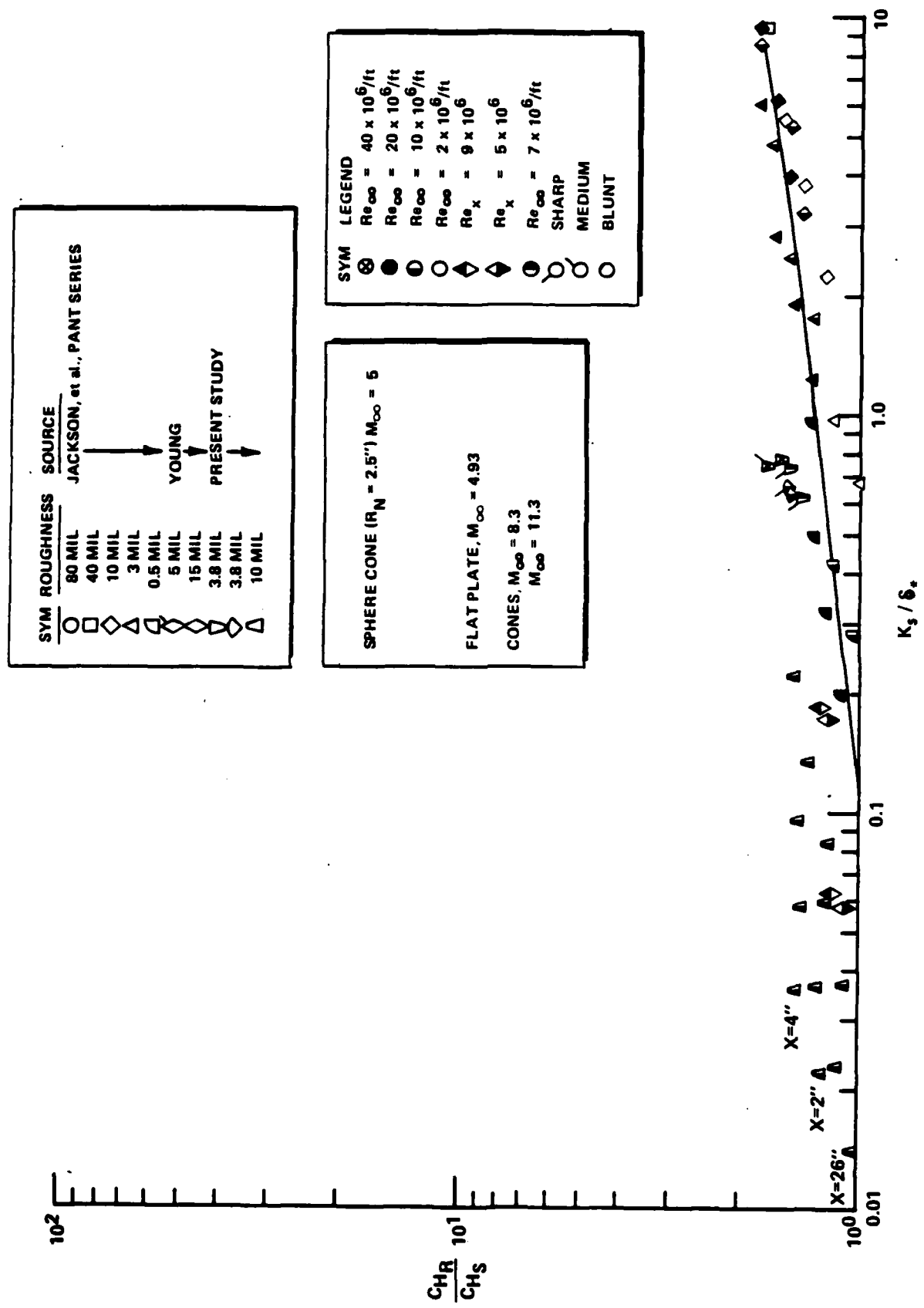


Figure 44 CORRELATION OF BICONIC MEASUREMENTS IN TERMS OF K_S / δ^0

the study was conducted with a single model configuration (the sharp 60° cone) for a series of surfaces of different roughness shapes and patterns. In each of these studies, we examined the effect of surface roughness on both the flap forces and the distribution of heat transfer and pressure over the flap. Two of the important effects of surface roughness on flap performance are illustrated in Figures 2 and 45, in which schlieren photographs and distributions of pressure and heat transfer are shown for a flap control system placed at the base of a conical forebody. Figure 2 shows that the boundary layer ahead of the flap is significantly thicker over the rough conical frustum, causing a larger viscous interaction region at the flap/forebody junction, a corresponding decrease in local pressure at the base of the flap, and resultant loss in flap force. This loss in flap force is associated principally with the roughness of the forebody. The increase in boundary layer thickness, coupled with a decrease in the local pressure, is principally responsible for a decrease in heat transfer to the base of the rough flap relative to the smooth-wall value. However, as the boundary layer thins rapidly through the compression process along the flap, K/θ and the local pressure become large enough to generate heating enhancement factors up to 3, as illustrated in Figure 2. Referring to Figure 3, it is clear that surface roughness can induce a significant degree of separation for model and freestream conditions under which the flow is unseparated over the smooth body.

Typical losses in flap effectiveness which can result from surface roughness effects are shown in Figure 46. Here, we observe flap force reductions of over 100% at flap angles of 25° . Holden⁶ showed that the pressure distribution on the flap in the interaction region can be predicted with good accuracy using a simplified method of rotational characteristics, coupled with the Coles⁷-Van Driest⁸ profiles and measurements of the boundary layer thickness just upstream of the interaction over the flaps. The good agreement between the theoretical and experimental pressure distributions along the flap for both rough and smooth configurations and the measured and predicted flap forces support a model which predicts that the surface roughness of the flap has a second-order effect on flap force. However, flap roughness exerts a first-order effect on flap heating and skin friction.

The studies of surface roughness effects on the aerothermal performance of flaps with sand-grain rough surfaces were conducted with roughness heights of 0, 10, and 15 mils for ranges of angles of attack, flap angles, and nosetip bluntness. Our measurements of heat transfer and pressure along the windward ray of the conical



SHARP



BLUNT

FLAP FORCE

$$\frac{C_{N_{BLUNT}}}{C_{N_{SHARP}}} = 0.35 \quad \frac{C_{N_{BLUNT}}}{C_{N_{SHARP}}} = 0.60$$

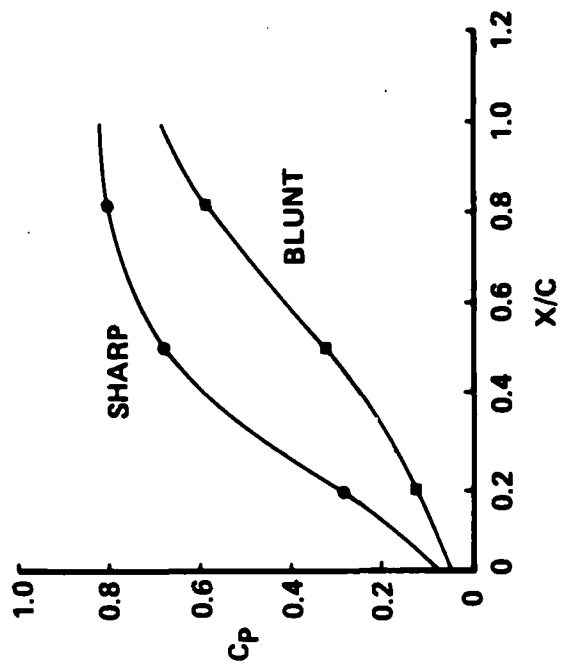
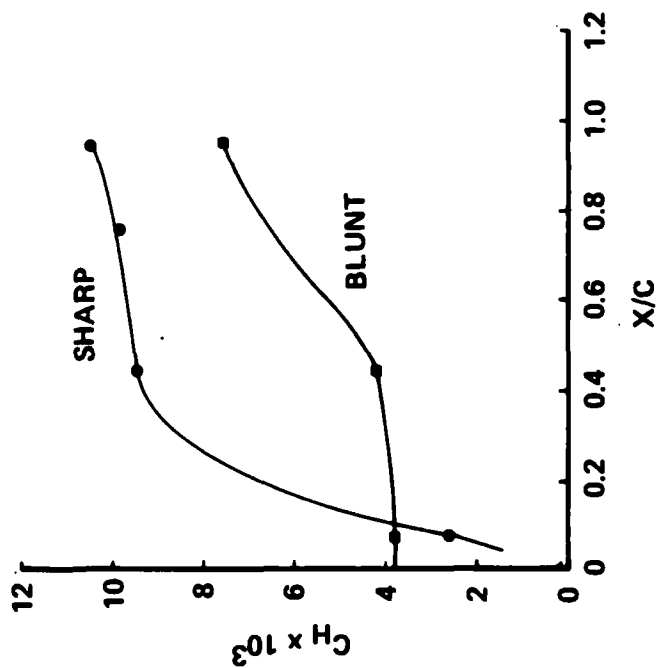


Figure 45 EFFECT OF NOSETIP BLUNTNESS ON FLAP FORCES, HEATING AND PRESSURE

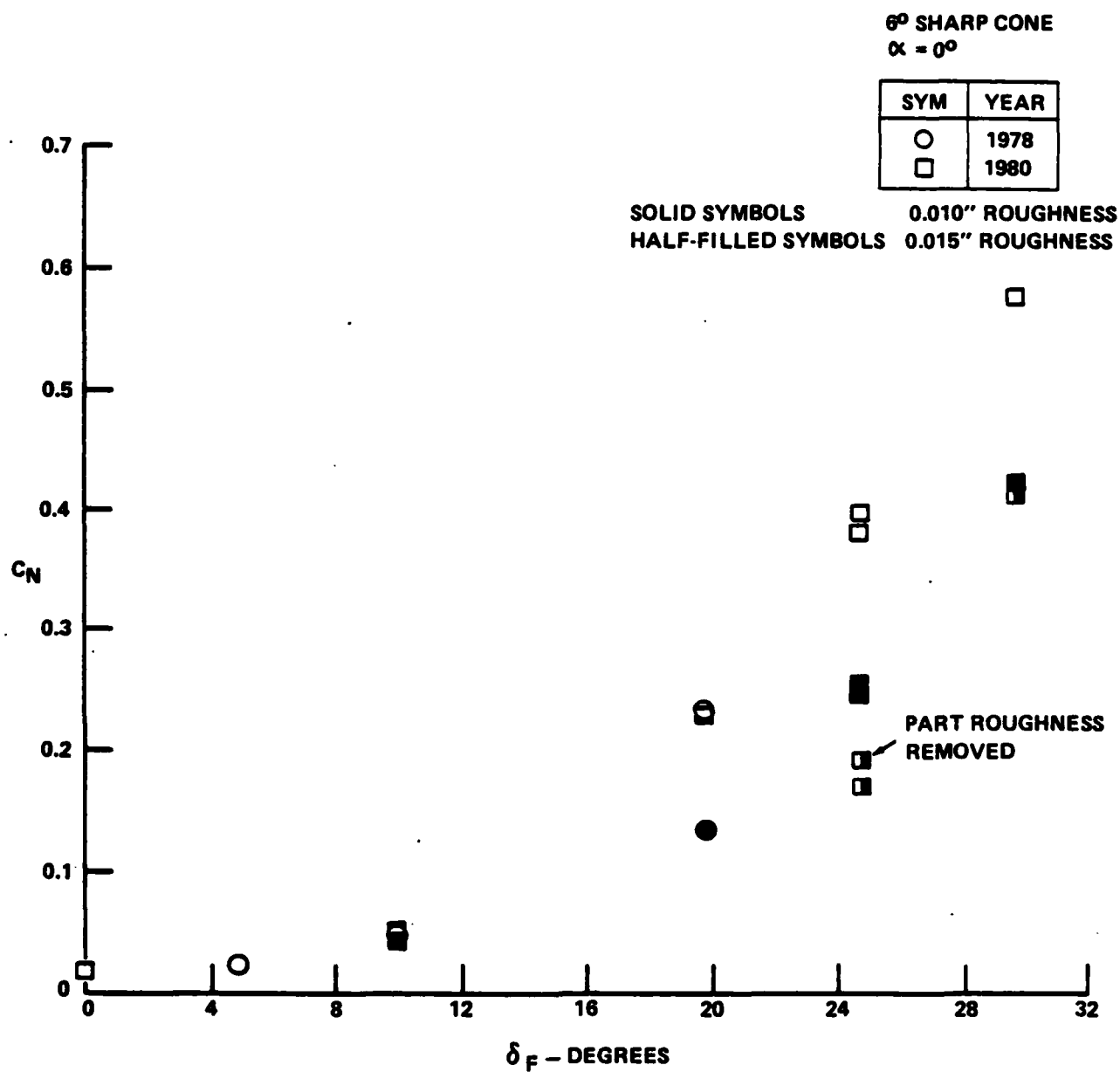


Figure 46 FLAP FORCE MEASUREMENTS WITH THE SHARP 6° CONE MRV CONFIGURATION AT $\alpha = 0^\circ$

frustrum and on the flap placed in the windward plane demonstrated that, for model incidences of greater than 40° , nosetip bluntness effects (for $r_n/R_D > 0.14$) are rapidly swept to the leeside of the body, leaving the properties along the windward ray and the flow over the flap virtually uninfluenced by the nosetip bluntness. It should also be noted that we found relatively uniform spanwise distributions of heat transfer and pressure over the flap for all the configurations studied. This gives us some justification for using a computational method based on two-dimensional flow to predict the centerline flow properties on the flap. The variation of the heating rate along the flap centerline with flap angle is presented in Figures 47 through 49 for surface roughness of 0, 10, and 15 mils, respectively. Here, we see that, for a given flap angle, the length of the interaction region on the flap (the region where heat transfer is increasing along the flap) increases with increasing surface roughness and decreasing flap angle. The peak heating occurs close to the end of the interaction region, where the pressure and K/q reach a local maximum. As can be seen from the photographs of Figure 3, the flow over the 15-mil flap set at 30° is separated; while the flap heating is a maximum at the end of the interaction on the roughest flap, the heating rate is less than on the smooth body at the base of this flap. It has been shown earlier by Holden that the maximum heat transfer to a smooth flap can be estimated from the power-law relationship $q_{\max} = q_0 (P_{\max}/P_0)^{0.85}$. Combining this empirical relationship with a correlation for the roughness-enhanced heating factor would enable the heating rate of a rough flap (in the absence of ablation) to be calculated. In Figure 50, we show our measurements of roughness-augmented heating on flaps, correlated in terms of the roughness Reynolds number \tilde{R}_{eK} . \tilde{R}_{eK} was calculated using simple inviscid flow and the smooth-wall heating measurements. Also shown in Figure 50 are our measurements on the biconic configurations and the Powars⁹ correlation of the PANT data. The augmentation heating factors measured on the flap varied strongly with \tilde{R}_{eK} , reflecting the dual effects of boundary layer thinning and density increase through the rapid recompression on the flap. This correlation could not be expected to embrace the complex phenomena, and these multi-scaled flow fields should be characterized with more than one scale length, e.g., K/q and \tilde{R}_{eK} . However, accurately calculating q through the interaction region is not simple in these flows; further work is clearly required to characterize the scale lengths of importance.

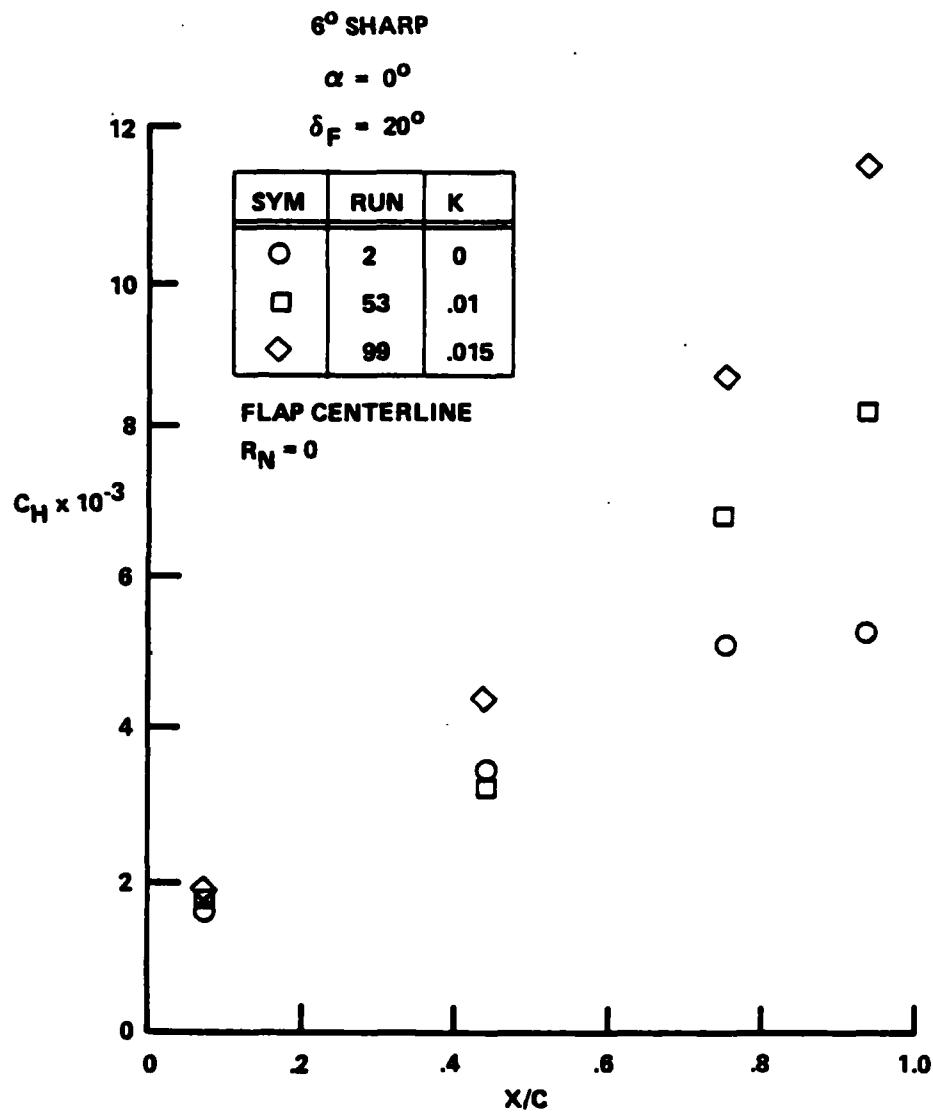


Figure 47 VARIATION OF HEAT TRANSFER DISTRIBUTION ALONG THE FLAP WITH SURFACE ROUGHNESS FOR CONICAL MRV CONFIGURATION

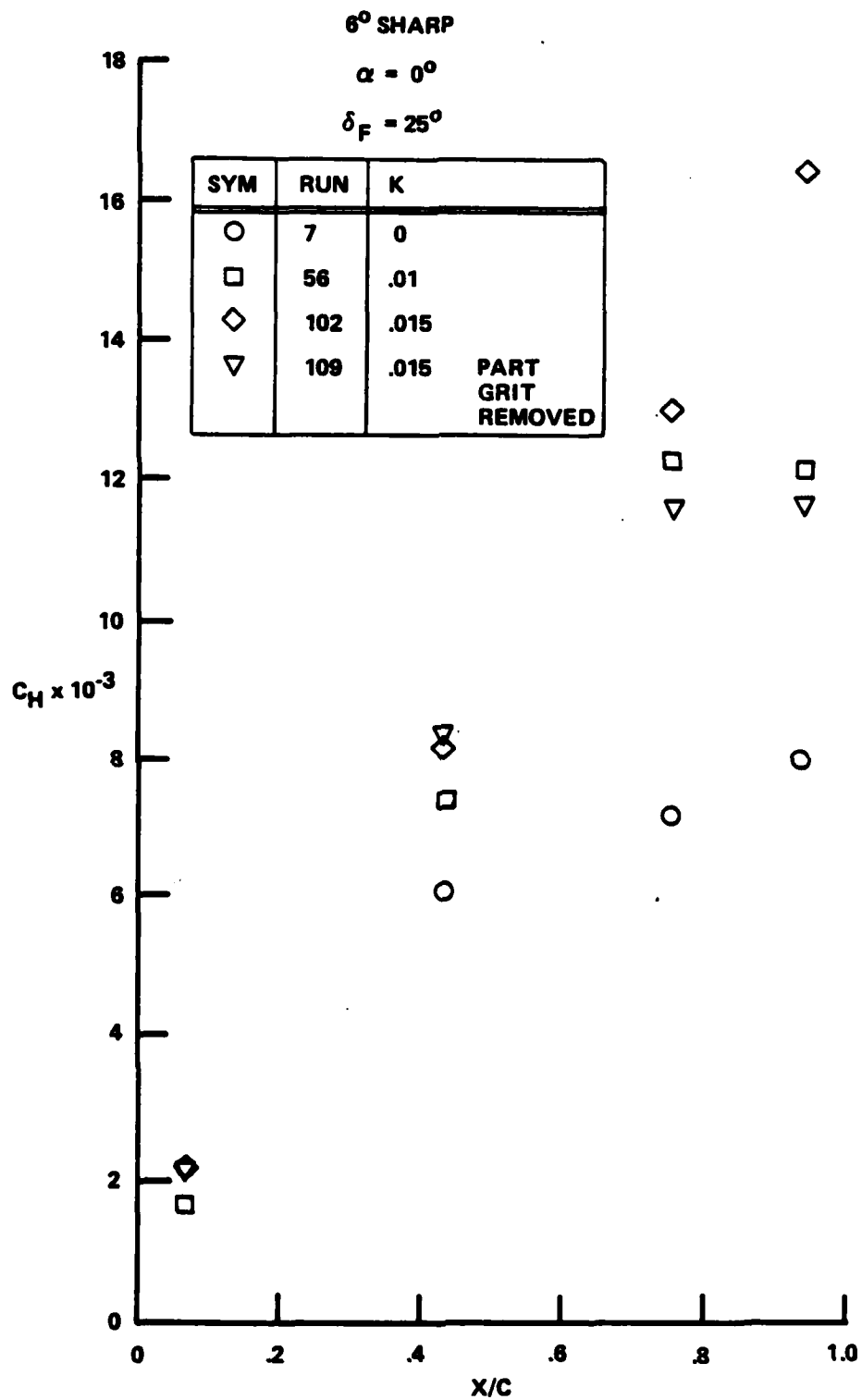


Figure 48 VARIATION OF HEAT TRANSFER DISTRIBUTION ALONG THE FLAP WITH SURFACE ROUGHNESS FOR THE CONICAL CONFIGURATION

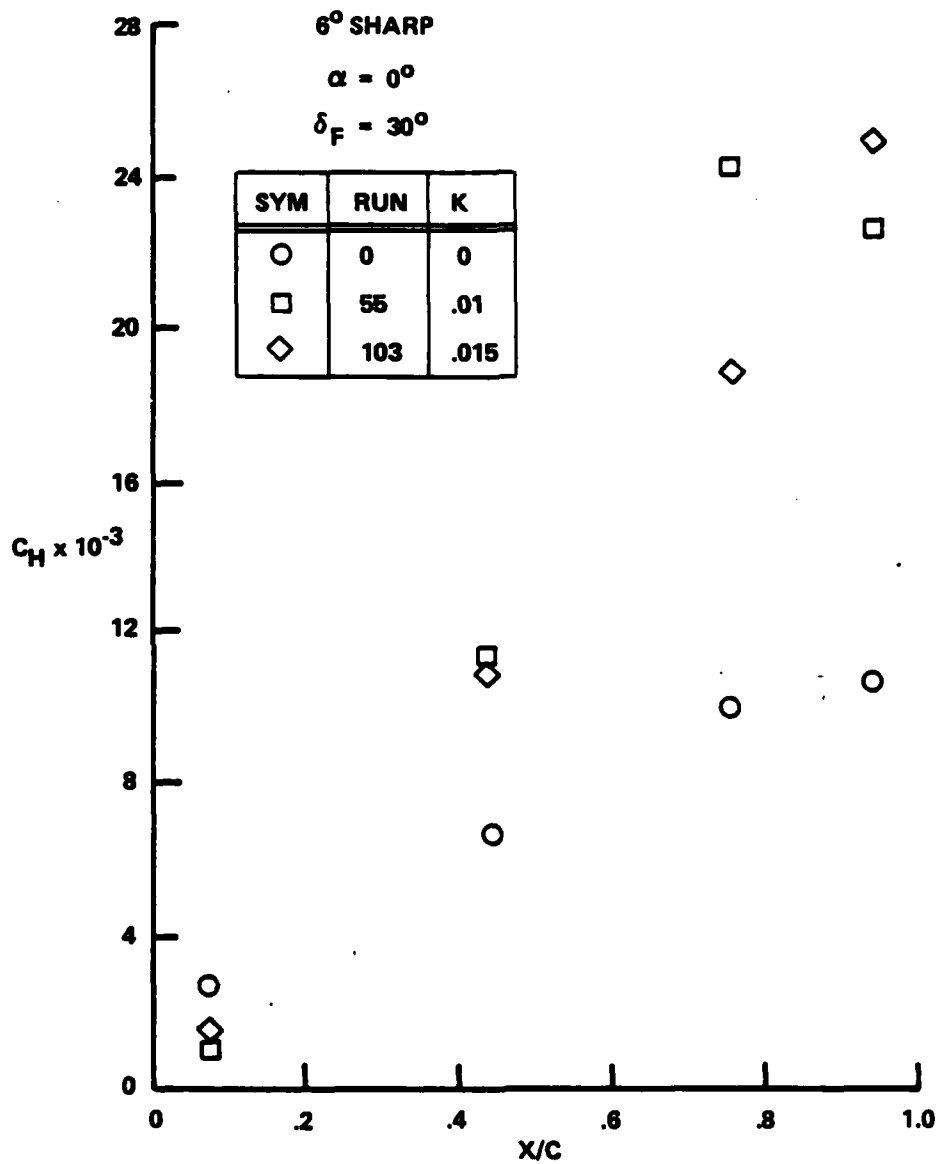


Figure 49 VARIATION OF HEAT TRANSFER DISTRIBUTION ALONG FLAP WITH SURFACE ROUGHNESS FOR 6° SHARP CONE FOREBODY CONFIGURATION

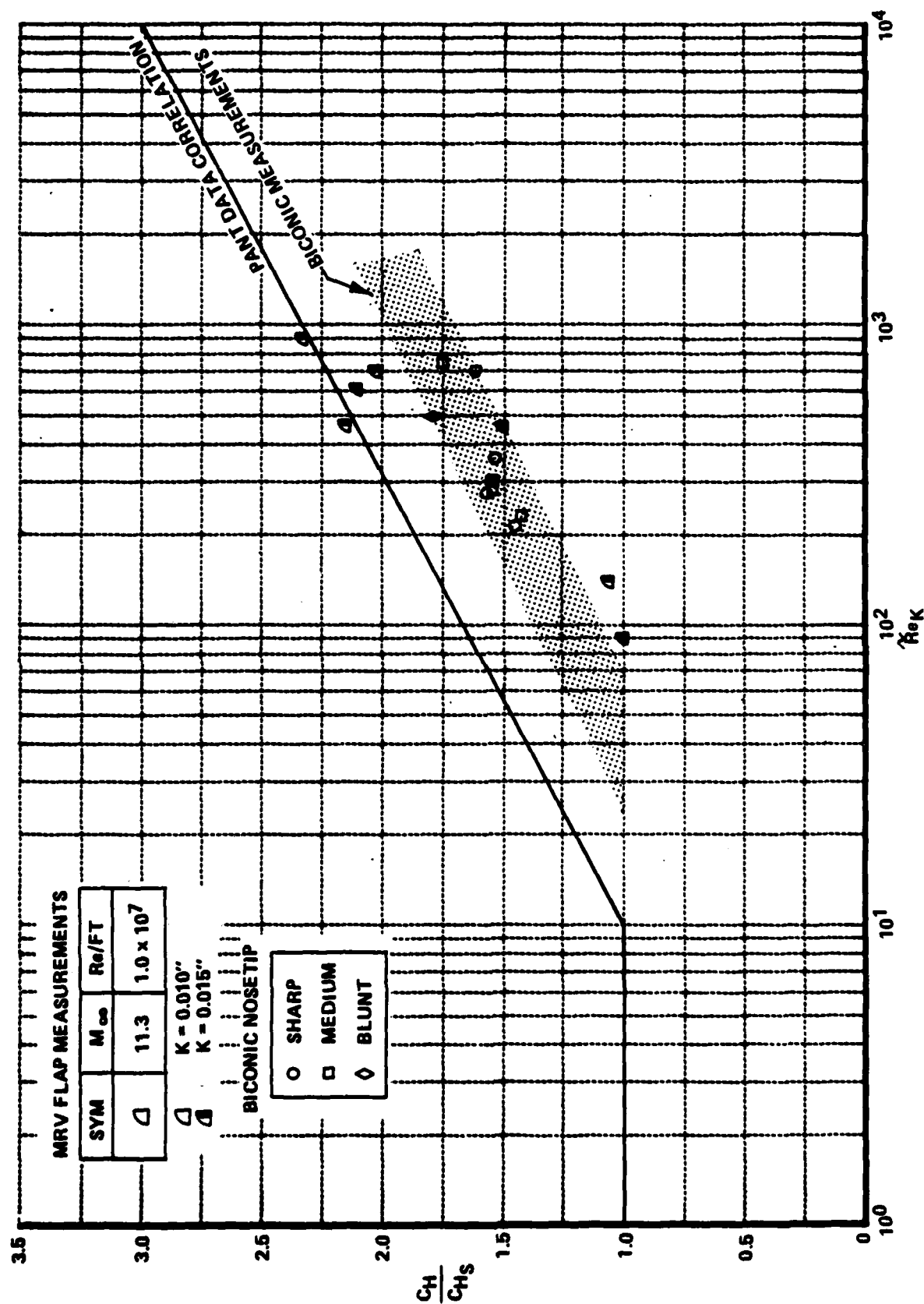


Figure 50 CORRELATION OF FLAP ROUGHNESS-AUGMENTED HEATING MEASUREMENTS
MADE CLOSE TO THE TRAILING EDGE WITH THE LOCAL ROUGHNESS
REYNOLDS NUMBER

The studies of the effects of patterned roughness shape and spacing on the aerothermal performance of control systems completed the third and final phase of the effects of roughness shape and spacing on the aerothermodynamics of rough re-entry vehicles.

Measurements of the distributions of heat transfer, skin friction, and pressure were made on the flap instrumented and covered with five different patterned rough surfaces. The sharp 6° conical forebody was used in these studies, and measurements were made at model incidences of 0° , 4° , 8° , 12° , and 16° for flap angles of 15° , 20° , and 25° . A plot showing a typical variation of the heat transfer distribution along the flap centerline with model incidence is provided in Figure 51. Here, the increase in model incidence results in an increase in the absolute pressure along the windward ray of the cone and flap and in a decrease in the thickness of the cone boundary layer ahead of the flap. In turn, the thinning of the boundary layer on the cone with increasing angle of attack is reflected in shorter lengths of interaction, larger heating enhancements, and more extensive regions of high heating rates close to the trailing edge of the flap. An example of the variation of flap heating with the shape and spacing of the roughness elements is shown in Figure 52. Here, we observe that the size of the interaction region and the maximum flap heating rates, which occur at the end of the interaction region, increase monotonically with increasing roughness density and roughness drag coefficient. The variation of roughness heating with flap angle is shown in Figure 53 for two different roughness shapes with the same spacing. It can be seen that there is a significant increase in rough flap heating with roughness shape for a common roughness spacing. For this tight spacing ratio, for which the λ is similar to that measured for sand-grain roughness, the correlations from measurements shown in Figures 52 and 53 demonstrate that the augmentation heating ratio is most strongly influenced by flap angle. Our measurements indicate that roughness-induced heating-augmentation factors of up to three can be obtained on flaps in the absence of mass addition.

As we found for nosetip and frustum measurements, plotting the flap heat transfer measurements in terms of either $(A_p/A_s)^{-1}$ or $(D^*/K)(A_{ws}/A_p)^{4/3}$ in a semi-log format (see Figures 54 through 57) gives a good correlation of the measurements, for

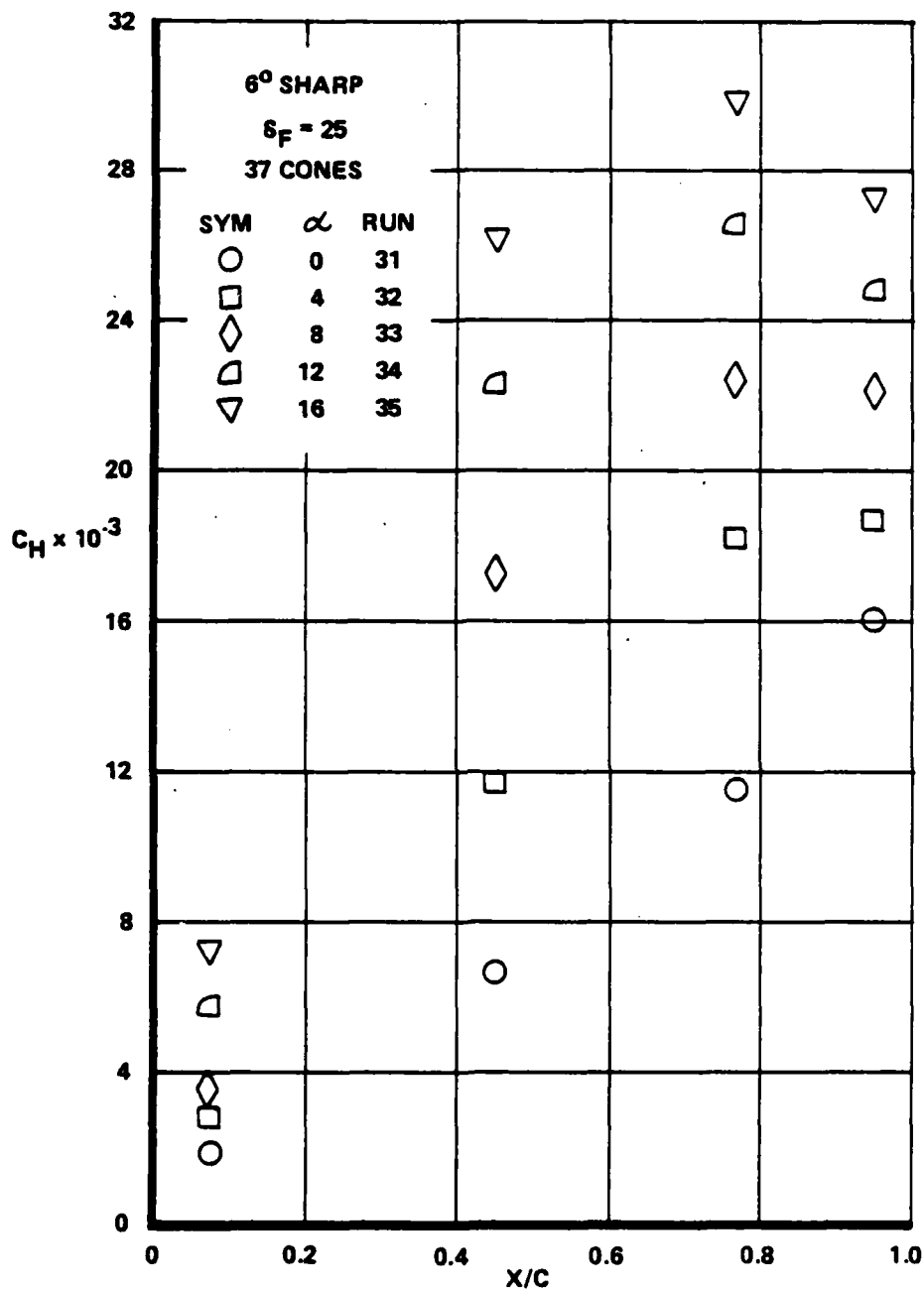


Figure 51 VARIATION OF ROUGH FLAP HEATING DISTRIBUTION WITH FLAP ANGLE

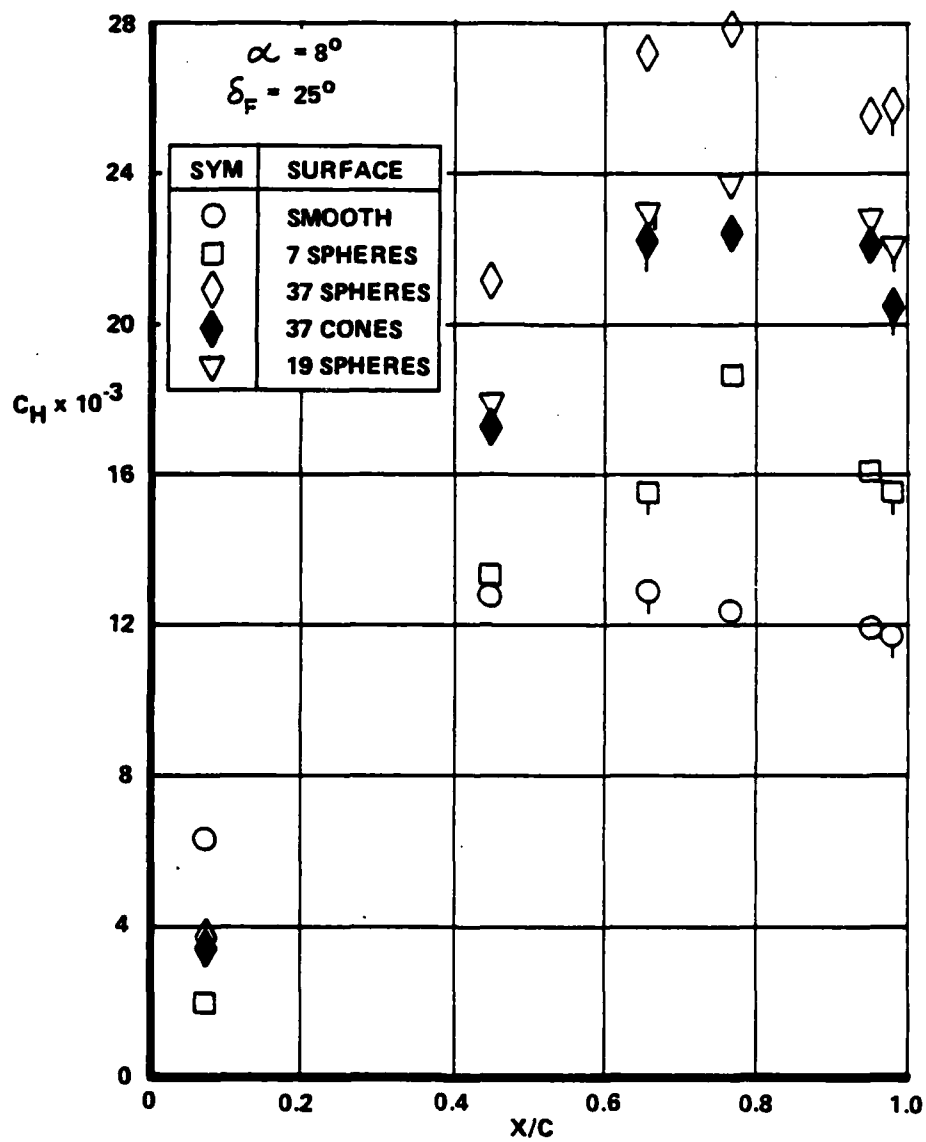


Figure 52 VARIATION OF FLAP HEATING WITH ROUGHNESS SHAPE AND SPACING

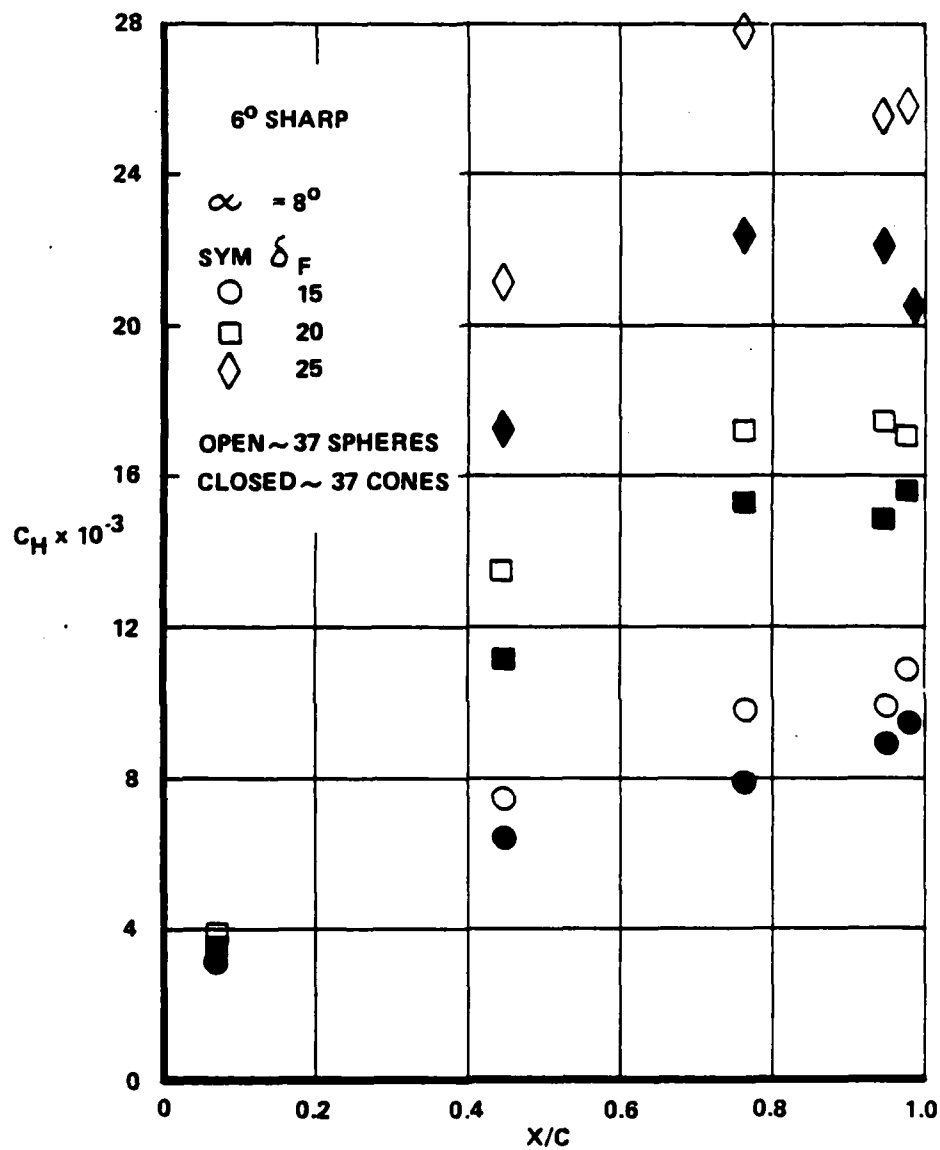


Figure 53 VARIATION OF FLAP HEATING WITH ROUGHNESS SHAPE FOR THREE DIFFERENT FLAP ANGLES

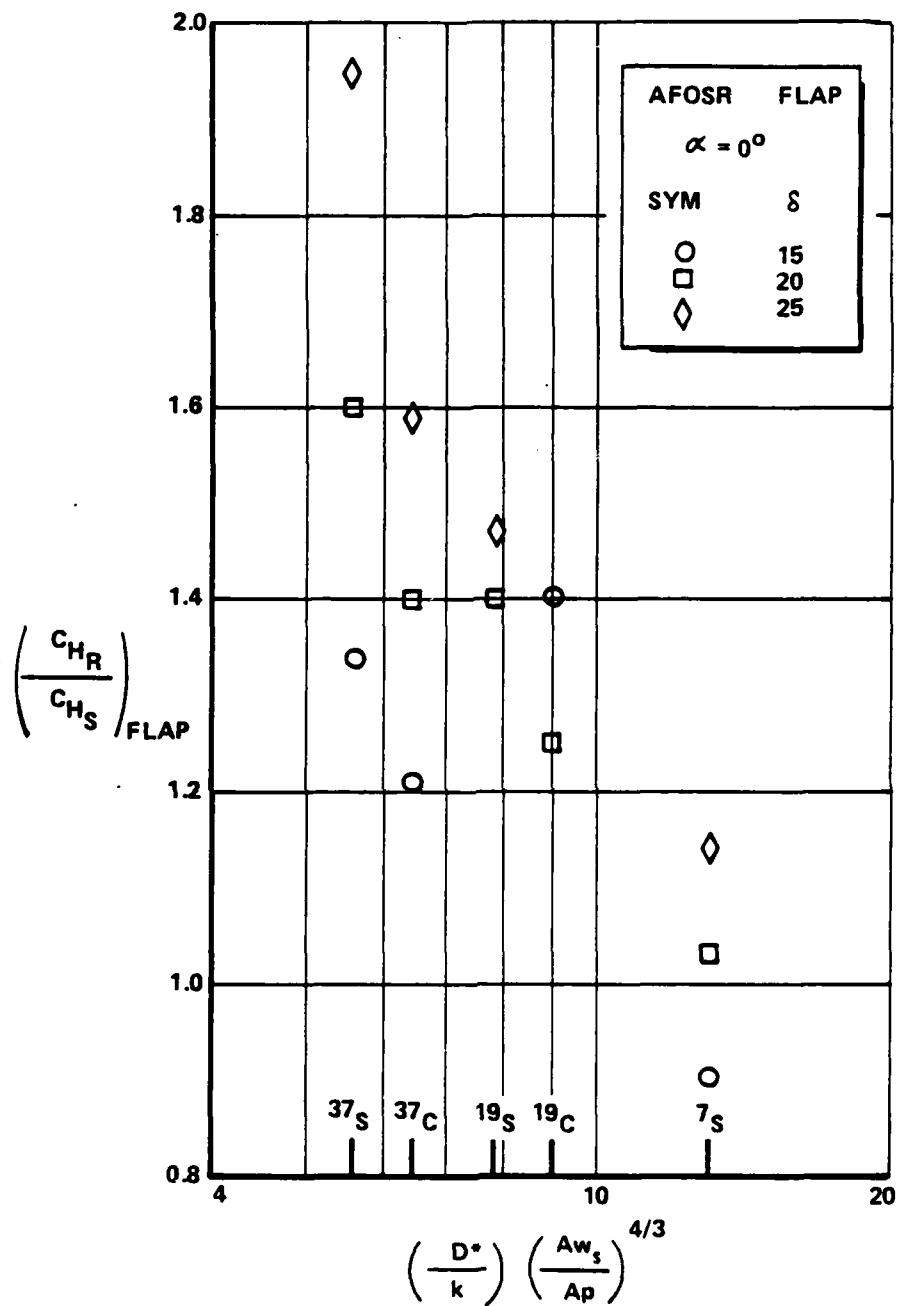


Figure 54 CORRELATION OF PATTERNED FLAP HEATING IN TERMS OF DIRLING'S SHAPE PARAMETER

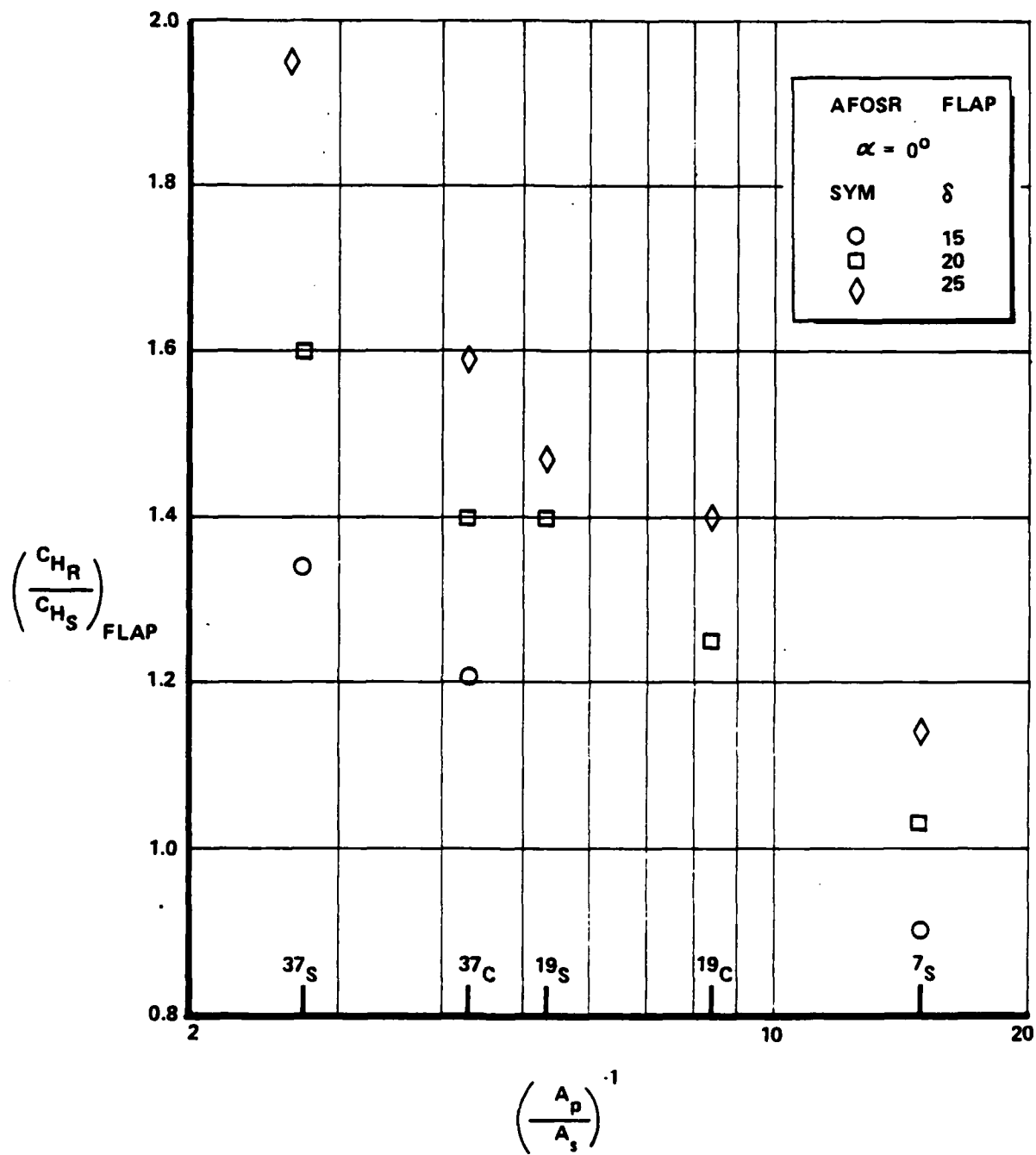


Figure 55 CORRELATION OF PATTERNED FLAP HEATING WITH EFFECTIVE WINDWARD AREA PARAMETER (A_p/A_s)

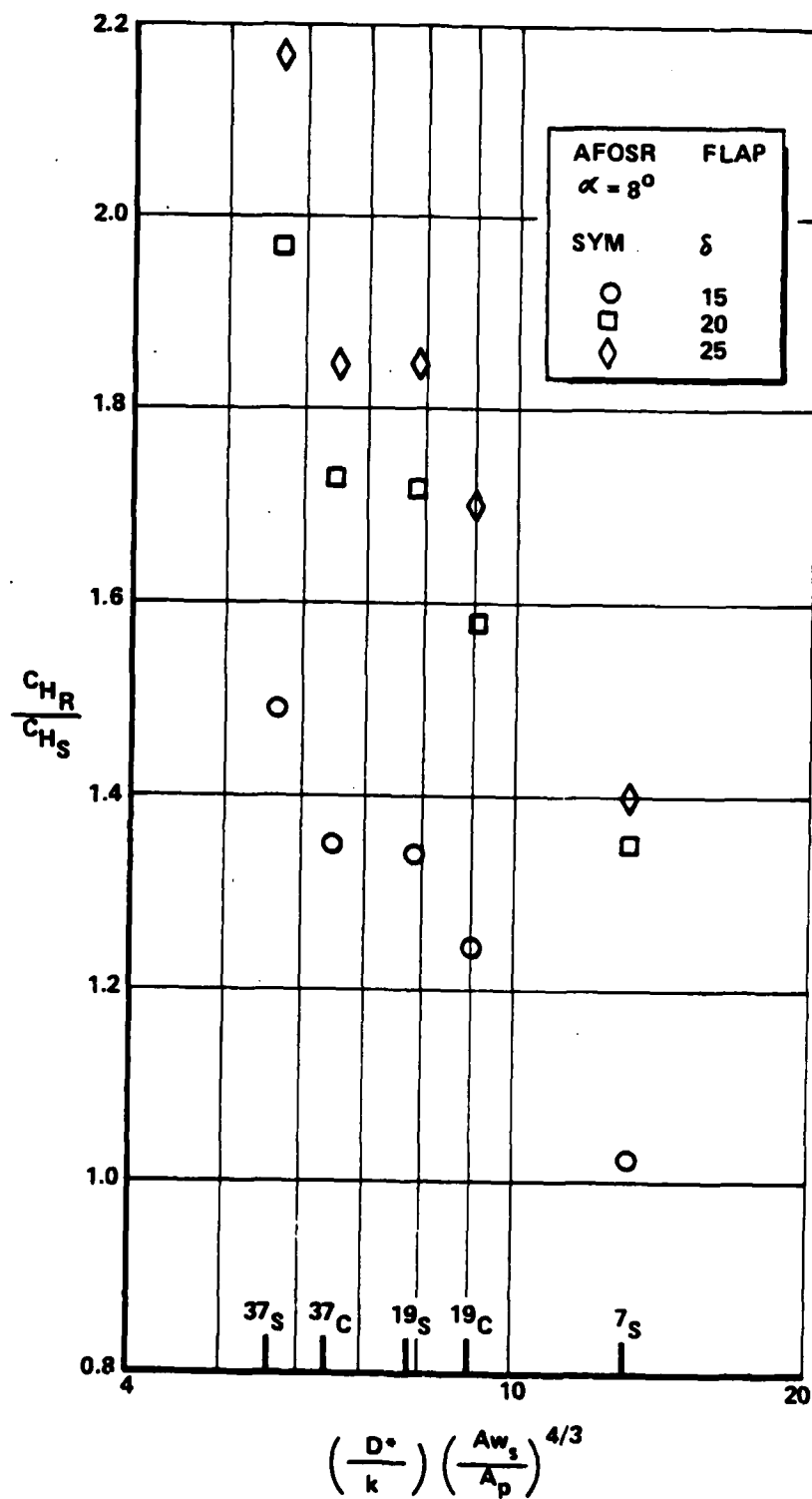


Figure 56 CORRELATION OF PATTERNED FLAP HEATING IN TERMS OF DIRLING'S SHAPE PARAMETER

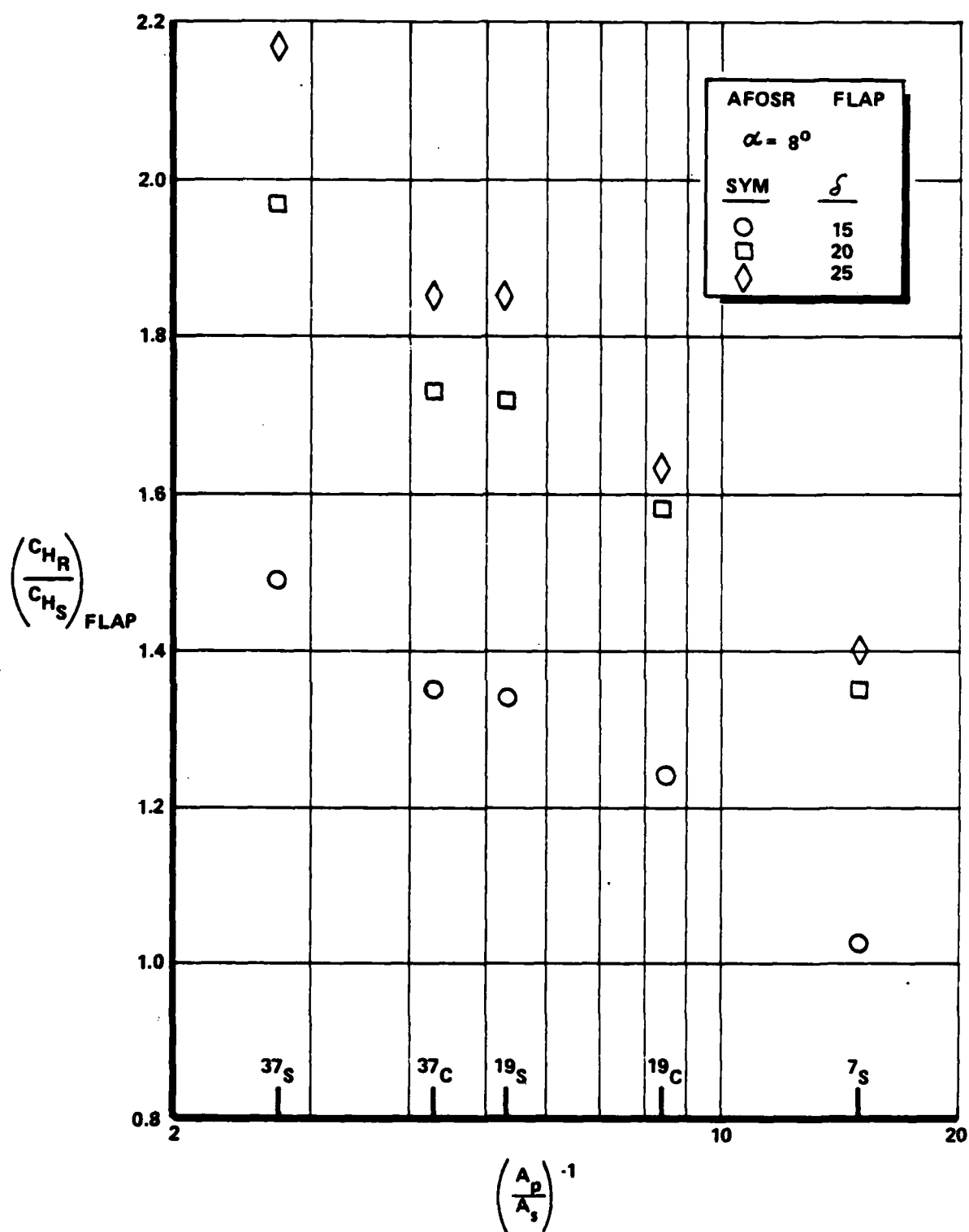


Figure 57 CORRELATION OF PATTERNED FLAP HEATING WITH EFFECTIVE WINDWARD AREA PARAMETER (A_P/A_S)

a fixed model configuration. The monotonic increase in the heating augmentation with roughness shape/spacing factor is similar to that displayed in the biconic studies.

To remove the effects of local conditions on the heating-enhancement factors, we have non-dimensionalized the measurements on the patterned rough surfaces by the heating rate of an equivalent 12.5-mil sand-grain surface deduced by interpolating our flap measurements with 10- and 15-mil sand-grain roughness. The correlations shown in Figures 58 and 59 demonstrate that measurements made at different model incidences and flap angles collapse into a single curve which exhibits a strong variation of C_{HR}/C_{HSG} with $(A_p/A_s)^{-1}$ or $D/K (A_{ws}/A_p)^{4/3}$. A key feature of these correlations is that they show, in strong contrast to results of low-speed studies, that the maximum heating rates generated on the patterned surfaces are no more than 10% greater than the sand-grain values. In addition, because of the surface roughness characteristics of heat shields, the low-speed studies predict that the heat transfer decreases with an increase in the bluntness of the roughness elements. This is clearly not the case.

The basic construction and ablation of flaps, frusta, and nosetips of conventional re-entry vehicles is such that the shape/spacing parameter is typically close to 10. Our measurements indicate that the heat transfer to such surfaces should be 70% of the heat transfer to a sand-grain rough surface, while the Dirling⁴/Simpson⁵/Finson² correlations would predict heating levels approximately 1.5 times the sand-grain values. In general, our studies on nosetips, frusta, and flaps suggest that the current prediction methods, which utilize a heating augmentation correlation (e.g., Powars⁹) in combination with an effective sand-grain roughness correlation (e.g., Dirling⁴), or semi-empirical methods combining the two effects, significantly overpredict the heat transfer to rough surfaces. However, the large roughness-induced heating-augmentation factors (up to 3) and the significant losses in flap force which were measured in these studies makes roughness effects of critical importance in the aerothermal design of control systems. How such effects are modified by ablation is the next key question.

As discussed in Section 3, our studies of combined surface roughness and blowing effects suggest that the initial effect of surface blowing, by eliminating the cavity flows between roughness elements, is to produce heat levels close to the smooth-wall turbulent values. We anticipate that ablation or mass addition from the frustum and flap could have significant effects on the aerothermal performance of the flap.

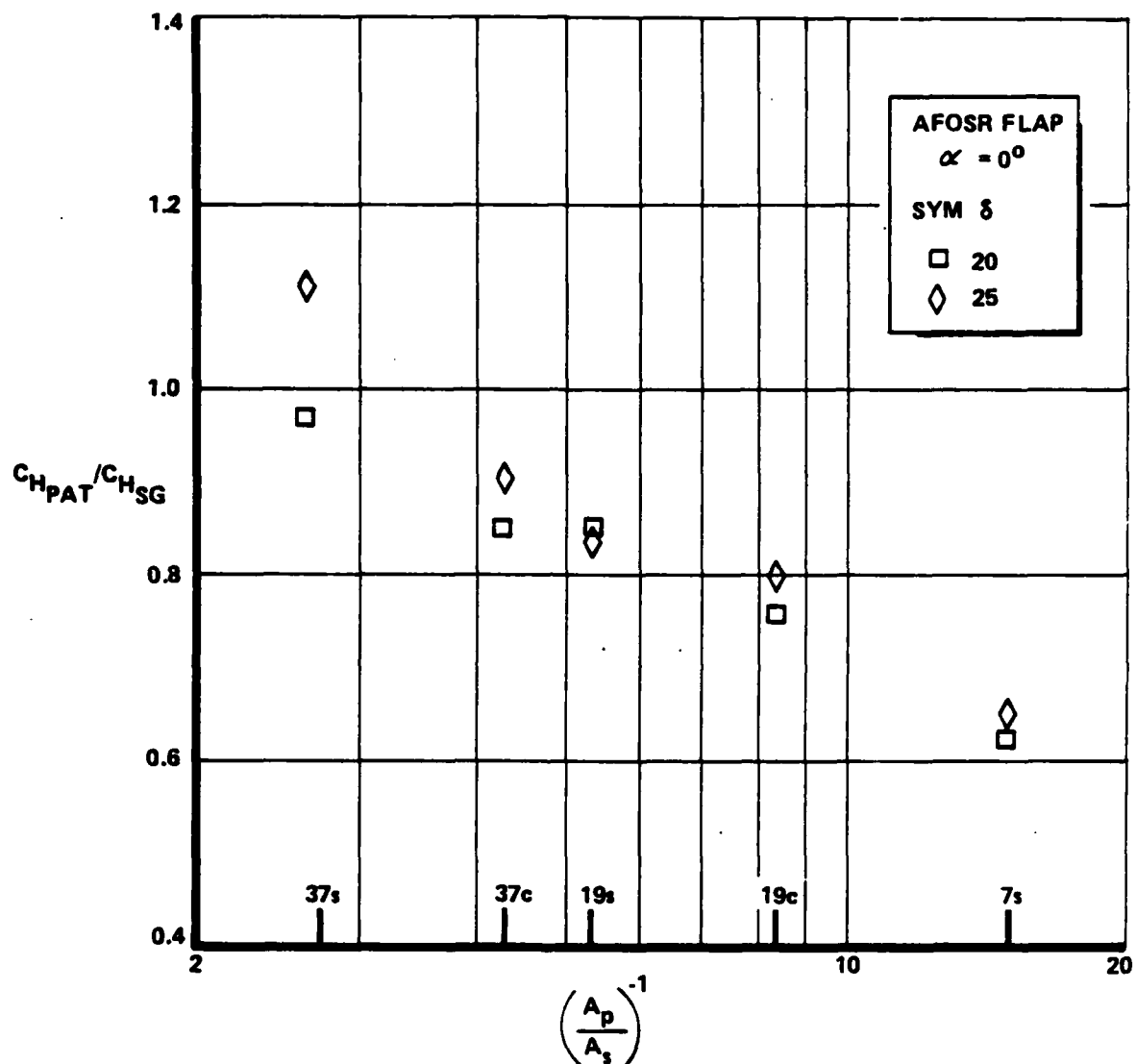


Figure 58 CORRELATION OF EFFECTIVE HEATING PARAMETER C_H/C_{HSG} ON FLAPS WITH DIRLING'S SHAPE PARAMETER

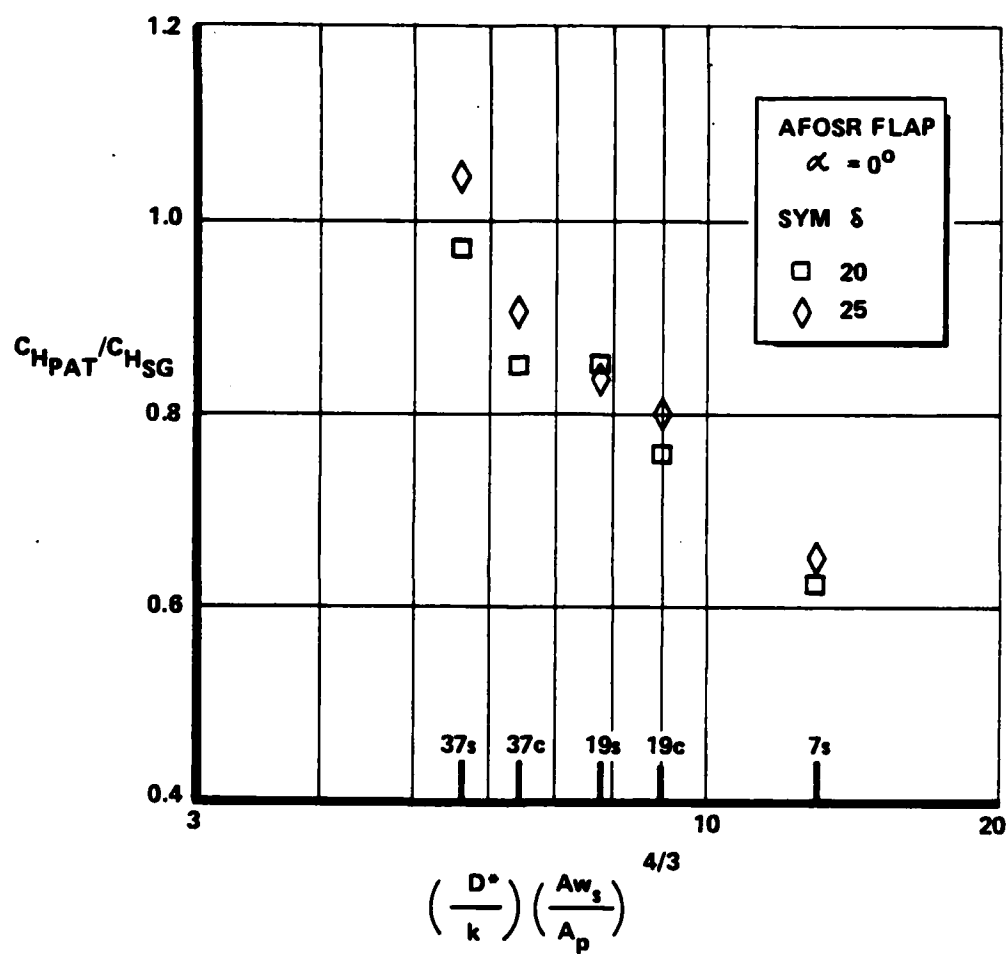


Figure 59 CORRELATION OF EFFECTIVE HEATING PARAMETER C_H/C_{HSG} ON FLAPS WITH DIRLING'S SHAPE PARAMETER

First, mass addition would increase the boundary layer thickness and reduce the momentum at the base of the boundary layer on the conical frusta ahead of the flap, both effects making the boundary layer more easily separated and the interaction region of greater length. While mass addition/ablation on the flap should reduce the heating, we again would anticipate that separation and more extensive interaction regions would result. However, the effects of mass addition on smooth or rough surfaces in high Mach number, high Reynolds number turbulent flows in constant-pressure or interacting flows remain to be examined.

Section 3
STUDIES OF POTENTIAL FLUID-MECHANICAL MECHANISMS
FOR ENHANCED STAGNATION-REGION HEATING

3.1 INTRODUCTION

Analysis based on conventional boundary layer theory decrees that, because the Reynolds number close to the stagnation point is small, the boundary layer there must remain laminar. However, flight measurements of stagnation-point recession on the nosetips of ballistic re-entry vehicles, and stagnation-point heat transfer measurements in ground test facilities, have indicated that, at high Reynolds numbers, where boundary layer transition occurs in or just downstream of the stagnation region, stagnation-point heating rates are significantly larger than those predicted on the basis of laminar theory. To match the flight measurements, the codes used to predict the performance of ablative nosetips must employ semi-empirical relationships to enhance the laminar stagnation-point heating rate, when the transition point has moved to within a certain fraction of the nosetip radius from the stagnation point. Since the flow is subsonic in the stagnation region, it is clear that pressure disturbances could be fed upstream. However, it remains to be determined whether such relatively small disturbances can induce the relatively large heating augmentations observed. While measurements of enhanced stagnation-point heating made in wind tunnels might be influenced by tunnel noise, no such explanation can be offered for those made in ballistic range studies. One method to overcome questions associated with the effects of wind tunnel noise in studies of stagnation-point heating enhancement is to control the position of transition mechanically by employing trips on the models, rather than changing the streamwise position of transition by varying the unit Reynolds number of the free stream. If transition effects in the stagnation region are important, measurements of heat transfer at the stagnation point and in the stagnation region should demonstrate this at a single test condition, when transition is moved toward the stagnation point with a series of annular trip rings. The stagnation-region heating measurements should then be correlated in terms of the distance to the beginning of transition, non-dimensionalized by the local momentum, energy, or displacement thickness of the boundary layer or the model radius. In this section, we describe the results of experimental studies performed to examine potential mechanisms of enhanced stagnation-region heating. The models and instrumentation used in the three experimental studies performed in this

program are described next. Then, we discuss measurements made on a smooth hemispherical model with trips. These measurements are compared with similar measurements on rough non-blowing and blowing models. Our conclusions on the mechanisms for enhanced stagnation-region heating are then presented.

3.2 MODELS AND INSTRUMENTATION

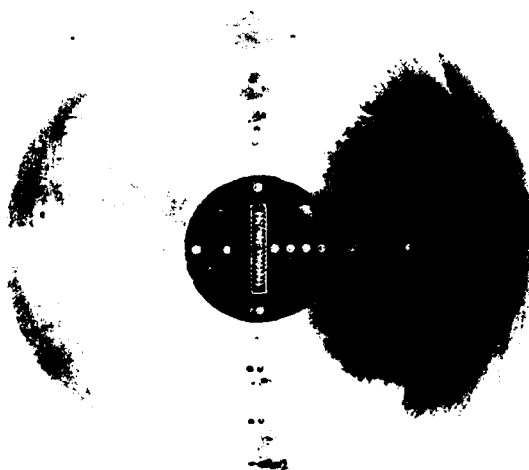
The smooth and rough hemispherical nosetips shown in Figures 60 and 61, and the transpiration-cooled hemispherical nosetip shown in Figures 62a and b, were used in studies performed in Calspan's 96-Inch Shock Tunnel to examine the distribution of heat transfer in transitional and fully turbulent flows over smooth, rough, and transpiration-cooled surfaces. The smooth hemispherical model is shown in the 96-Inch Shock Tunnel in Figure 63. Each model was highly instrumented with high-frequency thin-film heat transfer gages in the stagnation region, and with pairs of high-frequency pressure and heat transfer gages placed adjacent to one another along a streamwise ray. Both sets of gages have high enough frequency responses to follow both the mean and fluctuating components of heat transfer and pressure, to resolve any time-dependent flow mechanisms responsible for stagnation-region heating enhancement. Measurements were also made to determine heat transfer rates with silver-calorimeter gages. Here, we wished to examine how the relatively low-response calorimeter instrumentation averaged the perturbations in heating caused by the transitioned nature of the boundary layer. The rough spherical nosetip shown in Figure 61 was coated with 12.5-mil conical roughness elements and instrumented with calorimeter heat transfer gages, the construction of which is described in subsection 2.2.3. Our measurements of roughness shape and spacing effects have indicated that 12.5-mil conical roughness is approximately equivalent to the roughness of the transpiration-cooled model. This latter model was highly instrumented with thin-film heat transfer gages.

In the present studies, a new throat valve was developed to replace the mylar throat diaphragm in the 96-Inch Shock Tunnel. Under conventional operation, the mylar diaphragm is fractured by the incident driver shock and convected past the model at the beginning of a shock tunnel run. Since detailed heat transfer and pressure fluctuation measurements in the stagnation region were required for the blunt-body studies, we had to eliminate extraneous fluctuations that might have resulted from mylar particles. Earlier studies had suggested that disturbance to the stagnation region of large blunt bodies can persist well after the starting process.



91789

(a)



91790



(b)

**Figure 60 HEMISPHERICAL MODEL FOR BLUNT-BODY TRANSITION AND
ROUGHNESS STUDIES**

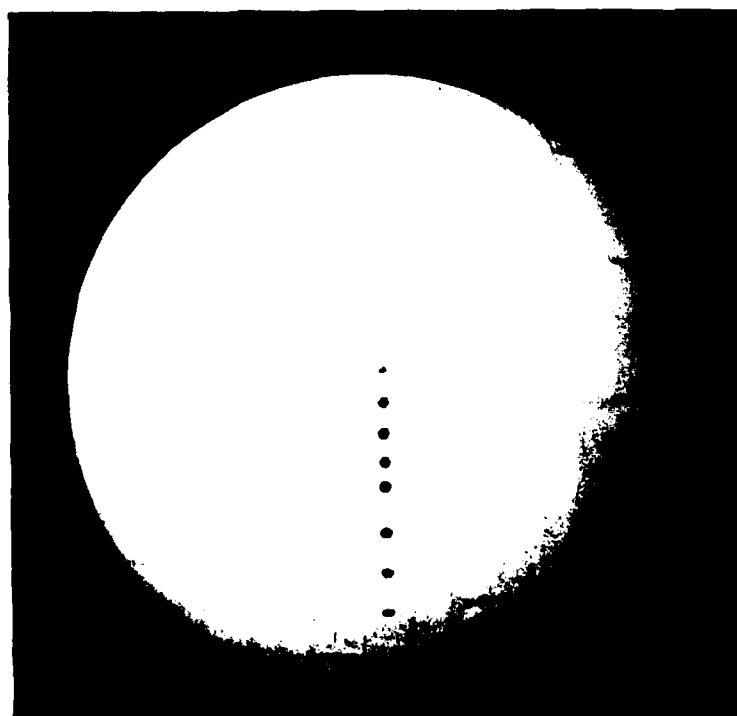
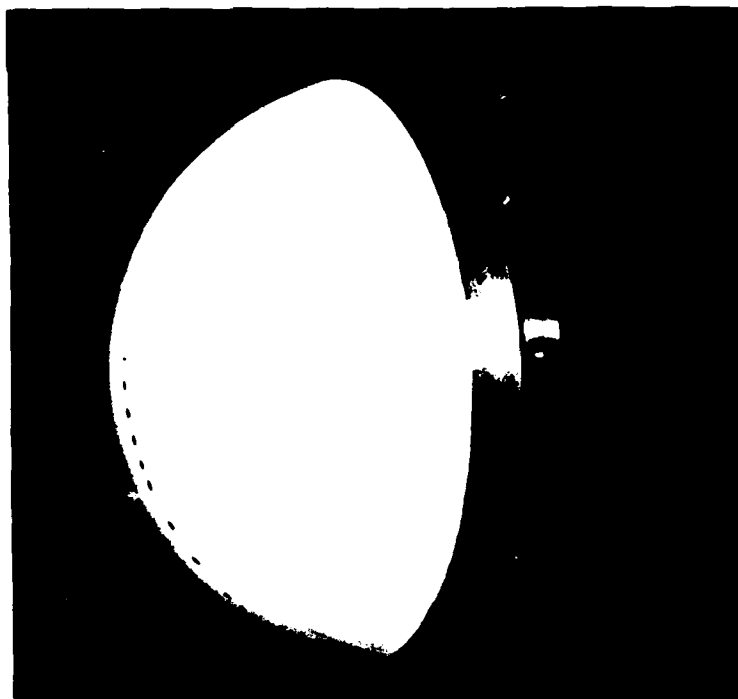


Figure 61 SPHERICAL NOSE TIP WITH 12.5 MIL CONICAL ROUGH SURFACE

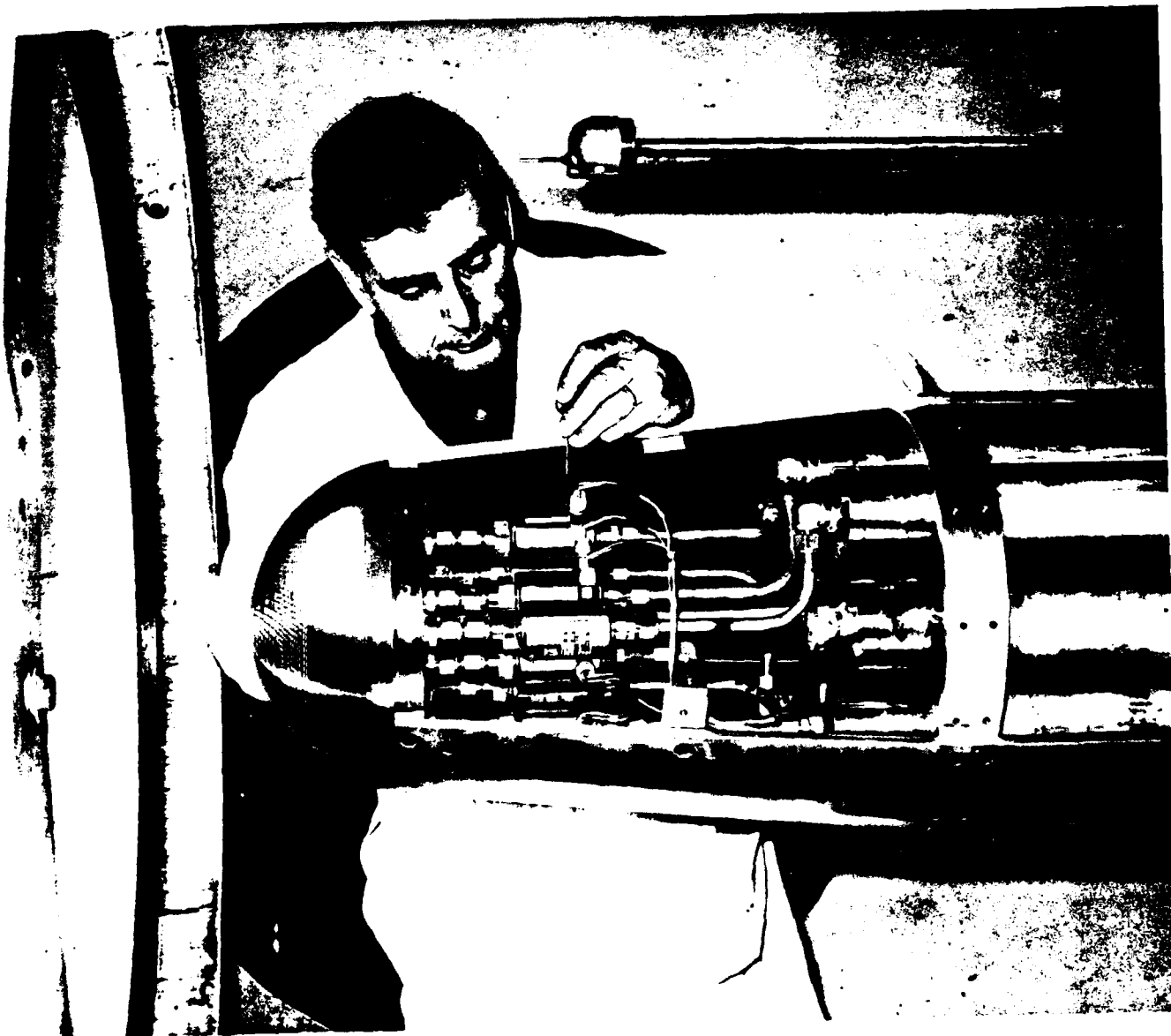


Figure 62a DETAILED VIEW OF MODEL IN SHOCK TUNNEL



Figure 6 SCANT NOSETIP INSTALLED IN TUNNEL FOR MASS FLOW CALIBRATION

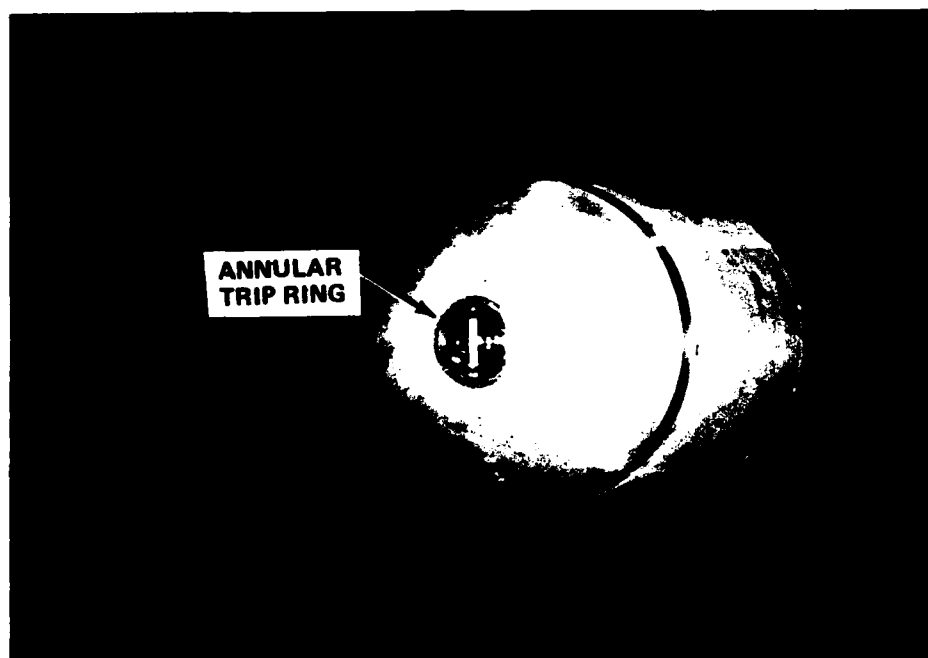
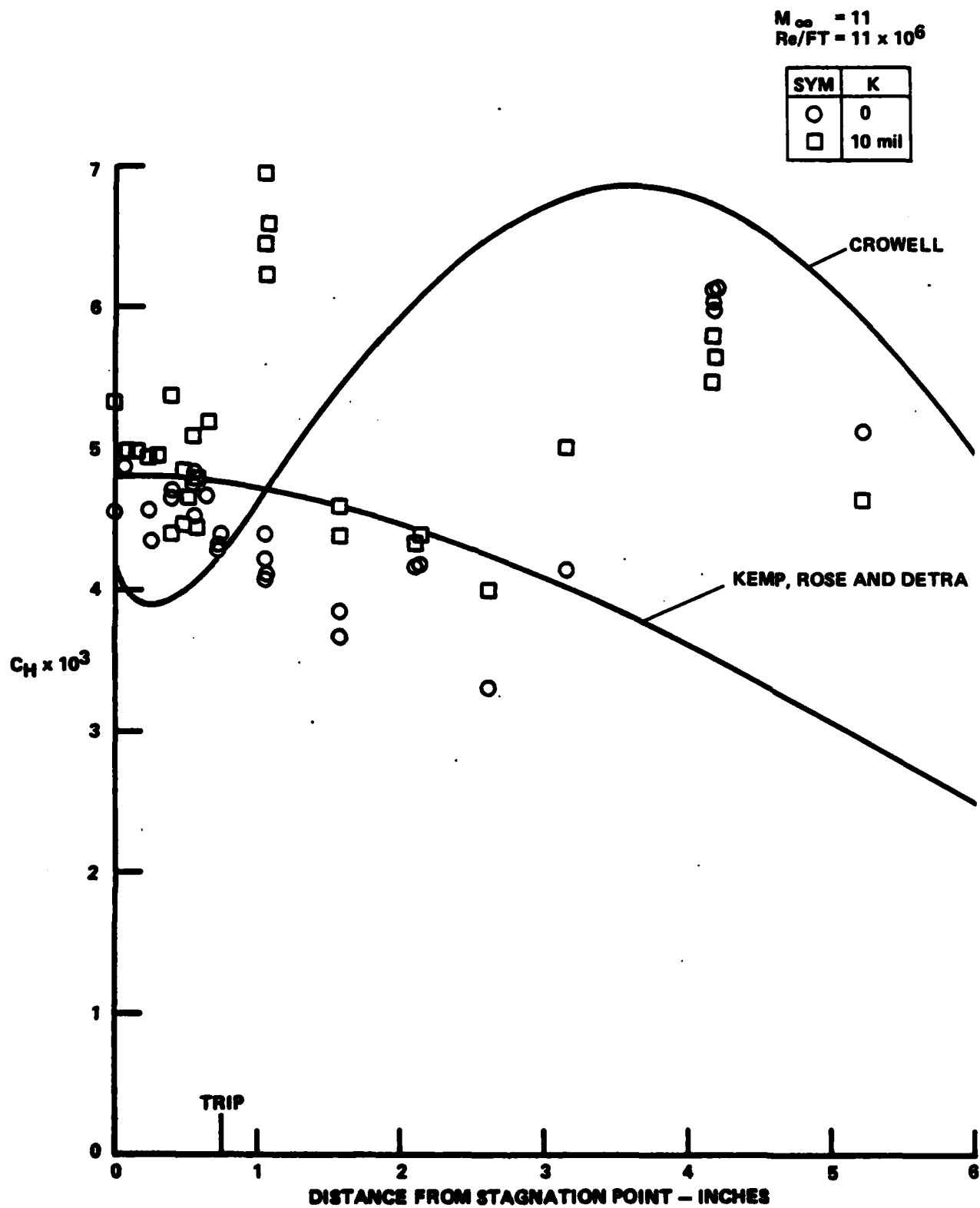


Figure 63 STAGNATION-REGION HEATING MODEL SHOWING POSITION OF TRIP RING

Our initial studies were conducted with the smooth hemispherical nosetip shown in Figure 60, first to obtain smooth-wall measurements with which to compare measurements made with the rough models and those made with combined roughness and mass addition, and then to explore the upstream influence of transition on stagnation-point heating. The heat transfer distribution on the totally smooth hemisphere, shown in Figure 64, indicates that transition occurs in the subsonic region of the flow at an $S/R = 0.33$, with peak heating occurring at $S/R = 0.6$ —close to the base of the sonic line. Placing an annular trip at $S/R = 0.17$ causes the transition to move upstream to the back of the trip, with the resulting heating distribution similar to the predictions made earlier by Crowell¹⁰. We observe that, upstream of the trip, the heating in the stagnation region is not influenced by the presence of transition. In fact, as discussed in detail in Reference 11, the only disturbances which were observed to induce transition in the stagnation region were those associated with minute dust particles in the airflow. These disturbances, which caused transients leading to increased time-averaged heating at the stagnation point, were observed to decay rapidly as the dust particles were convected downstream through the strong favorable pressure gradient over the hemisphere.

Our measurements made with the smooth hemispherical model were conducted in an ultraclean airflow, made possible because of special preparation, coupled with the inherent cleanliness of shock tunnel operation, where a relatively pure test gas is heated and compressed by a shock wave. In contrast, heating the air by passing it through a pebble-bed or graphite heater or an arc discharge, as is done in blowdown-type facilities, results in an intrinsically dusty flow. For blowdown-type facilities, our studies suggest that measurements of the time-averaged stagnation heating rates for high Mach number, high Reynolds number conditions, where large Re_θ 's are generated in the stagnation region, may exhibit values larger than those predicted by laminar theory, as a result of dust/boundary layer interaction. Again, dust-induced heating enhancement will occur only at large values of Re_θ (> 100), where the laminar boundary is unstable.

It is also possible that "clean-air" flight measurements which indicate stagnation-point heating rates larger than laminar values may also result from transition in the stagnation region tripped by minute dust or salt particles, convected into the



upper atmosphere. These particles could be too small, or exist in too low a concentration, for the environment to be classed as "dusty" and yet be responsible for turbulent heating in the stagnation region.

The remaining candidates for phenomena which cause enhanced stagnation-point heating are (1) surface roughness at the stagnation point and (2) transition induced by blowing in the stagnation region. We made preliminary studies of both of these phenomena, both separately and in combination, in studies with the rough hemispherical nosetip shown in Figure 61 and the rough transpiration-cooled nosetip shown in Figures 62a and b. The studies with the rough hemispherical nosetip were conducted in conjunction with studies of roughness effects on biconic and indented ablated nose shapes, while the measurements on the transpiration-cooled models were made in conjunction with studies with medium and large surface blowing, reported in References 12 and 13. Our measurements of roughness shape and spacing effects indicate, as noted earlier, that 12.5-mil conical roughness on the hemisphere is approximately equivalent to the roughness of the transpiration-cooled model. We made measurements of the heat transfer rate at the stagnation point and around the rough hemispherical model at Mach 11.3 for Reynolds numbers of 4×10^6 and 10×10^6 , which are compared in Figures 65 and 66 with measurements on the smooth configuration. The heat transfer distributions measured at both Reynolds numbers exhibit fully turbulent characteristics; however, we observe that, at both conditions, laminar heating levels were recorded at the stagnation point. Thus, despite values of K/θ at the stagnation point of greater than 10, and transition which has moved to within 10 boundary layer thicknesses of the stagnation point, we did not observe any significant increase in stagnation-point heating resulting from surface roughness.

It is of interest to compare the measurements of turbulent heating on the smooth hemisphere with the current production methods used in the "shape-change" codes. Figure 67 shows such a comparison with the codes developed by Crowell¹⁰ and Reeves¹⁴, TRW's SCATHE code, and the ASCC 80 code developed at Aerotherm. It is important to note that the ASCC 80 code was used by Aerotherm to compute turbulent smooth-wall heating in the roughness-induced heating-augmentation factors derived in the PANT studies.

Our measurements, which fall below ASCC 80 code predictions, give roughness-enhancement heating factors of 1.8, a figure which is consistent with the

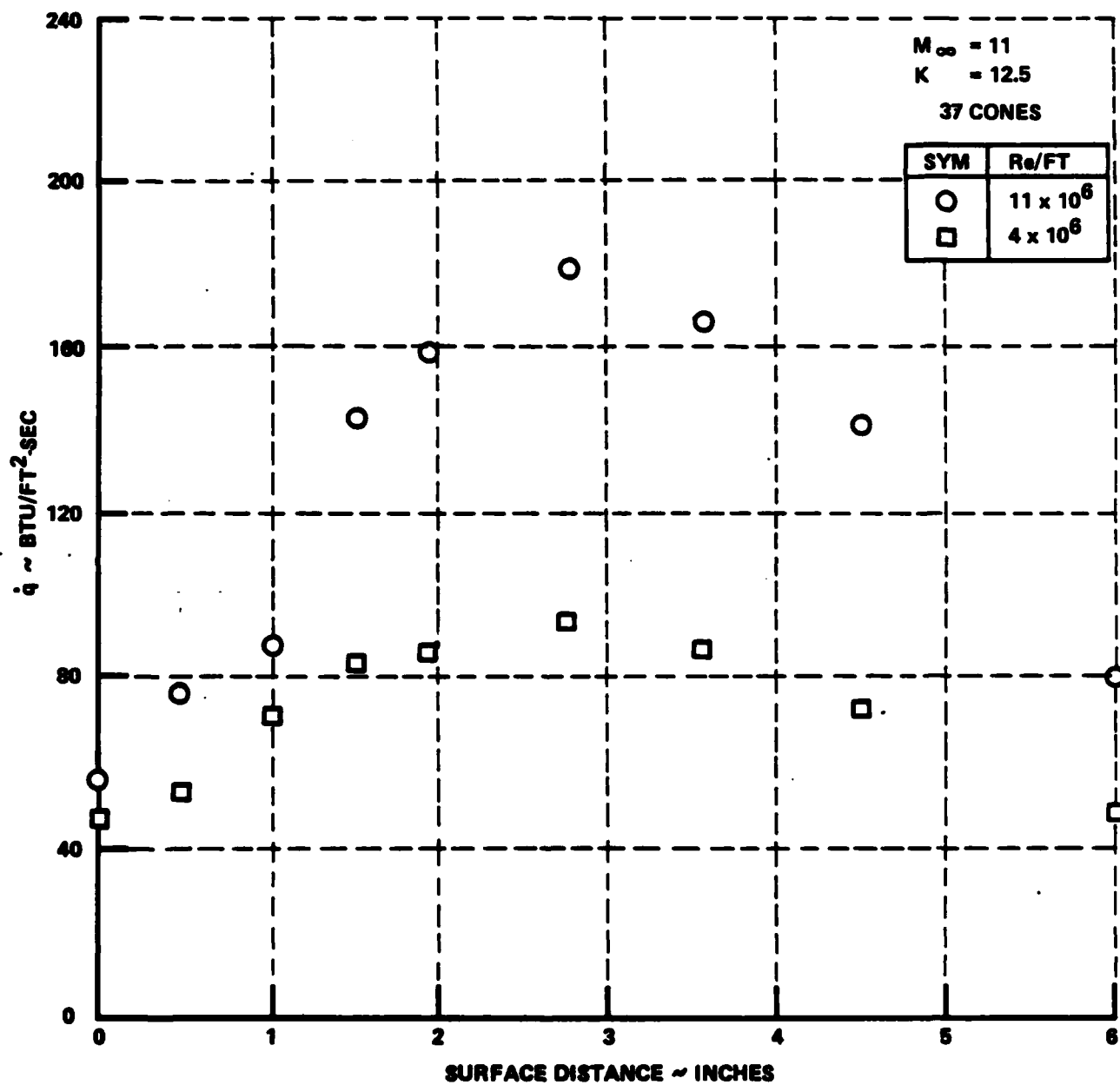


Figure 65 ROUGH-WALL HEATING TO HEMISPHERE ($M_{\infty} = 11$, $K = 12.5$ MILS)

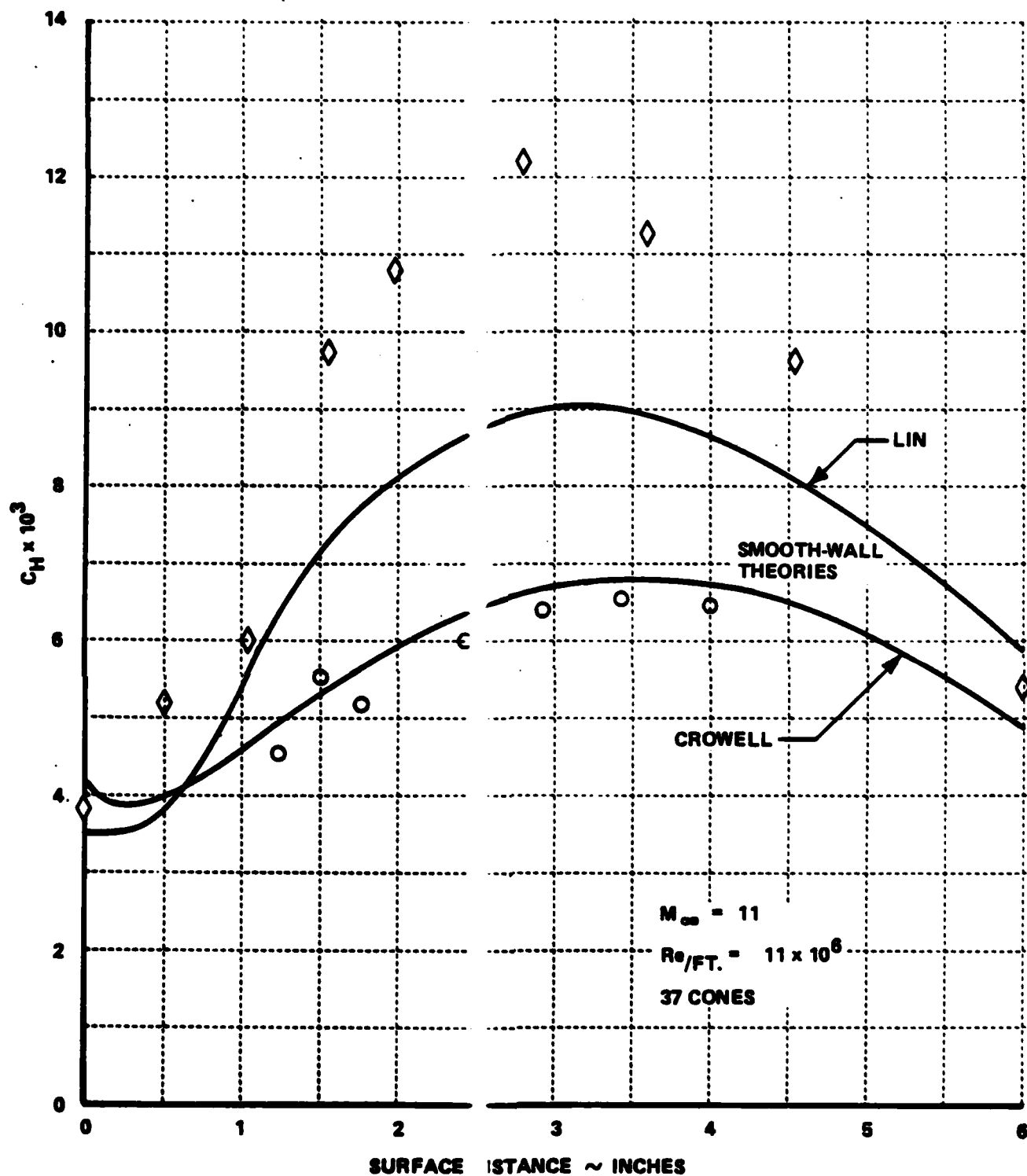


Figure 66 COMPARISON BETWEEN THE TURBULENT THEORIES OF LIN & CROWELL FOR SMOOTH-WALL AND ROUGH-WALL MEASUREMENTS OF HOLDEN ON 12" DIAMETER HEMISPHERE ($M = 11.2$, $Re_D = 11 \times 10^6$, $K = 12.5$)

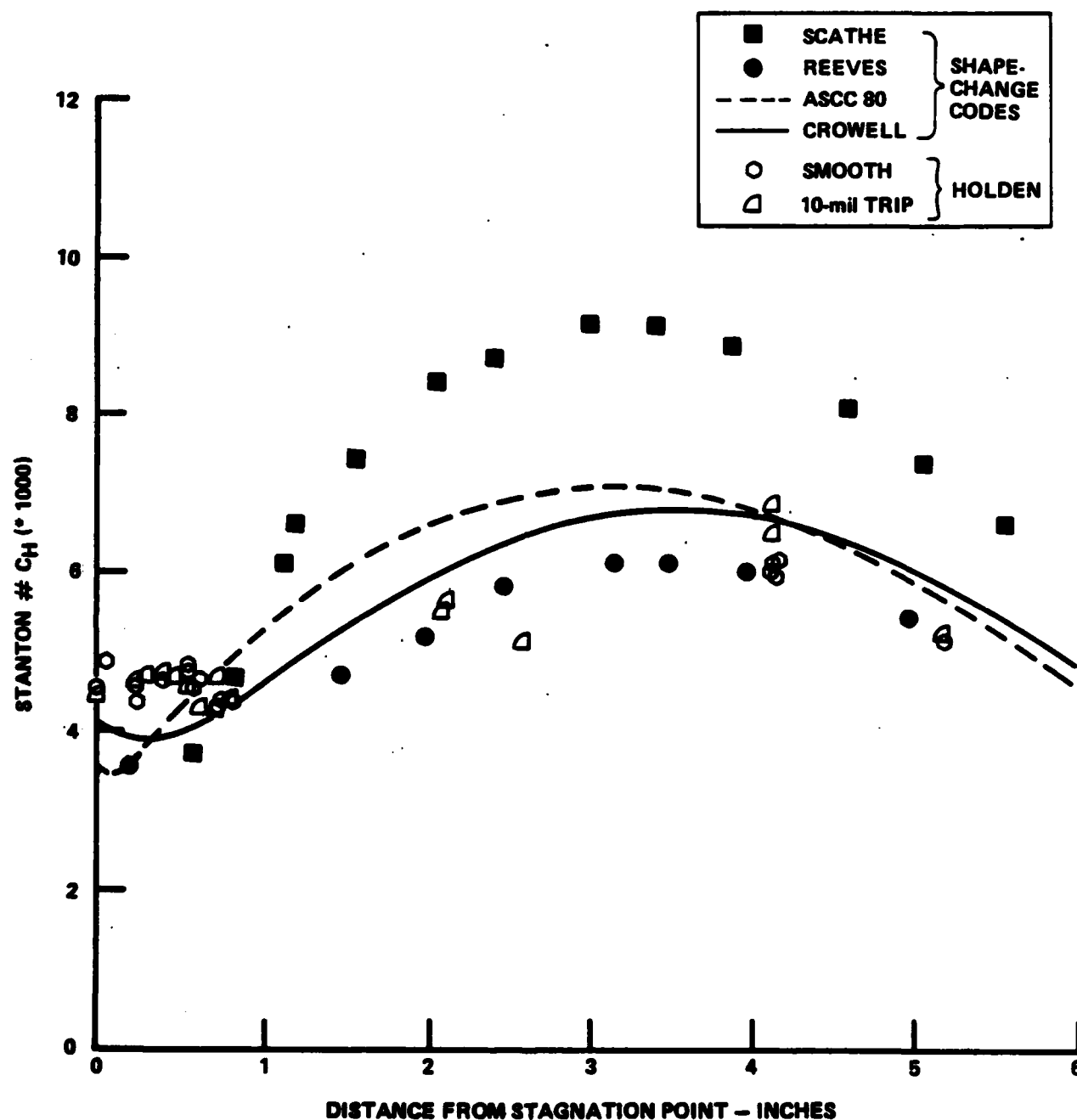


Figure 67 COMPARISON BETWEEN PREDICTING FROM FOUR OF THE SHAPE-CHANGE CODES CURRENTLY IN USE AND SMOOTH-WALL HEAT TRANSFER MEASUREMENTS ON HEMISPHERICAL NOSETIP

correlations obtained in other Calspan studies. We see that the predictions by Reeves¹⁴ are in good agreement with the measurements, while the SCATHE code significantly overpredicts the maximum heating rates. The surprisingly large disparities between the prediction methods for the smooth wall arises because of differences in the models of turbulence used to describe boundary layer development in a strong pressure gradient, and from differences in the reference enthalpy conditions selected. Clearly, this is an area which requires further investigation.

The measurements made in the studies of transpiration cooling conducted at Calspan were designed principally to determine whether blockage effects of mass injection are as large as predicted by the current codes. The measurements on the model with zero blowing, presented in Figure 68, clearly show that the intrinsic roughness of the surface causes heating enhancement factors of over 1.7. In fact, it can be seen by comparing Figures 66 and 68 that the heat transfer measurements on the conically rough hemisphere are in good agreement with those obtained on the non-blowing transpiration-cooled nosetip, with the exception of the region close to the stagnation point. In this region, the gages were mounted on the transpiration-cooled model such that they would be biased toward the larger heating level over the roughness. However, when a small amount of blowing ($\dot{m}/\rho UC_m = 0.032$) was introduced, the heating rates over a major part of the transpiration-cooled model dropped to levels close to those recorded on the smooth model, as shown in Figures 68 and 69. It could be postulated, on the basis of these measurements, that the initial effect of mass addition from a rough ablating nosetip is to modify the flow around the roughness elements, by eliminating the cavity flows, in such a way that the momentum defect introduced by the roughness is small.

If the effect of mass addition is to remove surface roughness as an important characteristic parameter, this poses serious questions for the correlation of flight measurements in terms of an effective surface roughness and the computational procedures in which the ablation rate is determined from heating levels enhanced by surface-roughness effects. Although experimental studies of the combined effects of mass addition and surface roughness are not easily constructed, the total lack of cold-wall measurements to validate the prediction methods in this area must be redressed.

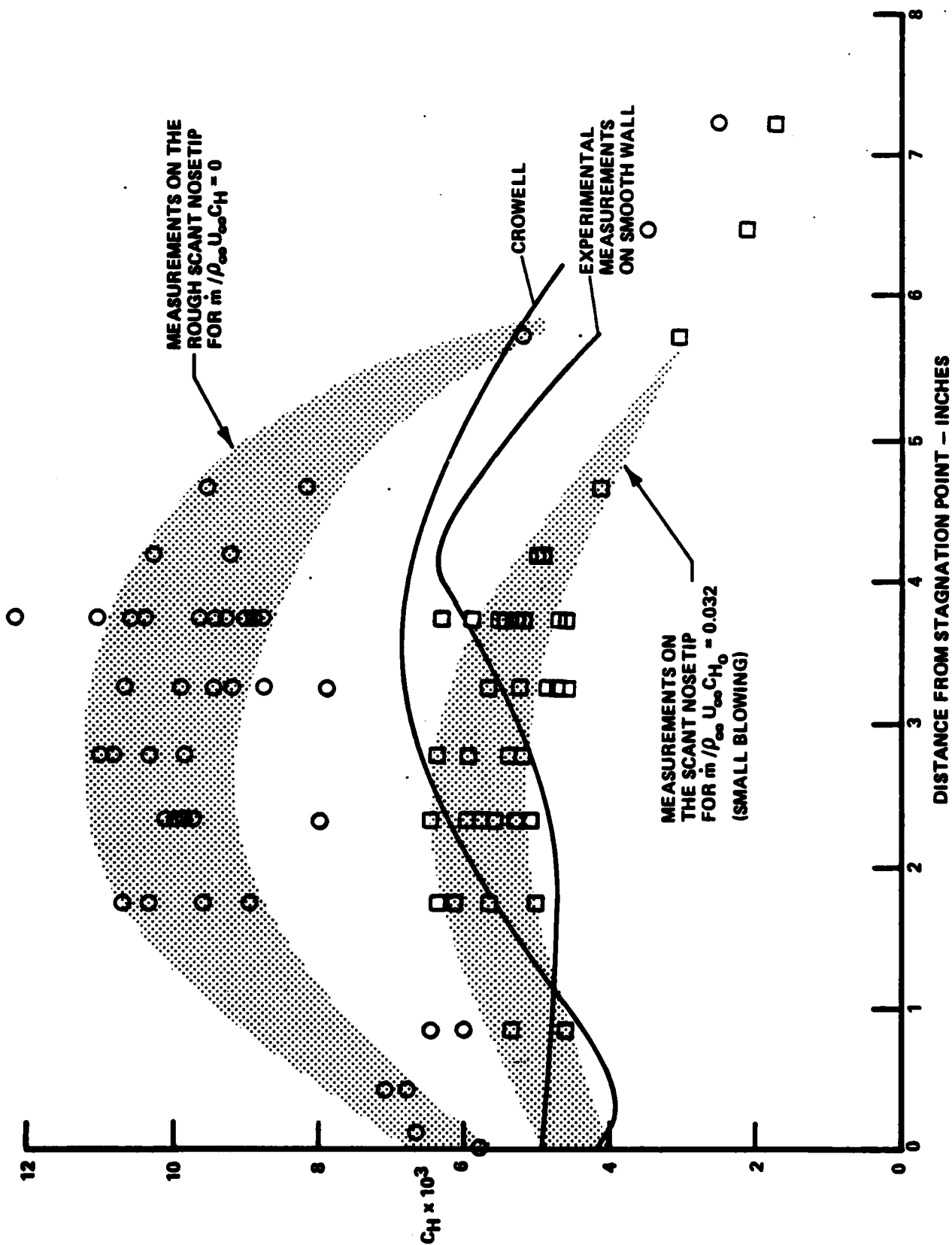


Figure 68 HEAT TRANSFER MEASUREMENTS ON SCANT AND SMOOTH HEMISPHERICAL NOSETIP SHOWING HOW SMALL BLOWING BRINGS DOWN HEATING LEVELS TO SMOOTH-WALL VALUES

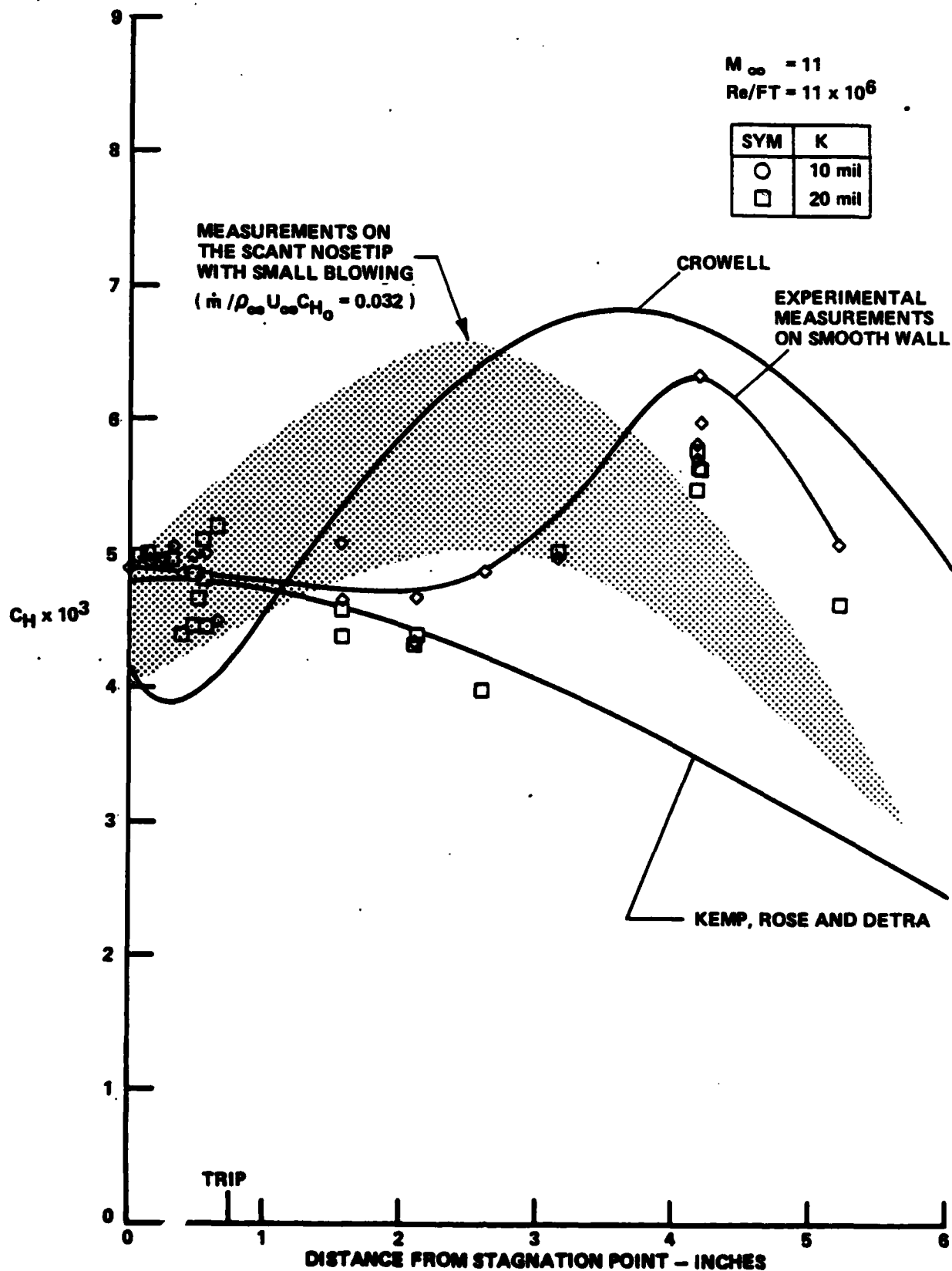


Figure 69 HEAT TRANSFER MEASUREMENTS INDICATING THAT SMALL BLOWING ON ROUGH NOSETIP INITIALLY ACTS TO BRING DOWN HEATING LEVELS TO SMOOTH-WALL VALUES

Section 4
STUDIES OF BASIC MECHANISMS OF ENHANCED HEATING
IN HYPERSONIC DUSTY FLOWS OVER BLUNT BODIES

4.1 INTRODUCTION

When a hypersonic vehicle encounters clouds of dust or ice particles, the interaction between the flow around the particles as they enter the shock layer and rebound, or cause secondary particles to be ejected from the vehicle surface, can give rise to key aerothermal effects which are of primary importance to the vehicle designer. Nose-tip erosion resulting from particle impact has been of primary concern to designers of ballistic re-entry vehicles. However, in flows with medium to light dust loading, the increased heating resulting from particle/shock-layer interaction can exceed the dust-free levels by as much as a factor of 5. The experimental studies conducted at Calspan of the increased heat resulting from particle/shock-layer interaction constituted the first systematic study of the basic phenomenon. These studies followed dust-tunnel studies which showed that the gross heating levels to a blunt nosetip in a dusty flow cannot be explained in terms of impact energy alone. The difference between the measured heating rate and the heating rate estimated on the basis of impact energy was termed the "particle-augmented convective heating rate." Systems studies of this phenomenon by others linked the augmented convective heating rate to "particle loading" through an assumption that the heating-enhancement mechanism is related to the increased vorticity introduced into the shock layer from the wakes of the particles. The relationships based on this assumption are still used today, despite its lack of validity. More recently, flight measurements have indicated that the disturbances to the shock layer resulting from particle interaction can produce an asymmetric aerodynamic load which causes a loss in accuracy of the trajectory of a ballistic re-entry vehicle. As discussed briefly in subsection 3.3, heat transfer measurements on blunt bodies in hypersonic facilities run at high Reynolds numbers may be influenced by disturbances induced by minute particles which trip the boundary layer in the stagnation region. This phenomenon, which we believe occurs only in hypersonic facilities capable of generating Re_θ 's large enough to make the laminar boundary layers unstable in the stagnation region on a blunt body, cannot be easily detected without high-frequency heat transfer instrumentation. Stagnation heat transfer measurements made with low-frequency instrumentation in such flows will most certainly be in error.

In this section of the report, we discuss the basic aerodynamic mechanisms which, on the basis of experimental studies conducted at Calspan, are responsible for enhanced heating in lightly loaded particle-laden flows over blunt bodies. We first describe the experimental apparatus, and the environment in which the studies were performed. We then discuss the various mechanisms which we believe result from particle/shock-layer interaction and are responsible for enhanced heating in these flows.

4.2 MODEL AND INSTRUMENTATION

The experimental studies were conducted in the Calspan 48-Inch Shock Tunnel at Mach numbers from 6.5 to 16 for Reynolds numbers ranging from 1×10^6 to 30×10^6 based on nose tip diameter. The model, which is shown in Figure 70, was constructed from two basic segments: (i) a highly instrumented nose segment (Figure 71) and (ii) an afterbody containing three launchers (Figure 72), mounted one above the other so that particles could be launched in a vertical plane. The launcher assembly was mounted in a seismic mass, which, in turn, was supported within the basic model by a soft rubber suspension system. In this way, the instrumented section was effectively isolated from mechanical disturbances, generated when the launcher was activated. The instrumented section of the model, a schematic diagram of which is shown in Figure 73, contained 80 heat transfer gages and 28 high-frequency pressure gages. Thin-film resistance thermometers were used to obtain detailed temporal measurements of surface heat transfer. These thermometers, which were fabricated by the deposition of a thin platinum film on a pyrex substrate, provide an instantaneous indication of the surface temperature. This quantity can be related by semi-infinite slab theory to the instantaneous heat transfer rate. The gages were positioned so that a high density of instrumentation was concentrated in one quadrant of the model, while the balance of instrumentation was distributed symmetrically about the model axis. In this way, we obtained detailed measurements on two mutually perpendicular axes, while retaining the ability to track asymmetric disturbances across the face of the model. The size and density of the particle launched and the velocity of the launch were chosen with the aid of a simple numerical code so that the particle penetrated specified distances relative to the position of the shock at each freestream condition. Particles from 30 to 800 microns in largest dimensions were launched from the surface of the model simultaneously or in a phased array, with velocities from 50 ft/sec to 300 ft/sec. We established that there was no measurable disturbance when the launchers were fired without the particles. The frequency response of both the pressure and heat transfer

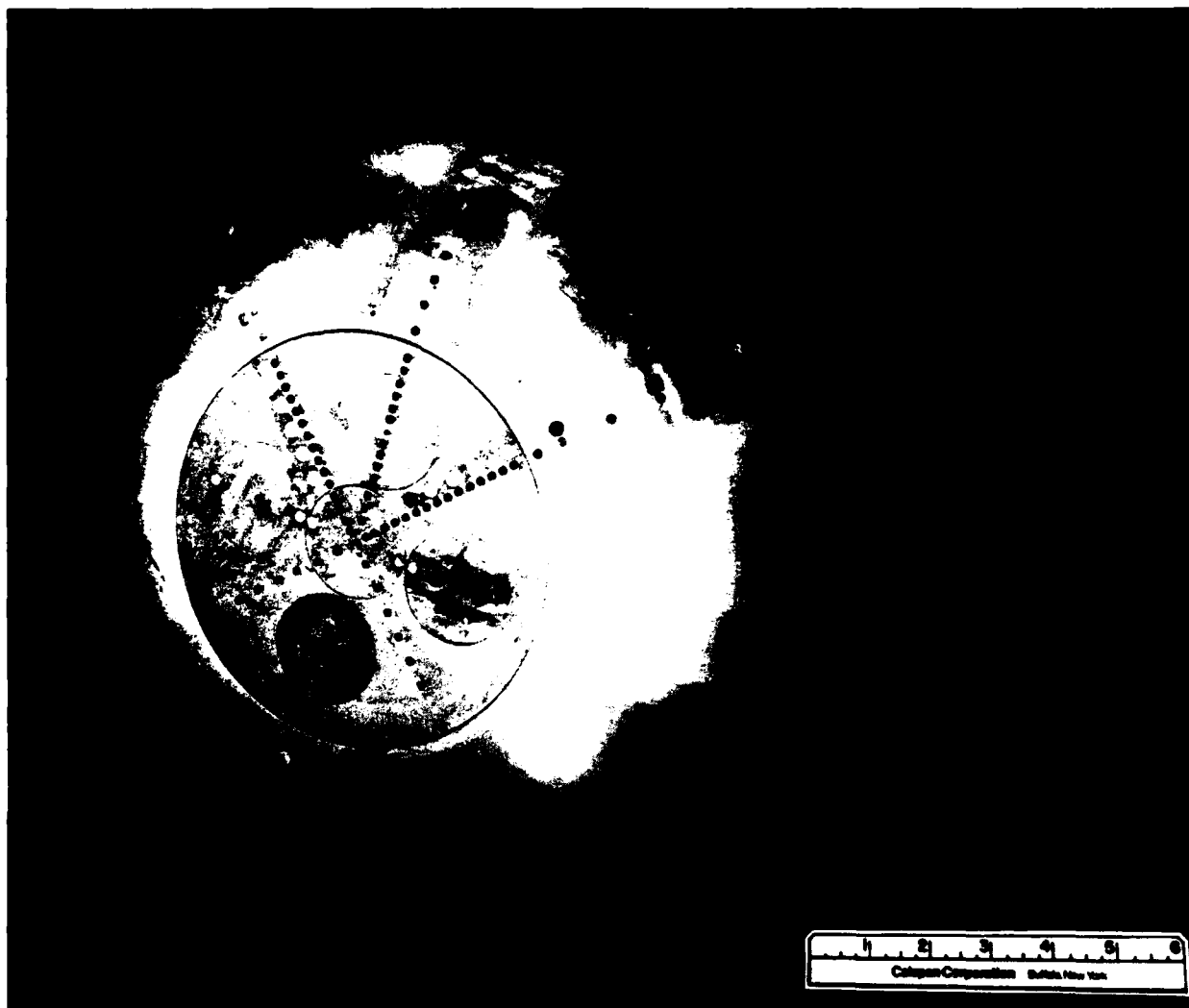


Figure 70 PARTICLE-LAUNCH MODEL EQUIPPED WITH THREE PARTICLE LAUNCHERS, 105 HEAT TRANSFER GAGES, 27 PRESSURE GAGES, AND 4 SKIN-FRICTION GAGES

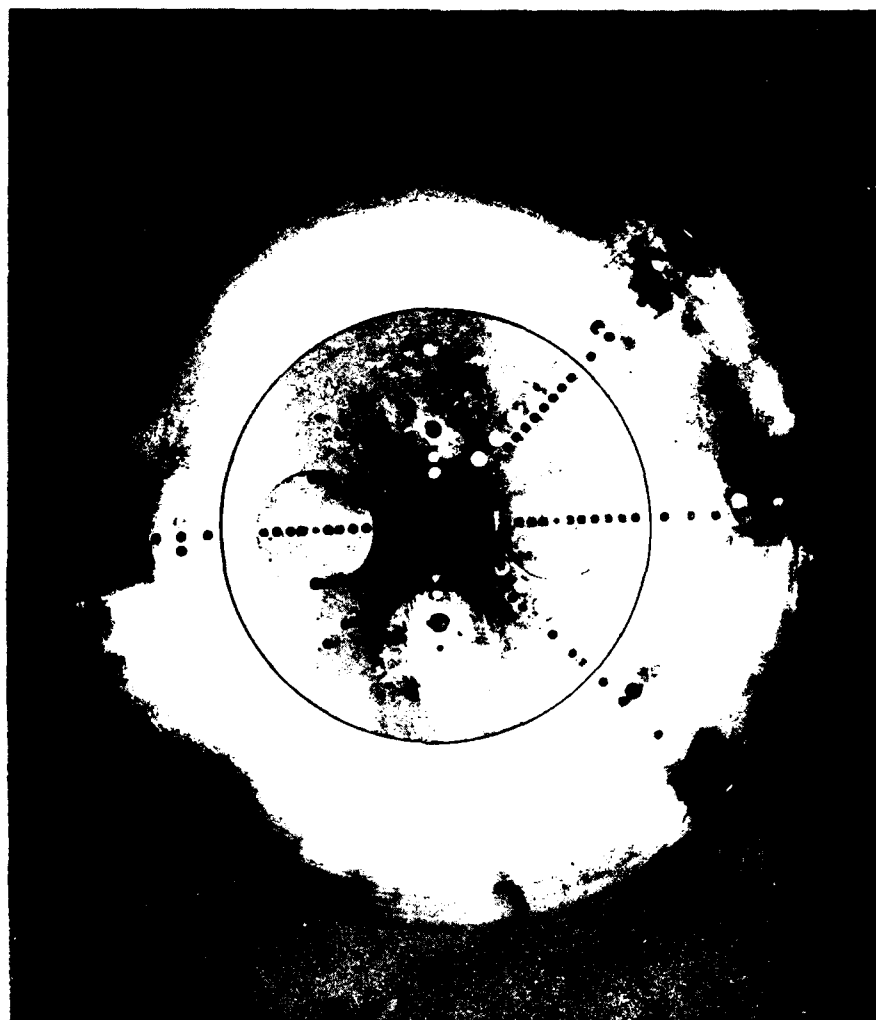


Figure 71 INSTRUMENTED SEGMENT OF PARTICLE-LAUNCH MODEL

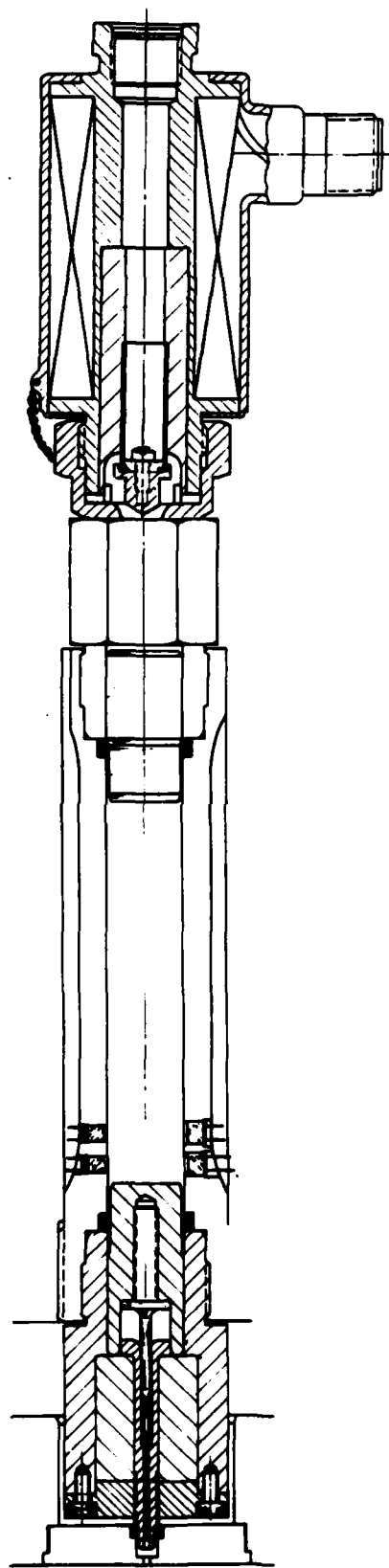


Figure 72 IMPACT PARTICLE LAUNCHER

SEE DETAIL "A"
 TYP. 1/4 PLATES
 SAGES 21 - PK

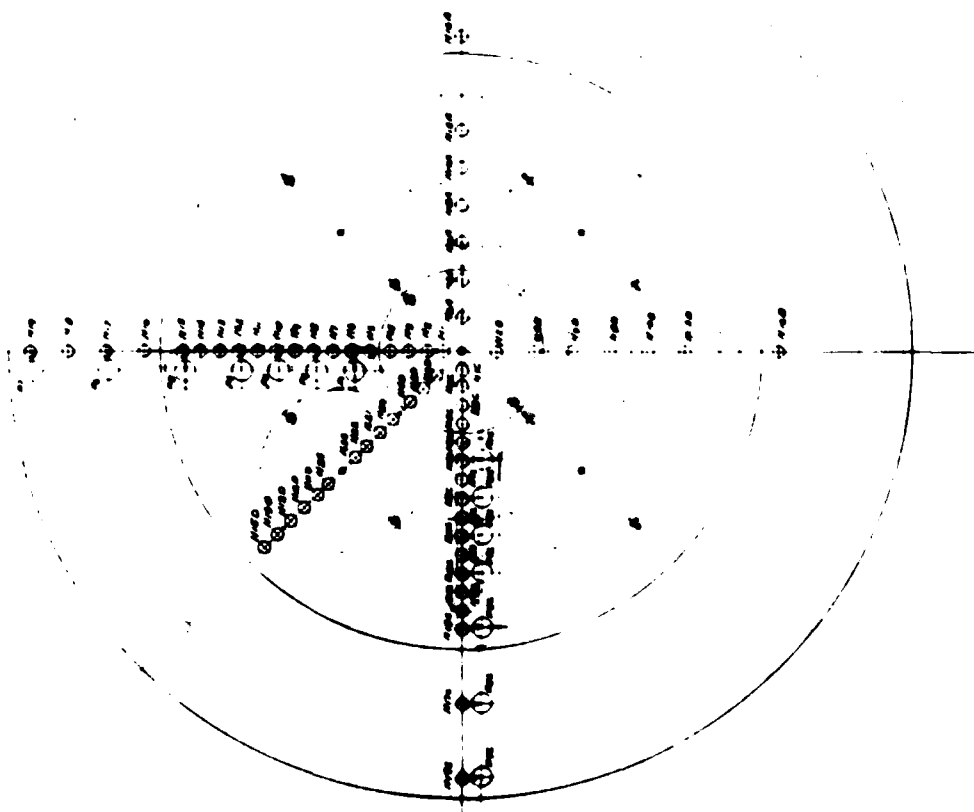
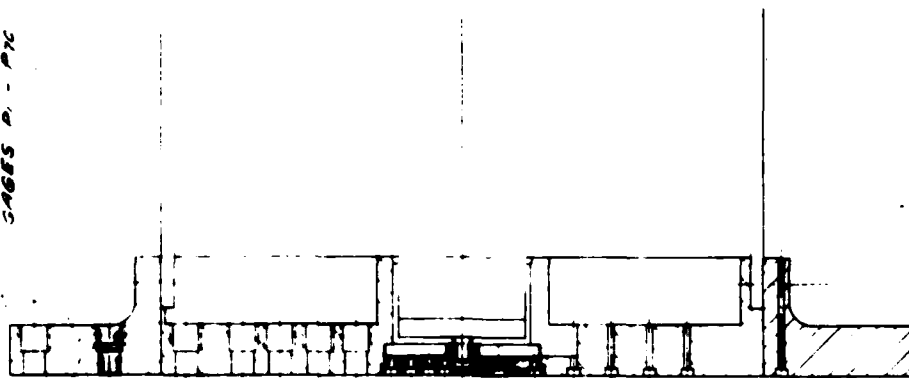


Figure 73 SCHEMATIC OF INSTRUMENTATION OF PARTICLE-LAUNCH MODEL

instrumentation with which the model was instrumented exceeded 300 kHz, well above that required to follow the disturbances resulting from particle-shock/bow-shock interactions. High-speed photography at intervals of approximately 200 microseconds was used to obtain the flow-field configuration.

4.3 DISCUSSIONS OF BASIC MECHANISMS OF PARTICLE-ENHANCED HEATING

4.3.1 Minute-Particle/Boundary Layer Interaction

In our studies with the hemispherical nosetips and the particle-launch model at the lower Reynolds numbers ($Re_p < 10^6$), we were unable to detect heating disturbances with the thin-film gages which could be associated with the wake of the large particles within the shock layer launched with the particle launcher, or disturbance introduced by minute mylar or dust particles from the driver section of the tunnel. However, for conditions where Reynolds numbers of over 10^7 were generated, examination of the high-frequency outputs from the thin-film gages on the hemispherical model indicated disturbances, which we recognized as being associated with transition from our previous studies, which were induced by minute dust particles.

The high-frequency response of the heat transfer gages and recording equipment (thin-film gages and Biomation recorders) enabled us to follow the disturbances as they were swept downstream over the closely spaced instrumentation. We observed that, while there was an initial growth of the disturbance in the stagnation region, downstream of the stagnation region the strong favorable pressure gradient caused the disturbance to decay rapidly and finally disappear well before the sonic line. Thus, time-averaging the measurements of the heat transfer gages in the stagnation region or using slow-response heat transfer instrumentation would lead to heat transfer distributions with larger than laminar values at the stagnation point, with the heating rates returning to laminar values away from the stagnation region as the instabilities were dissipated. We believe that this mechanism is the one principally responsible for the enhanced stagnation point in high Reynolds number hypersonic flow. Again, it must be emphasized that this phenomenon will occur only when the boundary layer in the stagnation region has a large enough Re_θ for it to be intrinsically unstable. We believe that, in order to conduct a meaningful study of transitional flow over blunt nosetips in high Reynolds number hypersonic flow, special precautions must be taken to ensure

that the test gas is ultra-clean. Further high-frequency highly resolved heat transfer measurements must be made to ensure that such effects are not present. Our experience suggests that tunnel noise causes enhanced heating through the mechanism of tripping the boundary layer, rather than increasing the vorticity in a laminar boundary layer.

4.3.2 Toroidal-Vortex/Boundary Layer Interaction

Measurements on blunt ellipsoids and on the laminar blunt configuration employed in the particle-launch studies indicate that a definitive mechanism which causes particle-enhanced heating is associated with the formation of toroidal vortices by particle/body-shock interaction. Two examples of the incipient formation of these vortices at the shock front are shown in Figure 74. When the particle arrives at the shock front with momentum sufficient only to cause a small dimple, a disturbance is generated which is propagated back through the shock layer as a toroidal vortex.

A sequence of photographs showing the small dimple which occurs as the particle reaches the bow shock and the subsequent formation of a toroidal vortex is provided in Figure 75. The abrupt change in shock curvature at the junction between the particle and the body shock creates a shear layer which subsequently rolls up into the vortex ring as the particle is driven back into the shock layer. The vortex ring is then convected toward the model, expanding in diameter as it approaches the surface. Correlating the heat transfer time histories with the movie sequence reveals that increased heating rates are observed at the model surface over a period of just over 1 millisecond, the time taken for the vortex to traverse the shear layer and expand across the model. As the ring passes over the heat transfer gages, their outputs increase from 1.5 to 3 times their undisturbed values. If the flow is initially laminar over the nosetip, the vortex acts to trip the boundary layer. Then, the basic enhancement mechanism is transitional to turbulent heating. For fully turbulent flows, the enhancement (which is significantly less) is associated with the enhanced local freestream vorticity.

4.3.3 Particle-Shock/Body-Shock Interaction

When particles are ejected from the shock layer such that they remain within one body diameter of the surface, a stable particle-shock/body-shock interaction



Figure 74 SHOCK/PARTICLE INTERACTION OVER A BLUNT ELLIPSOID



Figure 75 HEATING AUGMENTATION ASSOCIATED WITH PARTICLE-INDUCED RING VORTEX INTERACTION

occurs which induces enhanced heating by free shear layer/boundary layer interaction (free shear layer impingement).

A sequence of photographs showing the development of a region of shock/shock interaction leading to heating augmentation resulting from small-particle penetration is shown in Figure 76. Here, the momentum on the particle was just sufficient for the particle to reach 0.7 of the body diameter ahead of the model. As the particle moved ahead of the bow shock, the shock wave associated with the particle and the flow behind it interacted with the original bow shock, inducing a shear layer at their point of intersection. This shear layer swept radially outwards across the face of the model, increasing the local heat transfer at its base by as much as a factor of ten. In this sequence, the shear layer reached the model periphery just as the particle was being driven back to the model surface, and the shear layer then collapsed inward in a quasi-steady fashion, disappearing as the particle re-entered the shock layer. The period of increased heating was just over one millisecond, the time taken for the particle to exit and re-enter the shock layer. Pressure levels just above the pitot level were observed at the base of the shear layer, while those within the annulus corresponded roughly with those achieved by compression through the conical shock associated with the particle. The heating rates associated with such interactions have been explored by Holden in spiked body flows,¹⁵ by Edney,¹⁶ and by Keyes and Hains¹⁷ in regions of shock interference. It seems clear that major augmentation occurs when the "Edney Type IV" or "jet" interaction is established over the model. Until the shear layer is swept to the edge of the model for the first time, the movement of the particle can be predicted by simple drag models; however, when the flow begins to oscillate, the alternate formation and collapse of the recirculation region ahead of the body imposes a system of forces on the particle which makes its motion extremely complex.

4.3.4 Effects of Separated Pulsating Flow

When the particle is launched with sufficient momentum for it to reach one body diameter ahead of the body, a dramatic change occurs in both the character of the inviscid flow and the pressure and heat transfer on the model surface. Here, the entire flow field begins pulsating, as demonstrated by the high-speed movie sequences of Figures 77 and 78. These sequences, which were taken at Mach 6.5 and 13, respectively, at similar Reynolds number conditions, demonstrate considerable similarity in mechanics

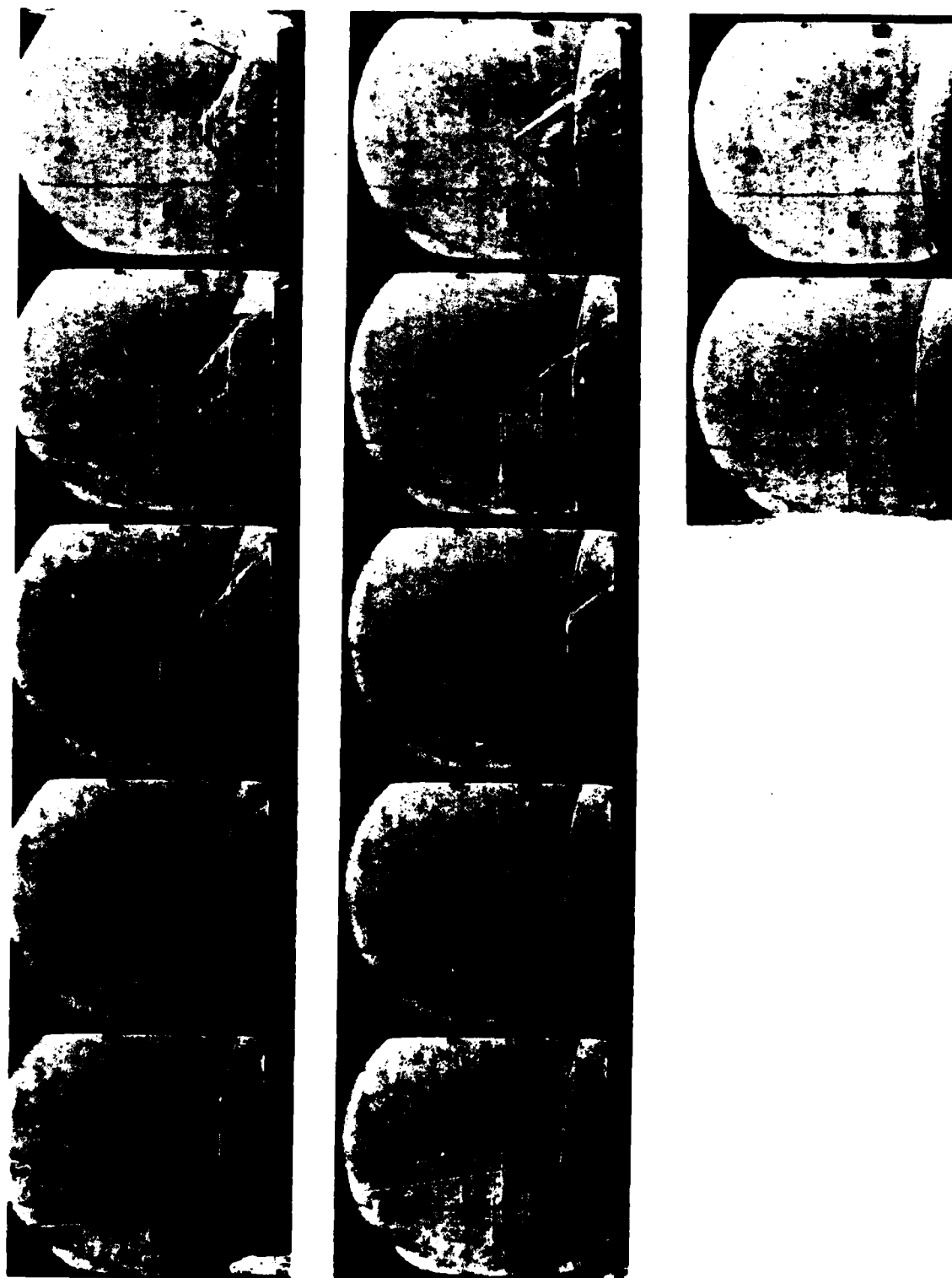


Figure 76 "STABLE" FLOW RESULTING FROM SMALL PENETRATION

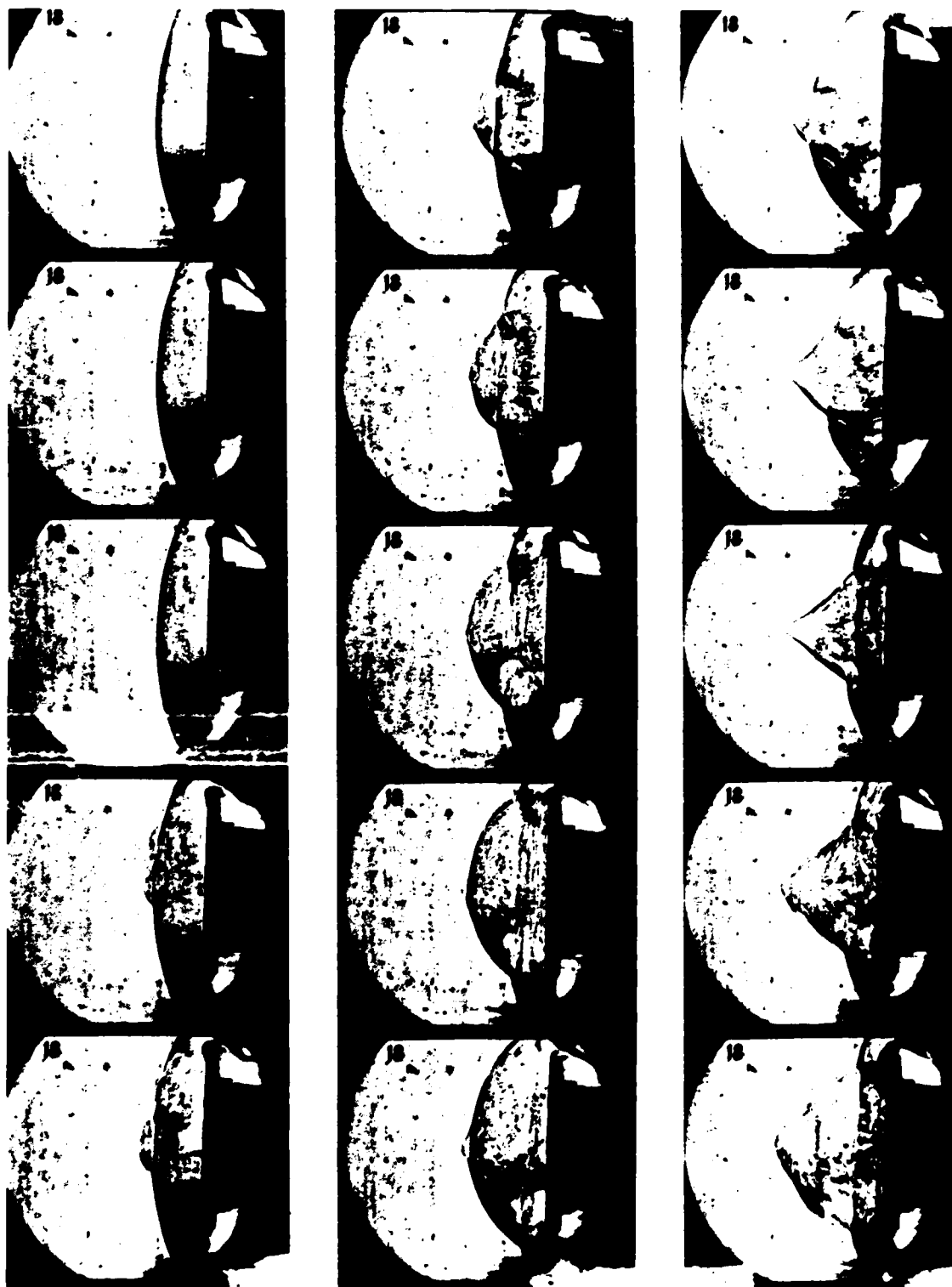


Figure 77a PARTICLE-INDUCED LARGE-SCALE ("E") OSCILLATION (MACH 6.5)

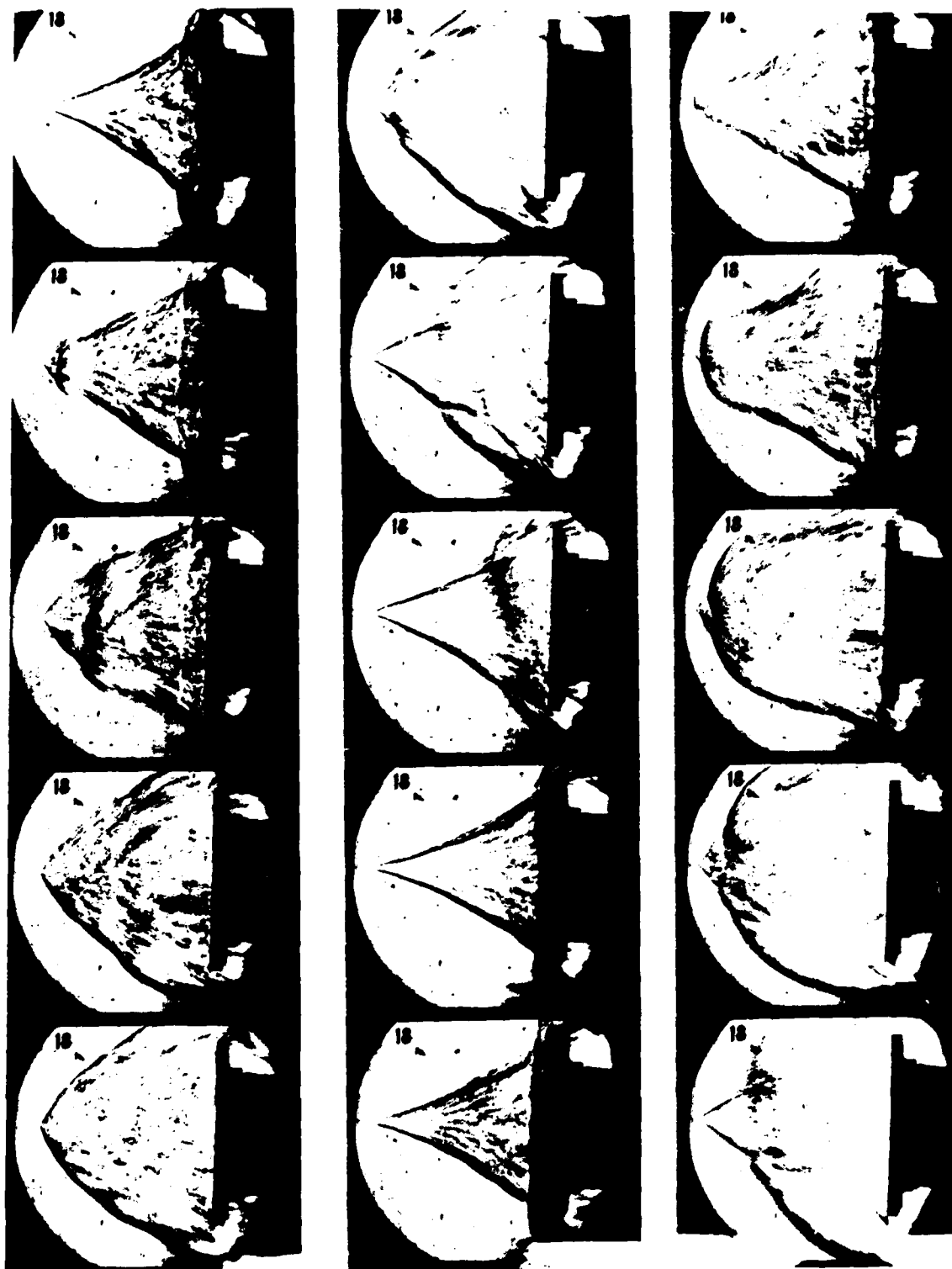


Figure 77b PARTICLE-INDUCED LARGE-SCALE ("E") OSCILLATION (MACH 6.5)

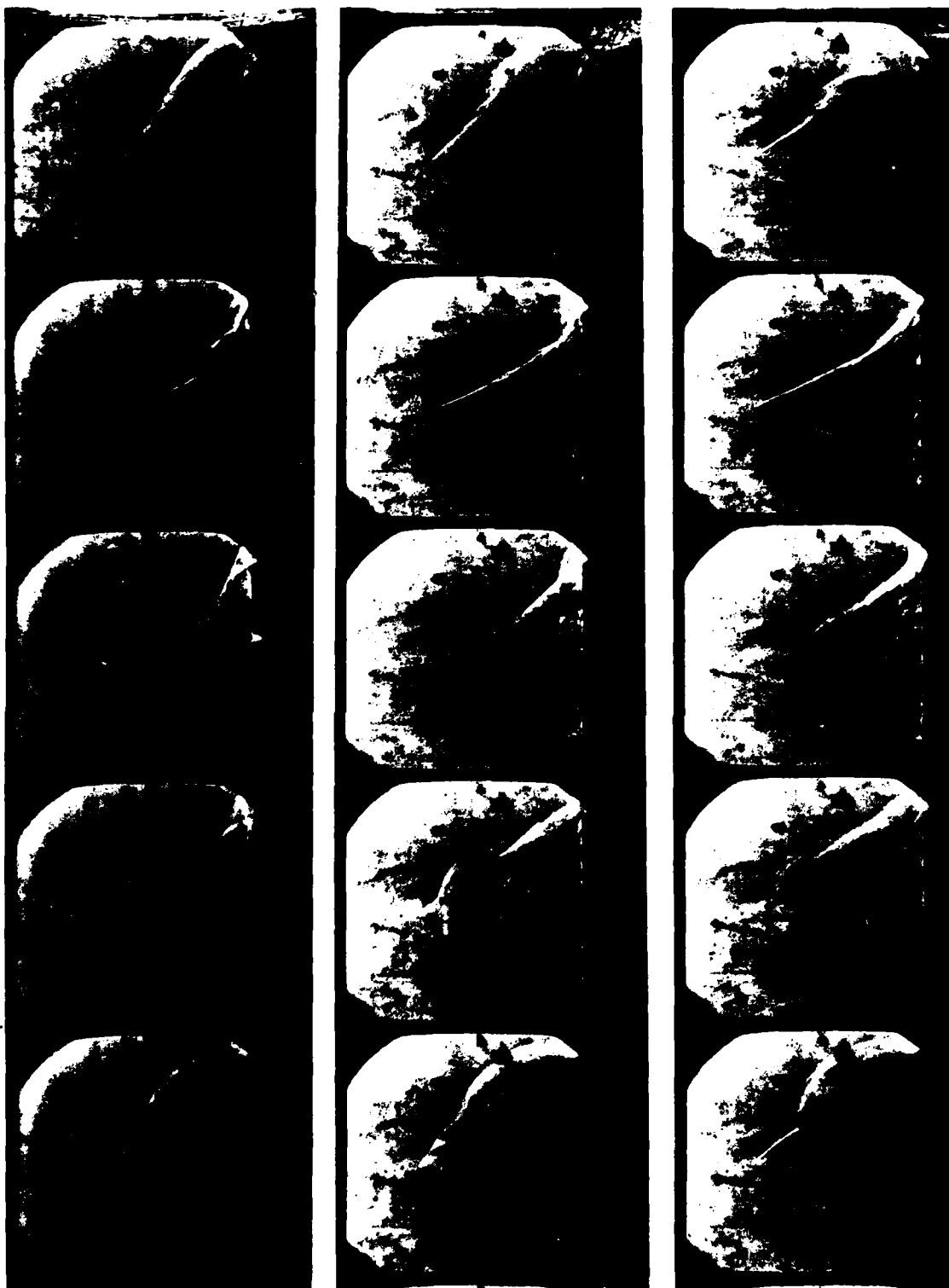


Figure 78a PARTICLE-INDUCED LARGE-SCALE ("E") OSCILLATION OF FLOW FIELD (MACH 13)

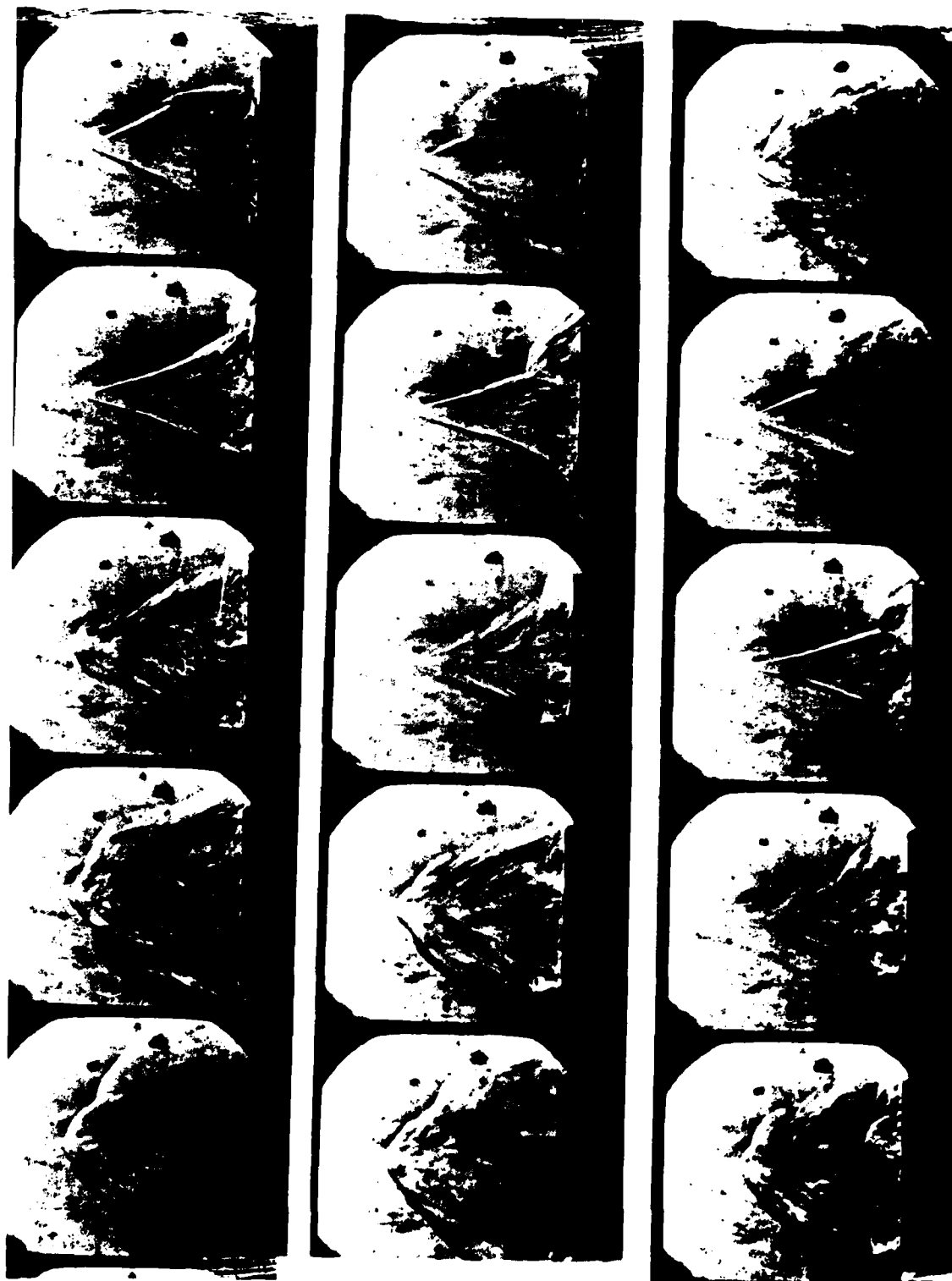


Figure 78b PARTICLE-INDUCED LARGE-SCALE ("E") OSCILLATION OF
FLOW FIELD (MACH 13)

of oscillation. This oscillation is very similar to pulsating flows* observed over spiked bodies¹⁵ or highly indented nose shapes¹⁸, as demonstrated by the movie sequence of flows shown in Figure 79. The occurrence of these massive pulsations appears independent of particle size, and, once the particle has reached one body diameter ahead of the surface, the axial motion of the particle is strongly influenced by the flow oscillations. The non-dimensional frequency (fD/U) was found to lie between 0.17 and 0.19 and appeared to be relatively independent of Mach number; particle velocity, size, or penetration; and model size. A Strouhal number of between 0.17 and 0.20 typifies the frequencies encountered over spiked and highly indented bodies, reinforcing the concept that the basic mechanism is associated with a simple inviscid filling and spilling mechanism. The oscillation is initiated when the shear layer or jet formed by particle/spike-shock/bow-shock interaction re-attaches to the body surface, trapping a conical region of gas. The mass which is being continuously added to this region through the conical shock drives the local stagnation point at the base of the shear layer toward the periphery of the model. This region collapses as the entrapped gas escapes when the shear layer moves off the body, and the sequence begins again with bow shock re-establishing and the particle-shock/bow-shock interaction reforming the shear layer. Perhaps the most intriguing question is why two distinct shock structures, one around the minute particle and a second around the model, are not formed at this juncture. Both the pressure and heat transfer records exhibit large excursions from ambient conditions. A typical record from a thin-film heat transfer gage on the face of the model is shown in Figure 80. After the tunnel starting process, the gage is exposed to a period of constant heating equal to that observed for the unperturbed flow. The heating rate increases sharply as the particle interacts with the shock and the shear layer sweeps across the face of the model. A decrease in heating occurs as a bulbous shock layer is formed and the flow "collapses" toward the body. This pattern is repeated in a flow oscillation of surprising regularity and persistence. While the heating rates across the model vary with time, the magnitudes of the maximum values do not appear sensitive to the exact particle trajectory, as can be seen from the measurements made in two runs (shown in Figure 81) at identical freestream conditions but with different particle trajectories. This figure illustrates that the edge of the cylinder experiences the largest heat transfer rates, which can exceed the ambient heating levels by as much as a factor of five. The minimum heating rates fall close to

*Termed the "E" oscillation in this study.



Figure 79 "E" OSCILLATION ON A_0 CONFIGURATION AT ZERO ANGLE OF ATTACK

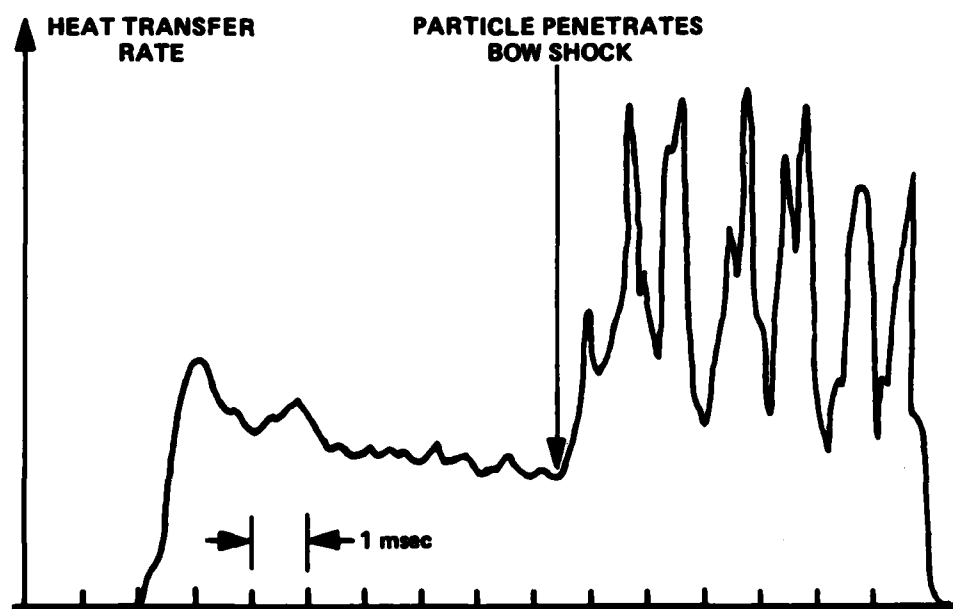


Figure 80 TYPICAL HEAT TRANSFER RECORD FROM THIN-FILM GAGES

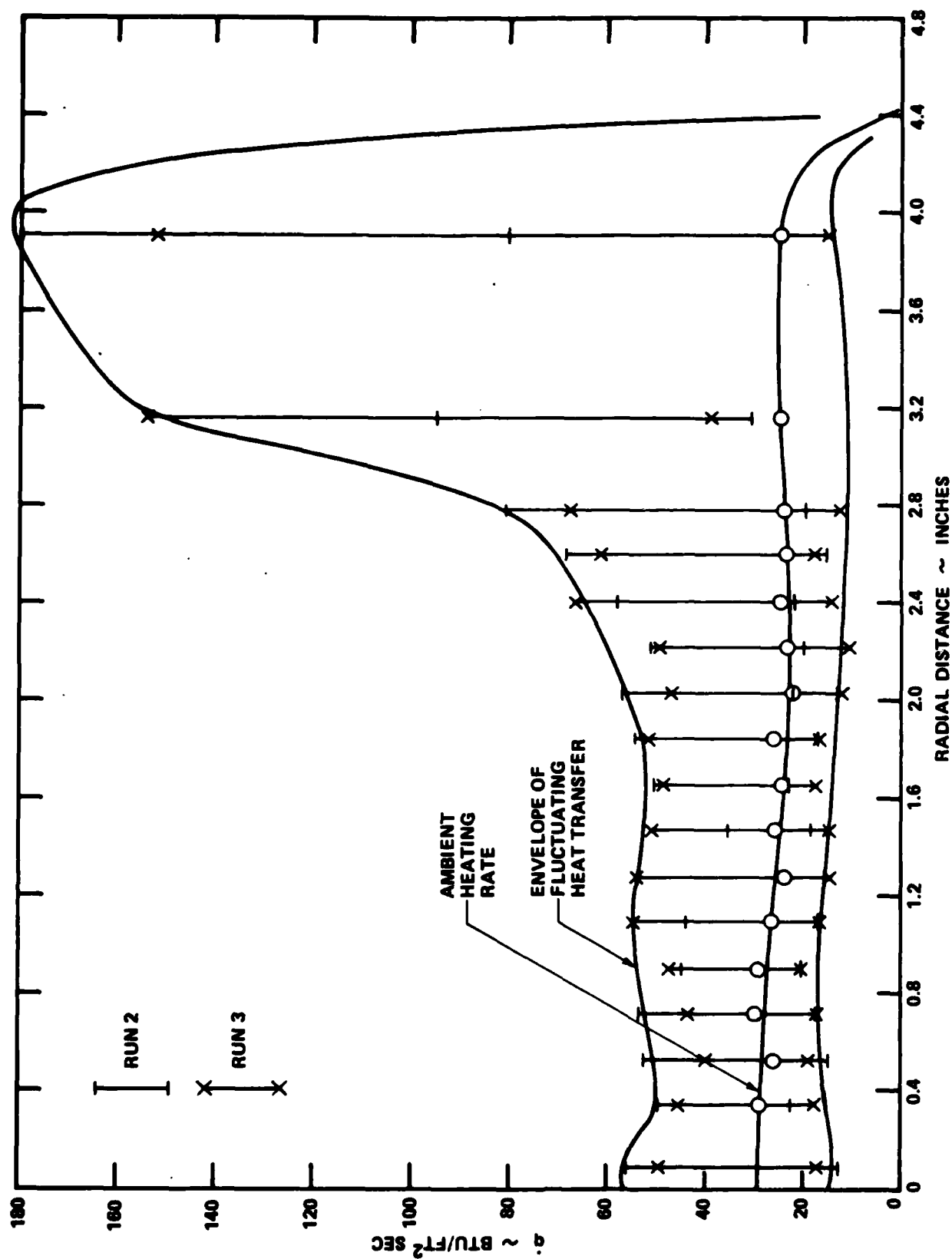


Figure 81 HEAT TRANSFER DISTRIBUTION TO THE FACE OF THE DISC FOR A FULLY OSCILLATING FLOW OVER THE MODEL

the ambient heating level in the absence of a particle and correspond to the flow condition where the bow shock is collapsing back to the body. A typical variation of the fluctuating surface pressure close to the center of the model for this condition is shown in Figure 82. The maximum levels are roughly equal to the pitot pressure, while minimum corresponds to the plateau pressure for conical separated flows over spiked bodies, supporting the postulation that recirculation region is formed over the model during part of each cycle. If the particle travels off-axis, permitting an asymmetric interaction region and asymmetric spillage, an oscillatory interaction region can still be observed, as shown in Figure 83. While the period of augmented heating is less for these cases, augmentation factors of over 5 are observed. Again, the major mechanism is interference heating resulting from shock/shock interaction.

4.3.5 Multiple-Particle-Shock/Shock-Layer Interaction

When three particles are launched simultaneously, a combination of extremely complex interactions occurs, as illustrated in Figure 84. The ambient heating, as well as the heating resulting from the particle-shock/bow-shock interaction, is shown in Figure 85. Here, we observe an increase in heating across the entire face of the model which exceeds the ambient heating by a factor of over 400 percent. Pulsations occur alternately about the particles in the shock layer in a manner dissimilar from the gross pulsations shown for a single particle launched along the axis. We have also observed that, in the latter case, a far greater penetration occurs for the same initial momentum. Here, we believe the flow reversal which occurs in the large pulsation decreases the drag of the particle or creates drag in the reverse direction. Clearly, increasing the number of particles in the shock layer increases the heating augmentation.

Launching a spray of 5-mil particles into the shock layer, as shown in Figure 86, produces interactions which are similar to those observed in ballistic ranges as well as the multiple particle interactions described earlier. The sequence of photographs taken with laser photography in the AEDC Ballistic Range given in Figure 87 shows the shock/particle interaction resulting from water-droplet impact in the stagnation region of a blunt body. The shock/shock interactions shown in these photographs are very similar to these shown in Figure 86, taken in the Calspan studies. While studies in the ballistic range can duplicate the particle/nose-tip impact, a very limited amount of data can be taken in these studies. Large increases in nose-tip heating occur as a result of such interaction, as shown in Figure 88. Here, we show

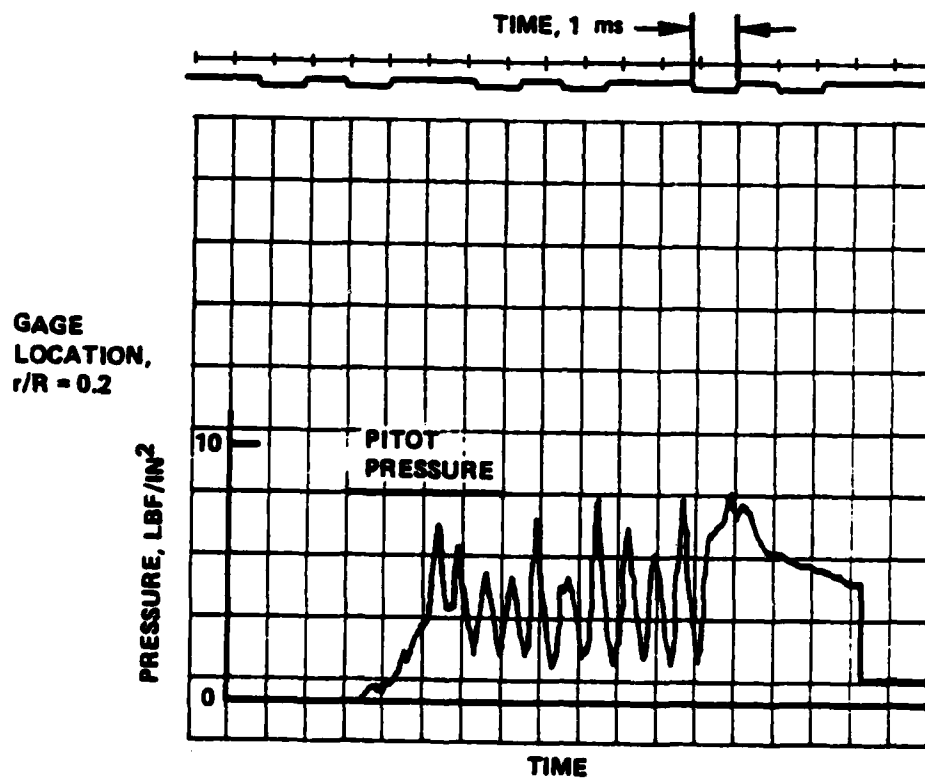


Figure 82 TYPICAL PRESSURE OSCILLOGRAM FOR FULLY PULSATING FLOW

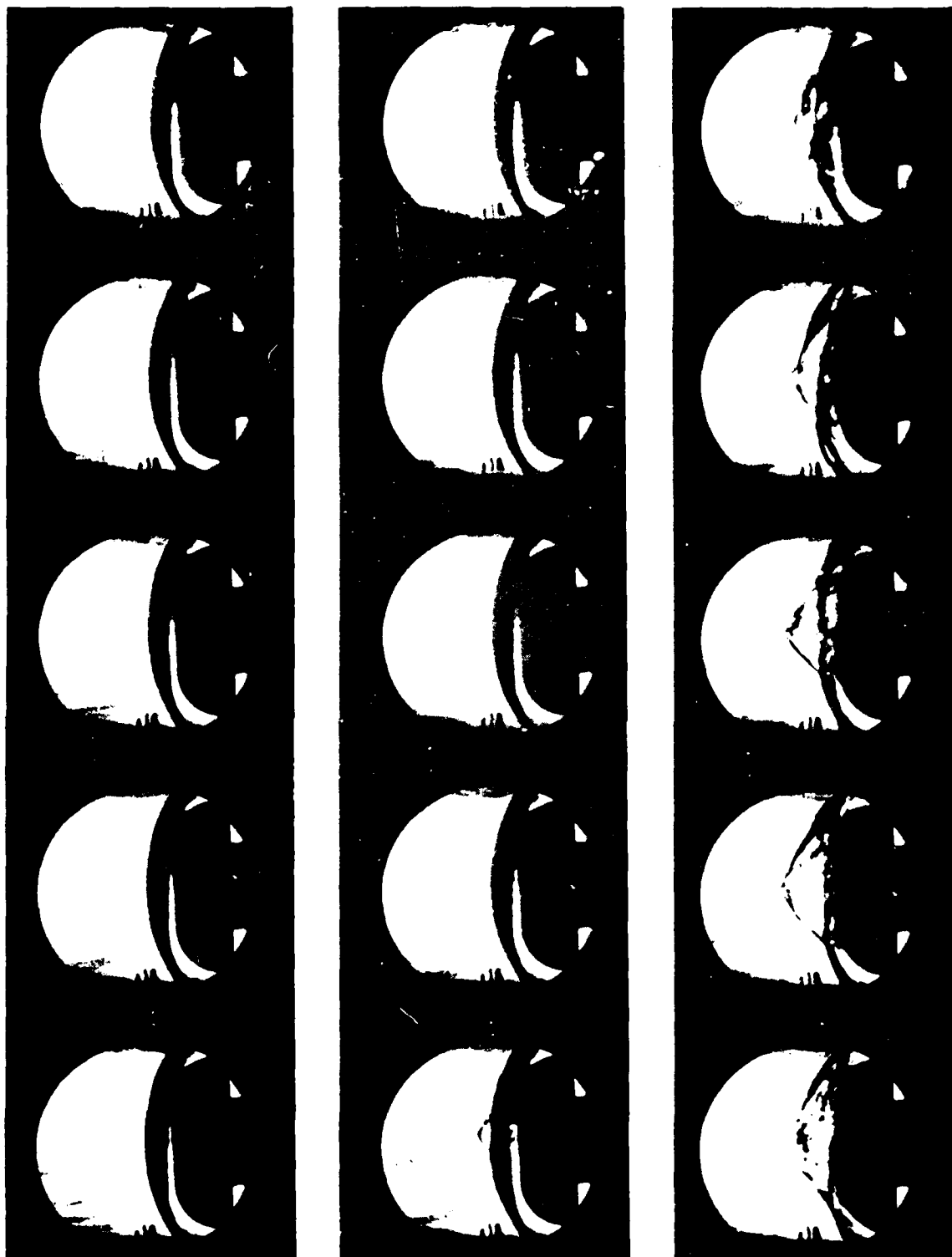


Figure 83a PHOTOGRAPHIC SEQUENCE FROM SINGLE PARTICLE LAUNCH

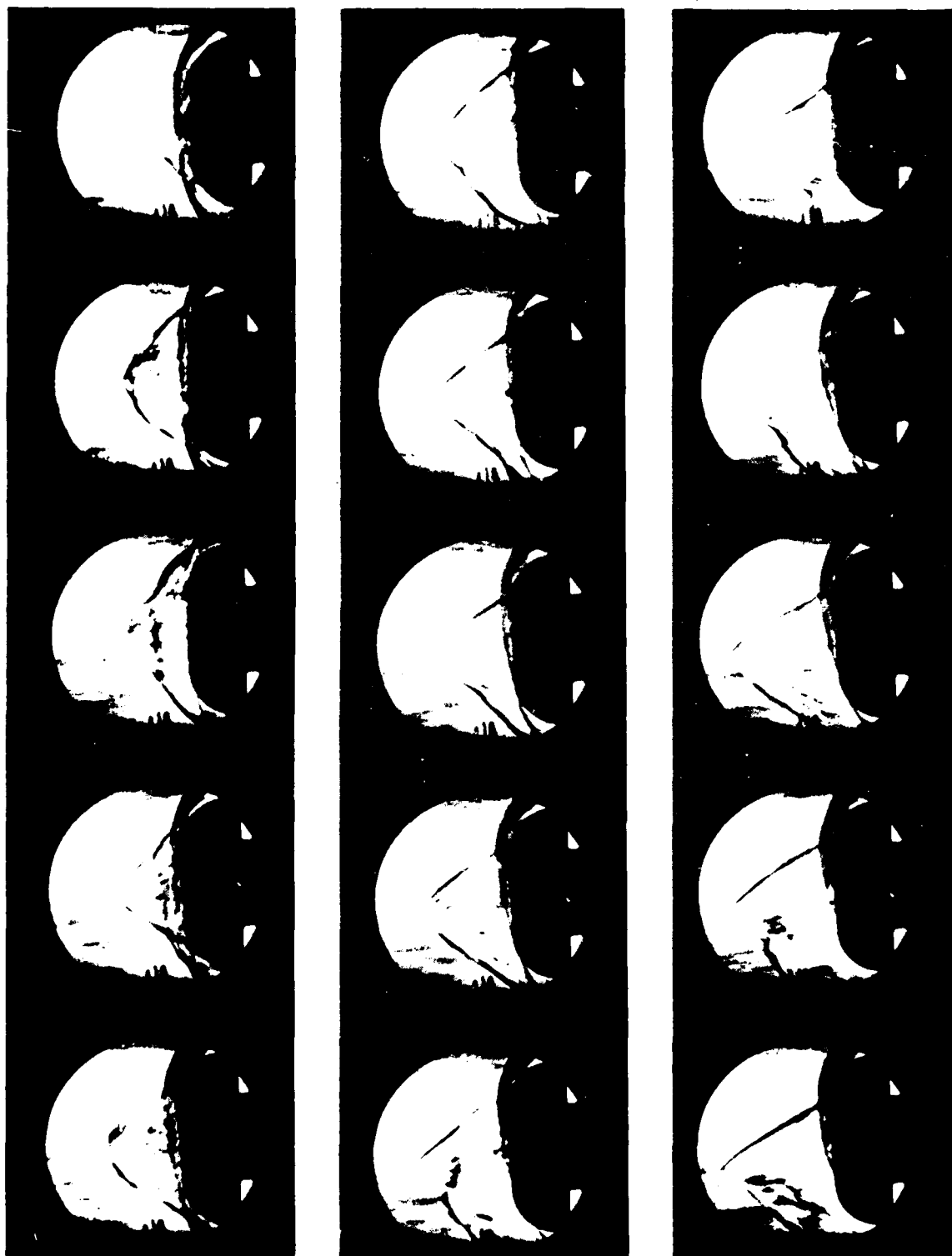


Figure 83b PHOTOGRAPHIC SEQUENCE FROM SINGLE PARTICLE LAUNCH

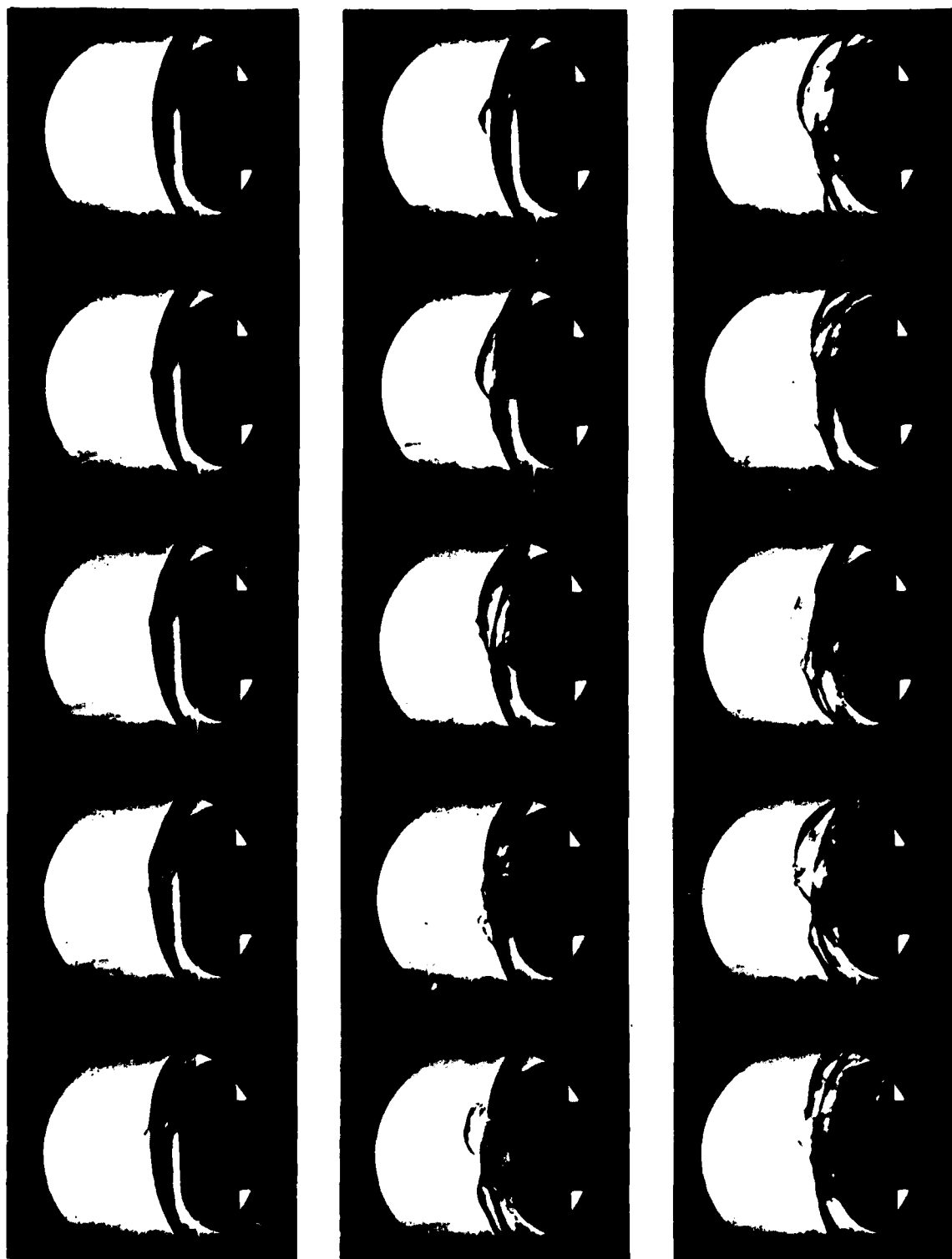


Figure 84a **MULTIPLE PARTICLE INTERACTIONS OVER THE BLUNT NOSE TIP**



Figure 84b MULTIPLE PARTICLE INTERACTIONS OVER THE BLUNT NOSETIP

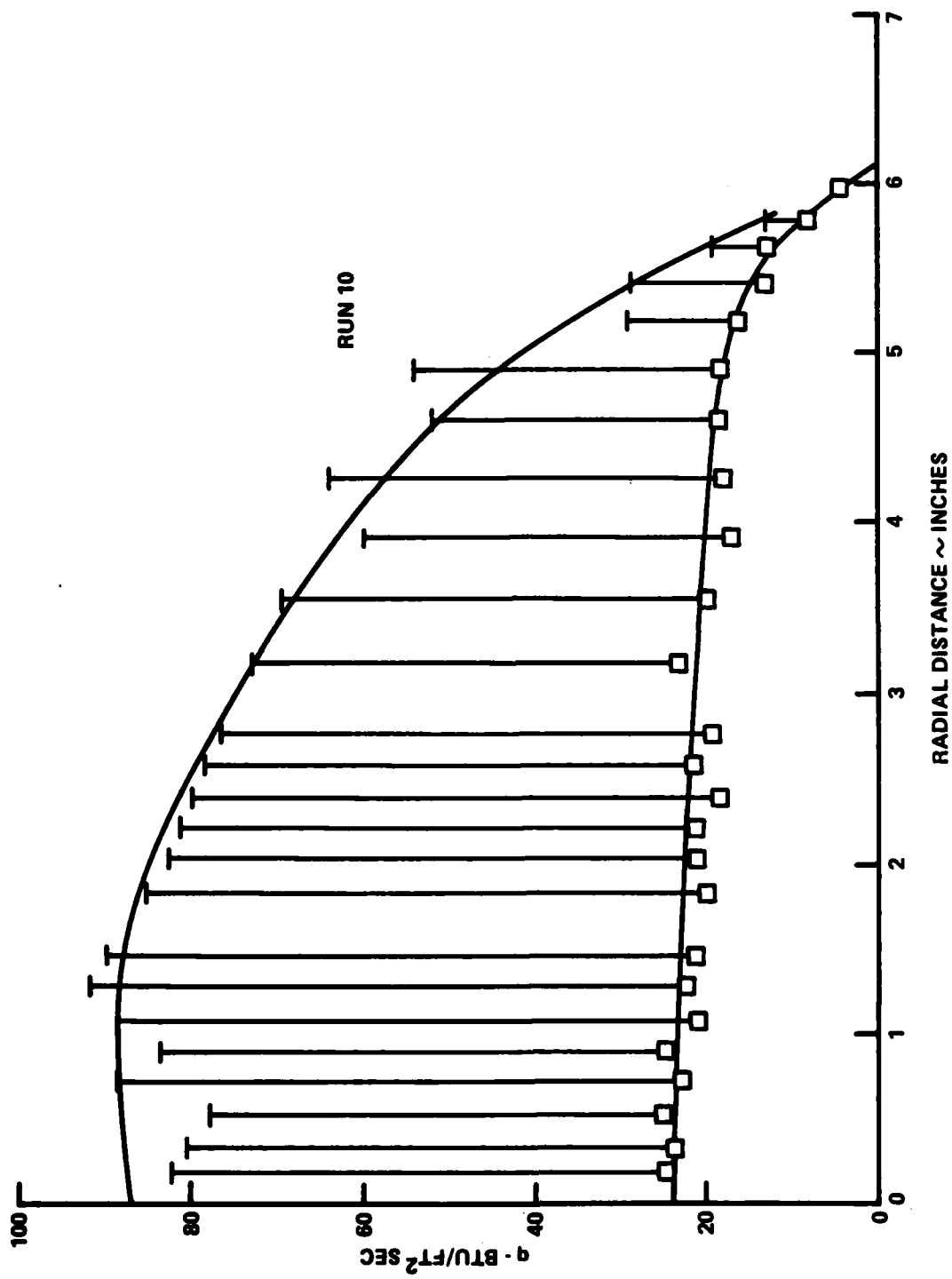


Figure 85 HEATING RATES RESULTING FROM MULTIPLE PARTICLE INTERACTIONS

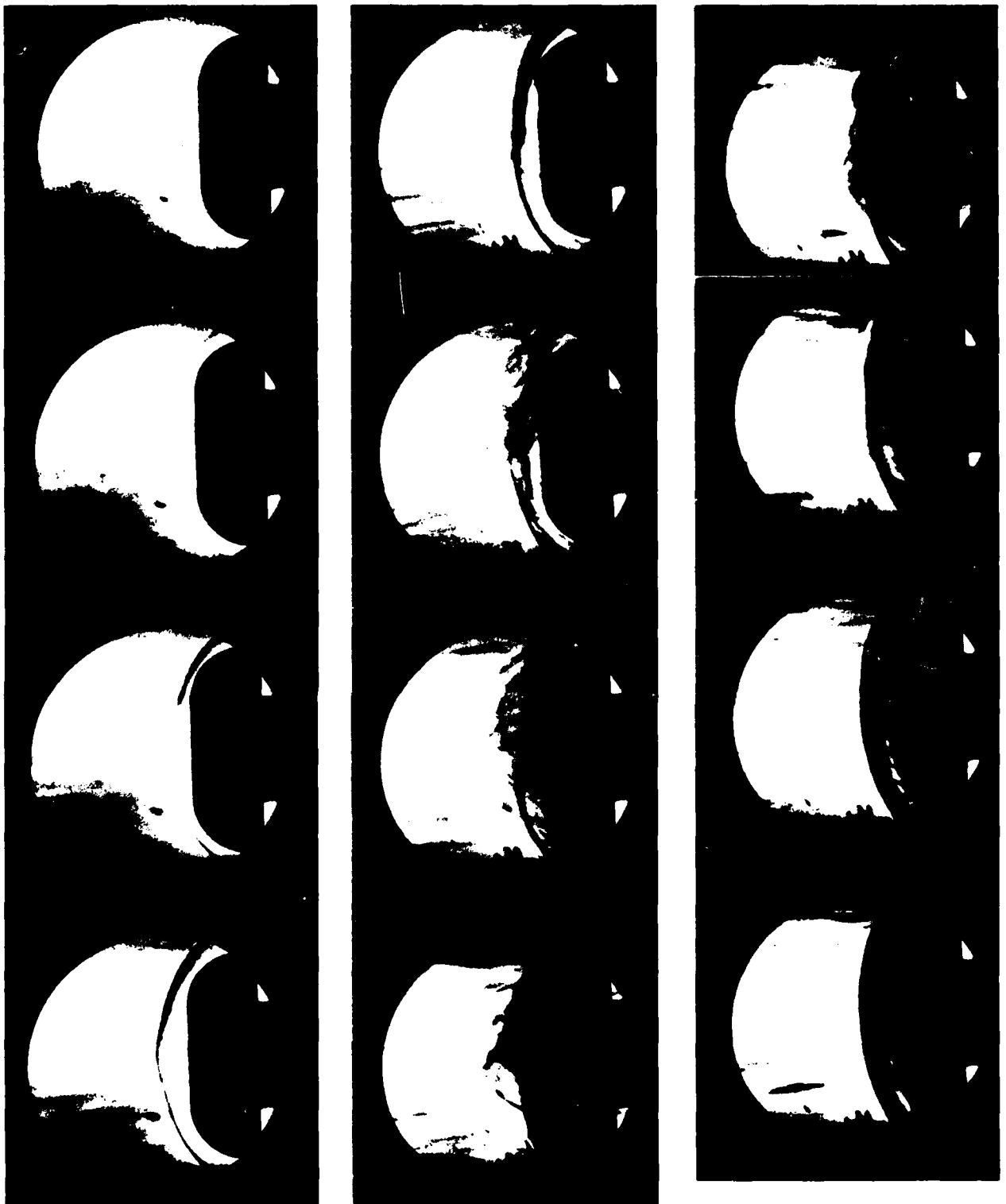
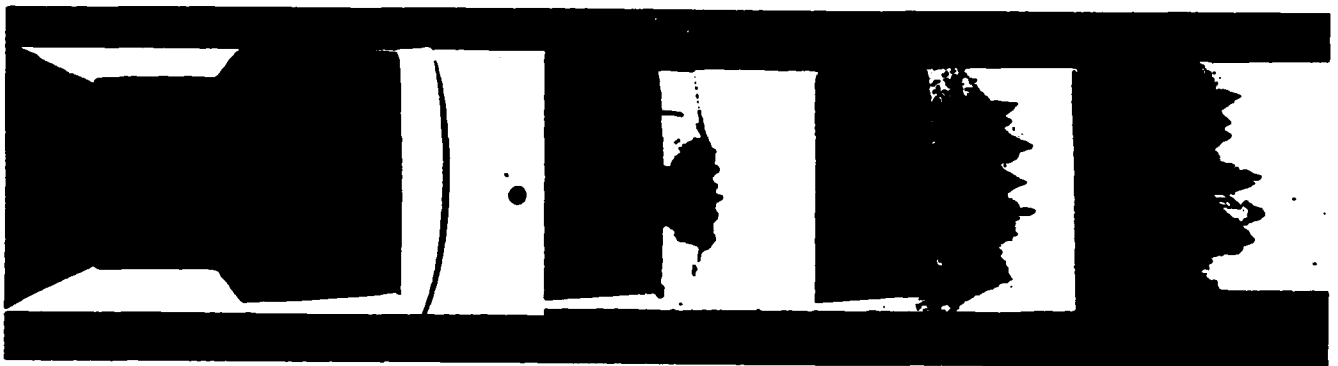


Figure 86 DUST INTERACTIONS IN THE SHOCK LAYER



MODEL VELOCITY: 11,500 fps
RANGE PRESSURE: 350 torr
WATER DROP DIAMETER - 1.5 mm
 $\Delta t = 5.5 \mu\text{sec}$

Figure 87 SEQUENTIAL LASER PHOTOGRAPHS OF DEBRIS FROM WATER-DROP IMPACT
(AEDC BALLISTIC RANGE)

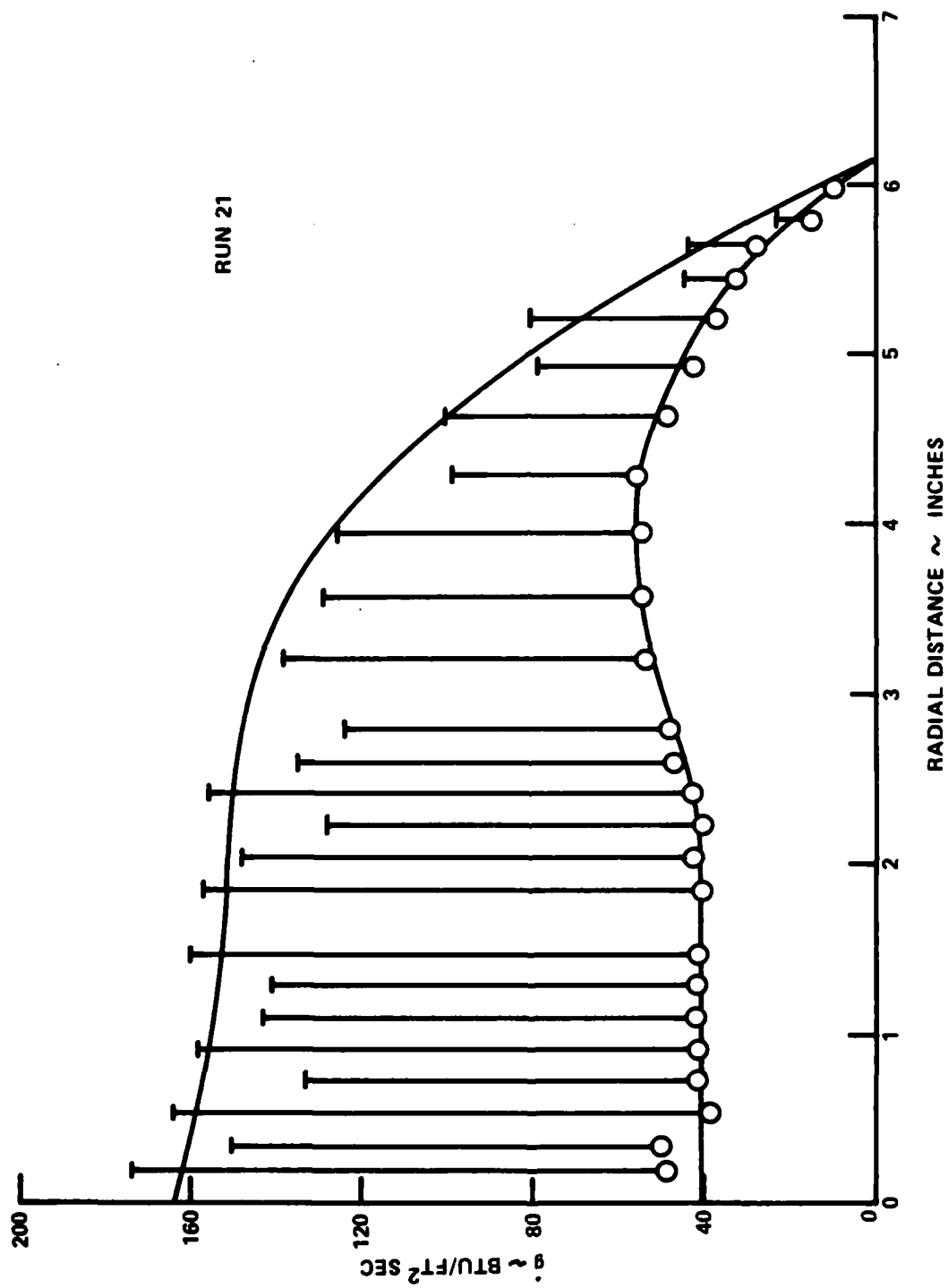


Figure 88 HEAT TRANSFER AUGMENTATION IN A DUST ENVIRONMENT

heating augmentation relative to the heat transfer over a rough model with transition in the stagnation region. Clearly, large heating augmentation occurs in the presence of both turbulent boundary layers and roughness.

4.3.6 Conclusions

Our measurements from the series of studies with particles launched from a blunt body, with the highly instrumented hemispherical and SCANT models described in Figure 74, and from earlier studies with ablated noseshapes in hypersonic high Reynolds number flows, have demonstrated that a very small concentration of minute particles within the airflow can induce significant effects on the structure of the shock layer and the boundary layer over blunt bodies. The relative influence of these particles is a function of the flow regime (Re_D , Me) and the momentum of the particle as it is ejected from the shock layer. For high Reynolds number flows when transition has moved to or ahead of the sonic line, the aerodynamic disturbances caused by small particles in the shock layer can induce transition in the stagnation region. We observed disturbances in the boundary layer, induced by a single particle, to persist within the stagnation region for the order of 1 millisecond before being swept downstream and decaying in the strong expansion process. Because the residence times are so large, a very low density of particles can induce significant effects in hypersonic flows. For flow at lower Reynolds numbers, where the laminar boundary layer in the stagnation regime is relatively stable, the first mechanism responsible for enhanced heating is toroidal-vortex/boundary layer interaction resulting from a small penetration of the bow shock by the ejected particle. The disturbance created by the ring vortex as it is swept across the model surface causes heating enhancements of the order of 50%. Again, the major mechanisms are associated with boundary layer tripping and vorticity enhancement. When the particle has sufficient energy to penetrate beyond the bow shock by between 0.5 and 1 body diameter, the quasi-steady particle-shock/bow-shock interaction can generate heating rates of 300% to 500% of the undisturbed value. Here, the basic heating mechanism is associated with shear-layer impingement (generated by shock/shock interaction) on the surface of the model. For particle penetrations beyond one body diameter, the pulsating separated flow is driven by the alternating attachment and re-attachment of a separated conical turbulent shear layer. Again, heating levels of over three hundred times the undisturbed values can be generated by shear-layer impingement.

Shear-layer impingement, as opposed to vortex interaction, as assumed in the systems models of convective heating augmentation, is the principal mechanism of heating augmentation for multiple particle interactions in a dusty environment. Although flow oscillations are observed about individual particles, we do not, in general, observe the gross pulsations characteristic of single particle interactions. The enhanced heating levels increase with the number of particles in the shear layer, up to the point that shocks from adjacent particle coalesce; thereafter, an increase in the number of particles does not increase convective heating augmentation. The complexity of these interactions and the mechanisms responsible for enhanced heating are such that the gross heating enhancement cannot be computed with any accuracy by existing theoretical models.

Section 5
EXPERIMENTAL STUDIES OF MECHANISMS OF
BOUNDARY LAYER TRANSITION IN HYPERSONIC FLOW

5.1 INTRODUCTION

5.1.1 Background

Boundary layer transition is one of the most important parameters in the design of hypersonic vehicles such as ballistic and maneuverable re-entry vehicles and the space shuttle. However, there remains a considerable gap between "engineering" efforts to correlate the occurrence of transition and fundamental theoretical studies. The engineering, or "systems," studies have concentrated on correlating experimental measurements of transition obtained in flight tests, ballistic ranges, and wind tunnels against almost every conceivable parameter, while the fundamental studies have been aimed principally at exploring the modes of instability of the laminar boundary. The basic problem is that boundary layer transition is controlled by the detailed aerodynamic environment and can occur through different mechanisms on different models in the same test environment or on the same model in different aerodynamic environments. In his classic studies of boundary layer transition, Osborn Reynolds¹⁹ not only demonstrated the importance of the Reynolds number to the transition process, but also showed that the particular experimental apparatus and the level of background noise play important roles in determining at what Reynolds number transition takes place.

Both theoretical and experimental studies of transition in incompressible flows have suggested that, in the absence of large freestream disturbances or disturbances from within the boundary layer, the two-dimensional Tollmien-Schlichting²⁰ model is a good representation of the initial breakdown of laminar flow. However, when velocity fluctuations of over 10 percent are introduced into the freestream, "by-pass" modes involving the generation of three-dimensional, streamwise, vortex-like instability may be the principal mechanisms involved in the transition process. The regular instabilities which precede transition are of key importance in understanding the basic transition mechanisms. While Tollmien-Schlichting waves have been identified in both theoretical and experimental studies at low speed in "quiet" wind tunnel facilities, the literature contains little reference to experimental observations of regular instabilities preceding

transition in supersonic or hypersonic flows. Mack²¹, among others, has speculated that a helical instability mode should be the dominant feature of the flow upstream of the non-linear breakdown into turbulence of a laminar boundary layer in supersonic flow. However, the lack of direct evidence to support this prediction has slowed theoretical developments of this nature. An understanding of how disturbances in the freestream influence transition requires knowledge of the coupling mechanisms between the laminar boundary and the outer, inviscid flow. While, in most instability problems, it is necessary only to calculate the conditions for the existence and growth of a disturbance, transition prediction using linear stability theory rests almost completely on the ability to trace the origin of the instability²². Unless the stability waves can be assigned a specific amplitude, there is no way to relate transition to a particular disturbance environment. Second-order closure models, which also require detailed knowledge of the coupling mechanisms, have been used to predict transition in the presence of surface roughness and tunnel noise. However, it remains to be demonstrated that the required closure approximation can be formulated to represent an adequate physical description of the transition process, for these methods cannot describe the occurrence in the laminar boundary layer of regular instabilities.

One avenue of progress in the prediction of boundary layer transition may come through an understanding of how the instability modes and the disturbances which caused them are related to the mechanics of the gross breakdown mechanisms which precede the development of fully turbulent flow. It is against this background that the observations of boundary layer transitions described in this section are presented. In general, the author is highly skeptical of the generality of the results of studies of boundary layer transition conducted in wind tunnels, ballistic ranges, or even in full-scale flight tests. However, there are reasons for believing that while, in a particular aerodynamic environment, the transition Reynolds number may be influenced by freestream or wall conditions, such disturbances may not influence the basic mechanisms involved in the transition process. However, a high degree of background disturbance may trigger instability modes which would "by-pass" the relatively weak Tollmien-Schlichting instability. In the following text, we first discuss the objective of these studies and the models and instrumentation employed. We next describe the experimental facility used and offer evidence to suggest that it is intrinsically quieter than most high-speed wind tunnels. Then, the flow-visualization techniques used in the experimental program are described. Finally, we discuss the basic results from the studies and

conclude with the description of the mechanics of the transition process observed in hypersonic flow.

5.1.2 Objectives of Experimental Program

The object of this study was to examine, using microsecond spark schlieren photography and ultra-high-speed cinematography, the structure and development of the transition process in hypersonic flows over slender bodies. We wished to examine the formation of the regular fluid-dynamic instabilities which precede transition and follow their development as they are swept downstream. The mechanics of the gross breakup of the laminar boundary layer was the next focus of interest. Finally, we attempted to examine the formation and growth of the eddies developed between the middle and the end of the transition process.

5.2 MODEL AND INSTRUMENTATION

These studies of the mechanisms involved in boundary layer transition were conducted in the Calspan 96-Inch Shock Tunnel. The measurements were made at Mach 11 and 13 for Reynolds numbers from 1×10^6 to 10×10^6 in the large contoured "D" nozzle. A sharp 6° conical model, which contained high-frequency thin-film instrumentation, was employed in these studies.

Flow-field visualization was accomplished with a single-pass schlieren system with 18-inch mirrors and 15-ft focal light. A Cordin Model 375 High Speed Camera and a single-shot system utilizing a microsecond spark were employed to capture the photographic record. The Cordin Camera (shown in Figure 89), which uses a rotating prism to place the images on a film wrapped around the inside of a circular enclosure, was run at the equivalent of 100,000 frames per second. Reconstructing the photographic sequence from this camera is not a simple matter, because successive images are placed in a complex geometric sequence around the drum. We found that, while we were able to successfully "stop" the movement of the transition instabilities in the boundary layer flows with a microsecond spark, the images obtained with the Cordin camera were blurred. Image-enhancement techniques were employed on the photographs from the Cordin camera, and the trained observer could readily interpret the timewise movement of the instabilities along the cone. However, for ease of interpretation, we have chosen to illustrate our findings with the photographs taken with the microsecond spark source.

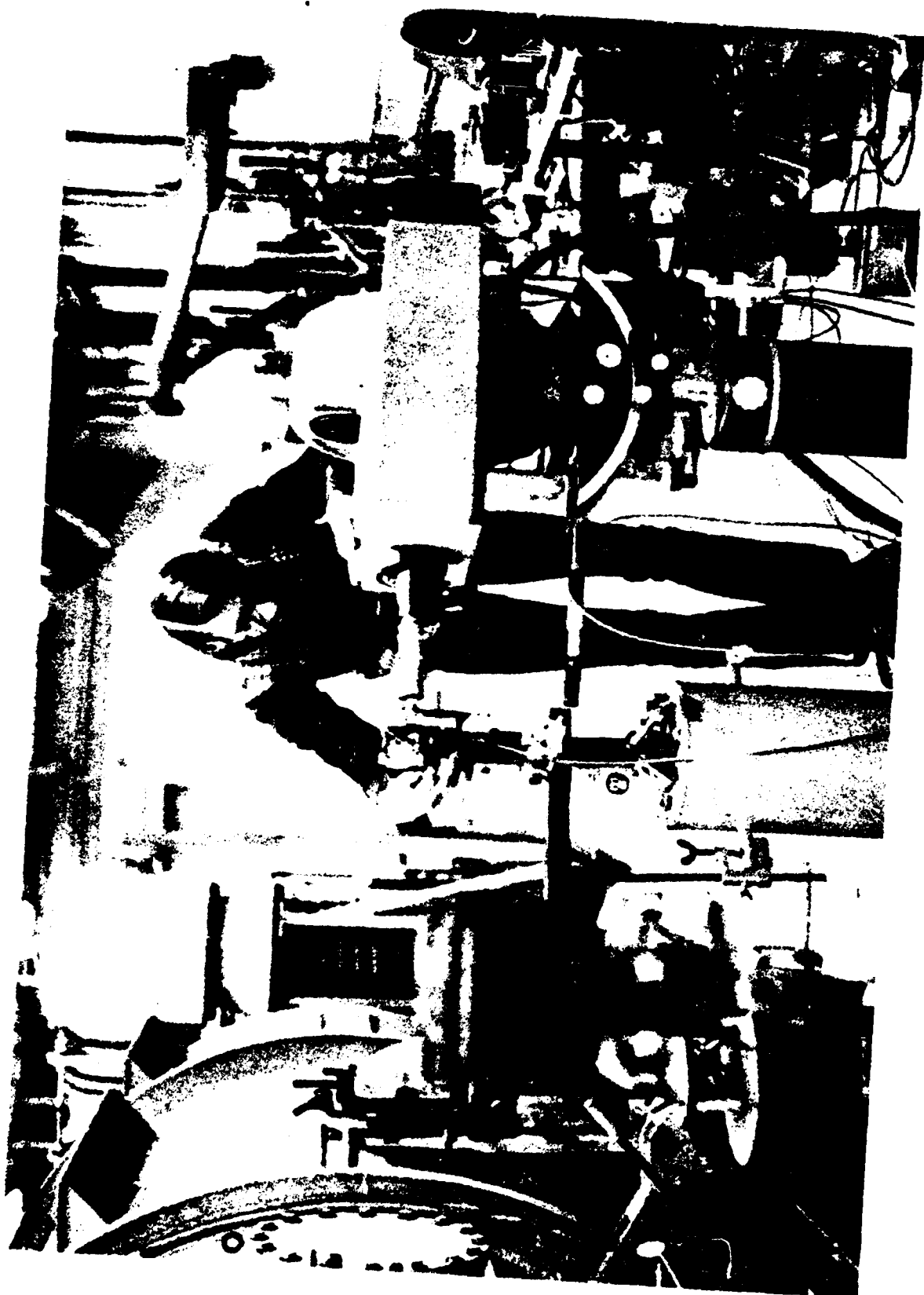


Figure 89 CORDIN MODEL 375 HIGH-SPEED CAMERA USED IN CALSPAN
TRANSITION STUDIES

SIGNIFICANCE OF TEST FACILITY USED IN THESE STUDIES
(TUNNEL NOISE VS. TRANSITION)

Experimental studies of transition are of little general value unless it can be shown that the instability modes in the boundary layer remain unexcited by disturbances in the freestream or respond to stronger disturbances generated, for example, by surface roughness. As discussed earlier, the author remains openly skeptical of the general usefulness of any transition data gathered in any wind tunnel. However, comparisons between the measurements of transition Reynolds number made in these and earlier studies at Calspan with free-flight measurements suggest that, because of its mode of operation, physical size, and the extremely large expansion ratios involved in generating Mach 13.0 flow, there is a very low level of noise in the freestream of the 96-Inch Shock Tunnel. Studies at AEDC²³ and NASA-Langley²⁴ have demonstrated that, in conventional supersonic wind tunnels, the Reynolds number at which transition occurs is strongly influenced by the fluctuating pressure level in the freestream. Pate and Schueler²³ have demonstrated that the level of pressure fluctuation can be related to the geometric features of the tunnel used and to the characteristics of the boundary layer on the tunnel walls. A direct result of Pate and Schueler's studies is that a decrease in tunnel size for the same freestream conditions *should result in a decrease* in the transition Reynolds number. When we compared our transition measurements obtained in the 96-Inch Shock Tunnel, equipped with a 24-inch-diameter "A" nozzle, with those obtained in the same tunnel equipped with the 48-inch-diameter "D" nozzle, we anticipated a significant difference in the Reynolds number at which transition took place. However, as demonstrated in Figure 90, where we have plotted $Re_0^{0.2}$ versus the freestream unit Reynolds number, the Pate and Schueler scaling does not appear to apply, even though a unit Reynolds variation is evident. It should be mentioned that the Calspan studies were conducted at Mach numbers and Reynolds numbers well above those used by Pate and Schueler in their studies. As a result, we believe that, in our test environment, the magnitude of the noise radiated from the walls and its intensity on the tunnel axis are significantly less than those found in the experiments analyzed by Pate and Schueler. Transition Reynolds numbers of over 200×10^6 are predicted if the Pate and Schueler correlation is extrapolated to the tunnel configurations and freestream test conditions at which our studies were performed. Clearly, such values are well in excess of meaningful physical quantities. Thus, it was not surprising to find that the measurements made in the Calspan studies fall below the Pate and Schueler correlation, as shown in Figure 91. These results suggest that, in our studies,

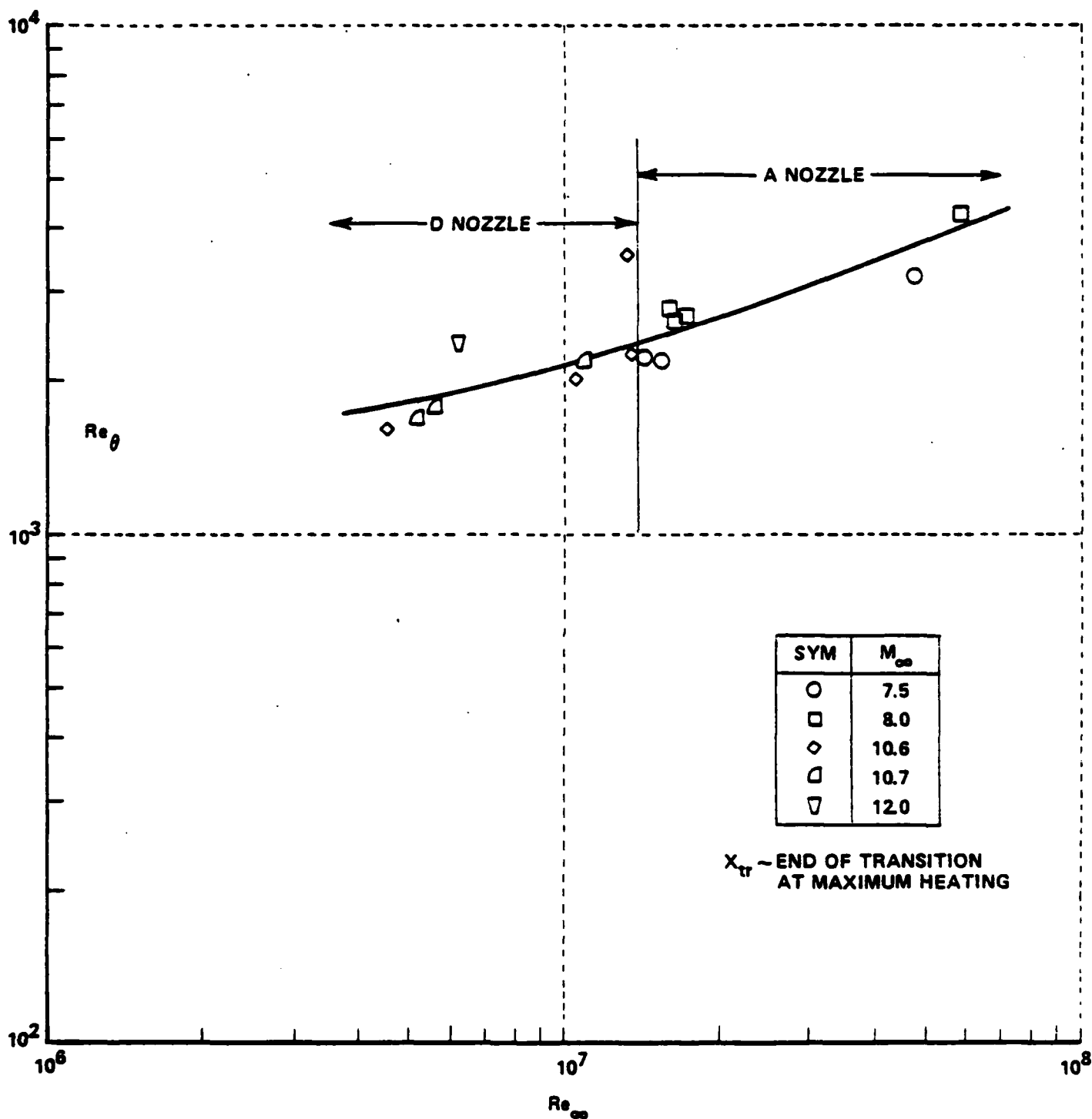


Figure 90 CORRELATION OF TRANSITION SHOWING EFFECTS OF TUNNEL SIZE

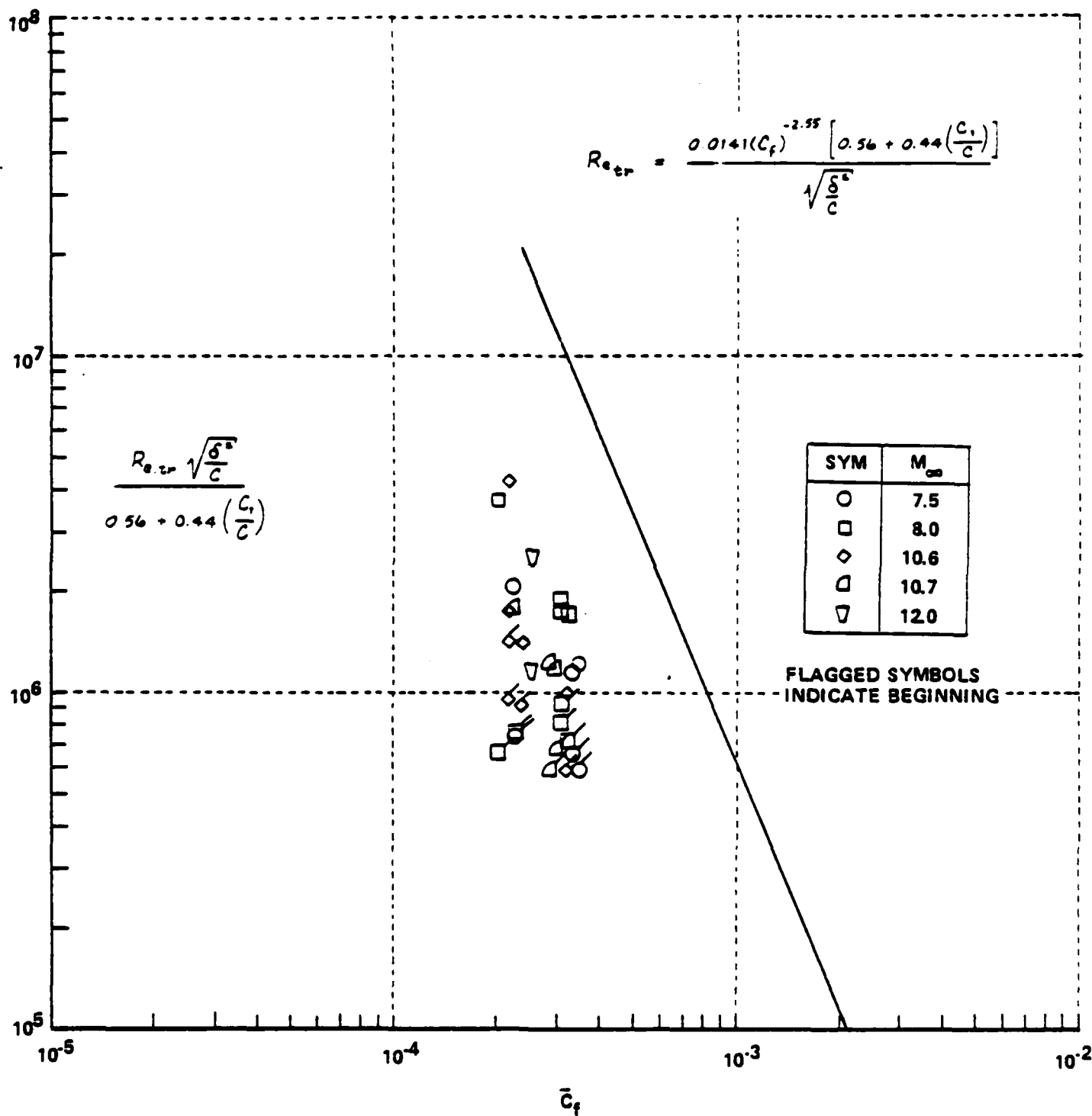


Figure 91 CORRELATION OF FLAT-PLATE TRANSITION DATA IN TERMS OF
 PARAMETERS SUGGESTED BY PATE AND SCHUELER

pressure fluctuations resulting from acoustic radiation from the tunnel walls may not be a dominant disturbance in the freestream. Thus, the position of transition on the model examined in the present studies may be controlled by disturbances more complex than simple acoustic noise. It remains to be determined whether transition can be related to the fluctuating pressure level in the freestream, which, in turn, might be related to fluctuations in the reservoir conditions. However, because of the large expansion ratios in the "A" and "D" nozzles, we must look to fluctuations in the enthalpy in the reservoir, as opposed to velocity fluctuations, as a potential source of freestream disturbances.

One of the most successful formats that we have found for comparing and correlating the transition measurements made in the 48-Inch and 96-Inch Shock Tunnels at Calspan with measurements from ballistic ranges and flight tests has been in terms of the Reynolds number based on local momentum thickness, and the local Mach number M_{LOCAL} . Correlations of the transition measurements made on sharp cones and flat plates in the present and earlier studies at Calspan, flight measurements reported by TRW, and measurements in the ballistic ranges at AEDC and NSWC are shown in Figure 92. We see that there is relatively good agreement between the shock tunnel measurements and those obtained in free flight. A further comparison between our measurements and those made in the more recent studies of Reda²⁵, plotted in terms of the unit Reynolds number, are shown in Figure 93. We find relatively good agreement between the two sets of measurements, and, in common with the studies of Potter²⁶, Sheetz²⁷, and Reda, we observe a unit Reynolds number effect. The source and significance of the unit Reynolds number effect have been the subject of extensive debate. The analyses of Morkovin²⁸ and Reshotko²⁹ have suggested that the unit Reynolds number effects may be traced to a sensitivity to the non-dimensional frequency (U_e^2/ν_e) or to the wavelength of the disturbance (U_e/ν_e); however, in reality, the disturbance-inducing transition may stem from superposition of a number of different mechanisms.

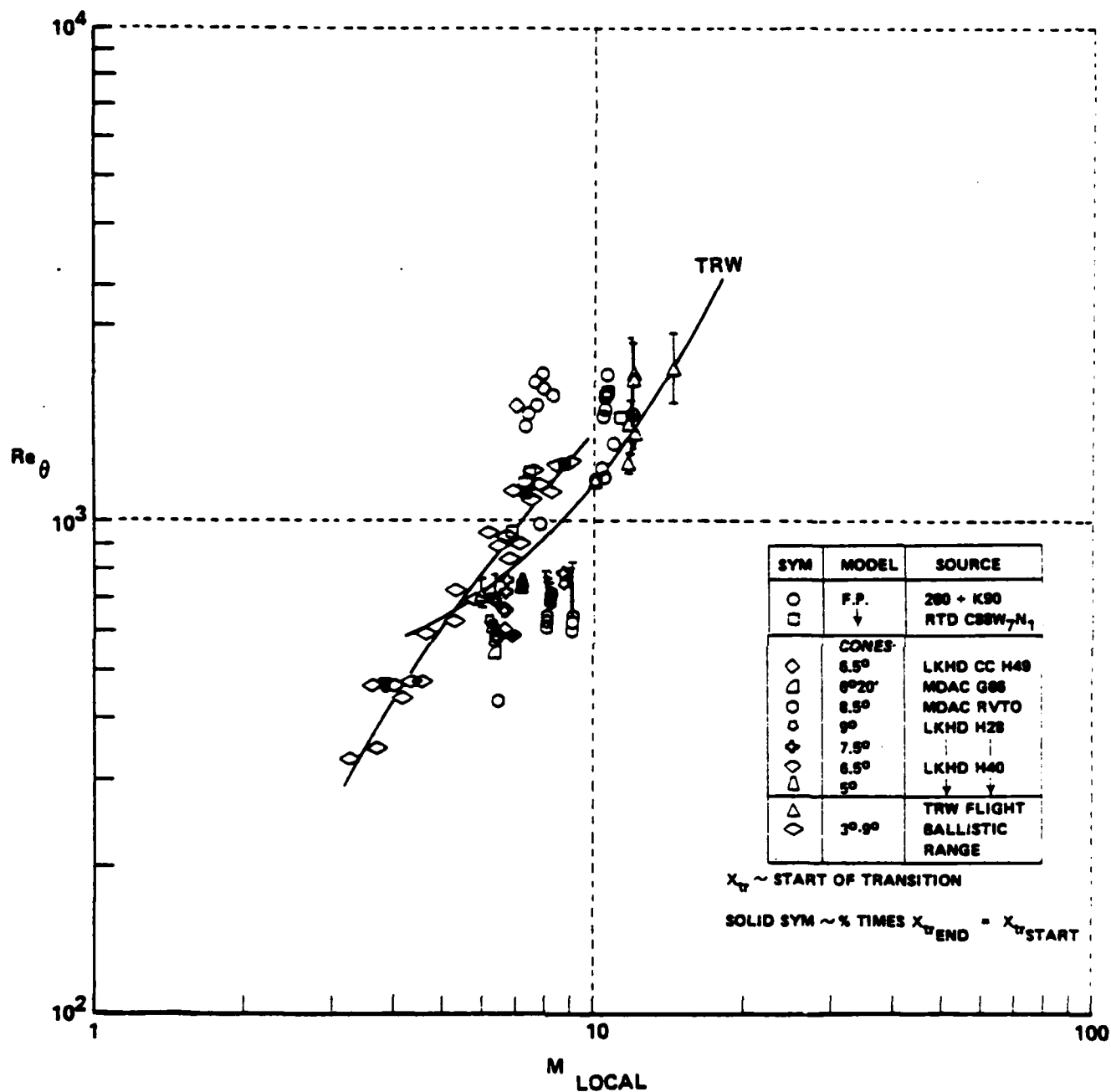


Figure 92 CORRELATION OF TRANSITION MEASUREMENTS IN CALSPAN SHOCK TUNNELS WITH BALLISTIC AND DOWNRANGE MEASUREMENTS

SOURCE	SYM.	θ_C	M_∞	M_e	$(T_W/T_{aW})_e$	U_e^2 / ν_e , 1/SEC.	FACILITY
REDA	○	5°	4.4	4.2	.22	$.28 - 1.66 \times 10^{11}$	RANGE
POTTER	— —	10°	5.0	4.3	.19	$.42 - 5.27 \times 10^{11}$	RANGE
		10°	2.3	2.1	.52	$.17 - 1.00 \times 10^{11}$	RANGE
SHEETZ	□	5°	5.0	4.8	.19	$1.40 - 1.71 \times 10^{11}$	RANGE
PRESENT STUDY	◐	6°	13.2	10.2 - 10.5	.14	$.34 \times 10^{11}$	SHOCK TUNNEL

PRESENT RESULTS ARE PRIMARY-RAY DATA ($\phi < 45^\circ$)

CORRECTED FOR $\phi > 0^\circ$, $\alpha > 0^\circ$, AFTER POTTER

— LEAST-SQUARES FIT OF PRIMARY-RAY DATA, $\left(\frac{U_e}{\nu_e}\right) > 10^6/\text{IN.}$

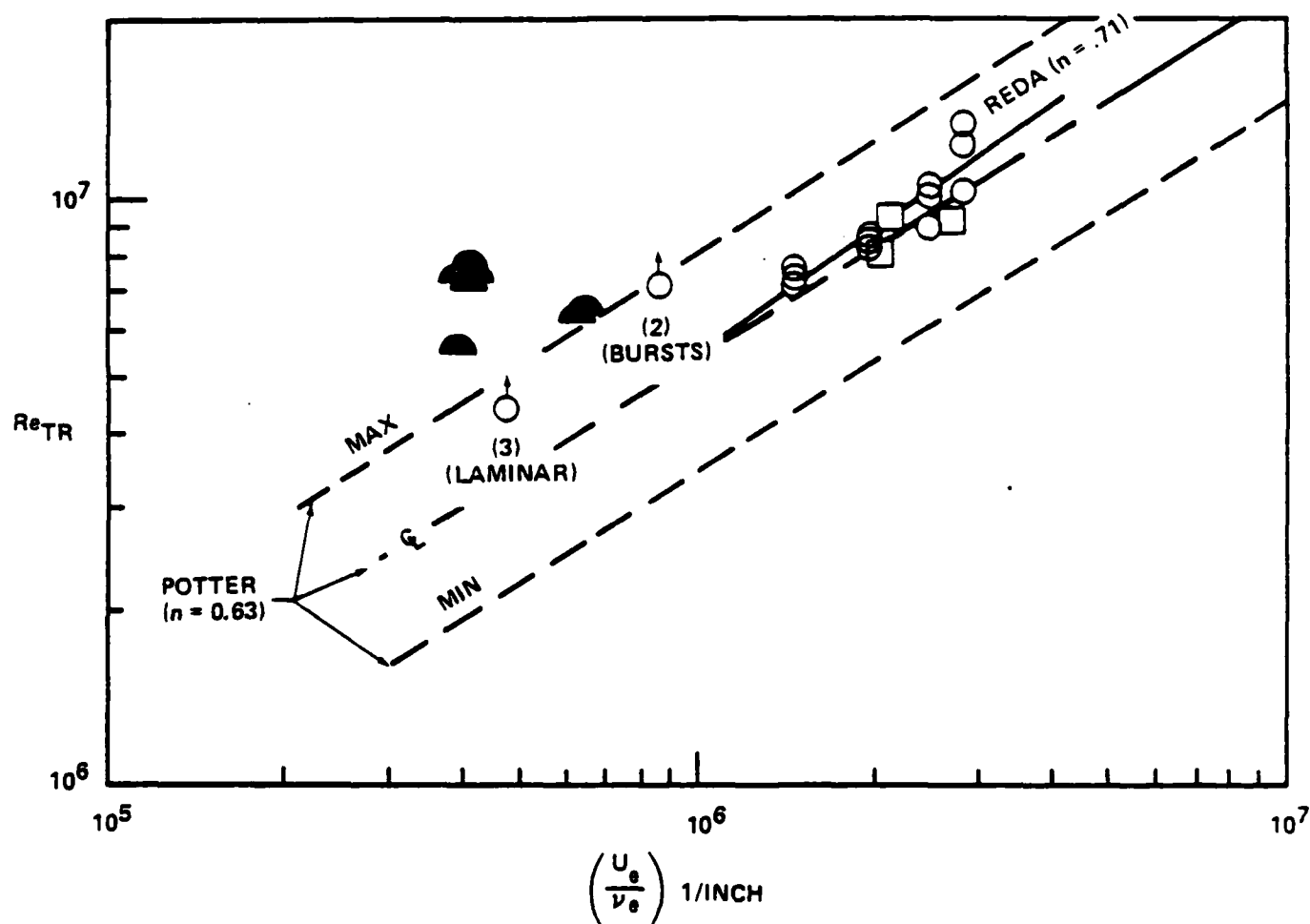


Figure 93 TRANSITION REYNOLDS NUMBER VS. UNIT REYNOLDS NUMBER;
PRESENT DATA VS. POTTER AND SHEETZ

5.4 RESULTS OF PHOTOGRAPHIC AND HEAT TRANSFER OBSERVATIONS OF BOUNDARY LAYER TRANSITION IN HYPERSONIC FLOW

5.4.1 Observation on General Characteristics of Transition Regions

The measurements discussed in this section were obtained principally at Mach 13 at unit Reynolds numbers of 1×10^6 to 5×10^6 . Simultaneous heat transfer and photographic records were obtained at each condition. A typical distribution of heating through a transition region is shown in Figure 94. We have found that the length of the transition region on a cone or a flat plate is very close to the length of the laminar flow which precedes it. The heat transfer records for the laminar flow ahead of the rise in average heating which marks the beginning of transition exhibit trains of spikes which, we show later, are "wave-like" instabilities which travel along the cone in "trains" at approximately the speed of the inviscid flow (6000 ft/sec). Then, as regular large-scale instabilities are formed and break up into large vortices, the average heating rises. A composite of the schlieren-photograph and heat transfer records obtained early in the studies, shown in Figure 95, presents a "good picture" of the general structure of the transition region. The "spikes" in the laminar heat transfer trace, which mark the beginning of the transition process, can be described as turbulent bursts, which are fairly well structured, and which travel at very close to the velocity of the inviscid flow. As these bursts are convected downstream, they begin to break up into large-scale instabilities. The convection of these large-scale eddies past a thin-film gage gives rise to the intermittent characteristics shown in Figure 95. In fact, the intermittency relationship

$$C_H = \gamma C_{HTURB} + (1 - \gamma) C_{HLAM}$$

where $\gamma = \frac{1 - e^{-2\xi}}{1 - e^{-2}}$ $\xi = \frac{x - x_{BEG}}{x_{END} - x_{BEG}}$

describes fairly well the distribution of average heating through the transition region as well as capturing the gross mechanics of the transition process. We believe that the intermittency increases along the interaction region because the primary eddies begin to break up and also induce the formation of secondary eddies. As the spectrum of turbulent scale sizes fills out, the heating to the surface approaches the turbulent

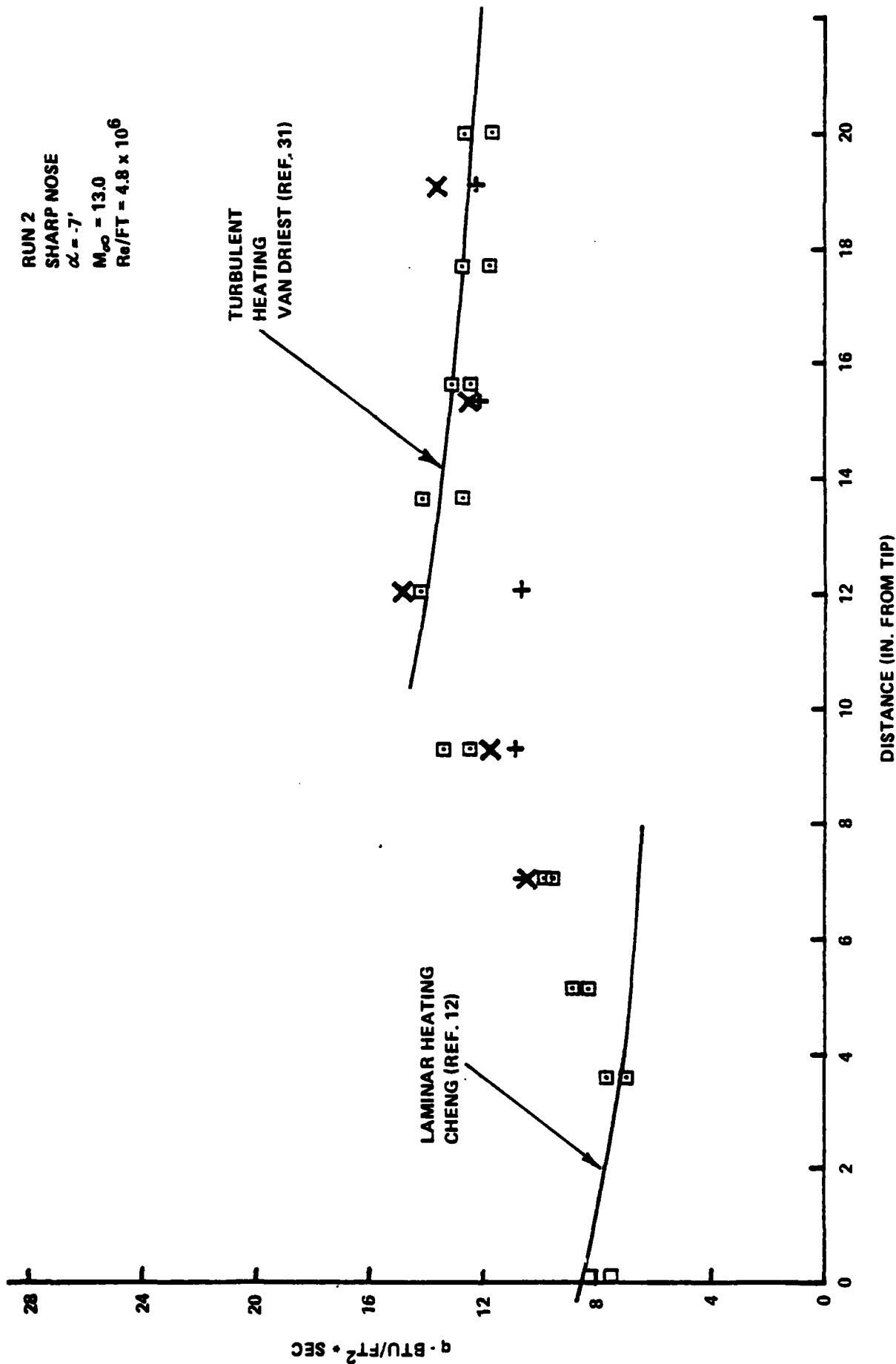


Figure 94 DISTRIBUTION OF HEAT TRANSFER THROUGH A TRANSITION REGION ON SURFACE OF A 6° CONE IN HYPERSONIC FLOW

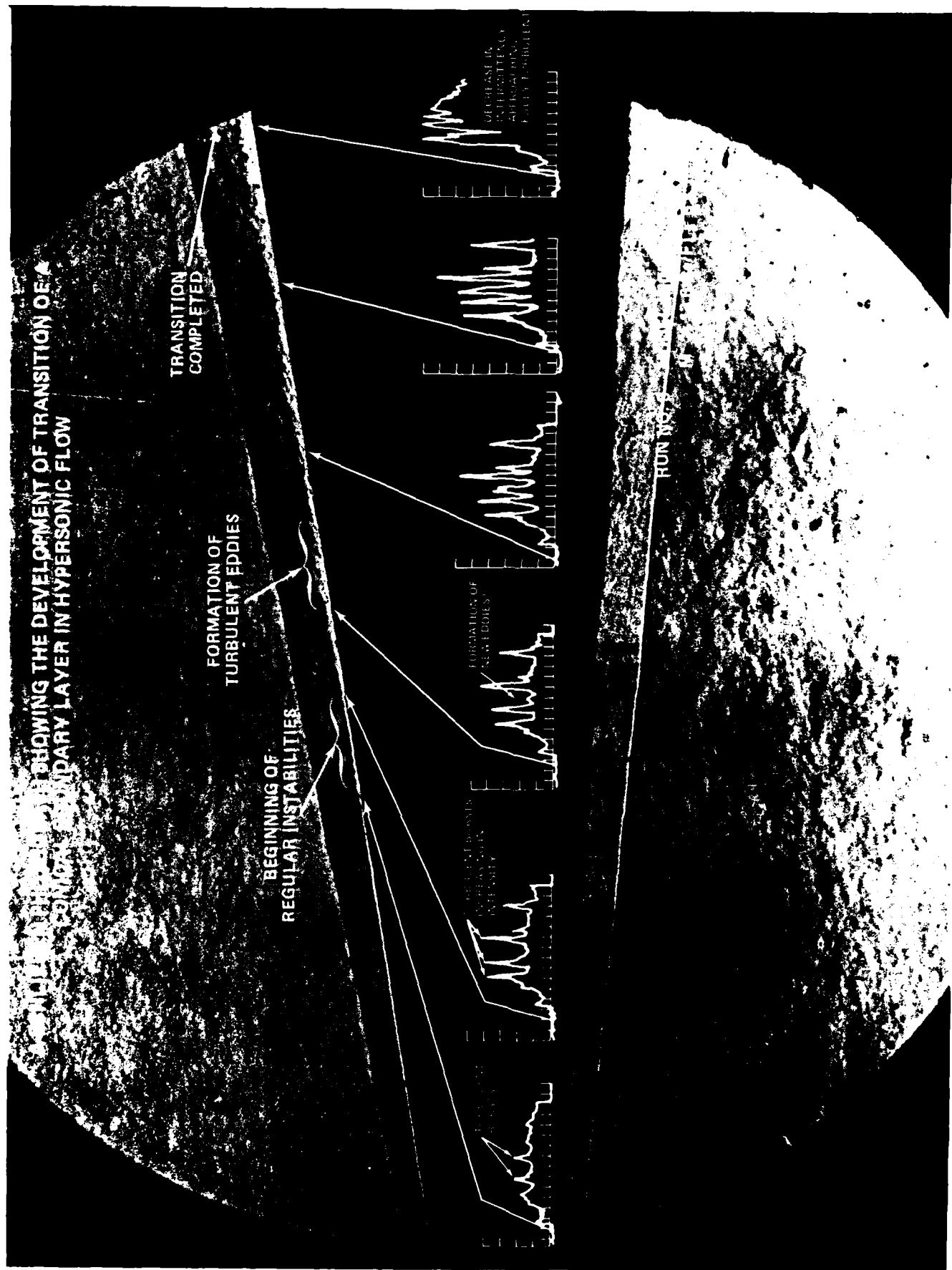


Figure 95 SCHLIEREN PHOTOGRAPH SHOWING DEVELOPMENT OF TRANSITION OF A CONICAL BOUNDARY LAYER IN HYPersonic FLOW

heating rate. As indicated in this general discussion, we observed three consecutive regions reflecting three basic mechanisms which occur as the laminar boundary layer becomes unstable and transition to turbulence takes place: (1) Wave-Like Instability Region; (2) Gross-Instability Region; and, finally, (3) Gross-Mixing Region. These are discussed individually in the following subsections.

5.4.2 Wave-Like Instability Region

Photographic examples of "wave-like" instabilities which preceded the large-scale breakdown into turbulence are shown in Figures 96a, 96b, 96c, and 96d. In many cases, wave trains would be a more accurate description for, as shown in Figure 95, there were many instances where these instabilities did not undergo a significant change in structure as they were convected along the cone. The high-speed photographs obtained with the Cordin camera indicate that, in fact, these instabilities "twisted" as they were convected downstream, suggesting a helical structure. Following the region of "wave-like" instability, the laminar boundary layer began to develop large-scale instabilities at an edge (see Figures 96c and 96d); then, transition began.

5.4.3 Gross-Instability Region

Photographic examples of the development of the transition region following the "wave-like" instabilities discussed in the previous paragraph are shown in Figures 97a, 97b, 97c, and 97d. In Figures 97a and 97b, we show examples of the precursor instabilities, which began at the outer edge of the boundary layer. In Figures 97c and 97d, we see the gross instabilities developing as they were swept downstream, culminating in some very-large-scale turbulent bursts. These disturbances traveled down the cone at convective velocities between 0.5 and 0.8 of the freestream velocity. The gross size of the eddies generated in this region is of the same order as the boundary layer thickness.

5.4.4 Gross-Mixing Region

In Figures 98a and 98b, we show examples of the gross mixing in the transition region which precedes the development of the turbulent boundary layer. These photographs show the "wave-like" instability, followed by the gross instability, followed by a region in which there is large-scale turbulent mixing. In the latter region, it appears that the scale of the turbulence exceeds that in the following, fully turbulent



(a)



(b)

Figure 96 SCHLIEREN PHOTOGRAPHS OF "WAVE-LIKE" INSTABILITIES



(c)

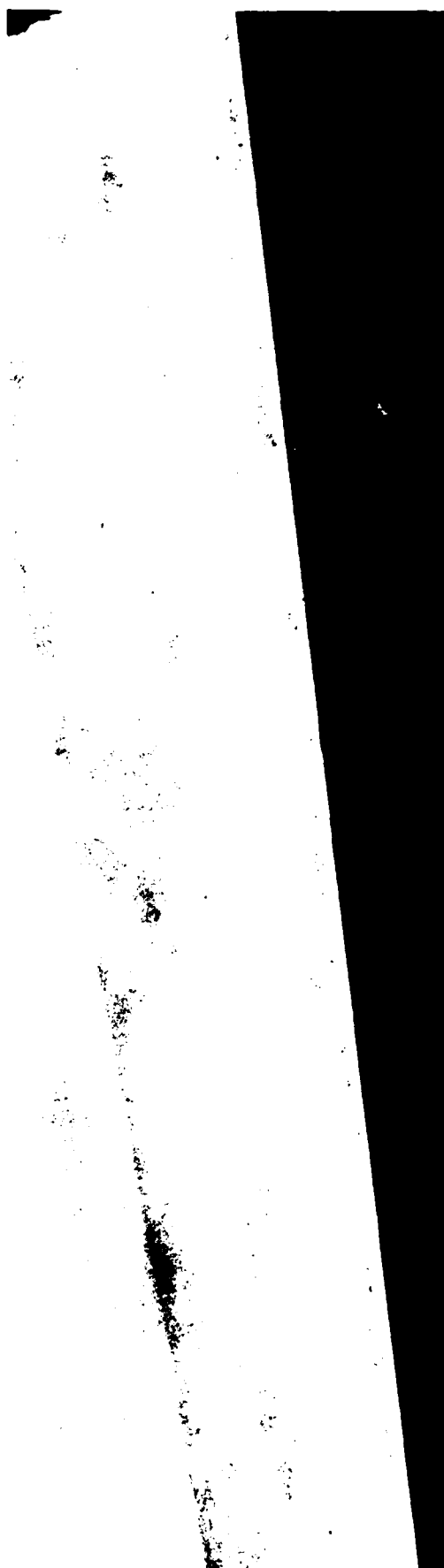


(d)

Figure 96 SCHLIEREN PHOTOGRAPHS OF "WAVE-LIKE" INSTABILITIES (Cont.)



(a)

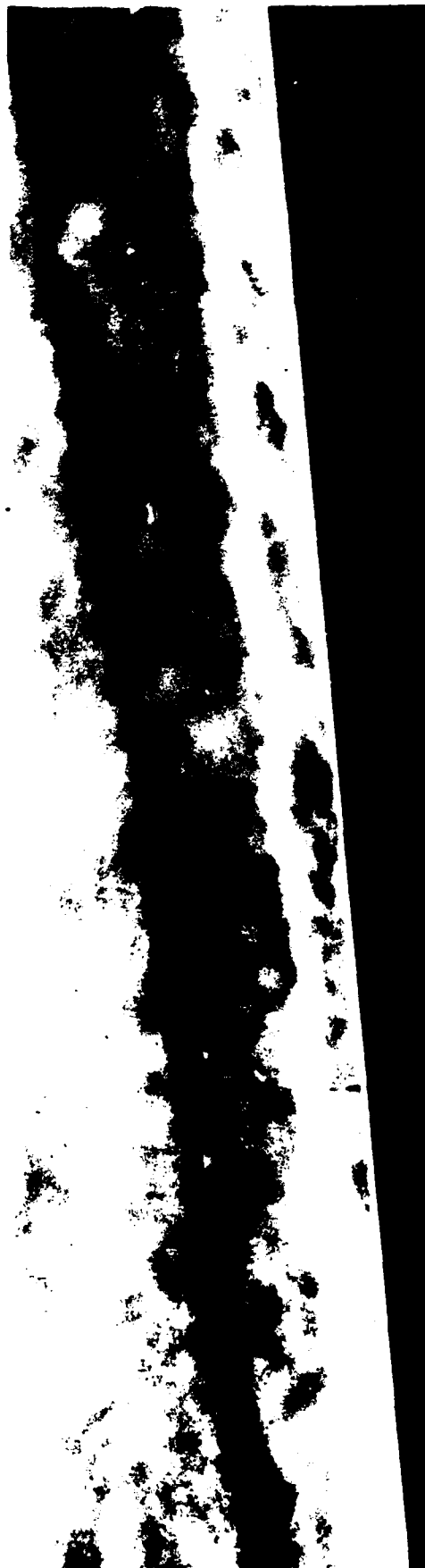


(b)

Figure 97 SCHLIEREN PHOTOGRAPHS OF GROSS-INSTABILITY REGION



(c)



(d)

Figure 97 SCHLIEREN PHOTOGRAPHS OF GROSS-INSTABILITY REGION (Cont.)



(a)

145



(b)

Figure 98 SCHLIEREN PHOTOGRAPHS OF GROSS-MIXING REGION

boundary layer; it is in this region that the heat transfer overshoot occurs. In earlier studies of shock-wave/turbulent boundary layer interaction, we observed that, although the heating levels at the "end" of the transition process approach the turbulent levels, it takes many boundary layer thicknesses (50 to 100) before the scale sizes of the turbulence generated in the transition process are no longer of importance.

5.4.5 Conclusions

Correlations of ballistic-range measurements and measurements made in Calspan's 96-Inch Shock Tunnel at Mach 13 suggest that, because of its relatively low noise characteristics, observations in the Tunnel on the mechanics of hypersonic boundary layer transition can be generally useful. We have identified three basic mechanism in the transition of a hypersonic turbulent boundary layer—a wave-like instability region, a gross-instability region, and a gross-mixing region. The wave-like instability region appears to be helical in nature, and, in fact, these studies suggest that the transition region is a region of gross three-dimensional mixing. In our photographic studies, we required exposure times of the order of 1 microsecond to resolve the turbulent motion in the transition region. Thus, while the thin-film instrumentation and the single-microsecond-shot schlieren system provided excellent diagnostics, a framing camera with an exposure time of approximately 1 microsecond would be required in any future studies of boundary layer transition in hypersonic flow.

REFERENCES

1. Holden, M.S., "Studies of Surface Roughness Effects in Hypersonic Flow," Final Report #7018-A-2, AFOSR, October 1983.
2. Finson, M.L. and Wu, P.K.S., "Analysis of Roughwall Turbulent Heating with Application to Blunted Flight Vehicles," AIAA Paper No. 79-0008, 17th Aerospace Sciences Meeting, 1979.
3. Dahm, T.J. et al., "Passive Nosedip Technology (PANT II) Program," SAMSO-TR-77-11, Acurex Corp., Mountain View, CA, 1976.
4. Dirling, R.B., Jr., "A Method for Computing Rough Wall Heat Transfer Rates on Reentry Nosedips," MDAC Paper WD 1778, AIAA 8th Thermophysics Conference, Palm Springs, 1973.
5. Simpson, R. L., "A Generalized Correlation of Roughness Density Effects on the Turbulent Boundary Layer," AIAA Journal, Vol. 11, No. 2, pp. 242-244, 1973.
6. Holden, M.S., "Maneuvering Vehicle Aerothermodynamics Experiments Program," Ballistic Missile Office, Report No. BMO TR-82-16, CA, 92409, 1981.
7. Coles, D.E., "The Turbulent Boundary Layer in a Compressible Fluid," The Physics of Fluids, Vol. 7, No. 9, pp. 1403-1423, 1964.
8. Van Driest, E.R., "Turbulent Boundary Layer in Compressible Fluids," Journal of Aeronautical Science, 18, pp. 145-160, 1951.
9. Powars, C.A., "Passive Nose Tip Technology Program, Interim Report, Vol. III, Surface Roughness Effects, Part II - Roughness Augmented Heating Data Analysis and Correlation," Aerotherm Report No. 74-96.
10. Crowell, P., "Some Calculations of the Flow Over Biconic Nosedip Configurations", Private Communication.
11. Nikuradse, J., "Stromungsgeretze en rauken Rohren," VDI Forschungsheft No. 361, 1933, Translated as NACA TM 1292, 1950.
12. Holden, M.S., "Studies of Transpiration Cooling, Surface Roughness and Entropy Swallowing in Transitional and Turbulent Boundary Layers Over Nose Tip," Paper presented at the XXXth International Astronautical Congress, Munich, Germany, 1979.
13. Holden, M.S., "An Experimental Study of Massive Blowing from a Nosedip During Jovian Entry," Calspan Report No. 6593-A-1, 1981, Also AIAA Paper 81-1070 presented at the AIAA 16th Thermophysics Conference, Palo Alto, CA, 1981.
14. Reeves, B.L., Todisco, A., Lin, T.C. and Pallone, A., "Turbulent Heating, Hypersonic Flow Over Indented Nosedips", AIAA Paper 76-1086, 1976.

15. Holden, M.S. "Experimental Studies of Separated Flows at Hypersonic Speeds--Part I: Separated Flows over Axisymmetric Spiked Bodies," *AIAA Journal*, Vol. 4, No. 4 (April 1966).
16. Edney, B.E., "Anomalous Heat Transfer and Pressure Distributions on Blunt Bodies in the Presence of an Impinging Shock," The Aeronautical Research Institute of Sweden, Report FAA-115, February 1968.
17. Keyes, J.W. and Hains, F.D., "Analytical and Experimental Studies of Shock Interference Heating in Hypersonic Flows," NASA TN D-7139, May 1973.
18. Holden, M.S., "Studies of Transitional Heating and Flow Instabilities Over Ablated Nose Shapes," Calspan Report Number AB-5646-A1-1, September 1975.
19. Reynolds, O., "An Experimental Investigation of the Circumstances Which Determine Whether the Motion of Water Shall Be Direct or Sinuous and of the Law of Resistance in Parallel Channels," Trans. Roy. Soc. (London) A174, 1883, pp. 935-982, *Sci. Papers* 2:51.
20. Schlichting, H., Boundary Layer Theory, 6th edition.
21. Mack, L.M., "Transition Prediction and Linear Stability Theory," in AGARD Conference Proceeding No. 224, "Laminar-Turbulent Transition," May 1977.
22. Mack, L.M., "Computation of the Stability of the Laminar Compressible Boundary Layer," in Methods in Computational Physics (B. Alder, ed.), Vol. 4, 1965, Academic Press, N.Y., pp. 247-299.
23. Pate, S.R. and Schueler, C.J., "An Investigation of Radiated Aerodynamic Noise Effects on Boundary-Layer Transition in Supersonic and Hypersonic Wind Tunnels," AIAA Paper No. 68-375, April 1968.
24. Stainbeck, P.C., Fischer, M.C. and Wagner, R.D., "Effects of Wind-Tunnel Disturbances on Hypersonic Boundary Layer Transition," AIAA 10th Aerospace Sciences Meeting, San Diego, California, 17-19 January 1972.
25. Reda, D.C., "Boundary-Layer Transition Experiments on Sharp, Slender Cones in Supersonic Freeflight," AIAA Paper 78-1129, July 1978.
26. Potter, J.L., "Boundary-Layer Transition on Supersonic Cones in an Aeroballistic Range," AIAA Journal, Vol. 13, No. 3, March 1975.
27. Sheetz, N.W., Jr., "Free-Flight Boundary Layer Transition Investigations at Hypersonic Speeds," AIAA Paper No. 65-127, 2nd Aerospace Sciences Meeting, New York, N.Y., Jan. 1965.
28. Norkovin, M.V., "Instability, Transition to Turbulence and Predictability," Keynote Address to AGARD Symposium on Laminar-Turbulent Transition, Technical University of Denmark, Copenhagen, Denmark, 2-4 May 1977.
29. Reshotko, E., "Boundary-Layer Stability and Transition," Annual Review of Fluid Mechanics, Vol. 8, 1976, pp. 311-349.
30. Van Driest, E.R., "Turbulent Boundary Layer in Compressible Fluids," J. Aero. Sci., 1951, 18, N. 3, pp. 145-160.